Development of Composite Material using Mine Waste

A Thesis submitted in partial fulfilment for the Degree of

DOCTOR OF PHILOSOPHY

In Civil Engineering

Goa College of Engineering, Farmagudi

GOA UNIVERSITY

By

SATYESH AVADHUT SHENVI KAKODKAR

GOA COLLEGE OF ENGINEERING

GOA UNIVERSITY

April 2026

Development of Composite Material using Mine Waste

A Thesis submitted in partial fulfilment for the Degree of

DOCTOR OF PHILOSOPHY

In Civil Engineering

Goa College of Engineering, Farmagudi

GOA UNIVERSITY



By

SATYESH AVADHUT SHENVI KAKODKAR

Under the Supervision of

PROF. ULHAS G. SAWAIKER

Department of Civil Engineering

GOA COLLEGE OF ENGINEERING, FARMAGUDI

GOA UNIVERSITY

April 2026

DEPARTMENT OF CIVIL ENGINEERING

GOA COLLEGE OF ENGINEERING, GOA UNIVERSITY

DECLARATION

I, Satyesh Avadhut Shenvi Kakodkar hereby declare that my thesis entitled "Development of Composite Material using Mine Waste" represents work that has been carried out by me and that it has not been submitted, either in part or full, to any other University or Institution for the award of any research degree.

Place: **Goa University,Taleigao.**

Date: **April 2026**

Satyesh Avadhut Shenvi Kakodkar

CERTIFICATE

This is to certify that the work contained in this thesis entitled"Development of Composite Material using Mine Waste" is submitted by Mr. Satyesh Avadhut Shenvi Kakodkar (P.R.No. 200106892) to the Department of Civil Engineering, Goa College of Engineering, affiliated to Goa University, for the thesis presentation required for the degree of Doctor of Philosophy in Civil Engineering.

Dr. Ulhas G. Sawaiker

Professor, Department of Civil Engineering &

Head, Department of Mining Engineering

Goa College of Engineering, Farmagudi, Goa , affiliated to Goa University

DEPARTMENT OF CIVIL ENGINEERING

GOA COLLEGE OF ENGINEERING, GOA UNIVERSITY

APPROVAL SHEET

The Thesis entitled "Development of Composite Material using Mine Waste" submitted by Mr.Satyesh Avadhut Shenvi Kakodkar (P.R.No. 200106892) to the Department of Civil Engineering, Goa College of Engineering, Farmagudi –Goa, affiliated to Goa University, is approved as partial fulfillment of the requirements for the award of degree of Doctor of Philosophy.

Sawaikar 21.8.26

Dr. Ulhas G. Sawaiker

(Supervisor)

G.S. Dwaralish 21.8.26

(G.S. Dwaralish)

(Examiner)

SRane 21/08/2026

(Suraj S. Rane)

(Chairman)

Date : 21st August 2026

ACKNOWLEDGMENT

My deepest gratitude goes to my supervisor, Prof. Ulhas G. Sawaiker. His invaluable guidance, support, and encouragement shaped this entire research journey. Words truly fall short in expressing how much his motivation in selecting this topic, along with his constant reassurance, meant to me. Simply put, he enabled me to achieve something I could never have accomplished on my own.

I am also incredibly thankful to the Departmental Research Committee (DRC) members, Dr. Pradip V. Sarmokadam and Prof. Nisha P. Naik. Their critical feedback during my progress seminars and thesis preparation was vital. I also wish to thank Prof. Krupashankara M. S., Principal, Goa College of Engineering, Farmagudi, for institutional support and encouragement. Thanks to Prof. Ganesh Hedge, Head , Civil Engineering Department, and former Head Prof. K. G. Guptha, for their unwavering support. I also take this opportunity to thank all the Teaching and Non-Teaching staff of the Civil Engineering Department of Goa College of Engineering.

I am deeply thankful to the Department of Science and Technology & Waste Management (DST&WM), Goa, for funding this research.

A special word of thanks goes to Shri. Ganesh Shetgaonkar, former Chairman of the Goa State Pollution Control Board, for helping arrange testing facilities.

This research heavily relied on industry support, and I sincerely thank Shri. Narayan Vatte (former CEO, Vedanta Pig Division, Ammona) and Shri. Anil Counto (Founder, Alcon - Anil Counto Enterprises) for providing testing materials and facilities. I am equally indebted to Shri. Sahil Adwalpalkar (Director, Adwalpalkar Group), Shri. Arman Bankley (Director, AR–Mines Group of Companies), Shri. Vedang Prabhudessai (Partner, P.K. Tiles and Industries), and Shri. Tanmay Karmali (Proprietor, Karmali Cement Products) for generously opening their facilities for casting various products. Sincere thanks to Mr. Sandeep Singh of the JSW-GGBS Division for providing ,GGBS.

To the technical and non-technical staff of various laboratories and industrial facilities, Shri. Siddhesh Kamat, Shri. Janki Prasad Sahu, Shri. Gaurish Kerkar, Shri. Swagat Salgaonkar, Shri. Mohit Dharne, Shri. Sarvesh Bandodkar, Shri. Lavlesh Verma, and Shri. Rupesh Velip, thank you for your assistance during the laboratory investigations.

I must also acknowledge Dr. Digamber G. Porob, Dr. Cherukulappurath Sudhir, Dr. Venkatesha R. Hathwar, and Dr. Anjani P. Nagvenkar of Goa University for granting me access to their laboratory for microstructural and XRD testing.

Balancing professional responsibilities with doctoral research is never easy; I am therefore tremendously grateful to my workplace, Don Bosco College of Engineering. My sincere respect and gratitude go to the management at Fatorda and the Principal, Dr. Neena Panandikar, for their continuous encouragement. I also extend my heartfelt thanks to Dr. Shwetha Prasanna, Head, Department of Civil Engineering, for her constant support. Special thanks to Mrs. Shruti Jambhale, Mrs. Nadya Baracho, Shri Gaurish Samant, Shri Swapnil Ramani, Shri Bhupesh Prabudessai, Shri Shantanu Desai, and everyone who stepped in to assist—thank you for your invaluable cooperation. I also owe a special thanks to Mr. Sudip Faldessai, Project Officer of the Goa State Innovation Council, for his timely support.

On a personal note, the blessings of my parents and the steadfast backing of my wife, Mrs. Samiksha, and family deserve far more than a brief mention. I am especially thankful to my son, Master Sharv, and my daughter, Miss Shruva, who showed remarkable patience and understanding during my marathon academic engagements and my endlessly busy schedule.

Finally, to all the teachers, relatives and well-wishers who have shaped my life, thank you from the bottom of my heart.

Date: April 2026 **Satyesh Avadhut Shenvi Kakodkar**

Place: Goa University, Taleigao

Dedicated to

my parents and my family

Abstract

Globally, mining generates over 100 billion tonnes of waste annually, leading to acid mine drainage, water contamination, and soil degradation. In Goa, iron ore mining produces 40 million tonnes of overburden and waste yearly against 15 million tonnes of ore, yielding a waste-to-ore ratio of almost 3:1. Over past two decades, ore processing has accumulated 7.7 million tonnes of iron ore tailings (IOTs). This study transforms IOTs, an environmental liability, into sustainable composite construction materials, advancing resource efficiency and circular-economy principles.

Five novel products, bricks, blocks, pavers, tiles, and cladding panels, were developed using optimized IOT blends, supplemented with cementitious materials (SCMs) and aggregates. IOT showed a specific gravity of 3.25, with key oxides including Fe_2O_3 (63.09%), SiO_2 (17.90%), and Fe (44.12%). SCMs comprised 53-grade Ordinary Portland Cement (OPC), Ground Granulated Blast-furnace Slag (GGBS) having specific gravity 2.81, and fineness of 397 m^2/kg, Class F Fly Ash with fineness 325 m^2/kg and $SiO_2 + Al_2O_3 + Fe_2O_3$ totaling to 88.95%, and lime having CaO content of 57.19% for pozzolanic activation. All materials met Indian Standards with minimal deleterious substances.

Optimal brick mix T50F10G30 (50% IOT, 10% fly ash, 30% GGBS, 5% OPC, 5% lime) delivered compressive strengths of 10.47 N/mm^2 (7 days) and 13.58 N/mm^2 (28 days), which were the highest amongst all cast trials and surpassed the IS 1077:2025 limit. It achieved a dry bulk density of 1839 kg/m^3, a water absorption of 5.05%, a strength loss of 21.56% after accelerated aging, and an electrical resistivity of 471.73 $k\Omega \cdot m$, with coefficients of variation <3.5%.

Concrete blocks incorporated recycled ceramic waste ranging from 0–30% as coarse aggregate replacement. Control mix A100CW00 reached 15.92 N/mm^2 (28 days), 2200 kg/m^3 density, and 4.64% absorption. Optimized mixes (A090CW10, A080CW20, A070CW30) yielded compressive strengths in the range of 14.89–15.50 N/mm^2, densities ranging from 1860-2030 kg/m^3, 4.91–5.30% water absorption, and coefficients of variation <0.073.

Pavers with 0–50% IOT and cement dosages (60–100%) showed water absorption of 1.77–10.61% (optimal <6% at 10–20% IOT). The C100Tx series attained compressive

strengths of 32.84–44.17 N/mm² at 28 days, while 28-day strengths increased to 34.95–44.14 N/mm² for C080Tx and 30.09–42.84 N/mm² for C060Tx across the different IOT replacement levels. Peak compressive strengths reached 53.63 N/mm² (C080T10) and 53.08 N/mm² (C060T10) at 56 days; splitting tensile was highest for 10% IOT substitution with a 100% cement mix, with a value of 6.79N/mm², whereas for 80% cement and 60% cement it was 6.36N/mm² and 6.02N/mm² respectively. Values of all trial mixes exceeded the 2.55 N/mm² minimum threshold mandated by the Indian Standard code for M30 grade concrete pavers. Mixtures containing 10% IOT maximized flexural strength; specifically, the 100% cement formulation yielded 9.04 N/mm², whereas the 80% and 60% cement proportions produced 10.9 N/mm² and 8.45 N/mm², respectively.

The wet transverse strength of tiles ranged from 5.7 to 9.67 N/mm² across all trials and was much higher than those reported in comparable research, and the minimum strength specified as 3N/mm² in the relevant IS code.

Tiles exhibited water absorption ranging from 2.52% (C100T10) to 12.96% (C060T50). Regression confirmed a strong inverse correlation between water absorption and strength.

Out of six cladding panel mixes cast, cladding panels with the C080G20T50F1 mix attained a compressive strength of 28.07 N/mm², breaking load 702.72 N, modulus of rupture 8.43 N/mm², thermal conductivity 0.9899 W/m·K, absorption 4.56%, and 23% strength loss in acid.

The financial analysis of the composite material showed unit manufacturing costs of ₹7.33/brick, ₹39.52/block, ₹8.70/paver, ₹13.83/tile and ₹6.20/cladding panel.

The total capital requirement of ₹174.87 lakhs facilitates the establishment of the manufacturing facility, integrating fixed capital of ₹79.10 lakhs and working capital of ₹95.77 lakhs.

Initial operational parameters set production capacity at 50% to accommodate the facility's recent commissioning and the gradual stabilization of market confidence, with the production model programmed to increase by 5% annually thereafter. Considering these factors, the payback period assessed was less than 4 years.

These IOT composites cut costs by 30–40% compared with conventional products, meet all IS standards, and offer a robust, economical, viable, environmentally sustainable product from mine waste, curbing virgin resource use worldwide for the construction industry.

CONTENTS

Chapter	Title	Page
	Content	I
	List of Figures	VII
	List of Tables	XI
	Abbreviations	XIV
1	**INTRODUCTION**	
1.1	Background	1
1.1.1	Classification and characteristics of mine waste	2
1.1.2	Historical evolution and context of mining in Goa	2
1.2	Mining Scenario	4
1.2.1	Global mining	4
1.2.2	National mining	5
1.2.3	Goa's mining industry	5
1.3	Challenges of mine waste	7
1.3.1	Environmental degradation	7
1.3.2	Socio-economic consequences	9
1.3.3	Complexities and regulatory pressures	10
1.4	Need for eco-friendly building materials	10
1.4.1	Multidimensional benefits of sustainable construction	10
1.4.2	Circular economy in construction	11
1.4.3	Opportunities for mine waste valorization in sustainable construction	11
1.5	Strategic approach	12
1.6	Research gap	13
1.6.1	Existing challenges and current solutions	13

	1.6.2	Identification of gap in mine waste-derived composites	14
	1.6.3	Significance and novelty of the proposed research	15
1.7	Objectives and scope of the work		16
1.8	Organization of thesis		17
2	**LITERATURE REVIEW**		
2.1	General		19
2.2	Utilization of mine tailing waste in composite material		20
2.3	Materials used in development of composite using mine tailing waste		22
	2.3.1	Iron Ore Tailings (IOTs)	22
	2.3.2	Cement	23
	2.3.3	Ground Granulated Blast Furnace Slag (GGBS)	25
	2.3.4	Fly ash	27
	2.3.5	Lime powder	28
	2.3.6	Ceramic waste	29
	2.3.7	Aggregate	31
2.4	Product development from mine tailing waste		33
	2.4.1	Bricks	33
	2.4.2	Blocks	38
	2.4.3	Concrete used for pavers and tiles	40
	2.4.4	Pavers	45
	2.4.5	Tiles	50
	2.4.6	Cladding panels	53
2.5	Financial analysis of Iron Ore Tailings based products		58
	2.5.1	Cost of manufactured products	58
	2.5.2	Project setting cost and payback period	59
	2.5.3	Economic feasibility of IOT based products	59
		2.5.3.1 Cost estimation of products	60
		2.5.3.2 Project setup and payback period	62
2.6	Critical Summary		65

3	**EXPERIMENTAL INVESTIGATIONS**		
3.1	General		69
3.2	Properties of material		69
	3.2.1	Iron Ore Tailings	69
	3.2.2	Cement	70
	3.2.3	Ground Granulated Blast-Furnace Slag (GGBS)	71
	3.2.4	Fly ash	71
	3.2.5	Lime powder	72
	3.2.6	Ceramic waste	73
	3.2.7	Fine and coarse aggregates	73
3.3	Chemical properties of material		75
3.4	X-ray diffractometer analysis		75
3.5	FE-SEM with EDX analysis		76
3.6	Mix proportion for brick		77
3.7	Casting of bricks		78
3.8	Laboratory investigations on cast brick		79
	3.8.1	Dimension test	80
	3.8.2	Compressive strength and dry bulk density	80
	3.8.3	Water absorption and wet bulk density	81
	3.8.4	Brick aging	81
	3.8.5	Efflorescence	81
	3.8.6	Electrical resistivity	82
	3.8.7	Falling test	82
	3.8.8	Soundness test	82
	3.8.9	Hardness test	83
3.9	Mix proportion for blocks		83
3.10	Casting of blocks		85
3.11	Laboratory investigations on cast block		86
	3.11.1	Dimension test	86
	3.11.2	Compressive strength and bulk density	86
	3.11.3	Water absorption	87
	3.11.4	Efflorescence test	88

3.12	Mix design for pavers and tiles		88
3.13	Casting of pavers and tiles		90
3.14	Laboratory investigations on pavers		92
	3.14.1	Length, width, and thickness measurement	93
	3.14.2	Water absorption	93
	3.14.3	Compressive strength	93
	3.14.4	Tensile splitting strength	93
	3.14.5	Flexural strength	94
	3.14.6	Acid resistance test	95
3.15	Laboratory investigations on tiles		95
	3.15.1	Water absorption	95
	3.15.2	Wet transverse strength	96
3.16	Mix design for cladding panel		97
3.17	Casting of cladding panel		98
3.18	Laboratory investigations on cladding panel		99
	3.18.1	Thermal conductivity test	99
	3.18.2	Breaking strength and modulus of rupture	100
	3.18.3	Water absorption	100
	3.18.4	Acid resistance test	101
3.19	Statistical analysis of cast products		101
	3.19.1	Experimental design and variables	102
	3.19.2	Descriptive statistics and dispersion metrics	102
	3.19.3	Correlation and regression analysis	103
	3.19.4	Criteria for evaluating statistical significance and optimization	103
3.20	Financial analysis of manufacturing of composite material		103
	3.20.1	Data collection framework	105
	3.20.2	Cost evaluation process for manufactured products	106
	3.20.3	Estimation of manufacturing unit setup costs	106
	3.20.4	Financial viability and payback period analysis	107

4	**RESULTS & DISCUSSION**			
	4.1	General		109
	4.2	Materials used in casting of composites		109
		4.2.1	Iron Ore Tailing (IOTs)	109
		4.2.2	Cement	113
		4.2.3	Ground Granulated Blast-Furnace Slag (GGBS)	116
		4.2.4	Fly ash	118
		4.2.5	Lime	122
		4.2.6	Ceramic waste	125
		4.2.7	Fine and coarse aggregate	128
		4.2.8	Coconut fiber	133
	4.3	Performance assessment and insights of bricks		135
		4.3.1	Mix proportion for bricks	135
		4.3.2	Tests on bricks	136
			4.3.2.1 Dimension test	137
			4.3.2.2 Compressive strength and bulk density	137
			4.3.2.3 Water absorption and wet bulk density	141
			4.3.2.4 Brick aging	143
			4.3.2.5 Electrical resistivity	145
			4.3.2.6 Efflorescence	146
			4.3.2.7 Falling Test	147
			4.3.2.8 Soundness Test	148
			4.3.2.9 Hardness Test	149
	4.4	SEM-EDX characterization of bricks		150
	4.5	Statistical analysis of various parameters of cast bricks		153
	4.6	Performance assessment and insights of blocks		155
		4.6.1	Mix proportion for blocks	155
		4.6.2	Tests on blocks	157
			4.6.2.1 Dimension test	157
			4.6.2.2 Compressive strength and density of the cast block	157
			4.6.2.3 Water absorption	160
			4.6.2.4 Efflorescence	161

	4.7	SEM-EDX characterization of blocks	162
	4.8	Statistical analysis of various parameters of cast blocks	165
	4.9	Performance assessment and insights of pavers and tiles	167
		4.9.1 Mix proportion for pavers and tiles	167
		4.9.2 Tests on pavers and tiles	169
		4.9.2.1 Dimension test	169
		4.9.2.2 Water absorption	170
		4.9.2.3 Compressive strength	173
		4.9.2.4 Tensile splitting strength	177
		4.9.2.5 Flexural strength	180
		4.9.2.6 Acid resistance test	183
		4.9.2.7 Water absorption of tiles	186
		4.9.2.8 Wet transverse strength on tiles	188
	4.10	SEM-EDX characterization of concrete for pavers and tiles	191
	4.11	Statistical analysis of various parameters of pavers	194
	4.12	Statistical analysis of various parameters of tiles	198
	4.13	Performance assessment and insights of cladding panels	201
		4.13.1 Mix proportion for cladding panels	201
		4.13.2 Tests on cladding panels	204
	4.14	SEM-EDX characterization of cladding panels	209
	4.15	Statistical analysis of cladding panels	212
	4.16	Cost analysis of construction materials	214
	4.17	Analysis for cost of setting a manufacturing unit	219
	4.18	Analysis for payback period	222
5	**SUMMARY AND CONCLUSIONS**		227
	5.1	Summary	227
	5.2	Conclusions	227
	5.3	Scope of future work	232
	REFERENCES		234
	LIST OF PUBLICATIONS		257

LIST OF FIGURES

Figure No.	Tittle	Page No.
1.1	Mining map of Goa	4
1.2	Circular economy in mining	11
3.1	Location of mine	69
3.2	Tailing dump	69
3.3	Iron Ore Tailing sample	70
3.4	OPC -53 grade sample	70
3.5	GGBS sample	71
3.6	Fly ash sample	72
3.7	Lime powder sample	72
3.8	Crushed stone sand sample	74
3.9	10 mm aggregate sample	74
3.10	X-Ray Fluorescence (XRF) spectrometer	75
3.11	X-ray diffractometer setup	76
3.12	FE-SEM with EDX setup	77
3.13	Cast brick with dimensions	80
3.14	Electrical resistivity of brick	82
3.15	Block making machine	85
3.16	Cast block with dimensions	85
3.17	Compression testing of block	87
3.18	Process of casting paving blocks and tiles	91
3.19	Cast paver with dimensions	92
3.20	Cast tile with dimensions	92
3.21	Tensile splitting strength of paver	94
3.22	Wet transverse strength of tile	96
3.23	Cladding panel manufacturing process	98
3.24	Thermal conductivity of cladding panel	100
3.25	Cube after undergoing acid test	101
4.1	Particle size distribution of IOTs	111
4.2	XRD diffractogram of IOTs	112

4.3	XRD diffractogram of Cement	115
4.4	XRD diffractogram of GGBS	117
4.5	XRD diffractogram of Fly Ash	121
4.6	XRD diffractogram of Lime	124
4.7	XRD diffractogram of Ceramic waste	127
4.8	Particle size distribution of crushed stone sand	130
4.9	Particle size distribution of 10 mm aggregate	130
4.10	XRD diffractogram of Crushed Stone Sand	132
4.11	XRD diffractogram of Coconut fiber	134
4.12	Compressive strengths of different trial mixes	136
4.13	Compressive strength of different bricks at 7 and 28 days	138
4.14	Compressive strengths of bricks with IS code limits	138
4.15	Dry and wet densities of brick	140
4.16	Water absorption of bricks with IS code limits	142
4.17	Relationship between compressive strength and water absorption	143
4.18	Variation in compressive strength over different cycles of wetting and drying	144
4.19	Relationship between compressive strength and electrical resistivity	146
4.20	SEM micrograph of brick composition T50F10G30	150
4.21	EDX spectrum detailing of principal elements for brick composition T50F10G30	151
4.22	SEM micrograph of brick composition T50F35G05	152
4.23	EDX spectrum detailing of principal elements for brick composition T50F35G05	152
4.24	Compressive strength of cast cubes at 7 and 28 days	156
4.25	Compressive strength of blocks with IS code limits	158
4.26	Densities of blocks with IS code limits	160
4.27	Water absorption results of blocks with IS code limits	161
4.28	SEM micrograph of block composition A100CW00	162
4.29	EDX spectrum detailing of principal elements for block composition A100CW00	163
4.30	SEM micrograph of block composition A90CW10	164
4.31	EDX spectrum detailing of principal elements for block composition A90CW10	165

4.32	Compressive strength of paver mix at 7 and 28 days for various IOT replacement levels	169
4.33	Water absorption of pavers with IS code limits	172
4.34	Relationship between water absorption and compressive strength of pavers	173
4.35	Compressive strength of paver at 7, 28 and 56 days for various IOT replacement levels	175
4.36	Compressive strength of paver at 28 and 56 days for various IOT replacement levels	175
4.37	Relationship between compressive strength and IOT replacement levels for 100%, 80%, and 60% cement mixes	177
4.38	Relationship between splitting tensile strength and compressive strength	179
4.39	Relationship between flexural strength and compressive strength	182
4.40	Comparison of variation in compressive strength between air dry sample and acid sample	184
4.41	Variation in water absorption levels over various IOT replacement levels	186
4.42	Wet transverse strength of tiles with IS code limits	189
4.43	Relationship between water absorption and wet transverse strength	190
4.44	SEM micrograph of concrete for pavers and tiles with composition C80T30	192
4.45	EDX spectrum detailing of principal elements for concrete for pavers and tiles with composition C80T30	192
4.46	SEM micrograph of concrete for pavers and tiles with composition C60T50	193
4.47	EDX spectrum detailing of principal elements for concrete for pavers and tiles with composition C60T50	194
4.48	Compressive strength of cube obtained at 7 and 28 days	202
4.49	Comparison of 7 and 28 days compressive strength in mix with and without coir fibre	203
4.50	Variation in thermal conductivity for different cladding panels	205
4.51	Modulus of rupture on cladding panel	206
4.52	Variation of water absorption over a period of time	207
4.53	Variation in strength due to acid attack	208
4.54	SEM micrograph of cladding panel with composition C80G20T50F1	209

4.55	EDX spectrum detailing of principal elements for cladding panel with composition C80G20T50F1	210
4.56	SEM micrograph of cladding panel with composition C60G40T50F1	211
4.57	EDX spectrum detailing of principal elements for cladding panel with composition C60G40T50F1	212

LIST OF TABLES

Table No.	Tittle	Page No.
2.1	Chemical composition of IOTs	23
2.2	Physical properties of Cement	24
2.3	Chemical composition of Cement	24
2.4	Chemical composition of GGBS	26
2.5	Chemical composition of Fly ash	27
2.6	Chemical composition of Lime powder	29
2.7	Chemical composition of Ceramic waste	30
3.1	Physical properties of Iron Ore Tailings	70
3.2	Physical properties of Cement	70
3.3	Physical properties of GGBS	71
3.4	Physical properties of Fly ash	72
3.5	Physical properties of Lime	73
3.6	Physical properties of Ceramic waste	73
3.7	Physical properties of fine aggregate	74
3.8	Physical properties of coarse aggregate	74
3.9	Mix proportions for bricks	78
3.10	List of tests carried out on cast brick	79
3.11	Percentage breakdown of aggregates in the mix	83
3.12	Mix proportions for blocks	84
3.13	List of tests carried out on cast block	86
3.14	Mix proportions for pavers and tiles	88
3.15	List of tests carried out on cast pavers	92
3.16	List of tests carried out on cast tiles	95
3.17	Mix composition for wall cladding panels	97
3.18	List of tests carried out on cast cladding panels	99
4.1	Physical and chemical properties of Iron Ore Tailings	110
4.2	Physical and chemical properties of Cement	114
4.3	Physical and chemical properties of GGBS	116
4.4	Physical and chemical properties of Fly ash	119

4.5	Physical and chemical properties of Lime	123
4.6	Physical and chemical properties of Ceramic waste	125
4.7	Physical and chemical properties of fine aggregate	129
4.8	Physical properties of coarse aggregates	129
4.9	Material quantities used per brick	135
4.10	Compressive strength measured on cube specimens for various mixes	135
4.11	Dimensions of bricks	137
4.12	Compressive strength results of different brick trial mixes	137
4.13	Dry and wet bulk densities for various brick mix trials	139
4.14	Water absorption of various brick mix trials	141
4.15	Compressive strength at various cycles of brick ageing	144
4.16	Electrical resistivity of bricks	145
4.17	Falling test results of bricks	148
4.18	Soundness test results of bricks	148
4.19	Test results of hardness test on bricks	149
4.20	Statistics of various parameters of bricks	153
4.21	Materials and their proportions for IOT mix design	156
4.22	Compressive strength obtained on cubes	156
4.23	Dimensions of blocks	157
4.24	Compressive strength obtained on blocks	158
4.25	Average bulk densities for various block mix trials	159
4.26	Water absorption of various block mix trials	160
4.27	Statistics of various parameters of block	166
4.28	Materials and their proportions for IOT mix design	167
4.29	Compressive strength of cubes	168
4.30	Dimensions of pavers	170
4.31	Water absorption of paver mix trials	171
4.32	Compressive strength of pavers	174
4.33	Tensile splitting strength of pavers	178
4.34	Flexural strength of pavers	180
4.35	Compressive strength of pavers at 56 days air drying and acid test	183
4.36	Water absorption test on tiles	186

4.37	Wet transverse strength on tiles	188
4.38	Statistics of various parameters of pavers	195
4.39	Statistical analysis of various parameters of tiles	198
4.40	Material quantities used per cladding panel	201
4.41	Compressive strength measured on cube specimens for various mixes	202
4.42	Summary of test results	204
4.43	Rate of water absorption over a period of time	206
4.44	Compressive strength measured on cube specimens for various mixes	208
4.45	Statistical analysis of cladding panel	212
4.46	Rates of material used in casting composite construction materials	215
4.47	Rate analysis of brick	215
4.48	Rate analysis of block	216
4.49	Rate analysis of paver	217
4.50	Rate analysis of tile	218
4.51	Rate analysis of cladding panel	219
4.52	Manufacturing unit setup cost analysis	221
4.53	Annual sales performances	223
4.54	Cash flow statement	223
4.55	Pay back calculation	224

ABBREVIATIONS

AAS	:	Asset Administration Shell
ACI	:	American Concrete Institute
AMD	:	Acid Mine Drainage
ASTM	:	American Society for Testing and Materials
BCR	:	Benefit-Cost Ratio
BEP	:	Break-even point
BIS	:	Bureau of Indian Standards
C&D	:	Construction and demolition waste
CSH	:	Calcium Silicate Hydrate (Secondary gel)
CAG	:	Comptroller and Auditor General
CCF	:	Coconut coir fiber
CCT	:	Compression Casting Technique
CI	:	Confidence Intervals
COV	:	Coefficient of Variation
cps	:	Counts per second (intensity in XRD)
CSD	:	crushed stone dust
CSEBs	:	Compressed stabilized earth blocks
CSR	:	Corporate Social Responsibility
CSS	:	Crushed Stone Sand
CW	:	Ceramic Waste
EAF	:	Electric arc furnace slag / Electric Arc Furnace
ECC	:	Engineered Cementitious Composites
EDS	:	Energy Dispersive X-ray Spectroscopy
FA	:	Fly Ash
FWHM	:	Full Width at Half Maximum
g/cm^3	:	Grams per cubic centimeter (density)

GGBS / GGBFS	:	Ground granulated blast furnace slag / Ground Granulated Blast-Furnace Slag
GHG	:	Global greenhouse gas
GMT	:	Gold mining tailings
GVA	:	Gross Value Added
HMV	:	Heavy Motor Vehicle
HPFRC	:	High-performance fiber-reinforced concrete
IBM	:	Indian Bureau of Mines
ICP-OES	:	Inductively Coupled Plasma Optical Emission Spectroscopy
IOT / IOTs	:	Iron Ore Tailings
IRR	:	Internal rate of return / Internal Rate of Return
IS	:	Indian Standard
JCPDS	:	Joint Committee on Powder Diffraction Standards
kg/m^3	:	Kilograms per cubic meter (density)
LCC	:	Lifecycle Costing
LOI	:	Loss on Ignition
m^2/kg	:	Square meters per kilogram
mm	:	Millimeters
MoM	:	Ministry of Mines
MPa	:	Megapascals
MSW	:	Mine spoil waste
N/mm^2	:	Newtons per square millimeter (compressive strength)
NAC	:	Natural aggregate concrete
NGOs	:	Non-Government Organisation
nm	:	Nanometers
NPV	:	Net Present Value
NRC	:	Noise reduction coefficient
OPC	:	Ordinary Portland Cement
PAT	:	Profit After Tax
PBP	:	Payback Period

PBT	:	Profit Before Tax
PM	:	Particulate Matter
RCA	:	Recycled concrete aggregate
RHA	:	Rice husk ash
RM	:	Red mud
RSPM	:	Respirable suspended particulate matter
SCB	:	Sand Crete Blocks
SCC	:	Self-compacting concrete
SCMs	:	Supplementary Cementitious Materials
SD	:	Mean and Standard Deviation
SE	:	Standard errors / Standard Error of the Mean
SEM	:	Scanning electron microscopy
SEM-BSE	:	Scanning electron microscopy with backscattered electrons
SPM	:	Suspended particulate matter
SSA	:	Specific Surface Area
TCLP	:	Toxicity Characteristic Leaching Procedure
TGA	:	Thermogravimetric analysis
TSFs	:	Tailings Storage Facilities
UHPC	:	Ultra-high performance concrete
W/C	:	Water-to-cement
XRD	:	X-ray diffraction / X-Ray Diffraction
XRF	:	X-Ray Fluorescence
μm	:	Micrometers or microns

CHAPTER 1
INTRODUCTION

1.1 Background

Mineral extraction operations remove valuable minerals and geological materials from Earth's surface or subsurface (Worlanyo & Jiangfeng, 2020). This process encompasses solid commodities such as gold, diamonds, iron, and coal, as well as fluid resources such as oil and natural gas (White, 2005). Archaeological evidence documents hematite extraction at Lion Cave in Swaziland dating to 40,000 years ago (Nex & Kinnaird, 2018).

Geological characteristics, mineral type, depth, technology, regulations, and economic viability dictate extraction methods. Surface mining (open-pit, dredging) targets near-surface ore, predominating in developing nations due to lower capital costs and suitability for smaller operations. Deep deposits necessitate underground extraction utilizing sophisticated machinery and substantial workforces.

The complete mining cycle comprises four sequential stages:(i) exploration identifies economically viable deposits through prospecting and geophysical surveys; (ii) extraction employs surface or underground methods based on geological characteristics; (iii) mineral processing and dressing physically and chemically concentrates valuable minerals through crushing, grinding, classification, and beneficiation; and (iv) metallurgical processing applies thermal and chemical treatments to extract desired metals from concentrated ore, converting compounds such as bauxite to aluminum oxide (Worlanyo & Jiangfeng, 2020; Balasubramanian, 2017).

While mining technologies have evolved from simple tools to complex processes, fundamental operations remain similar, but now function at a vastly greater scale and with a vastly greater environmental footprint (Ghose, 2009). These modern intensities demand innovative, sustainable waste management solutions that are long-term, adaptable, and societally integrated rather than temporary interventions.

This research develops novel composite materials incorporating Iron Ore Tailings (IOTs) to address environmental and resource challenges. Contextualizing Goan mining history and disposal imperatives, the study proposes a structured approach to valorize IOTs into sustainable composite construction materials.

1.1.1 Classification and characteristics of mine waste

Mine waste streams exhibit distinct physical and chemical properties that determine their environmental risk profiles. Categories include waste rock, fine-grained tailings generated during mineral processing; slag produced from smelting operations, and contaminated mine water. The specific characteristics of these waste materials, such as the presence of sulfide minerals in waste rock and tailings, are key factors in environmental risk. Sulfide minerals present in waste rock and tailings facilitate Acid Mine Drainage (AMD) formation through oxidation reactions (Gairola et al., 2025; Silva-Rêgo et al., 2022). The fine-grained nature of tailings also poses a risk of dust emissions and tailing dam failures (Silva-Rêgo et al., 2022).

IOTs are fine-grained, watery waste generated during iron ore concentration, with their volume linked to the ore grade. Heavy metals and dissolved salts comprise these tailings. Pipelines transport the tailings as slurry to Tailings Storage Facilities (TSFs). The large surface area of these fine-grained materials accelerates weathering, especially if sulfide minerals are present, increasing the risk of AMD. While submerged storage can curb sulfide oxidation, the collapse of tailings dams poses a severe threat of toxic spills into ecosystems (Guo et al., 2025; Ikotun et al., 2022; Zhang et al., 2020).

Mining operations extensively use mine water across milling and processing stages, with recycling and reuse practices minimizing freshwater consumption. Modern mining facilities implement zero-discharge policies for mine drainage (Tomiyama & Igarashi, 2022; Gunson et al., 2012).

Processing chemicals, though volumetrically insignificant compared to waste rock and tailings, present disproportionately high toxicity risks. Phosphate and aluminum production generate wash slimes, watery by-products that retain substantial moisture even after extended drying, posing challenges for utilization. These materials typically accumulate in large holding ponds. Spent oil shale deposits demonstrate potential for use as fine aggregate or mineral filler in asphalt paving, though coarse spent oil shale requires crushing and sizing prior to application (Collins & Ciesielski, 1994).

1.1.2 Historical evolution and context of mining in Goa

Goa's mineral deposits supported extraction activities for centuries, with historical records documenting gold mining by Jains in Cudnem and continuous iron ore extraction by the Dovolos tribe in Salcette during the Portuguese colonial period (Pai,

2018). Initial Portuguese extraction restrictions aimed to prevent territorial vulnerability, though mineral wealth became documented as early as 1636 (Jakati, 2021).

Modern extraction commenced in the early 1900s, as French and Bombay-based firms initiated prospecting for iron and manganese ore in 1905–1906, subsequently consolidated through geological surveys and the establishment of new companies. Post-World War II ore exports began in 1951, accelerated by Dr. Oertal's geological mapping of Goa (1954–1957) and Portuguese legislation permitting private mining concessions. By the time Portuguese rule concluded, mechanization had become widespread in Goan mining operations, from exploration to transportation (Jakati, 2021).

Extraction techniques evolved from manual labour to mechanized operations, replacing pickaxes and hand shovels with explosives and substituting bullock carts with mechanized transport (Pai, 2018). Mechanization initiatives pioneered by Chowgule & Co. in 1953 and V.M. Salgaocar & Bro. Ltd. in the mid-1960s substantially increased operational scale and efficiency (IIT (ISM- Dhanbad, 2019).

This increased scale and mechanization brought profound social and environmental consequences. Economic incentives associated with mineral extraction fractured traditional societal frameworks, precipitating significant demographic shifts toward mining centers (Pai, 2018). Simultaneously, logistical operations compromised regional ecology; vehicular emissions and particulate dispersion degraded ambient air and soil quality, while heavy barge traffic destabilized the structural integrity of the Khazan agricultural embankments (Jakati, 2021; Pai, 2018; Mascarenhas & Kalavampara, 2009).

Legislative evolution has subsequently dictated the industry's trajectory. The 1987 Abolition Act reconfigured tenure mechanisms, converting perpetual concessions into fixed-duration leases. However, the export demand surge driven by China's economic expansion in the 2000s incentivized irregular extraction, necessitating statutory prohibitions and the eventual establishment of the Goa Iron Ore Permanent Fund to enforce governance. Situated within ecologically sensitive zones, 154 leases preclude operational reactivation, necessitating rigorous safeguards to mitigate systemic liabilities and social inequity (Pai, 2018). Figure 1.1 presents the mining map of Goa.

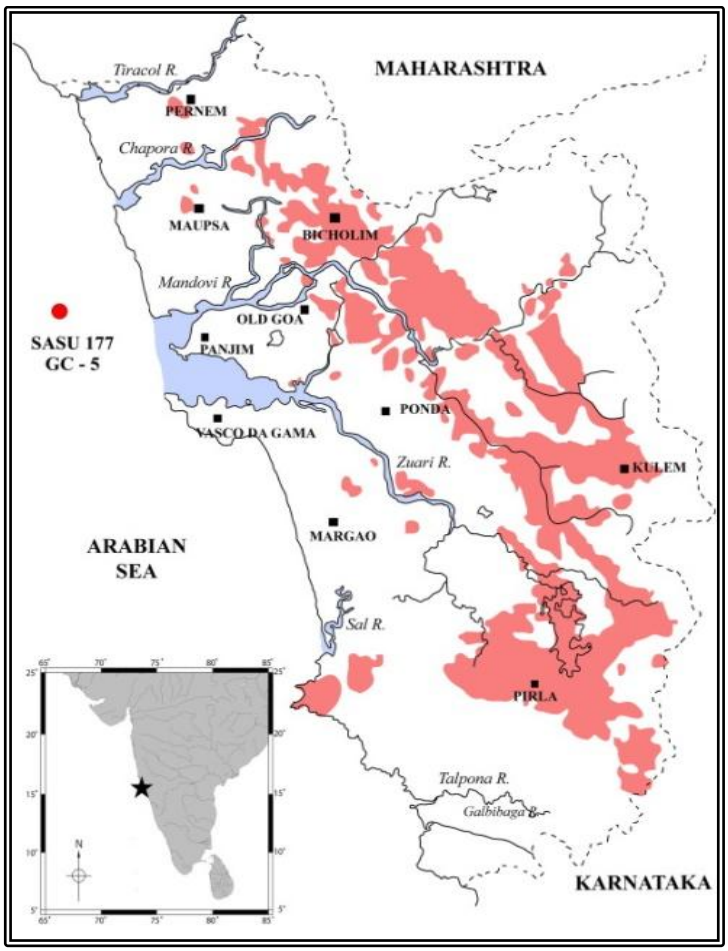


Figure 1.1: Mining map of Goa
Source :Marine Pollution Bulletin, Vol. 114(2),(Jan. 2017)

1.2 Mining scenario

Statistical analysis and trend assessment characterize global, national (Indian), and regional (Goan) mining dynamics, highlighting the immense scale and evolving nature of resource extraction operations.

1.2.1 Global mining

Global mining has transformed over the past two decades, driven by shifting production dynamics and sustainability trends. In 2014, global iron ore production reached 3.22 billion tonnes, with Brazil contributing 412 million tonnes (12.8%), comprising 10% granular and 90% fines—sinter feed 64.8%, pellet feed 25.2%, averaging 63.5% Fe. Australia and Brazil's domination of global iron ore supply creates highly competitive trade conditions, with significant Asian importers such as China, Japan, and South Korea engaging in intense rivalry, particularly between China and Japan (2000 -2015) (Pedro et al., 2019).

Interconnected supply networks demonstrate increasing globalization, with Europe, Asia, South Africa, and Ukraine contributing to supply diversification. The post-2004 commodity boom transformed mining economics as demand shifted toward emerging Asian markets, now consuming three-quarters of global minerals, while spot pricing mechanisms replaced long-term contracts, heightening market volatility (Hao et al., 2018). Chinese enterprises expanded globally, while operational costs escalated due to lower ore grades and stricter environmental regulations. Resource nationalism intensified through export restrictions and local beneficiation mandates (Humphreys, 2018).

Continuous reassessment of value drivers remains essential, while valorizing mine waste for construction materials advances sustainable resource utilization and circular economy objectives (MacDiarmid et al., 2018; Lottermoser, 2010).

1.2.2 National mining

India's substantial metallic and non-metallic mineral reserves position mining as a crucial economic sector, with the country currently producing 95 different minerals, including fuel, metallic, non-metallic, atomic, and minor categories. The mining and quarrying sector demonstrated steady growth, with Gross Value Added (GVA) valued at 2011–12 prices estimated at ₹3,50,870 crore for 2023–24, representing 8.1% growth from the previous year and contributing approximately 2.31% to total GVA (MoM, 2024).

The Index of mineral production reached 128.9 in FY 2023–24, representing 7.51% growth, while the total estimated mineral production value is ₹1,92,734 crore, with metallic minerals contributing ₹1,10,785 crore (57.5%) and non-metallic minerals ₹81,949 crore (42.5%). The Wholesale Price Index for minerals demonstrated significant increases, reflecting the mining sector's critical economic role (MoM, 2024).

The correlation between India's mining boom and increased waste generation demands a paradigm shift. Management of this waste is no longer merely an ecological obligation; it has become a national imperative for securing long-term resources and stabilizing the economy.

1.2.3 Goa's mining industry

Goa, India's smallest state, possesses a remarkable abundance of industrial minerals, particularly significant iron ore, bauxite, manganese, limestone, and dolomite deposits

(Jakati, 2021), supplemented by 20 different minor minerals (CAG, 2023). Mineral deposits concentrate primarily in Bicholim and Sattari talukas in North Goa and Quepem, Dharbandora, and Sanguem in South Goa, spanning approximately 700 square kilometers (Jakati, 2021) with 42 reporting mines documented in 2020–21 (IMB, 2022). Deposits consist predominantly of hematite ore containing an average iron content of 63%, concentrated in North-North West and South-South East regions (IBM, 2021). Annual production comprises approximately 80% fines from total iron ore extraction, with approximately 31.13 million tonnes extracted from 2002 to 2022 and exported primarily to Japan, European countries, China, and South Korea through Mormugao Harbour (IWAI, GoI, 2010). Goa supplies over 60% of the nation's iron ore exports (Jakati, 2021).

Lateritoid manganese deposits are concentrated in southern regions and are embedded within pink shales, phyllites, and quartzites, with manganese content ranging from 30–45%, occasionally reaching 58–60% in specific areas. Metallurgical-grade bauxite deposits occur in three principal regions: North Goa (Chapora River, Mopa, Pernem, Morjim, Dargalim, Ibrampur, Korgaon), Central Goa (Dabolim, Verna, Canua, Raia, Quelossim, Sancoale), and the southwestern Quepem area in South Goa (CAG, 2023).

Open-cast mining methods combining manual and mechanical techniques predominate for Goa's major minerals, while sand mining in the Zuari and Mandovi rivers remains strictly regulated, requiring traditional manual extraction and prohibiting mechanized machinery (Notification No. 34/10/2012 Official Gazette, GoG).

Since commercial mineral production commenced in 1947, Goa's inland waterways, particularly the Mandovi, Zuari, and Cumberjua canal network, have facilitated iron ore transportation, substantially supporting the mining industry's economics through efficient transport infrastructure (IWAI, GoI, 2010).

Goa's mining sector faced a complex regulatory landscape and significant operational disruptions, with Supreme Court decisions invalidating lease renewals, precipitating an industry shutdown from 2012 to 2024 (Shah Commission report, 2012), followed by a brief resumption from 2016 to 2018 (Pai, 2018). Historical Portuguese-era mining concessions numbering 806 declined to 595 leases by 1987, with many subsequently cancelled (Mascarenhas & Kalavampara, 2009).

Goa's unique geographical and political context, marked by mining leases covering nearly 19% of the land area and high waste-to-ore ratios of 2.5–3 tonnes of waste per

tonne of iron ore, creates a disproportionate environmental burden and regulatory complexity. Mining operations in ecologically sensitive areas, including forests and agricultural land, combined with a history of legal interventions, reflect ongoing tension between economic activity and environmental protection (Jakati, 2021). Stringent regulations, public advocacy, and large volumes of waste in small, ecologically sensitive regions mandate sustainable management. Waste valorization in construction offers dual benefits: alleviating pressure on disposal and reducing reliance on raw materials.

1.3 Challenges of mine waste

Multifaceted mine waste problems encompassing environmental, socio-economic, and management complexities necessitate innovative solutions.

1.3.1 Environmental degradation

Mine waste generates complex environmental impacts across multiple domains, including water, soil, air quality, and ecosystem integrity. Mine waste generation occurs at a rate exceeding 100 billion tonnes globally per annum (Tayebi-Khorami et al., 2019), with ore extraction producing approximately one to three tonnes of waste per tonne of ore extracted (Bini et al., 2017). This immense waste volume necessitates extensive disposal land areas, causing habitat destruction and land degradation (Shettima et al., 2016). Certain waste constituents, particularly heavy metals and acid-forming materials, cause disproportionately severe and persistent environmental and public health impacts even at low concentrations (Tayebi-Khorami et al., 2019).

India's mining sector substantially contributes to global waste, with iron ore exhibiting stripping ratios of 2:1 to 2.5:1, which is considerably higher than those of limestone at 1.05:1. Coal extraction produces 1.92 cubic meters of overburden per tonne. Bauxite operations exhibit a 1.2:1 ratio, indicating ore that is more difficult to mine than Australian deposits, where the ratio is approximately 0.13:1 (Sahu & Das, 2011). Surface metal ore mining typically produces waste-to-ore ratios of 2:1 to 8:1, whereas underground operations generate approximately 0.2:1 ratios (Anon,2007). Goa's surface mining operations exhibit ratios of 3:1 to 5:1 (Yellishetty et al., 2009), with approximately 19% of land under mining leases (Jakati, 2021). From 2002 to 2022, Goa's iron ore mining produced 7.7 million tonnes of tailings (Kakodkar & Sawaiker, 2025), exacerbating land shortages for disposal and positioning the region at the

forefront of mining waste management challenges. Annual iron ore extraction generates approximately 40 million tonnes of overburden and waste material for every 15 million tonnes of ore produced (TERI, 2001; Jakati, 2021).

This massive amount of waste threatens air, water, and soil quality. Sulfidic tailings create risks like AMD, groundwater contamination, and land degradation, initiating centuries-long pollution cycles that harm aquatic ecosystems and render water unsafe (Adiguzel et al., 2022; Kuranchie et al., 2015). Tailings dam failures release acidic slurry, posing severe economic and safety risks. However, disparities between corporate safety investments and societal security demands increase failure probability and environmental degradation (Gou et al., 2019; Tayebi-Khorami et al., 2019; Falagán et al., 2017).

Specifically, ferromanganese mining effluent pollutes Goa's Mandovi River estuary and mangroves with metal-rich solids, highlighting the cumulative, often irreversible degradation of sensitive coastal systems. Decades-long discharge of clay and fine iron ore causes chronic water turbidity and continuous sedimentation in the subtidal environment (Nayak, 2002). Mining operations severely degrade soil properties by disrupting soil structure, microbial communities, and the nutrient cycle, and by destroying natural vegetation. Tailings with high acid-generating potential exacerbate degradation by causing substantial pH reductions and severe metal contamination, often exceeding safe agricultural soil standards (Ali et al., 2021).

Open-pit mining generates substantial atmospheric emissions, elevating concentrations of critical air pollutants—suspended particulate matter (SPM), respirable suspended particulate matter (RSPM), ozone, sulfur oxides, and nitrogen oxides. These elevated pollutant concentrations pose substantial health risks to nearby populations, contributing to respiratory diseases and cardiovascular complications (Hota & Behera, 2015). Mining cumulatively causes widespread habitat destruction and biodiversity loss through deforestation, direct habitat loss, and ecosystem disruption (Ali et al., 2021).

Mining alters regional material and energy cycles, causing subsidence, groundwater and soil contamination, and biodiversity loss. These disturbances degrade ecosystem structure and function, leading to long-term instability. Intensifying adverse effects necessitate sustainable management and restoration (Dong et al., 2019).

IOTs utilization offers significant environmental benefits by substantially reducing waste volumes, thereby lessening adverse environmental impacts and enhancing the sustainability of mining operations within the state (Kuranchie et al., 2015).

Improper waste disposal has a negative environmental impact, resulting in higher operational costs, regulatory fines, and remediation efforts (Leyton - Flor et al., 2024; Thejas & Hossiney, 2021). Valorizing IOTs mitigates environmental hazards, reduces waste management costs for mining operations, improves public health, and aligns with sustainable development objectives (Segui et al., 2023; Filho et al., 2017).

1.3.2 Socio-economic consequences

Mining releases particulate matter PM 2.5 and heavy metals that saturate air, water, soil, and food. PM 2.5 inhalation is linked to cardiovascular failure and reduced life expectancy, while exposure to Uranium, Zinc, and Mercury causes respiratory, inflammatory, and neurodegenerative diseases. Cadmium and Lead are particularly concerning due to bio-accumulation and kidney/cardiovascular toxicity, especially in developing nations (Silva-Rêgo et al., 2022; Stewart, 2019).

These environmental impacts disproportionately affect marginalized and indigenous communities, causing livelihood loss through agricultural and property decline (Leyton-Flor et al., 2024). Furthermore, catastrophic tailings dam failures cause destruction and displacement (Segui et al., 2023; Falagán et al., 2017; Kossof et al., 2014); although financial penalties are rare, mismanagement erodes corporate and government credibility (Segui et al., 2023).

Addressing these liabilities requires shifting to resource repurposing, transforming waste into economic assets (Tayebi-Khorami et al., 2019). Circular economy mandates reuse and recycling, where valuable metal recovery accompanies total residue valorization (McLellan et al., 2013).

Effective mine waste management requires governance involving residents, indigenous groups, and NGOs to address environmental, technical, and socio-economic challenges. Corporate Social Responsibility (CSR) initiatives must align with global sustainability imperatives by prioritizing infrastructure, conservation, and education to foster trust (Jackson et al., 2022). This convergence of regulatory compliance and social accountability creates an ethical imperative for innovative solutions that generate local employment, restore land, and improve community health.

1.3.3 Complexities and regulatory pressures

Effective mine waste management presents substantial complexities, where economic drivers and legal implications serve as critical factors that establish new paradigms and enable innovative approaches (Jose et al., 2024; Tayebi-Khorami et al., 2019).

Environmental liabilities arise when mining operations cause damage or risk (Leyton-Flor et al., 2024). While core composition remains consistent, IOTs vary significantly by location and extraction method, creating storage and management challenges defined by site-specific waste quality (Thejas & Hossiney, 2021). This variability demands tailored management; for instance, high-sulfide tailings are at risk of acid drainage and heavy metal release (Mohapatra & Kirpalan, 2016).

Although data deficiencies hinder management at legacy sites, transforming waste into construction materials offers environmental benefits. However, widespread adoption faces challenges related to quality consistency, long-term performance, market perception, and regulatory obstacles that lack incentives (Abraham & Gundimeda, 2018).

In Goa, the 1987 Abolition Act (Pai, 2018) and Supreme Court shutdowns illustrate a stringent regulatory landscape that drives innovation beyond compliance. Given Goa's high waste-to-ore ratios and land scarcity, valorizing IOTs into composite materials emerges as a strategic response. This pathway enables companies to meet strict standards, reduce liabilities, and align economic sustainability with environmental protection.

1.4 Need for eco-friendly building materials

Understanding the growing need for sustainable construction practices highlights how mine waste valorization integrates into this broader area.

1.4.1 Multidimensional benefits of sustainable construction

The construction sector contributes substantially to global greenhouse gas (GHG) emissions and global warming drivers (Akan et al., 2017). Effective material management is fundamental to minimizing construction's environmental footprint. Sustainable practices utilize holistic lifecycle approaches to promote circular-economy principles and minimize sourcing impacts (Lin, 2021). Furthermore, the long-term environmental and community benefits of responsible mining significantly outweigh implementation costs (Goodland, 2012).

Transforming mine waste into construction materials addresses the industry's heavy resource consumption by converting a problematic by-product into a valuable resource (Yu et al., 2024; Ghose, 2009). This research advances the circular economy, reducing virgin material demand and environmental damage while fostering a resilient, resource-efficient future.

1.4.2 Circular economy in construction

The circular economy offers a restorative alternative to the linear take-make-dispose model, fostering economic and ecological sustainability while ensuring operational stability (Jesus & Mendonça, 2018). Integrating this framework into mining demands a paradigm shift prioritizing long-term sustainability—including carbon reduction and social impact—over short-term profit, transforming mine waste from a discarded by-product into an untapped resource (Jose et al., 2024). Figure 1.2 illustrates the circular economy of mining industry.

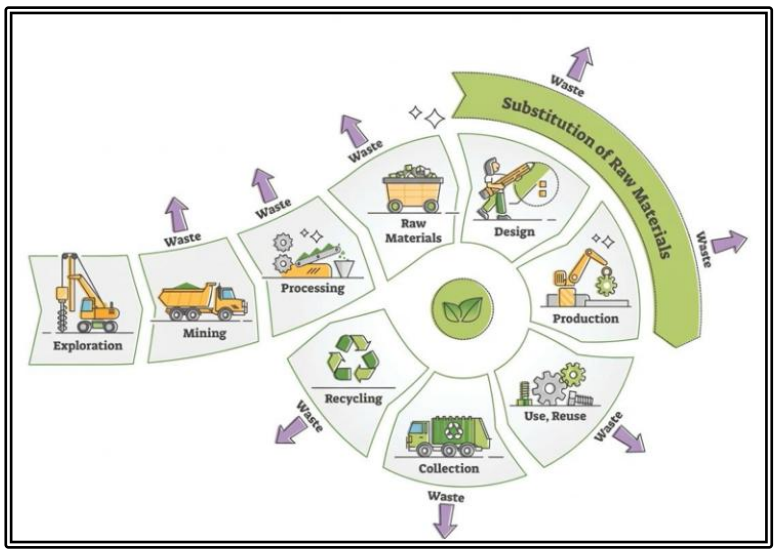


Figure 1.2: Circular economy in Mining

By converting mine waste into construction materials, this research supports circularity in both sectors: reducing mining liabilities and decreasing construction's reliance on virgin materials. This conversion strategy establishes a tangible pathway for cross-sector collaboration, turning waste challenges into sustainable solutions.

1.4.3 Opportunities for mine waste valorization in sustainable construction

Driven by environmental pressures and rising costs, mine waste is transforming from a liability into a valuable asset (Zhang et al., 2020; Tayebi-Khorami et al., 2019; Da Silva

et al., 2014). Implementing these innovative paradigms depends on economic drivers and legal frameworks (Tayebi-Khorami et al., 2019). While tailings often contain recoverable metals (Falagán et al., 2017), a circular economy framework maximizes value by repurposing waste into construction materials, geopolymer cement, and soil restoration resources (Tayebi-Khorami et al., 2019).

Compelling economic incentives and global demand for sustainable building solutions position repurposed products, including aggregates, bricks, and tiles, as key export commodities (Chen et al., 2024; Yu et al., 2024; Evdokimov et al., 2016; Chen et al., 2013). This strategic shift enhances resource security and supply chains, offering a credible business case for reducing reliance on virgin materials and lowering environmental footprints.

While these circular economy principles apply globally, Goa's context demands targeted application. Given 40 million tonnes of overburden generated by iron ore mining (Section 1.3.1) and limited disposal land, this research targets Goan IOTs explicitly. By developing high-performance composite construction materials such as bricks, blocks, pavers, and cladding panels, this study bridges the identified gap between generic mine waste research and regionally optimized, durable solutions that meet Goa's unique regulatory and environmental constraints.

1.5 Strategic approach

The study aims to create innovative composite materials from IOTs, addressing disposal issues and meeting sustainable construction demand. Research involves systematic investigation, characterization, and sustainability assessment of new composites, with evaluation of environmental and economic benefits.

Material development follows an iterative process of material selection, precise processing, thorough characterization, and detailed performance evaluation. This multidisciplinary research, drawing on findings from materials science, environmental engineering, and civil engineering, seeks to advance sustainable engineering by demonstrating how material innovations offer practical solutions to complex environmental challenges.

The study's findings will contribute fundamental scientific knowledge and practical sustainable solutions to critical global challenges, with a localized focus on Goa. Furthermore, this research could serve as a valuable model for other regions confronting

similar mining waste issues, fostering ripple effects on global sustainable development practices.

1.6 Research gap

The literature review establishes a significant research gap. This section synthesizes the introductory framework to articulate the specific problem addressed by this study and clarifies the original contribution to existing knowledge.

1.6.1 Existing challenges and current solutions

Given the massive global volumes of mine waste outlined in Section 1.2.1, current management practices remain inadequate. AMD, habitat destruction, and socio economic burdens on local communities create an urgent demand for sustainable solutions (Tayebi-Khorami, 2019; Falagán et al., 2017). Socio economic disruptions cascade through mining affected regions, including increased living costs, elevated accommodation expenses, school dropouts, and drug abuse, which compound community insecurity. Mining operations displace farmers, trigger unemployment, and cause livelihood losses by converting agricultural land for mining (Mensah et al., 2025). Notably, mining's economic benefits fluctuate with volatility in foreign demand, while environmental and human impacts persist over extended timeframes (Leyton - Flor et al., 2024).

Current practice diverts a minor proportion of tailings to mined out areas as backfill material. At the same time, the majority accumulates in environmental stockpiles or specialized tailings dams designated for long term storage (Kuranchie et al., 2015). Persistent failure risks and the potential for widespread pollution characterize these storage systems (Stark, 2022). Recognition increasingly positions mine waste, historically regarded as a liability, as a significant resource with untapped potential.

The transition to sustainability and the circular economy in construction and mining goes beyond technology, requiring legal and regulatory reforms and strong international partnerships. Integrating innovation with adaptive frameworks encourages resource efficiency and circularity. Regulatory support shapes enabling conditions, while rigid frameworks can hinder progress. Continuous reform and global co-operation are crucial for the mining sector to meet sustainability goals and ensure economic and environmental resilience (Jesus & Mendonça, 2018).

The low grade composition and immense volume of IOTs render traditional recovery methodologies insufficient, perpetuating liabilities and catastrophic risk potentials (Lumbroso et al., 2019; Patra et al., 2018). Valorization emerges as a transformative solution gaining sectorial traction. Systematic planning and execution convert mine waste from a liability to marketable products, repositioning waste streams as potential resources rather than containment dependent materials (Shettima et al., 2016).

1.6.2 Identification of gap in mine waste derived composites

Mine waste valorization transforms liabilities into assets, yet substantial research and development are needed to identify efficient, effective solutions across key implementation areas (Tayebi-Khorami et al., 2019). Sustainable composite construction materials derived from mine waste deliver dual benefits: environmental remediation of waste disposal concerns and meeting the accelerating demand for eco-friendly building materials (Das et al., 2023; Vo et al., 2022; Shreekant et al., 2016).

A persistent research gap pervades the literature, which includes insufficient long term durability data for mine waste derived materials (Zhang et al., 2020). Chemical-attack resistance and freeze-thaw-cycle performance of mine-waste-derived construction materials require substantially expanded experimental documentation. Laboratory to industrial scaling encounters substantial technical and operational challenges (Wang et al., 2020).

Goa's extensive iron ore mining history and corresponding waste volumes create a distinct and critical research gap: limited investigations focus on developing high value composite materials from Goan mine waste. Such research must accommodate the unique mineralogical composition of local waste and address specific environmental pressures and regional regulatory contexts.

Existing investigations predominantly focus on partial or complete substitution of fine aggregates with mine waste, particularly IOTs. These studies comprehensively characterize the physicochemical properties of mine wastes and the resulting composite mechanical performance, particularly compressive strength and workability parameters (Arbili et al., 2022; Mendes et al., 2021; Shettima et al., 2016).

Waste valorization in Goa's mining industry centers on converting IOTs. The critical research imperative demands the optimal transformation of these tailings into high performance, durable, and eco-friendly composite materials that satisfy construction

requirements. Generic solutions prove inadequate; targeted investigation must resolve unique material science challenges specific to these tailings, yielding dependable products. This study bridges theoretical mine waste reuse potential and real world implementation, particularly addressing waste management challenges faced by the mining industry.

1.6.3 Significance and novelty of the proposed research

The research demonstrates multifaceted significance across environmental, economic, and societal dimensions:

Environmental Mitigation: The investigation directly targets critical environmental degradation pathways driven by mine waste, including land degradation, water pollution, and habitat destruction, particularly in ecologically sensitive areas. Waste utilization pathways reduce disposal volumes and mitigate the release of harmful contaminants.

Resource Conservation: Converting mine waste into valuable construction materials actively reduces demand for virgin raw material extraction, aligning with circular-economy principles and advancing efficient resource use.

Economic Opportunity: The work transforms a significant waste liability into a valuable resource, potentially generating new industries and revenue streams for mining and construction sectors. The shift converts cost centers into value generating activities.

Sustainable Development: The research advances broader sustainable development objectives by fostering circular, environmentally responsible built environments, promoting resilience, and resource efficiency.

This research advances a novel, systematic methodology for developing composite materials from Goan iron ore mine waste, calibrated explicitly to local mineralogical characteristics and environmental conditions. The investigation generates optimal processing techniques, comprehensive material characterization, and robust performance-evaluation protocols, ensuring long term durability. By bridging global mine waste valorization theory with regionally optimized, commercially viable solutions, offering a scalable model for other mining-impacted regions.

The studies will also bridge waste management imperatives and advanced materials science, establishing scientifically rigorous pathways for high value utilization of abundant and challenging waste streams. The work highlights the transformative

potential at the intersection of waste management and materials science, shifting paradigms from disposal centric approaches to resource recovery.

Study findings contribute fundamental scientific knowledge and practical, sustainable solutions to a critical global challenge with a localized Goan application. Furthermore, this research models approaches applicable to other mining-waste-affected regions, fostering the advancement of sustainable development practices worldwide.

1.7 Objectives and scope of the work

Driven by literature findings, the study explores the practical application of mine waste recycling for construction materials. As reflected in the thesis entitled, 'Development of Composite Material using Mine Waste', the study addresses the environmental and economic challenges generated by overburden dumps in Goa, which dictate the following research objectives:

1. To analyse and understand the physicochemical parameters of mine waste samples.
2. To assess the suitability of other materials for their potential use as a construction material, along with mine waste.
3. To investigate various combinations of binding materials with mine waste for determining the optimal performance.
4. To utilize mine waste in the manufacturing of various composite construction materials, such as bricks, blocks, pavers, tiles, and cladding panels.
5. To assess the cost of setting up a manufacturing unit, calculate the production cost per item, and determine the payback period.

The research scope includes a comprehensive feasibility investigation of mine waste as a construction material. The multifaceted approach begins with the collection and thorough physicochemical analysis of diverse mine waste samples to establish an understanding of material properties.

Optimization investigation focuses on binding agent combinations with mine waste to identify peak-performing formulations for final products. Optimized mixtures enable the manufacturing of diverse construction materials, including bricks, blocks, pavers, tiles, and cladding panels.

Economic analysis completes the scope, assessing manufacturing unit establishment investment requirements, calculating per unit production costs, and establishing financial feasibility through payback period determination.

1.8 Organization of thesis

Chapter 1: Establishes the foundational context, outlining the initiation of mining operations and the progression of associated waste generation. The comprehensive mining scenario summary progresses from a global perspective to a focused examination of the state of Goa. The chapter presents the methodological frameworks employed, the critical problem of mine waste disposal, and the imperative for sustainable construction materials. The articulation of the research gap justifies the study's necessity and concludes with a clear delineation of the research objective.

Chapter 2: A comprehensive literature review examines prior investigations into mine waste utilization, specifically IOTs, in construction material development contexts. A critical assessment of research on mine waste management and disposal methodologies establishes a foundational understanding for subsequent analyses. The investigation elaborates on studies that incorporate IOTs into diverse construction products, notably bricks, blocks, pavers, tiles, and cladding. The summary of salient findings and emerging trends concludes the chapter.

Chapter 3: Exhaustive experimental protocols and analytical techniques outline assessment methodologies to evaluate the viability of incorporating mine waste into various construction materials. A comprehensive experimental model overview encompasses the characterization of raw-material physicochemical attributes and the detailed mix-proportioning for brick, block, paver, tile, and cladding panel fabrication. The experimental investigation results complete the chapter presentation.

Chapter 4: Results and Discussion section meticulously analyzes experimental data, transforming raw findings into meaningful insights. An introductory overview precedes the individual product performance analysis, including bricks, blocks, pavers, tiles, and cladding panels.

Discussion sections present comprehensive testing results for each product type, interpret the data, and highlight key findings. The literature comparison establishes the contextual positioning of the results obtained. Furthermore, the successful mechanical and durability outcomes highlight the products' inherent sustainability, demonstrating that mine waste can be reliably repurposed to offset demand for virgin resources. Economic evaluation encompasses manufacturing unit establishment costs, per-unit production costs, and the determination of the payback period, thereby establishing the

economic viability of mine waste construction materials. The chapter evaluates both performance and economic feasibility simultaneously.

Chapter 5: Key findings and insights synthesis consolidates research outcomes. A comprehensive study summary precedes concise conclusions that highlight the research's significance and the relevance of IOTs as a composite construction material. Outcome-based recommendations specify practical applications and the potential for improvement in material development and utilization. Future work scope delineation identifies areas for expansion for further investigation and research advancement.

CHAPTER 2
LITERATURE REVIEW

2.1 General

A rigorous, systematic literature review established the foundational framework for this investigation. An analysis of prior studies mapped historical research progress, highlighted critical knowledge gaps, and subsequently directed the focus toward utilizing mining waste as a raw material for composite construction materials.

Previous analyses indicated that iron ore extraction and beneficiation operations generated substantial amounts of mineral waste, necessitating urgent improvements in disposal practices. Although iron ore tailings (IOTs) presented substantial potential for valorization within circular economy frameworks, limited techno-economic validation and unresolved scalability challenges constrained large-scale deployment. Intensive production volumes in major iron-ore-producing nations, such as Australia, Brazil, and China, amplified the severity of this issue. Within India, the immense concentration of the nation's iron ore reserves in Goa escalated the local criticality of the problem. Prolonged mining activities in this region resulted in massive stockpiles of tailings and overburden, leading to severe environmental impacts, including land degradation, water contamination, and ecological instability.

Historically, inadequate extraction methods for low-grade ores generated unutilized tailings, accounting for approximately 10–15% of India's mined iron ore. The safe disposal or productive application of this substantial mineral resource, particularly in the form of ultra-fines or slimes, presented a significant, unresolved challenge for the Indian iron-ore industry. Furthermore, overburden—comprising the massive quantities of overlying waste rock displaced to access the ore body—constituted another critical waste fraction. Specifically, open-cast mines and quarries yielded significantly higher volumes of this waste compared to underground operations (Shreekant et al., 2016).

Consequently, recent material development frameworks incorporated IOTs into construction applications to address these environmental concerns. IOT-based composites, when blended with supplementary binders such as fly ash, ground granulated blast furnace slag (GGBS), and lime, exhibited enhanced mechanical strength, durability, and impermeability. This performance profile underscored a dual opportunity: mitigating environmental risks associated with mining by-products while

advancing sustainable, resource-efficient construction practices. Concurrently, a substantial global and domestic demand for building materials persisted, which rendered the integration of mining wastes into the production of bricks, concrete blocks, and other value-added products both environmentally necessary and strategically advantageous.

2.2 Utilization of mine tailing waste in composite material

Continuous extraction of natural resources for traditional construction materials—including concrete, bricks, hollow and solid blocks, pavement blocks, and tiles—led to severe environmental degradation and escalated production costs amid high demand, raw material scarcity, and rising energy prices (Safiuddin et al., 2010). Concrete, the second most-consumed natural resource after freshwater, registered an approximate per capita consumption of 3 tonnes annually, thereby intensifying pressure on natural reserves (Gagg, 2014; Collins & Ciesielski, 1994). Portland cement, the principal constituent in concrete production, alone contributed up to 5% of global CO_2 emissions (Humphreys, 2018; Hasanbeigi et al., 2012; Adiguzel et al., 2012). Construction practices, therefore, increasingly targeted alternative materials to reduce associated carbon footprints.

Industrial by-products, such as Iron Ore Tailings (IOTs), have significant potential as mineral additives because their granulometry and chemical composition align with cementitious systems (Franco et al., 2022). Global iron ore production, which reached approximately 2.5 billion tonnes in 2019, continuously generated large volumes of IOTs, occupying extensive land areas and requiring substantial investment in tailing dam construction. Circular economy strategies that repurposed mine waste converted environmental liabilities into resource assets and increased value through materials recovery (Kinnunen et al., 2022).

Recycling pathways for iron ore tailings transformed this industrial waste into sustainable construction resources (Thejas & Hossiney, 2022; Kuranchie et al., 2015). Utilization methodologies that manufactured bricks, concrete pavers, ceramics, and geopolymers simultaneously valorized tailings and mitigated tailings storage challenges. Iron ore tailings thereby demonstrated technical, economic, and ecological viability not only in such products but also within a broader range of cementitious composites (Almada et al., 2022).

The brick formulations reported by Thejas & Hossiney (2022) used IOT as the primary aggregate, thereby replacing natural materials. Binder systems that combined fly ash and Ground Granulated Blast-furnace Slag (GGBS), activated by sodium silicate, integrated IOT into the brick composition and contributed to the development of the microstructure. Geopolymerization at ambient temperature converted silicon- and aluminum-rich industrial waste into inorganic polymers that functioned as solid binders analogous to Ordinary Portland Cement (OPC). These geopolymer systems delivered an 80–90% reduction in CO_2 emissions and enhanced resistance to fire and chemical attack (Kumar et al., 2020). These eco-friendly bricks eliminate the need for fuel and produce negligible greenhouse gas emissions.

As an alternative to river sand, IOT served as a viable aggregate in concrete and reduced the environmental burden of alluvial sand extraction (George, 2023). The higher proportion of fine particles in IOT relative to natural sand impaired the workability of fresh concrete, primarily through increased water demand and altered particle packing (George, 2023; Zhao et al., 2021). However, low IOT contents exploited filler effects, thereby enhancing compressive strength. Systematic investigations identified an optimal IOT inclusion range of approximately 30–40%, with recent studies reporting compressive strength gains of 11.56–18.41% relative to conventional aggregates (Arbili et al., 2022; Zhao et al., 2021). Substituting Cement and aggregates with fine-grained tailings correspondingly reduced consumption of virgin raw materials and mitigated associated environmental impacts (Adiguzel et al., 2022).

Concrete paver production in Filho et al. (2017) incorporated IOT at replacement levels of 10%, 20%, and 80%, and these mix designs maintained structural integrity while providing a sustainable alternative to natural aggregates. The resulting pavers mitigated ecological risks linked to tailings dams and advanced circular resource flows in construction.

Paver mixtures in Mantilla et al. (2017) replaced natural and industrial sand with IOT at substitution levels of 50% natural sand (T1), 50% industrial sand (T2), and 100% industrial sand (T3), and all mixtures exceeded the minimum compressive strength requirement of 35 MPa. Mix designs examined by Kumar et al. (2014) replaced fine aggregates with IOT at 10–50% by mass; increasing IOT content reduced workability because higher water absorption and surface roughness of the IOT demanded greater

mixing water, yet the mixture containing 40% IOT achieved the maximum compressive strength and outperformed the control mixture at both 28 and 56 days of curing.
Repurposing mine tailings as building materials significantly reduced the environmental impacts of mining operations and waste disposal, promoted sustainable development, and enabled innovative, resource-efficient construction solutions.

2.3 Materials used in the development of a composite using mine tailing waste

Previous literature indicated that composite material development extensively employed various waste materials, with selection guided by the physical and chemical characteristics of the constituent raw materials. Notable examples included Iron Ore Tailings (IOTs), Ground Granulated Blast-Furnace Slag (GGBS), Cement, Fly Ash, Lime, Ceramic Waste, and both Fine and Coarse aggregates. The following sections detail the specific roles and properties of these materials as applied in existing studies.

2.3.1 Iron Ore Tailings (IOTs)

IOTs constituted a major industrial by-product of beneficiation processes—such as crushing, screening, grinding, washing, jigging, and cyclizing—used to separate valuable iron fractions from raw ore (Kumar et al., 2020). Tailing disposal presented a significant challenge, as heavy metals possessed the potential to contaminate soil and water. Furthermore, land constraints on dumping led to deforestation, erosion, and landslides. The lack of advanced beneficiation techniques for low-grade ores left most tailings unused, exacerbating ecological risks and wasting potentially valuable resources (Thejas & Hossiney, 2022).
Chemical compositions of IOTs varied across geographic locations due to the diverse nature of iron ore deposits and the different processing methods employed worldwide. High silica content (≥60%) enhanced pozzolanic reactivity and Cement compatibility, while exceptionally high iron content underscored variations in ore quality and beneficiation. Compositional analysis revealed that IOTs did not behave as a uniform material, necessitating site-specific characterization for optimal utilization strategies. Compositional analysis revealed that iron ore tailings did not behave as a uniform material, necessitating site-specific characterization for optimal utilization strategies. The varying chemical composition of different IOT sources required detailed testing

before large-scale application. Specifically, the distinct chemistry of each source determined the manufacturing parameters.

Table 2.1 summarizes the chemical compositions of IOTs reported in six different studies.

Table 2.1: Chemical composition of IOTs (in Wt %)

Composition	Singh et al. 2021	Chinnappa & Karra 2019	Jiang et al. 2019	Thejas & Hossiney 2022	Yang et al. 2014	Chen et al. 2011
SiO_2	49.00	49.75	73.85	30.37	36.48	24.40
Al_2O_3	23.22	9.74	5.92	12.43	11.67	10.95
Fe_2O_3	24.76	27.03	15.4	46.33	18.58	31.15
CaO	0.23	4.06	0.48	3.88	16.85	6.20
MgO	0.53	3.109	1.20	1.68	5.66	0.99
K_2O	0.3	0.50	1.00	0.25	0.84	0.86
TiO_2	1.15	--	--	3.96	0.46	0.42
LOI	0.04	--	5.85	1.10	7.8	6.95

2.3.2 Cement

Oxides of calcium, silicon, aluminum, and iron imparted the requisite hydraulic properties to Cement, the primary binder in concrete. At temperatures around 1450^{o}C, these oxides reacted to form clinker minerals, which imparted setting characteristics and mechanical strength to the final product. Processing involved crushing and homogenizing raw materials such as limestone, clay, and iron-rich residues, followed by feeding them into a rotary kiln where thermal decomposition and solid-state reactions yielded clinker nodules. Subsequent milling of the cooled clinker with gypsum ($CaSO_4 \cdot 2H_2O$) regulated setting time and ensured concrete performance (Dunuweera & Rajapakse, 2018).

Cement manufacturing functioned as an energy-intensive process, accounting for roughly 15% of global industrial energy consumption (Mokhtar & Nasooti, 2020) and 26% of industrial CO_2 emissions (Guo et al., 2025). To mitigate environmental impacts, the industry incorporated supplementary cementitious materials (SCMs)—including GGBS and fly ash—to replace a fraction of clinker, thereby lowering the clinker factor and carbon footprint (Basavaraj & Gettu , 2024; Jhatial et al., 2019). Strict oxide proportions defined Portland Cement, the most widely used hydraulic Cement: calcium oxide (60–65%), silicon dioxide (17–25%), aluminum oxide (3–8%), and iron oxide

(0.5–6%), with minor constituents such as MgO, alkalis ($Na_2O + K_2O$), and SO_3. Clay provided SiO_2, Al_2O_3, and Fe_2O_3, while calcined lime supplied CaO; kiln reactions and subsequent grinding fineness influenced hydration kinetics and strength development.

According to Indian standards, Ordinary Portland Cement (OPC) is classified into grades 33, 43, and 53 based on compressive strength, with setting times ranging from 45 minutes to 10 hours, as per IS 4031-1988 (Dunuweera & Rajapakse, 2018). Optimizing mix design through SCM integration, enhancing grinding fineness, and adopting advanced kiln technologies substantially reduced the cement industry's environmental footprint without compromising performance.

The physical properties of cement, as reported in the literature, emphasized the need for consistent setting behaviour and soundness, which remain vital for structural applications. Tables 2.2 and 2.3 present the physical and chemical properties of Cement.

Table 2.2: Physical properties of Cement (in Wt %)

Property	**Chinnappa & Karra 2019**	**Kattoli et al. 2018**	**Ugama et al. 2014**
Specific gravity	3.14	3.10	--
Standard consistency	29.00%	32.00%	31.00%
Initial setting time	60 min	50 min	80 min
Final setting time	450 min	270 min	170
Fineness	300 m^2/kg	5%	0.05%
Soundness	2 mm	2 mm	1mm

Table 2.3: Chemical composition of cement (in Wt %)

Composition	**Farooq et al. 2023**	**Mendes et al. 2021**	**Dunuweera & Rajapakse 2018**	**Aruna & Kumar 2010**
SiO_2	20.6	18.76	17-25	22
Al_2O_3	5.08	4.57	3-8	5
Fe_2O_3	3.27	3.17	0.5-6	3
CaO	62.5	61.99	60-65	62
SO_3	1.57	3.14	1-2	--
MgO	2.56	1.73	--	2
$K_2O + Na_2O$	--	0.59	0.5-1	1

Physical parameters generally adhered to international testing standards but showed some variation between different studies, reflecting differences in raw material sources and experimental conditions. Such variability proved important for assessing workability, strength development, and dimensional stability of cementitious mixes.

OPC is composed of four principal oxides: calcium oxide (CaO), silica (SiO_2), alumina (Al_2O_3), and ferric oxide (Fe_2O_3). These oxides accounted for about 90% of the cement's weight and played a critical role in its properties and performance. Calcium oxide, the most abundant, drove strength development through hydration reactions. Silica contributed to strength and durability; alumina improved early strength and workability, while ferric oxide influenced colour and specific performance characteristics. Minor constituents included sulfates (SO_3), which controlled setting time; magnesia (MgO), which required limitation to prevent unsoundness; and alkali oxides (K_2O and Na_2O), which affected potential deleterious reactions. Critical assessment of both physical and chemical parameters optimized the mix design and ensured the long-term performance of sustainable composites.

2.3.3 Ground Granulated Blast Furnace Slag (GGBS)

GGBS, an industrial by-product of pig iron production, gained recognition as a sustainable supplementary cementitious material (SCM) in concrete. Rapid cooling of molten slag followed by fine grinding produced GGBS, which possessed a chemical composition similar to Portland Cement, predominantly containing CaO (30–50%), SiO_2 (28–38%), Al_2O_3 (8–24%), and MgO (1–18%) (Snellings et al., 2012). Its application contributed to reduced CO_2 emissions, enhanced durability against corrosion and sulfate attack, a lower heat of hydration, and extended service life of structures (Sheikh et al., 2018; Shreyas, 2017).

Global GGBS production ranged from 140 to 330 million metric tons annually, offering significant potential for integration into the Cement and construction industries. When incorporated into concrete, GGBS promoted secondary hydration by forming additional calcium silicate hydrate (C–S–H) gel, thereby lowering porosity and enhancing strength (Gong & White, 2016). Performance requirements dictated GGBS replacement levels of 20–80%, with 40–50% as the standard in ready-mix concrete. Lower percentages facilitated early strength gain, while higher ratios improved long-term durability (Suresh

& Nagaraju, 2015). Table 2.4 presents the chemical compositions of GGBS from four different studies.

Table 2.4: Chemical composition of GGBS (in Wt %)

Composition	Smita et al. 2020	Sudhir et al. 2020	Gong & White 2016	Arivalagan 2014
SiO_2	27.4	34.16%	31.62 to	10%–19%
Al_2O_3	14.2	17.54%	8.95 to	1–3%
Fe_2O_3	3.4	1.99%	0.28 to	20%–30
CaO	45.94	37.10%	33.92 to	40%–52%
Na_2O	0.26	0.57%	0.00 to	--
MgO	5.34	7.17%	1.17 to	5–10%
TiO_2	1.62	1.00%	0.44 to	--
LOI	1.72	0.10%	--	--

Moreover, alkali activation of GGBS produced alkali-activated slag cement, further expanding its application in sustainable construction (Zhu et al., 2024). In practice, structures incorporating GGBS exhibited improved impermeability, reduced maintenance needs, and extended lifespans, sometimes lasting 50–100 years (Shumuye & Zhao, 2018).

Silicon dioxide, aluminum oxide, ferric oxide, and calcium oxide constituted the principal oxides in GGBS. Their proportions varied significantly across sources and production processes. Silicon dioxide and aluminum oxide exhibited wide variations, reflecting differences between international industrial samples and specific regional studies. Ferric oxide content showed notable disparity, likely due to variations in raw materials or testing methods. Calcium oxide remained consistently high, highlighting GGBS's inherent calcium-rich nature. These variations influenced the material's reactivity and performance in concrete applications.

Minor oxides in GGBS, such as magnesium oxide, were present at moderate levels, consistent with industry standards. Sodium oxide and titanium dioxide existed in smaller quantities but played important roles in enhancing durability. Loss on ignition generally remained low, reflecting the minimal presence of uncombined water and volatile substances. Understanding this compositional variation proved crucial for interpreting the performance and suitability of GGBS in cementitious applications.

2.3.4 Fly ash

Fly ash, a coal combustion by-product composed of glassy, spherical mineral particles, primarily contains silicon, aluminum, and iron oxides. Trace heavy metals in fly ash cause environmental issues when not disposed of properly. Global production projections anticipated an increase of up to about 2000 Mt in 2020 (Gamage et al., 2011), yet much of it went unused. Classification divides fly ash into two main types:

- Class F: Produced from bituminous coal, this type contained low lime and high silica, alumina, and iron oxides. It effectively improves sulfate resistance in concrete.
- Class C: Sourced from sub-bituminous and lignite coals, this ash possessed high lime content and self-hardened, contributing to early strength in concrete.

Table 2.5 shows the composition of Fly ash presented by Permatasari et al. (2023).

Table 2.5: Chemical composition of Fly ash (in Wt %)

Component	Hardjito et al. 2016	Abdullah et al. 2013	Bakria et al. 2011	Temuujin & Riessen 2009	Thokchom et al. 2009	Kong et al. 2007
SiO_2	47.8%	26.4%	52.11%	-	56.01%	48.8%
Al_2O_3	24.4%	9.25%	23.59%	23.63%	29.8%	27%
Fe_2O_3	17.4%	30.13%	7.39%	15.3%	3.58%	10.2%
TiO_2	1.328%	3.07%	0.68%	1.32%	1.75%	1.3%
CaO	2.42%	21.6%	2.61%	1.74%	2.36%	6.2%
MgO	1.19%	--	0.78%	1.2%	0.3%	1.4%
Na_2O	0.31%	--	0.42%	0.38%	0.61%	0.37%
BaO	--	--	--	--	--	0.19%
SrO	--	--	--	--	--	0.16%
K_2O	0.55%	2.58%	0.8%	0.84%	0.73%	0.85%
P_2O_5	2.0%	0.67%	1.31%	1.31%	0.44%	1.2%
SO_3	0.29%	1.3%	0.49%	0.28%	Nil	0.22%
MnO	0.12%	--	0.03%	--	--	0.15%
ZrO_2	--	--	--	--	--	--
LOI	1.1%	4.34%	--	1.78%	0.4%	1.7%

Fly ash shared many chemical compounds with Portland cement, but remained richer in reactive silicates. When added to concrete, fly ash reacts with free lime, increasing strength and durability. It also improved concrete workability by reducing water demand and minimizing segregation and bleeding. Using fly ash as a 25% replacement

for cement helped maintain strength and durability, offering a sustainable solution for the cement industry (Gamage et al., 2011).

2.3.5 Lime powder

Lime powder, derived from finely ground calcium carbonate ($CaCO_3$), served as an extensively studied sustainable supplementary cementitious material (SCM) for partial replacement of Portland cement or fine aggregates. Industrial limestone powder typically exhibited particle sizes comparable to those of cement and fly ash, consisting predominantly of calcite with minor $MgCO_3$ and SiO_2, and minimal alumina or iron oxides. Its moderate specific gravity and high calcium content contributed to buffering capability and dimensional stability within cement matrices (Basavaraj & Gettu , 2024; Hake et al., 2018).

Limestone powder affected cementitious composites via four main mechanisms. Predominantly at low dosages, the filler effect occurred, with fine limestone particles filling the voids between larger cement grains, enhancing packing density, reducing capillary porosity, and improving early-age impermeability and mechanical interlock (Wang et al., 2018; Ramezanianpour et al., 2009). Additionally, limestone surfaces provided nucleation sites that facilitated calcium-silicate-hydrate (C–S–H) gel precipitation, thereby accelerating hydration kinetics and enhancing early strength, especially when limestone particles were finer than the cement particles (Hake et al., 2018; Burroughs et al., 2017). When limestone replacement exceeded optimal levels, the dilution effect became dominant; the inert $CaCO_3$ lowered clinker content, reducing heat of hydration and chemical shrinkage but causing late-age strength reductions due to fewer hydraulic phases (Wang et al., 2018). Moreover, in the presence of alumina-rich SCMs, limestone underwent a chemical effect, reacting with aluminate phases to form carboaluminate hydrates that enhanced long-term matrix stability and refined pore structure (Hake et al., 2018).

Fresh-state behaviour benefited from moderate limestone additions, resulting in improved workability and reduced water demand, attributed to the spherical morphology and filler action, which lowered plastic viscosity and yield stress. However, irregular or angular limestone morphologies increased water demand and superplasticizer doses (Wang et al., 2018). Mechanically, low limestone levels increased early compressive strength via filler and nucleation effects, with significant gains

observed in ultra-high-performance concretes. Beyond optimal content, dilution effects led to progressive reductions in strength; flexural and tensile strengths followed similar trends, with minor limestone additions enhancing toughness, particularly with nano-limestone forms. Table 2.6 shows the composition of Lime powder.

Table 2.6: Chemical composition of Lime powder (in Wt %)

Composition	Hake et al. 2018	Ramezanianpour et al. 2009
SiO_2	3.92	1.47
Al_2O_3	2.74	0.22
Fe_2O_3	0.38	0.29
MgO	0.28	0.30
SO_3	--	0.06
Na_2O	--	0.05
CaO	51.01	54.77
LOI	41.56	42.23
K_2O	0.04	0.08
TiO_2	0.09	0.05

Limestone powder has a refined pore structure that reduces water permeability, sorptivity, and chloride diffusion, thereby extending service life under aggressive exposure conditions. Nonetheless, excessive limestone or high C_3A cement content increased vulnerability to sulfate and carbonation attack due to the formation of ettringite and thaumasite, and to diminished alkalinity. Optimal limestone use balances these durability benefits while minimizing adverse chemical effects.

Environmentally, limestone substitution significantly reduced CO_2 emissions and embodied energy while maintaining strength and durability comparable to those of fly ash concrete. Life-cycle assessments confirmed that limestone-calcined clay (LC_2) composites delivered superior sustainability indices relative to Ordinary Portland cement or fly ash concrete (Basavaraj & Gettu, 2024; Wang et al., 2018; Hake et al., 2018).

2.3.6 Ceramic waste

Industries producing tiles, sanitary ware, pottery, and electrical insulators generate ceramic waste, with estimates that 15–30% of total production is discarded as ceramic waste (Awoyera et al., 2018; Senthamarai & Manoharan, 2005). In Europe alone,

annual ceramic waste reached 3–7% of global ceramic production, amounting to millions of tons landfilled each year. Increasing landfill restrictions and disposal costs have driven research into sustainable reuse strategies. The construction industry, as the primary consumer of both coarse and fine aggregates, offered a promising pathway for the valorization of ceramic waste (Ahmad et al., 2023; Pacheco-Torgal & Jalali, 2010).

Ceramic waste exhibited specific gravity in the range of 1.89–2.68 and water absorption in the range of 0.10–6.1%, depending on source and processing. Scanning electron microscopy revealed that CW particles were irregular and angular with rough surfaces, reducing concrete workability. Chemically, ceramic waste contained high silica (55–75%) and alumina (9–20%) contents, imparting pozzolanic activity when finely ground (Ahmad et al., 2023; Song et al., 2019; Pacheco-Torgal & Jalali, 2010; Senthamarai & Manoharan, 2005). Table 2.7 shows the composition of Ceramic Waste presented by Ahmad et al. (2023).

Table 2.7: Chemical composition of ceramic waste (in Wt %)

Composition	Arab et al. 2022	Atkuri et al. 2021	Ali et al. 2019	Olawale et al. 2018	Hasan et al. 2014
SiO_2	67.3	68.11	55.3	64.56	75.4
Al_2O_3	19.8	16.48	18.3	15.07	9.10
Fe_2O_3	2.5	0.59	6.22	6.01	1.90
MgO	2.0	1.61	0.39	2.04	1.88
CaO	2.3	0.85	11.06	4.15	8.60
Na_2O	--	3.78	0.68	--	--
K_2O	--	3.14	1.20	--	--

Complete replacement of coarse aggregate with crushed CW resulted in only modest reductions of 3.8% in compressive strength and 6% in flexural strength, alongside comparable workability to conventional concrete (Senthamarai & Manoharan, 2005). Incorporating ceramic waste reduced slump flow due to the rough, angular particles, but optimizing the admixture restored workability. Fresh density decreased proportionally with ceramic waste content, reflecting its lower specific gravity, while entrained air content remained essentially unchanged (Pacheco-Torgal & Jalali, 2010).

Ceramic waste concrete compressive strengths varied with replacement level: up to 10% cement replacement yielded satisfactory strengths for normal-strength applications; a 100% coarse-aggregate replacement reduced strength by only 3.8% (Senthamarai & Manoharan, 2005).

Splitting tensile strength typically declined more than compressive strength (up to 18.2% reduction at complete ceramic waste aggregate replacement), and flexural strength decreased by approximately 6% under similar conditions (Senthamarai & Manoharan, 2005). Cost analyses indicated up to 9.8% savings per cubic meter with 75% replacement of ceramic waste aggregate, and 13.06% savings at 100% replacement, while preserving landfill space and reducing carbon emissions from cement production (Ahmad et al., 2023; Pacheco-Torgal & Jalali, 2010).

2.3.7 Aggregate

a) Crushed Stone:

The increasing scarcity of natural sand as a fine aggregate, driven by rapid infrastructure development and environmental concerns, led to the exploration of alternative materials such as crushed stone dust (CSD). As a by-product of aggregate crushing processes, CSD has shown promising potential as a sustainable and economical substitute for concrete and mortar (Rajput et al., 2018; Sahu et al., 2003).

Comparative analyses demonstrate that CSD exhibits physico-chemical properties closely analogous to those of natural sand. Furthermore, elemental characterization indicates a composition dominated by silica, aluminum, and calcium, while scanning electron microscopy (SEM) reveals comparable particle morphology.

However, due to the angular and rough texture of CSD particles—alongside a higher fine content—the mixes generally exhibited higher surface area and greater water absorption than those of rounded natural sand grains. Consequently, these physical characteristics reduce concrete workability, thereby requiring increased water content or higher superplasticizer dosages to achieve optimal mixing. Despite this, slump values remained within acceptable limits for casting (Prasetia & Maulana, 2019; Rajput et al., 2018; Sahu et al., 2003).

Rajput et al. (2018) reported that the compressive strength of M20 and M30 grade concrete increased progressively with the percentage replacement of natural sand by CSD, achieving higher strengths at both 7 and 28 days of curing. Sahu et al. (2003) found that partial replacement (up to 40%) yielded compressive, flexural, and tensile strengths comparable to or better than those of conventional concrete. Nanda (2010) confirmed that paving blocks with up to 50% replacement maintained mechanical integrity and met Indian standards, with marginal strength reductions beyond this

threshold. Prasetia and Maulana (2019) observed that a blend of 75% CSD and 25% river sand produced the highest compressive strength among tested mixes, highlighting the benefits of combined gradations for strength and density.

The use of CSD offered considerable economic benefits, primarily through lower procurement and transportation costs. For instance, Rajput et al. (2018) reported a cost advantage in Bhopal, India, where CSD was approximately one-ninth the price of natural sand, significantly reducing overall material and construction costs. Furthermore, environmental benefits included mitigating impacts from natural sand mining and mitigating waste-disposal issues associated with the accumulation of crusher dust.

b) Coarse Aggregate:

Coarse aggregates accounted for approximately 70% of the concrete volume; they served as the structural framework and critically influenced both the fresh and hardened properties of the material. Specifically, the 10 mm size fraction exhibited distinct behavioural patterns that significantly shaped overall concrete performance (Kalra & Mehmood, 2018; Hu & Wang, 2011).

Aggregate size, shape, gradation, and surface texture heavily dictated the flow behaviour of fresh concrete. Single-sized 10 mm crushed aggregates, such as basalt, possessed a higher surface area than larger fractions due to their angular shape and rough texture. This increased surface area elevated interparticle friction, uncompacted void content, yield stress, and plastic viscosity, thereby increasing the demand for water and cement paste and reducing overall slump. Specific modifications to the mixture effectively mitigated these workability losses. Integrating the 10 mm fraction into a well-graded blend, along with larger and smaller sizes, optimized particle packing. Optimized packing reduced both the void content and the volume of cement paste required to fill those voids; this microstructural efficiency subsequently lowered yield stress and viscosity, thereby restoring workability (Hu & Wang, 2011). Furthermore, precise adjustments to the mortar composition and water-to-cement ratio actively counteracted the friction introduced by angular aggregates.

The mineralogical composition of the parent rock fundamentally governed the mechanical performance of the aggregate. High-quality crushed basalt, for example, possessed high inherent strength, which directly enhanced the concrete's compressive strength and elastic modulus (Kalra & Mehmood, 2018; Wu et al., 2001).

Furthermore, the physical dimensions and quality of this aggregate fraction critically dictated the characteristics of the interfacial transition zone between the cement paste and the aggregate. Finer aggregate sizes increased the total aggregate surface area; this microstructural expansion altered the interfacial transition zone and, in some cases, compromised the concrete's tensile strength (Kalra & Mehmood, 2018).

Basaltic 10 mm aggregates provided exceptional long-term durability, characterized by high abrasion resistance, low water absorption, and superior mechanical strength. These material properties reduced concrete permeability and improved freeze–thaw resistance, rendering the composite highly suitable for high-performance applications in aggressive environments (Karasin et al., 2022; Choi & Park, 2022). Additionally, the inherent chemical stability of basalt—specifically its moderate SiO_2 content and low alkali levels—limited the potential for deleterious alkali-silica reactions(Karasin et al., 2022).

2.4 Product development from mine tailing waste

The existing literature documents the incorporation of mine waste, specifically iron ore tailings (IOTs), into the manufacture of diverse construction materials.

2.4.1 Bricks

Almada et al. (2022) evaluated four IOT samples from different Brazilian mines and added them to Portland cement mortars with 40% fine-aggregate replacement, forming a cementitious composite. Comprehensive XRF, XRD, SSA, porosity, and specific gravity tests guided the mix design. At the same time, performance metrics included compressive strength, elastic modulus, water absorption, porosity, electrical resistivity, carbonation depth, pore-solution pH, and microstructure analysis via SEM-BSE, EDS, and image analysis. The BS40 mix delivered a 22.9% gain in compressive strength and increased stiffness, driven by a filler effect and a lower effective water-to-cement (w/c) ratio. All IOT mixes exhibited slightly reduced absorption and porosity, enhanced carbonation resistance (the AR40 mix showed zero depth), and safe resistivity despite the presence of conductive iron oxides. SEM analysis revealed denser matrices, refined pores, and strong interfacial transition zones, especially for finer IOTs (SF, BS). Despite variability in Fe_2O_3 (44.8–81.2%) and SiO_2 (10.6–54.1%) content, the 40% IOT addition uniformly improved mortar performance, confirming that Brazilian IOTs are viable, sustainable mineral additives.

Thejas and Hossiney (2022) investigated the incorporation of iron ore tailings (IOT) in alkali-activated brick production to address India's demand for sustainable construction materials. The researchers developed six ambient-cured brick mixes (AABI40–AABI90) incorporating 40–90 wt.% IOT with fly ash, Ground Granulated Blast Furnace Slag (GGBS), and an 8 wt.% sodium silicate activator. Detailed XRF, XRD, SEM, and particle-size analyses guided the mix design. They revealed that AABI40 delivered the best performance, achieving a compressive strength of 18.45 MPa, the lowest water absorption at 12.6%, and only 14.7% strength loss after seven wet–dry cycles. While higher IOT content increased bulk density, it reduced strength and increased porosity, efflorescence, and unreacted particles. Electrical resistivity (1600–2000 kΩ·m) met commercial standards. The study showed that up to 60 wt.% IOT could produce durable, first-class bricks, advancing circular-economy goals and warranting pilot-scale and lifecycle evaluations.

Beulah et al. (2021) demonstrated the viability of valorizing mining and metallurgical wastes—specifically IOT, red mud (RM), and GGBS—to create sustainable, kiln-free construction materials. Leveraging sodium hydroxide (8 M) and sodium silicate as activators, the researchers formulated mixes ranging from 90:10 to 50:50 ratios of IOT/GGBS (Mix-1I to Mix-5I) and RM/GGBS (Mix-1R to Mix-5R). Comprehensive testing—aligned with IS 1077:1992, IS 3495 (Part 2):1992, ASTM C20, D854, D4318, and D698, assessed bulk density, porosity, water absorption, compressive strength at 7 and 28 days, and microstructural features using SEM, XRD, and XRF. Mix-3I (70% IOT + 30% GGBS) achieved a 28-day strength of 28.23 N/mm², 4.98% water absorption, and 18.2% porosity, classifying it as Class A. Meanwhile, Mix-3R (70% RM + 30% GGBS) reached 16.67 N/mm², 9.86% water absorption, and 24.17% porosity (Class B). SEM revealed high agglomeration and heterogeneous, rod-like morphologies in the RM blends, and XRD confirmed that mix proportions influenced quartz, hematite, mullite, and amorphous GGBS phases. By eliminating kiln firing, these geopolymer bricks offered significant energy and CO_2 savings, transforming hazardous residues into high-performance, sustainable building blocks.

Singh et al. (2021) blended iron ore tailings from Karnataka's Donimalai mines with 10–25 wt.% Ordinary Portland Cement (OPC), sodium silicate, and sand, subsequently kiln-curing the mixtures at 115 ± 10 °C for 24 hours to produce unfired bricks. XRF and XRD analyses confirmed the IOTs' high SiO_2 (49%), Al_2O_3 (23.22%), and Fe_2O_3

(24.76%) content, with quartz, kaolinite, and hematite as the dominant phases. The optimal IOT: OPC ratio of 8:2 achieved a compressive strength of 8.58 MPa, well above the 3.5 MPa threshold of IS 1077:2025, and a water absorption of 5.50%, well below the 20% limit. SEM revealed dense matrices in cement-rich mixes, whereas sodium silicate-rich mixes exhibited porous structures and higher efflorescence. While cement-based bricks remained free of efflorescence, formulations with high silicate and low binder contents exhibited noticeable efflorescence. The study demonstrated that IOT, combined with minimal cement, can replace clay to produce durable, eco-friendly bricks, facilitating large-scale waste reuse, CO_2 reduction, and soil conservation.

Mendes et al. (2021) reviewed the use of eco-friendly, waste-derived activators as substitutes for conventional alkali activators such as sodium hydroxide (NaOH) and sodium silicate (Na_2SiO_3) in alkali-activated materials. The review highlighted their dual sustainability benefits: reducing dependence on commercial chemicals while promoting the valorization of waste streams. The authors' classified alternative activators into three groups: agro-industrial residues like rice husk ash and sugarcane bagasse ash, which provide silica-rich alkaline solutions after calcination; mining and metallurgical by-products such as red mud and slag leachates, which are rich in alkaline oxides but chemically variable; and biomass residues or alkaline wastewater streams that supply low-cost alkalis while addressing disposal issues. Although several systems demonstrated strengths comparable to those of conventional activators, durability remained inconsistent, and the need for pre-treatment processes such as calcination or leaching remained a significant challenge. The study concludes that eco-activators represent a feasible pathway to sustainable alkali-activated materials, provided that future research addresses standardization, low-energy processing, durability, and regulatory frameworks.

Kumar et al. (2020) presented a robust framework for sustainable brick production using multiple industrial by-products. The research demonstrated the feasibility of producing stabilized geopolymer bricks entirely at ambient temperature—without kiln firing—using IOT, slag sand, fly ash, and GGBS, activated with NaOH and Na_2SiO_3, to replace clay and cement. Six mixes (GB-1 to GB-6) with a constant binder content (15% fly ash + 15% GGBS) and varying IOT/slag-sand ratios and NaOH molarity (8 M, 10 M) achieved 28-day dry compressive strengths from 16.68 MPa (40% IOT/20% slag, 8 M) to 25.30 MPa (20% IOT/40% slag, 10 M), all exceeding IS 3495-Part 1:1992

requirements. Water absorption (2.83–6.67%), density (1978–2120kg/m^3), slight efflorescence, and metallic-ring soundness all met Class AA standards, while SEM confirmed a homogeneous, compact microstructure. By valorizing four industrial wastes and eliminating the need for firing energy, this approach advanced circular-economy principles and built on prior geopolymer and IOT-block studies.

Sudhir et al. (2020) examined the use of red mud, an alumina refinery residue, in geopolymer brick production, with the partial replacement of river sand by Granulated Blast Furnace Slag (GBFS). The demand for resource-efficient construction has led to the use of industrial by-products such as Red Mud (RM), Fly Ash (FA), and GGBS as cementitious or pozzolanic binders. RM, a highly alkaline refinery process residue rich in Fe_2O_3, Al_2O_3, and SiO_2, required careful mix design; FA offered spherical, glassy particles with latent pozzolanic reactivity; and GGBS provided a calcium-rich, latent hydraulic binder. Experimental studies varied the RM: FA and RM:GGBS ratios (100:0 to 60:40) with a 4% lime activator and 11% water, and employed both ambient curing (28 days) and thermal firing (700–900 °C). Characterization by SEM, XRD, XRF, and standard mechanical tests revealed that fired samples exhibited denser microstructures and new strength-contributing phases. Ambient-cured RM: GGBS bricks (60:40) achieved 7.22 MPa, exceeding Class III standards (>7.5 MPa) upon firing, while RM: FA blends reached only 2.89 MPa (ambient) and 5.88 MPa (fired). GGBS blends outperformed FA blends due to enhanced C-S-H formation. Key challenges identified included controlling RM's alkaline efflorescence, optimizing firing schedules for energy efficiency, and evaluating long-term durability.

Freitas et al. (2018) demonstrated that unfired bricks made from 100% steel slag and iron ore tailings, pressed at 20 MPa, cured for 14 days, and optionally blended with 5% OPC, met the ISO 13006 flexural strength requirements. The bricks achieved 4.04 MPa for slag alone, 3.07 MPa for slag–tailings, and 3.61 MPa for slag–tailings–cement. The study showed improved density and particle synergy. Furthermore, lifecycle simulations for Minas Gerais indicated that the process could consume 2.6 Mt/year of slag, reduce CO_2 emissions by over 98% compared to concrete blocks, and generate approximately $4.3 million in carbon credits, highlighting a viable low-carbon industrial symbiosis pathway.

Weishi et al. (2018) used fine-grained, low-silicon IOT to manufacture unfired bricks using 75 wt.% IOT, a fly ash–lime–gypsum curing system, 0.3 wt.% stearic acid

emulsion for waterproofing, and triethanolamine as an accelerator. Curing at 50–60^{o}C for 48 hours yielded a 28-day compressive strength of 27.2 MPa (24.3 MPa when saturated), exceeding the JC/T 422-2007 standards. The softening coefficient increased from 0.61 to 0.71, and the bricks endured 15 freeze–thaw cycles. Stearic acid emulsion formed hydrophobic films in capillary pores, while higher curing temperatures enhanced hydration and pore densification. XRD and FT-IR confirmed the formation of C–S–H gel and ettringite, and SEM revealed dense matrices with reduced porosity. This low-energy process yielded high-strength, water- and frost-resistant bricks, offering a sustainable solution for large-scale IOT valorization.

Kumar et al. (2017) used iron ore tailings (IOT) and slag sand to replace 20–40 wt.% of natural sand/clay in fly ash–GGBS geopolymer bricks, eliminating Portland cement and high-temperature firing. Six mixes (GB-1 to GB-6) with 15 wt. % fly ash and 15 wt. % GGBS were activated with 8 M or 10 M NaOH and sodium silicate (Na_2SiO_3: NaOH = 2.5, solution-to-binder = 0.35) and cured at ambient temperature for up to 28 days. All mixes achieved 28-day strengths of 16.68–25.3 MPa, exceeding IS 3495-1:1992 standards; water absorption ranged from 2.83% to 6.67%. Durability tests (drop, efflorescence, soundness, and hardness) showed high quality with only mild edge damage and slight efflorescence. SEM revealed denser matrices with enhanced C–S–H and geopolymeric gels in high-slag mixes. Increasing NaOH molarity and slag sand content improved performance, demonstrating that 100% industrial by-product bricks can provide a low-carbon, resource-efficient alternative.

Nagaraja & Shreyasvi (2017) explored the use of iron mine spoil waste (MSW) from the Sandur region of Karnataka, India, for preparing compressed stabilized earth blocks (CSEBs). The MSW, characterized by substantial silica and alumina content (~53% combined), was blended with quarry dust to improve mechanical properties and workability. Using a cement-lime mix, the study reported wet compressive strengths exceeding 5 MPa at 6 months, making them suitable for residential construction. Blocks produced with 40% MSW showed optimum strength gain, and the water absorption of all blocks met Indian standards. The research demonstrated an eco-friendly approach to the utilization of mine waste, addressing both waste management and resource conservation.

Kuranchie et al. (2015) demonstrated that Western Australia's 632 million t/year iron ore tailings could be transformed into high-performance geopolymer bricks using 31

wt.% sodium silicate (SiO_2/Na_2O = 3.58) as the sole activator and 212 μm milled tailings, eliminating kiln firing and cement. Optimized conditions: an initial set of 15 min, 80 °C curing, and a 7-day duration yielded compressive strengths up to 50.35 MPa and water absorption of 7.18–10.21%. The bricks passed durability tests, were electrically resistive (>682 kΩ·m), and were cost-effective. The study noted that the bricks leveraged partial alumino-silicate dissolution into an amorphous geopolymeric gel, aligning with ASTM/Australian Standards and supporting circular-economy goals.

Yang et al. (2014) used low-silicon IOT, supplemented with 5, 10, 15, and 20 wt% fly ash, as a partial clay substitute to support China's waste-valorization objectives. The IOT's high Fe_2O_3 (18.58%) and CaO (16.85%) contents, but low SiO_2 (36.48%), were balanced by fly ash (SiO_2:48.28%, Al_2O_3:29.84%), improving aluminosilicate content and plasticity. When fired at 900–1000 °C, the bricks developed quartz, diopside, hematite, anorthite, and anhydrite phases, and SEM analysis revealed a porous microstructure. All mixes exceeded the 10 MPa compressive strength thresholds, which increased with increasing firing temperature but declined with increasing fly ash content. Water absorption remained below 20%, bulk density decreased from 2.0 to 1.8 g/cm^3, sintering shrinkage stayed under 1.6%, and weight loss on ignition (6.5–8.6%) met acceptable limits.

2.4.2 Blocks

Investigations detailed by Méndez et al. (2022) assessed the feasibility of replacing natural sand with Ecuadorian gold mine tailings in concrete block production. Mineralogical and chemical characterizations classified the tailings as inert and indicated a low environmental risk. Concrete blocks incorporating 50% tailings exhibited favourable mechanical performance; however, their compressive strength and water absorption at this replacement level did not fully meet the relevant standards. This performance deficit indicated that replacement levels below 50% constituted a more viable option. Leaching tests confirmed compliance with inert waste regulations and supported the reuse of tailings as a sustainable alternative raw material for concrete block manufacturing, aligning with circular economy principles.

The study presented by Castillo et al. (2021) examined variables governing geopolymer compressive strength and emphasized aluminosilicate sources such as fly ash, mine tailings, and slags. Key parameters included the Si/Al molar ratio, which showed

optimal values between 1.5 and 2; curing temperatures of 80–90°C; the type and concentration of the alkaline activator; and water content. Moderate curing temperatures and controlled curing times enhanced reaction kinetics and gel formation, thereby increasing compressive strength. Calcium contributed beneficially when present in controlled amounts, whereas impurities reduced strength. The consideration of ambient-temperature curing and long-term strength development positioned geopolymers as sustainable binders for partial or total cement replacement in construction materials.

The work by Likhith et al. (2017) investigated the utilisation of iron ore tailings for the manufacture of building blocks and paving materials. The high volumes of iron ore tailings generated in India motivated the reuse of this waste stream to mitigate environmental impacts. Experimental concrete mixes featuring iron ore tailings as a replacement for natural sand developed promising compressive strengths for M10 to M20 grade concretes. These results underscore the suitability of iron ore tailings as sand substitutes in Concrete, thereby promoting sustainability through waste utilisation and the reduced depletion of natural aggregates. Furthermore, the review outlined production techniques, mix design considerations, and environmental benefits associated with recycling mining waste.

The investigation by Venugopal et al. (2016) demonstrated that formulations of fly ash, ground granulated blast-furnace slag, and manufactured sand produced solid and hollow geopolymer masonry blocks upon ambient-temperature curing. These geopolymer blocks exhibited superior mechanical performance relative to traditional cement blocks, including higher compressive, flexural, and bond strengths, as well as lower water absorption. Durability under wetting–drying cycles remained satisfactory, and masonry efficiency met structural requirements, thereby supporting the use of these geopolymer units for structural masonry as eco-efficient alternatives to conventional units.

A mix design framework established by Patankar et al. (2015) formulated fly ash-based geopolymer concrete that entirely replaced Portland cement. The procedure incorporated fly ash fineness, water content, aggregate grading, and alkaline solution ratios as primary design variables. Mixtures activated with sodium silicate and 13 M sodium hydroxide achieved adequate workability and compressive strengths comparable to those of M20 to M40 grades. A curing regime comprising heat curing at 60°C for 24 hours, followed by 7 days of ambient curing, produced compressive strengths close to

target values. This methodology provided practical guidelines for cost-effective and sustainable geopolymer concrete mix designs suitable for structural applications.

2.4.3 Concrete used for Pavers and Tiles

A study by George (2023) assessed the mechanical performance of M20-grade concrete by partially replacing the fine aggregate with IOTs at 20%- 60% replacement levels. This evaluation centered on the analysis of substitution impacts on both compressive and split tensile strength. The inclusion of IOTs positively influenced the mechanical properties of the concrete. Compressive strength increased steadily with increasing IOT content. The angular shape of the IOT particles helped them lock together more tightly in the concrete, leading to this increase. The most significant improvement occurred at the 60% replacement level, with compressive strength increasing by 18.41% compared to the conventional mix. Split tensile strength likewise improved with IOT replacement, registering a 10.3% increase at the 60% substitution level. These results aligned with findings from similar studies, which indicated that the partial replacement of fine aggregate with IOT constituted a viable and beneficial approach. This approach not only enhanced concrete performance but also advanced sustainable, circular-economy practices by valorizing a waste product and reducing the environmental footprint associated with river sand extraction.

A review by Adiguzel et al. (2022) highlighted that mining generated 65–80 billion tons of waste annually, including 10–15 billion tons of tailings. The disposal of these tailings in dams posed serious environmental threats, including acid mine drainage and the release of heavy metals. The incorporation of tailings into concrete mitigated waste volumes, curtailed CO_2 emissions, and diminished the consumption of virgin materials. The review detailed the mechanical properties of concrete incorporating tailings, revealing that tailings effectively replaced fine aggregates at an optimal rate of 10–40% and cement at a lower rate of 5–20%. The tailings' chemical composition (with a combined $SiO_2 + Al_2O_3 + Fe_2O_3$ content $\geq 70\%$ proving ideal), particle size, and type dictated the resulting mechanical performance. Finer particles boosted compressive strength through a filler effect. Excess tailings (>40%) reduced strength by increasing porosity and increasing water demand. Regarding environmental properties, the article noted that raw tailings typically exhibited pH values between 5.0 and 8.3 and contained heavy metals, yet integration into concrete substantially reduced the leaching of these

harmful substances. The improved density and lower porosity of the concrete successfully immobilized the metals, reducing their leachable concentrations to safe, non-toxic levels.

A critical assessment in Arbili et al. (2022) evaluated the potential of IOTs as a sustainable substitute for natural fine aggregates. A synthesis of findings from numerous research works evaluated the fresh, mechanical, and durability properties of concrete incorporating IOTs. IOTs angular texture and high water absorption reduced workability, yet acceptable slump and flowability persisted up to a 40% substitution rate. Mechanical strengths, including compressive, tensile, and flexural, exhibited significant improvement at moderate IOTs levels. Compressive strength specifically increased by 14–15% at a 20–40% substitution, owing to superior particle packing and strengthened interfacial bonding. From a durability standpoint, IOT inclusion reduced water absorption, indicating enhanced impermeability, and substantially curbed drying shrinkage by up to 58% through pore refinement. SEM and XRD results supported these macroscopic gains, revealing a more compact interfacial transition zone and the generation of extra cementitious gels. Overall, a 30–40% IOTs replacement emerged as generally optimal, balancing mechanical performance and durability without sacrificing concrete workability.

Investigations by Dom et al. (2022) evaluated the potential of Ground Granulated Blast-Furnace Slag (GGBS) as a partial replacement for Ordinary Portland Cement (OPC), aiming to mitigate the cement industry's substantial environmental impact, which accounts for approximately 5–6% of global CO_2 emissions. A synthesis of findings on GGBS's physical and chemical properties noted its lower specific gravity and higher fineness relative to OPC, both of which enhance concrete reactivity. GGBS's hydration proceeded more slowly than OPC's, yet generated additional Calcium Silicate Hydrate (CSH) over time. This process densified the concrete matrix and markedly elevated long-term strength and durability. GGBS further enhanced workability and reduced water absorption, thereby conferring superior impermeability. Compressive strength showed lower early-age values, but long-term strength after 28 days increased notably with 30–60% GGBS replacement, achieving optimal performance at 40–60% substitution after 90 days. This substitution practice delivered substantial environmental benefits; a 50% cement replacement with GGBS curtailed CO_2 emissions by roughly

500,000 tons per million tons of cement produced, thereby advancing circular economy principles.

A review article by Ikotun et al. (2022) examined the potential of various mine tailings, specifically iron, copper, and gold, as full or partial replacements for natural sand in both concrete and bituminous mixtures. The mitigation of environmental hazards from tailings stockpiles and the reduction of sand quarrying's ecological impact constituted the primary objective. A comparison of the mine tailings' physical and chemical characteristics with traditional fine aggregate encompassed properties such as fineness modulus, specific gravity, density, water absorption, particle shape, and the principal oxides SiO_2, Al_2O_3, and Fe_2O_3. The physical and chemical properties of the tailings resided within acceptable ranges for engineering aggregates, affirming their feasibility as fine aggregate substitutes. In concrete mixtures, where aggregates comprised up to 80% of the volume, outcomes varied according to the type of tailings. Iron and gold tailings typically exhibit reduced slump and flowability due to their angular texture and high water absorption.

Research presented by Mendes et al. (2021) explored the potential of iron IOTs from Brazil's Germano dam as a sustainable alternative to natural sand in concrete. Particle size distribution, X-ray diffraction (XRD), and thermogravimetric analysis (TGA) collectively characterized the fundamental properties of the IOTs. Quartz (90.7%) and hematite (9.3%) predominated in the tailings' composition, exhibiting no significant pozzolanic activity due to their high crystallinity. Replacing natural sand with IOT at 10%, 20%, and 30% by weight improved mechanical performance. A peak compressive strength of 40.9 MPa emerged at 90 days in the 10% IOT mix. Micro-CT analysis revealed that IOT acted as filler, reducing porosity and resulting in a finer pore structure within the concrete. Higher IOT content reduced workability due to increased surface area, yet no substantial chemical interaction occurred between IOT and cement hydration products. The incorporation of IOT, even at 30% replacement, adversely affected concrete workability due to the grains' high specific surface area. Despite this drawback, up to 30% IOT substitution proved both technically feasible and environmentally beneficial. This substitution diverted millions of tons of tailings from dam disposal, advancing circular economy principles in the construction industry.

An investigation detailed by Chinnappa & Karra (2019) investigated iron IOTs as a fine aggregate replacement and alccofine as a partial cement replacement in M40 grade

concrete. IOT, a by-product of iron ore beneficiation, generated significant environmental issues through large-scale disposal in landfills and tailings dams. The high surface area and water absorption of IOT curtailed concrete workability, yet the tailings' elevated specific gravity augmented concrete density. The incorporation of IOTs markedly enhanced mechanical properties, peaking at a 40% replacement level. At this dosage, the concrete attained a maximum compressive strength of 70 MPa at a water-to-cement ratio of 0.35, a splitting tensile strength of 4.86 MPa, and a flexural strength increased by 15% compared to the control mix. The development of highly accurate statistical models with predictive compressive-strength accuracy exceeding 98% facilitated performance-based mix design optimization. The experimental findings confirmed the technical feasibility of IOT as a sustainable construction material.

A review paper by Gou et al. (2019) identified three key pathways for the reuse of mine tailings: replacement of natural fine aggregates, deployment as supplementary cementitious materials (SCMs), and integration into raw mixes for clinker production. The physical and chemical properties of mining tailings, including specific gravity, fineness, and composition, varied substantially depending on the original ore and the beneficiation process. The review advocated the sustainable utilization of these tailings to conserve virgin resources and mitigate environmental impacts associated with waste stockpiles in the construction sector. As fine aggregate replacements, tailings profoundly altered concrete properties. The high surface area and angularity of tailings diminished workability yet elevated mix density. The filler effect increased compressive strength up to a 30% replacement level; however, exceeding this threshold led to a reduction in strength. Tensile and flexural strengths followed similar trends, peaking at optimal tailings contents of 20–40%. Cement hydration effectively immobilized heavy metals within the tailings, substantially mitigating leaching-related environmental risks.

As SCMs, tailings required pre-treatment, such as grinding or calcination, to activate their pozzolanic potential. Conversely, using tailings in clinker production provided an energy-efficient recycling method. The high silica (SiO_2) and alumina (Al_2O_3) content successfully replaced up to 10% of the raw feed, thereby reducing the required sintering temperature. However, when used as a fine aggregate substitute, the replacement level had to be kept below 30% to maintain an optimal balance between workability and structural strength.

A critical examination in Saranya et al. (2018) examined Ground Granulated Blast Furnace Slag (GGBS) as a sustainable partial cement replacement. GGBS, a steel industry by-product, furnished a low-carbon alternative to cement production, a principal source of global CO_2 emissions. Optimal GGBS replacement ranged from 40–45%, with long-term compressive strength, workability, and durability improving markedly. GGBS concrete demonstrated superior resistance to sulfate attack, chloride ingress, and alkali-silica reaction. The exploration of specialized mixes encompassed ultrafine GGBS variants, which accelerated hydration rates and elevated mechanical performance, alongside self-compacting GGBS concrete. GGBS's hydraulic action and pozzolanic reactions were slower than cement hydration, which drove enhanced performance through pore refinement and long-term stability. The absence of C_3A further bolstered sulfate resistance.

Assessments outlined by Shettima et al. (2016) evaluated the feasibility of iron ore tailings (IOT) as a partial or complete replacement for natural river sand in concrete. Five distinct concrete formulations were formulated with varying IOT replacement levels from 0% to 100%, using a uniform water-to-cement ratio of 0.5 across all batches. Increasing IOTs content reduced concrete workability due to its fine texture and high surface area; mechanical and durability properties improved substantially. Compressive strength and splitting tensile strength both escalated, peaking at 25% IOT replacement, where compressive strength exceeded the control mix by 12.9%. This upward trend extended to the modulus of elasticity, which rose appreciably with greater IOT content. Durability benefits manifested as increased carbonation resistance and marked reductions in drying shrinkage (up to 58%) in IOT mixes. Higher replacement levels induced modest elevations in water absorption and chloride penetration, though these metrics stayed within acceptable limits. Heavy metal concentrations in the IOT fell well below regulatory limits, confirming environmental safety. IOT emerged as a viable, eco-friendly, natural sand alternative, with a 25% replacement delivering optimal performance, waste valorization, and sustainability gains.

Arivalagan (2014) provided detailed evaluations of the mechanical properties and sustainability of M35-grade concrete incorporating Ground Granulated Blast Furnace Slag (GGBS) as a partial replacement for Ordinary Portland Cement (OPC). Replacing OPC with up to 40% GGBS augmented concrete workability, as the 40% GGBS mix recorded a 28 cm slump versus 24 cm for the control mix. The mechanical performance

of GGBS concrete has advanced over time. The 20% GGBS mix recorded slightly lower 7-day compressive strength than the control, yet its 28-day compressive strength exceeded that of the control, reaching 36 MPa. Split tensile and flexural strengths showed comparable gains, attributable to GGBS's prolonged hydration and filler effect, which fostered a denser microstructure. GGBS production required only 1300 MJ of energy and emitted approximately 0.07 tons of CO_2 per ton, figures markedly lower than those for OPC production. The use of up to 20% GGBS as a cement replacement in M35 concrete improved mechanical performance and durability while substantially reducing the environmental impact of concrete production.

A sustainable concrete study by Ugama et al. (2014) evaluated iron ore tailings (IOT) as a partial or complete replacement for natural river sand in grade-35 concrete. Repurposing iron ore tailings serves dual purposes: managing environmental waste and reducing the construction industry's dependence on depleting river sand reserves. ACI 211.1-91 mix proportions underpinned the study, which revealed a decline in concrete workability with increasing IOT content attributable to finer tailings particles and higher water demand. Nonetheless, the mechanical properties of the 20% IOT replacement mix matched those of the control mix. Specifically, the 28-day compressive strength was 43.67 N/mm², which is close to the reference mix of 45.02 N/mm². Split tensile strength at 20% IOT reached 2.69 N/mm², marginally surpassing the reference mix of 2.64 N/mm². The higher density of IOT positioned it as a heavy aggregate, rendering the resultant pavement more resilient to deformation. A 20% replacement level proved optimal for rigid pavement concrete, as both compressive and tensile strengths declined beyond this threshold. Targeted optimization of mix proportions and the integration of specialized admixtures offer promising pathways to enhance IOT-concrete performance further.

2.4.4 Pavers

The Compression Casting Technique (CCT) described by Farooq et al. (2023) enabled the production of sustainable concrete pavers from 100% recycled aggregates. The experimental program targeted high-strength paver manufacture while simultaneously mitigating the environmental burden associated with construction and demolition (C&D) waste. A matrix of 72 concrete mixes systematically varied the fine-to-coarse recycled aggregate ratio, cement content, and casting pressure to isolate performance-

governing parameters. Mix proportioning with 60% fine and 40% coarse recycled concrete aggregate (RCA), 20% cement content, and a casting pressure of 20 N/mm² established the optimum formulation for subsequent evaluation. This mix developed compressive strengths of 35 N/mm² at 7 days and 55 N/mm² at 28 days, thereby satisfying relevant international standards. Recycled aggregate concrete (RAC) pavers delivered mechanical performance comparable to that of natural aggregate concrete (NAC) pavers, exhibiting only a marginally lower Modulus of Rupture that remained within acceptable specification limits. Durability assessments showed that RAC pavers exhibited higher water absorption and drying shrinkage than NAC pavers, but offered superior resistance to acid and salt attack. Regression analysis of the compressive strength data yielded a predictive equation with an average absolute error of 7.7%, enabling reliable strength estimation for CCT-produced RAC pavers. Overall, CCT provided a viable, eco-efficient route to manufacturing high-strength pavers from 100% recycled aggregates, thereby advancing circular-economy practices in the construction industry.

Mtarfi et al. (2023) explored the feasibility of using electric arc furnace (EAF) slag as a replacement for natural gravel in concrete pavers to establish a slag valorization pathway for the steel industry and to reduce the environmental impact of slag stockpiles. Physicochemical characterization of the slag revealed a composition dominated by CaO, SiO_2, MgO, and FeO, together with a density of 3.62 g/cm³ and a Los Angeles abrasion coefficient of 20, all within the prescribed limits for use as a gravel substitute. The material exhibited a water absorption rate of 2.6-2.8%, confirming its suitability for incorporation into concrete paving units. The Dreux–Gorisse mix-design method governed the formulation of concrete pavers, and systematic adjustment of the water-to-cement (W/C) ratio identified an optimal mixture. This optimal design, incorporating 53.49% slag, generated dense, high-strength pavers classified as heavy concrete with densities approaching 3000 kg/m³. The pavers attained a 28-day splitting tensile strength of 3.9 N/mm² and a breaking load of 386 N/mm, substantially exceeding the 250 N/mm requirement specified in NF EN 1338. EAF slag thus replaced more than half of the natural gravel content without compromising mechanical or durability performance, offering a robust and sustainable solution for waste valorization in concrete paver production.

Balegamire et al. (2022) replaced natural river sand entirely with gold mining tailings (GMT) in concrete pavers produced in Misisi, Eastern Congo, thereby serving as the primary fine aggregate. The mix design targeted a sustainable outlet for the large volumes of GMT that posed significant environmental risks. Despite physical differences such as higher fines content and higher density, concrete pavers incorporating 100% GMT developed an average breaking stress of approximately 27 N/mm² at 7 days, statistically equivalent to that of pavers produced with natural river sand. Adjustments in the mixture proportions, specifically increased gravel and water contents, compensated for the finer GMT particle size distribution. The resulting GMT-based pavers demonstrated that complete substitution of natural river sand with gold mining tailings remained technically feasible while simultaneously yielding a valuable, sustainable local building material.

Filho et al. (2017) used iron ore tailings (IOTs) to replace natural fine aggregate in interlocking concrete pavers. They thereby addressed environmental and safety concerns associated with tailings dams in Minas Gerais, Brazil. Environmental characterization classified the IOTs as non-dangerous and inert, with negligible toxic leachates, confirming their suitability for construction use. Concrete pavers incorporating 10%, 20%, and 80% IOT as a sand replacement exhibited increased unit weight up to 23% at 80% replacement due to the higher specific gravity of the tailings. The fine-particle filler effect of the IOTs reduced porosity and water absorption across the tested mixtures. All mixes, including the 80% IOT mix, exceeded the 35 N/mm² 28-day compressive strength requirements, and the 10% and 20% IOT mixes exceeded 50 N/mm², satisfying specifications for both commercial and heavy-traffic applications. The pavers also showed reduced mass loss under abrasion and no dimensional expansion, thereby confirming adequate durability. Iron ore tailings, therefore, acted as effective inert fillers that enhanced the performance of conventional interlocking pavers while supporting sustainable waste management and conservation of natural sand resources.

Mantilla et al. (2017) used iron ore tailings (IOTs) to replace fine aggregate in concrete pavers, evaluating the mixtures for compressive strength and static modulus of elasticity in accordance with Brazilian standards. The comparison evaluated four mixtures: a natural sand reference and three mixes in which IOT replaced 50% of the natural sand, 50% of the industrial sand, and 100% of the industrial sand. All four mixtures achieved

the minimum compressive strength of 35 N/mm^2 required for pedestrian and light-vehicle pavers. The T2 mixture, in which IOTs replaced 50% of industrial sand, delivered optimal performance, attaining a compressive strength of 59.2 N/mm^2 at 31 days and surpassing the 50 N/mm² threshold for heavy-traffic applications. T2 also reached the highest static modulus of elasticity, 33.41 GPa, at 31 days. Incorporation of a moderate tailings content, specifically the 50% industrial sand replacement, significantly increased both strength and stiffness. In contrast, a clear linear correlation between compressive strength and elastic modulus enabled a predictable mix design when employing IOTs in concrete pavers.

Iron ore tailings (IOTs) in Kumar et al. (2014) partially substituted conventional river sand in M30 rigid concrete, and the modified mixtures targeted both mitigation of natural sand depletion and reduction of environmental hazards from mining residues. Material characterization indicated higher specific gravity and water absorption for IOTs than for river sand. Increasing the IOTs content reduced workability, yet the mechanical performance improved across several replacement levels. A 40% IOT replacement produced the maximum 28-day compressive strength of 55.10 N/mm^2, substantially exceeding the control mix strength of 38.58 N/mm^2. Flexural strength for the IOT-modified concretes ranged from 7.4 to 9.2 N/mm², with the 40% IOT mix ranking among the most favourable compositions. A fatigue life model calibrated to the experimental data showed that the 40% IOT mix exceeded standard fatigue predictions by sustaining more load cycles to failure. Replacement of up to 40% of river sand with IOTs therefore generated concrete pavements with superior compressive strength, acceptable flexural behaviour, and enhanced fatigue life, establishing a technically and environmentally attractive alternative for pavement construction.

Iron-ore concentration tailings in Da Silva et al. (2014) replaced traditional aggregates in concrete pavers, and tailings from three sources—fine and coarse magnetic-separation tailings and flotation tailings—governed the physical and chemical variability of the mixes. High Fe_2O_3 content correlated with increased density among the tailings types. Five aggregate combinations with varying tailings proportions, but constant cement and water, produced pavers evaluated for compressive strength, porosity, and colour. However, the control mix with conventional aggregates exhibited higher 7-day strength, and pavers containing coarse tailings matched or surpassed the reference strength by 28 days. A mix formulated with fine tailings alone produced the

lowest strength, underscoring the critical role of granulometry in hydration and microstructural development. Tailings-modified mixes showed higher porosity than the control, thereby providing greater drainage capacity for outdoor paving applications. Incorporation of tailings also shifted paver colour toward red, providing aesthetic differentiation and additional commercial value. Iron-ore tailings thus enabled partial or complete replacement of conventional aggregates in pavers while improving drainage potential and offering marketable colour variations.

Ravikumar et al. (2012) partially replaced cement in interlocking concrete block pavers, and replacement levels from 5% to 25% controlled the resulting microstructural and mechanical changes. Cement substitution with 5% to 15% iron-ore tailings enhanced early-age and 28-day compressive strength, yielding increases of up to 16% at 7 days and 14% at 28 days relative to the control mix. Higher replacement levels of 20% and 25% reduced compressive strength, indicating an optimal cement-replacement limit of approximately 15%. All mixes maintained water absorption below 6%, meeting precast block requirements and indicating low permeability and satisfactory durability. Partial cement replacement with iron-ore tailings up to 15% therefore improved mechanical performance for light-traffic paving applications while simultaneously supporting circular use of mining residues.

Iron-ore tailings in Aruna & Kumar (2010) replaced conventional fine aggregates in concrete paving blocks as part of a sustainable paving strategy, and the resulting mixtures quantified the influence of tailings substitution on compressive strength and water absorption. Three mix categories—a reference mix, a sand-modified mix, and a tailings-modified mix—provided the comparative framework. Increasing the tailings content consistently elevated the compressive strength of the pavers. The formulation with the highest iron-ore tailings content, designated 15(T), achieved a peak compressive strength of 36.5 N/mm² at 28 days, markedly outperforming the weakest sand-modified mix, which reached only 6.8 MPa. Tailings incorporation produced a modest increase in water absorption; however, absorption values remained within acceptable limits and did not compromise permeability performance. Substitution of conventional fine aggregates with iron-ore tailings, therefore, emerged as a practical strategy for enhancing the compressive strength of paving blocks while simultaneously valorizing an industrial waste stream.

2.4.5 Tiles

Deshmukh et al. (2021) investigated the valorization of raw bauxite residue (red mud) for the production of chequered concrete tiles and demonstrated its potential as a sustainable cement substitute. The research examined partial cement replacement in the bottom course of the tiles at levels up to 20% by weight. Results indicated that all tile samples, even with the maximum 20% red mud content, met or exceeded the requirements of IS 13801-1993 for wet transverse strength, water absorption, and abrasion resistance. Minor reductions in performance occurred with increased red mud content, confirming its pozzolanic compatibility and contribution to the mix. In addition to lowering energy demands, this material substitution delivered significant environmental benefits by preventing the emission of approximately 1 tonne of $CO_2$for every 5,000 tiles produced. Ultimately, this research provided a viable, high-volume application for a challenging industrial by-product, contributing to both a circular economy and the creation of durable, sustainable building materials.

Fontes et al. (2021) investigated the utilization of iron ore tailings (IOT) in hydraulic tile production through a comprehensive approach that combined raw IOTs and beneficiated fractions obtained via dry-route segregation processes. The beneficiation process effectively separated raw IOT into three distinct fractions: iron ore concentrate (~35%), high-purity siliceous sand (~50%), and Fe-rich clay (~15%), demonstrating the potential for multiple valorization pathways. When used as fine aggregate replacement, both raw IOT and IOT sand exhibited superior mechanical performance compared to conventional river sand, with flexural strength improvements of 38% and 46% respectively, despite requiring higher water-to-cement ratios (0.60 vs. 0.50) due to increased fineness and angular particle morphology. The IOT clay fraction, when calcined at 1050°C and 1150°C and subsequently ground, produced effective pigments with improved colour stability and homogeneity compared to commercial synthetic pigments. However, it required longer grinding times for raw IOT-based pigments. Physical characterization revealed that IOT-based materials increased tile density due to their high iron oxide content (36.3% in raw IOT, 57.3% in IOT clay), while maintaining acceptable water absorption and void index values. Firing promoted dehydroxylation of goethite and kaolinite, converting goethite to hematite and enhancing pigmentation properties, with colour analysis showing distinct brownish-red-ochre shades and superior colour uniformity. All produced hydraulic tiles exceeded the minimum flexural

strength requirement of 3.5 N/mm^2 specified by Brazilian standards, confirming the technical feasibility of IOTs utilization while contributing to sustainable construction practices and tailings dam impact mitigation.

Hamid et al. (2021) explored the potential of incorporating various industrial and domestic waste materials, such as Electric Arc Furnace (EAF) slag, boron waste, red mud, and fly ash, into tile manufacturing to produce high-quality, sustainable building materials. A four-stage process—identification, inspection, qualification, and inclusion—evaluated materials based on key properties, including firing shrinkage, water absorption, density, and strength. Results revealed that certain waste materials served as effective substitutes for conventional raw materials. EAF slag emerged as the most promising option, demonstrating exceptional properties that met or exceeded current ISO standards for tile production. Tiles made with EAF slag exhibited low firing shrinkage (as low as 2.34%), minimal water absorption (down to 0.15%), and high compressive strength (up to 90 N/mm²). This low water absorption made EAF slag particularly suitable for tile production, while its low firing shrinkage indicated a lower flammability risk compared to other materials. Although other waste materials, such as red mud and fly ash, showed potential, proper mix design and material ratios remained critical for optimal performance. Using these materials advances the circular economy, reduces landfill waste, and enables the production of durable, sustainable building materials.

Pati & Sahu (2020) addressed the environmental challenge of fly ash disposal by investigating its high-volume use as a fine-aggregate substitute in M40 concrete tiles, thereby conserving natural sand resources. Class F fly ash replaced mixes at 0–40% in 10% increments. Casting and curing followed, with evaluation measuring wet transverse strength, water absorption, abrasion resistance, and dynamic stiffness per IS 1237:2012. Tiles with up to 30% fly ash achieved superior performance: a 21% gain in 28-day transverse strength at 20% replacement, a 19% reduction in water absorption, and a 15% improvement in abrasion resistance compared to controls, while all strengths remained above minimum standards. Natural frequencies declined slightly with increasing fly ash content, indicating a marginally reduced dynamic stiffness, but all values met the requirements. These results demonstrated that replacing up to 30% of fine aggregate with fly ash produced durable, sustainable concrete tiles and offered a scalable strategy for fly ash valorization and sand conservation.

Çiçek et al. (2018) demonstrated the potential of using six different boron-rich waste tailings (with 16–31 wt% B_2O_3) for the production of wall and floor tiles. Incorporation occurred at varying percentages—3–8 wt% for floor tiles and 4–22 wt% for wall tiles—while maintaining similar chemical ratios (CaO/MgO, Na_2O/K_2O, and SiO_2/Al_2O_3) to commercial products. Boron oxide (B_2O_3) acted as a fluxing agent, which significantly reduced the required sintering temperatures: by 70°C to 1050°C for wall tiles and by 65°C to 1130°C for floor tiles. The resulting tiles met all required standards (TS EN ISO 10545). Specifically, floor tiles with 5.66 wt% waste achieved a water absorption rate of 0.49% and a flexural strength of 38.4 N/mm^2. Wall tiles with 5.64 wt% waste had water absorption of 19.4% and strength of 20.5 N/mm^2. Phase analysis showed that the waste promoted the formation of enhanced plagioclase, without negatively affecting the tiles' mechanical or optical properties. This research confirmed that using boron mining waste for low-temperature sintering is a viable, industrially scalable method for valorizing mining waste and reducing energy consumption in tile manufacturing.

Fontes et al. (2018) developed sustainable cement tiles utilizing iron ore tailings (IOTs) from tailing dams as both aggregate and pigment replacement in conventional cement tile production. A comprehensive methodology combined technical feasibility assessment through physical, chemical, and morphological characterization, environmental analysis via leaching and dissolution tests, and value analysis using empathy mapping to understand consumer perspectives. IOT demonstrated fine, crystalline particles with no toxicity, classified as Class II-A (non-dangerous, non-inert) waste, making it technically and environmentally suitable for construction applications. When used as an aggregate replacement, IOT achieved superior performance, with more homogeneous coloration and reduced porosity compared to conventional tiles, due to its filler effect from its fine particle size distribution (D90 = 0.17 mm). Fired IOTs (P-IOT) showed enhanced pigmentation properties after calcination at 950°C, though requiring higher content percentages compared to conventional synthetic pigments to achieve similar colour intensity. Value analysis revealed that incorporating IOT not only reduced production costs by utilizing waste materials but also increased esteem value by addressing consumer demands for sustainability, environmental ideology, and social expression. This research demonstrated the technical feasibility of transforming mining waste into value-added construction materials while advancing circular-economy principles and reducing the environmental impact of tailings-dam disposal.

2.4.6 Cladding panels

Kapicová et al. (2024) explored the development of pervious concrete specifically for interior applications, aiming to create a material that served as both an aesthetic cladding and an effective sound absorber. The study examined the prevalence of reflective surfaces in modern architecture, which often results in poor acoustic comfort. An extensive experimental program tested 29 concrete mixes, systematically varying aggregate types, cement content, water-cement ratio, and additives, including silica fume and polypropylene fibers. Lightweight, porous aggregates such as pumice yielded the best sound absorption, with a noise reduction coefficient (NRC) of up to 0.7, making them highly effective at mid- to high-frequency noise. However, these porous mixes often exhibited lower compressive strength. Additives like silica fume improved strength but slightly reduced acoustic performance due to pore clogging. Conversely, polypropylene fibers provided no acoustic benefit. Pervious concrete could be successfully engineered for interior sound absorption by carefully optimizing the mix design, particularly the aggregate type and water-cement ratio, to achieve a desirable balance of acoustic performance, mechanical integrity, and aesthetic appeal.

Li et al. (2023) investigated the viability of utilizing iron ore tailings (IOT) as a sand substitute in cement mortar. Characterization of IOT's fundamental properties preceded a detailed experimental program on mortar samples with IOT substitution rates of 0%, 25%, and 50%. Uniaxial compressive and tensile strength tests and crack resistance assessments evaluated the mechanical performance of the mortar at various curing ages. Advanced analytical techniques, including ICP-OES, XRD, NMR, SEM, and EDS, were used to examine the specimens' chemical, mineralogical, and microstructural characteristics. Incorporating IOT at substitution rates up to 50% improved the mortar's mechanical properties, with strength increasing alongside the IOT content. Microstructural analysis revealed that IOT induced notable changes in the formation of hydration products and in the pore size distribution, although it produced no significant direct chemical reactions. These microstructural changes accounted for the observed improvement in mortar mechanical performance, thereby confirming that IOT constituted a viable and effective sand replacement material.

Martinelli et al. (2023) reviewed the growing adoption of plant fibers in cementitious composites as a strategy for sustainable construction. Natural fibers offered notable benefits, such as lower density, reduced fragmentation, and enhanced crack resistance,

compared to conventional reinforcement. Coconut fibers are abundant in tropical regions but remain underutilized, leading to environmental disposal challenges. This paper systematically examined coconut fiber production, properties, and incorporation methods in cement-based materials, including the innovative use of textile mesh to improve fiber integration. Surface treatments boosted fiber durability and performance within cement matrices. This study outlines a framework for future applications and prospects of coconut fiber-reinforced composites, highlighting their potential to advance eco-friendly building materials.

Yousef et al. (2023) focused on using recycled construction and demolition waste (CDW) to manufacture sustainable, prefabricated wall claddings. Various cladding mixtures substituted conventional materials with crushed concrete and crushed bricks sourced from CDW; testing followed. Different insulation layers, such as compressed foam boards and mineral wool, enhanced thermal performance. Findings demonstrated that these CDW-based claddings significantly reduced heat gain by up to 86% in the best-performing samples compared to traditional clay bricks. A substantial increase in time lag delayed heat transfer into a building's interior, and a decrease in the decrement factor indicated a more stable indoor temperature. These prefabricated claddings offered a highly scalable and effective solution for sustainable construction, providing a beneficial use for the large volumes of CDW generated annually while simultaneously improving the energy efficiency of residential buildings. Waste materials not only reduced environmental impact but also created superior building products.

Shao et al. (2022) introduced an innovative double-skin concrete façade system designed to significantly improve the thermal performance of buildings in tropical climates. A façade with multiple air gaps, combined with ultra-thin skins of textile-reinforced ultra-high performance concrete (UHPC), effectively minimized heat transfer through conduction, convection, and radiation. This design reduced the façade's thermal conductivity by up to 92% compared to a solid concrete alternative. Sustainability credentials highlighted that, although the specialized green UHPC material had a higher individual carbon footprint, the overall design required a significantly lower volume of concrete, leading to a 34–44% reduction in total embodied carbon compared to traditional solid or sandwiched façades. A detailed cost analysis revealed a payback period of approximately 3.5 years, driven by substantial operational energy savings. The façade's efficiency depended highly on the window-to-wall ratio, underscoring the need

for high-performance glazing to maximize energy savings. Advanced material science addressed the dual challenges of energy consumption and embodied carbon in this blueprint for sustainable building design.

O'Hegarty et al. (2021) addressed the environmental challenges of using high-performance fiber-reinforced concrete (HPFRC) for building cladding by developing a new, low-carbon mix. Balancing exceptional mechanical properties with a reduced embodied carbon footprint was achieved by significantly reducing the cement content through 50% replacement with ground granulated blast-furnace slag (GGBS) and microsilica, and by introducing coarse aggregates to reduce the overall paste volume. The mix achieved a compressive strength of over 90N/mm² while remaining industrially feasible. Coated glass and basalt FRP fibers enabled a ductile, strain-hardening behaviour in the concrete, eliminating the need for traditional steel reinforcement. This approach provided comparable performance to conventional cladding but at a significantly reduced panel thickness (56-59 mm vs. 150 mm). This reduction in material volume led to a 50-53% decrease in the embodied carbon per square meter of façade area. The low-carbon HPFRC mix proved not only mechanically superior but also environmentally friendly, offering a sustainable alternative for future building cladding applications.

Raj et al. (2021) investigated the use of high-volume fly ash foam concrete reinforced with natural rice straw fibers to produce lightweight, sustainable wall-cladding panels. Various mixes replaced 60% of the cement with Class F fly ash and incorporated rice straw fibers at different percentages. The optimal mix, containing 1% rice straw and 60% fly ash, provided a balanced performance across mechanical, durability, and functional properties. Higher fiber content (≥3%) negatively impacted strength by increasing porosity, whereas the 1% mix showed improved compressive and flexural strength. The porous nature of the rice straw and the morphology of the fly ash reduced thermal conductivity and improved sound absorption, particularly in the 500–1500 Hz range. This material offered a cost-effective and environmentally friendly alternative for cladding applications. However, the inherent porosity of the fibers and fly ash could increase water absorption, necessitating additional surface treatments for long-term durability.

Syed et al. (2020) investigated the potential of using coconut coir fiber (CCF) as a sustainable and effective reinforcement in concrete, aiming to reduce reliance on

synthetic alternatives. Evaluation assessed the mechanical properties and durability of concrete incorporating CCF at varying volumes. An optimal fiber content of 0.6% by volume significantly improved the material's compressive strength. In comparison, a higher concentration of 1.2% led to a decrease in strength due to challenges with fiber dispersion and weak transition zones within the concrete matrix. CCF addition produced notable enhancements in concrete's tensile, flexural, and impact resistance. The material's resistance to cracking and its ability to absorb energy improved substantially, making it a promising material for applications in thermally demanding or seismic-prone regions. CCF's unique hollow structure provided effective thermal and acoustic insulation. Although CCF addition negatively impacted workability, a superplasticizer mitigated this issue. Coconut coir fiber, when used in proper proportions, served as a viable and sustainable alternative to traditional synthetic and asbestos fibers, offering significant performance benefits.

Aravind et al. (2019) investigated the development of sustainable external wall panels fabricated from rice-husk foamed concrete containing 60 wt.% fly ash, aiming to reduce thermal conductivity and enhance indoor thermal comfort. Foamed concrete mixes substituted sand with rice husk at 0%, 5%, 10%, and 15% by volume; fly ash partially replaced cement at a constant 60 wt.%. Experiments evaluated the thermal, mechanical, and durability properties of the developed panels. Thermal conductivity decreased progressively with increasing rice husk content, achieving a 19.05% reduction at 15% replacement compared to the control. However, flexural performance, both bending strength and modulus of rupture, declined by 18% at the same rice-husk level. Water absorption rose with higher rice husk and fly ash contents, indicating increased porosity, while acid resistance improved with fly ash addition but diminished as rice husk content increased. Incorporating up to 15% rice husk in high-fly-ash foamed concrete panels yielded significant insulation benefits without excessively compromising mechanical strength or durability. Maintaining a rice-husk proportion of 10–15% achieved an optimal equilibrium between thermal insulation and mechanical strength, demonstrating the panels' viability for use in energy-efficient building envelopes.

Borges et al. (2019) investigated that iron ore tailings (IOT), specifically jig and spiral wastes, could replace natural quartz sand in metakaolin-based geopolymers activated with sodium silicate and sodium hydroxide. The experimental program evaluated twelve mix formulations by varying the solution-to-binder ratios (1.2 and 1.3), waste types, and

quartz replacement levels (50% and 100%). Across these variations, the resulting geopolymers maintained structural integrity, yielding compressive strengths of 36.3-49.5 N/mm² without notable degradation.

Higher IOT content increased apparent density due to Fe_2O_3, while water absorption and porosity increased with s/b ratio and with the use of jig waste. Spiral waste improved particle packing and reduced porosity, and combining both wastes further enhanced density. Micro-CT confirmed greater porosity and pore size than quartz controls. Given Brazil's large IOTs generation (~200 million tons/year), tailings as aggregates presented a scalable, sustainable option, though elevated porosity and absorption required further durability studies.

Rumbayan et al. (2019) examined the potential of coir, a natural fiber derived from coconut trees, for sustainable construction materials. Evaluation of the flexural, compressive, and tensile properties of concrete incorporating coir fibers at varying contents of 0%, 0.25%, 0.5%, 0.75%, and 1% by weight of aggregates occurred. Testing of specimens followed Indonesian National Standards (SNI) for mechanical properties. Slump and unit weight decreased with increasing fiber content; 0.25% fiber addition yielded optimum mechanical performance—significant improvements in flexural, compressive, and tensile strength—relative to control samples.

Zhadanovsky et al. (2018) investigated production and surface treatment of exterior wall panels from exposed porous concrete to enhance durability, freeze resistance, and aesthetic appeal. Air-entangling additives in the carefully formulated mix generated a homogeneous material with robust pore structure, boosting workability and markedly improving freeze-thaw resistance—essential for cold-climate exterior use. Mechanized processing with diamond grinders and steel brushes produced striated, corrugated, and bumpy textures. These mechanical methods proved far more efficient and reliable than manual techniques. For instance, a diamond grinder produced panels with a smooth, grinded texture that had a freeze resistance of 200 cycles, far surpassing the 50–75 cycles of manually processed panels. A combination of optimized mix design and mechanized finishing provided a viable, scalable solution for producing high-quality, durable, and aesthetically pleasing concrete panels for modern civil engineering projects.

Andiç-Çakir et al. (2014) investigated the influence of both untreated and alkali-treated coconut coir fibers (CCF) on the mechanical, physical, and thermal properties of

cement-based mortar composites. A systematic evaluation assessed how different fiber dosages and a simple alkali treatment with 5% NaOH solution affected key properties. CCF addition significantly improved flexural strength, with gains of up to 17%, and compressive strength, which increased by up to 17.9%. Toughness increased by up to 87.7% in composites containing alkali-treated fibers. Alkali treatment enhanced fiber-matrix bonding by increasing the fiber's hydrophobicity and surface functional groups. CCF improved thermal insulation and reduced the composite's unit weight, but water absorption increased significantly after boiling, highlighting a potential long-term performance issue. CCF, as a sustainable reinforcement, offered benefits but required further research to address long-term durability challenges.

2.5 Financial analysis of Iron Ore Tailings-based products

The financial analysis of iron ore tailings (IOT)- based products evaluated the costs associated with manufacturing these materials and assessed their economic viability. This analysis determined whether producing IOT-based construction materials such as bricks, blocks, pavers, and tiles proved financially sustainable and competitive in the market.

2.5.1 Cost of manufactured products

Mining activities generated significant environmental impacts due to the large volumes of material extracted and residues produced, primarily overburden and tailings. Overburden—non-valuable material above the ore—was excavated and stockpiled, while tailings remained after valuable ore separation (Sá et al., 2022). The urgent need to mitigate environmental damage drove research into economical technologies for tailings reuse, with recycling and reduction of tailings volume as key strategies (Cui, et al., 2021).

Iron ore tailings (IOT) offered promising applications in sustainable construction, providing green products, reducing landfill use, and conserving natural resources (Shettima et al., 2016). India's iron ore industry generated 10-15% waste, including low-grade ore and ultra-fines, which, through effective repurposing, was effectively transformed into bricks and concrete blocks to address environmental challenges and meet building material demand (Shreekant et al., 2016).

The study occurred in Goa, India, a small state with a per capita GDP about 2.5 times the national average. The selection of the area stemmed from its robust infrastructure,

high quality of life, and the presence of approximately 40 registered manufacturers of bricks, blocks, tiles, and pavers.

Production costs encompassed both direct costs (such as raw materials, including cement, IOT, and sand, as well as direct labour wages) and indirect costs (such as administration, utilities, maintenance, and depreciation). Analysis of these costs and production quantities over a calendar year revealed the financial viability of using IOT in manufacturing. Traditional brick making remained labour-intensive, with labour accounting for about a third of the total costs. Cost data underwent categorization by characteristics, production relationships, accounting periods, and company functions.

2.5.2 Project setting cost and payback period

India's construction sector constituted a significant source of environmental issues, including CO_2 emissions from cement production and the consumption of finite natural resources. The country's burnt clay brick industry produced up to 200 billion bricks annually with undocumented environmental impacts, highlighting an urgent need for sustainable practices (Barbhuiya et al., 2024; Chockalingam et al., 2021).

The evaluation assessed IOT's financial feasibility based on production costs, including both direct and indirect expenses.

Production costs underwent categorization using four main classifications: first, by their characteristics, distinguishing between minor, aggregated expenses (General Costs) and those directly related to the product (Specific Costs); second, by their relationship to production, separating expenses directly tied to manufacturing (Direct Costs) from those that supported the overall process (Indirect Costs); third, by the accounting period, ensuring costs appropriately matched to the correct fiscal period; and fourth, by their company function, breaking them down into Production, Administrative, and Marketing costs.

Data collection included direct raw material costs, direct and indirect labour costs, and other indirect production expenses. Production quantity data from a full calendar year determined the project setup cost and payback period.

2.5.3 Economic feasibility of IOT based products

Studies analyzed the costs of manufactured products, including financial assessments of manufacturing units and their payback periods. The following paragraphs highlight the work of various researchers in this area.

2.5.3.1 Cost estimation of products

Maraseni et al. (2025) presented repurposing waste materials for construction as a cost-effective and environmentally friendly alternative to traditional methods. Plastic waste as a binder in paver blocks reduced production costs by over 35% compared to conventional concrete blocks. Rapid setting time enabled higher daily production rates, and waste materials offset disposal costs. Similarly, geopolymer bricks made from clay cut costs by 5% compared to fired bricks, and those made from waste doubled the compressive strength for the same price. Elimination of the high-temperature curing phase significantly reduced energy consumption. Financial analyses of various waste-to-product ventures, such as turning ceramic waste into bricks, showed profitability with a high internal rate of return (IRR) and a short payback period.

Joyner & McGowan (2024) provided a simple, practical framework for calculating manufacturing costs using T-Accounts. Managerial accounting tracked costs—direct materials, direct labour, and factory overhead—to support internal decision-making. A detailed example illustrated how T-Accounts visualize cost flows from raw materials to finished goods, helping calculate key metrics such as under-applied overhead and inventory values. The distinction between product and period costs, along with the use of predetermined overhead rates, avoided pricing errors and ensured profitability.

Sinha (2022) provided a thorough financial evaluation of low-cost housing strategies in urban India, emphasizing the economic viability of alternative construction materials and techniques. Locally available resources—such as fly ash bricks, filler slabs, and bamboo reinforcement—significantly reduced overall construction costs, with savings ranging from 16% to over 40% across components. Filler slabs saved up to 44% in steel and 25% in total slab cost compared to conventional methods, while soil-stabilized bricks proved 27.7% cheaper than country-fired bricks. Transportation costs, which accounted for nearly 30% of the construction budget, were minimized by sourcing materials locally. Prefabrication and innovative roofing systems, such as brick panel roofing, reduced labour, material use, and time, further enhancing cost efficiency. These financial insights supported the broader goal of making housing more accessible to economically weaker sections by promoting sustainable, cost-effective building practices.

Hafez et al. (2020) presented a detailed financial analysis of the production of modified sand and clay bricks using rice husk ash (RHA), a low-cost agricultural waste abundant

in Egypt. Substitution of conventional raw materials with RHA—5% in sand bricks and 10% in clay bricks—demonstrated significant cost reductions in unit production. RHA-modified sand bricks achieved a 14% decrease in unit cost compared to traditional sand bricks, while clay bricks saw a dramatic 42.8% reduction. The cost advantage resulted from the zero-cost valuation of rice husk, reduced energy consumption due to optimized curing processes, and efficient material utilization. A comprehensive breakdown of raw material requirements, production volumes, and annual cost estimates confirmed the economic viability of scaling up RHA-based brick manufacturing. The integration of agricultural waste into construction materials offered financial benefits as a sustainable, cost-effective alternative for the building industry.

Youssef et al. (2019) presented a comprehensive economic analysis of geopolymer brick manufacturing in France, comparing it with traditional fired brick production. Seven formulations of geopolymer bricks made from clay and waste bricks received evaluation, focusing on raw material costs, energy consumption, and compressive strength. Clay-based geopolymer bricks offered a 5% cost advantage over fired bricks for the same strength of 20 N/mm², while waste brick-based geopolymers delivered up to 350% higher strength with only a modest increase in cost. The environmental and economic benefits of geopolymer bricks arose particularly from the elimination of high-temperature curing, which significantly reduced energy use. Analysis of production costs per metric ton and integration of real-world data from French brickworks demonstrated the industrial feasibility of geopolymer bricks. It encouraged further research into adapting existing manufacturing processes to accommodate this sustainable alternative.

Sitompul (2019) investigated the cost structure of brick production at Toba Trading Company in Indonesia, using a full-costing method to evaluate direct and indirect production costs. The company's assigned cost per brick exceeded the theoretical cost derived from accounting principles, primarily due to discrepancies in the recognition of raw materials and overhead costs. Direct costs—such as raw materials and labour—and indirect costs—including utilities, depreciation, and administrative expenses—were meticulously broken down. Monthly data analysis and forecasting using trend equations highlighted how fluctuations in production capacity directly influenced unit cost. Accurate cost calculation proved essential for pricing strategies, production planning,

and financial control, advocating a more systematic, theoretically grounded approach to cost determination in manufacturing operations.

2.5.3.2 Project setup and payback period

Amjad et al. (2025) demonstrated that using iron ore tailings (IOT) in cement composites constituted a promising strategy for cutting costs and advancing sustainability in the construction industry. Replacing cement and natural aggregates with IOT substantially lowered material costs, especially when sourcing and processing IOT was effective. Financial benefits proved significant. Replacing up to 50% of cement with IOT powder (which costs half as much as cement) reduced concrete production costs by 2.5%. Greater savings occurred when IOT served as an aggregate; at a 40% substitution level, costs dropped by up to 15%. Acquisition of IOT at no cost yielded savings exceeding 40%. Reduced need for new raw materials and lower environmental management expenses enhanced these savings. Alignment with carbon pricing initiatives occurred due to lower global warming potential, offering long-term economic incentives for climate-conscious construction. Integration of IOT into cement and aggregate mixes boosted the financial sustainability of concrete production while supporting broader environmental objectives.

Alexandra, & Vitaliy (2024) underscored the economic value embedded in technological standardization and compatibility. A systematic literature review revealed that frameworks such as RAMI 4.0, OPC UA, and Asset Administration Shell (AAS) streamlined data exchange and process integration while serving as cost-effective enablers of digital transformation. The integration of legacy systems into modern industrial ecosystems reduced the need for complete infrastructure overhauls, thereby minimizing capital expenditures. Service-oriented architectures and middleware solutions enhanced scalability and flexibility, allowing manufacturers to adapt to evolving market demands without incurring high costs. Harmonization of communication protocols and data models reduced downtime, optimized resource utilization, and improved asset lifecycle management, translating into measurable financial gains.

Smart manufacturing technologies foster long-term economic resilience by simultaneously driving operational efficiency and mitigating systemic risks.

Akan & Kiraci (2022) introduced a financially significant model for evaluating depreciation under uncertainty, particularly in capital-intensive sectors like maritime transport. An interval type-2 fuzzy set (IT2FS) framework enhanced traditional depreciation methods—specifically the straight-line and double-declining balance approaches—by incorporating uncertainty in asset values, salvage prices, and future cash flows. This fuzzy-based model enabled more flexible, realistic financial forecasting, especially in volatile environments where cash flow projections proved unreliable. Depreciation directly influenced investment decisions, tax liabilities, and shareholder value, with accelerated depreciation methods improving early cash flow and deferring tax payments, thereby enhancing financial resilience. Application of the IT2FS model to a $23 million bulk carrier demonstrated that fuzzy depreciation yielded more adaptable and informative financial outcomes than conventional methods. Investors and managers gained a robust tool for capital budgeting and long-term financial planning in uncertain economic conditions, making this approach a valuable contribution to the literature on financial decision-making under risk.

Tempa et al. (2022) demonstrated that using plastic waste (PW) as a binding agent for paver blocks was a cost-effective, eco-friendly alternative to traditional concrete blocks. Production of these cement-less blocks costs significantly less—between Nu. 7.44 and Nu. 7.85 per unit, or about 35% less than a standard concrete block (Nu. 12.15). The elimination of cement and water, and the simplification of the overall manufacturing process, largely accounted for this. Beyond production cost, laying costs for these blocks proved much lower, saving between 29% and 32% compared to concrete pavers. A lifecycle cost analysis ranked them second among paving options in Bhutan. The financial and environmental advantages of PW-based blocks make them an ideal solution for affordable infrastructure projects while simultaneously addressing plastic waste.

Toncheva et al. (2022) outlined a comprehensive financial plan to establish a factory to produce replicas of Bulgaria's historic "yellow paving stones" and related silicate-based products. Total capital investment required estimation at €2.5 million, covering land acquisition, infrastructure, building construction, and a specialized technological line. Detailed cost breakdowns included raw materials, energy, labour, depreciation, and auxiliary expenses. At full production capacity (900 tons/year), the average factory price per ton ranged from €1,567 to €2,456, depending on material type and colour, with

profitability margins reaching up to 38.8% in the second stage of operation. Labour costs accounted for approximately €455.61 per ton, and energy consumption averaged 1,755–1,875 kWh per ton. Projected selling prices ranged from €7.84 to €12.28 per paver and €4.70 to €7.37 per tile, ensuring competitive market positioning. Strong demand from municipal councils and urban infrastructure projects received anticipation, with a production program designed to scale from 450 to 900 tons annually. These financial insights affirmed the project's economic viability and its potential to contribute to sustainable urban development and heritage restoration.

Tarigan et al. (2018) investigated the economic feasibility of converting ceramic solid waste into lightweight concrete bricks, offering a sustainable and financially viable solution to industrial waste management. Financial analysis revealed that the proposed brick sold at Rp 7,751.75 per unit, with a break-even point (BEP) of 318,621 units annually. The project demonstrated strong profitability, with an Internal Rate of Return (IRR) of 43.17%, significantly exceeding typical market rates, and a Payback Period (PBP) of just 1 year and 10 months. The Profitability Index (PI) was calculated at 4.429, indicating high investment efficiency. The value added to ceramic waste through brick production is estimated at Rp 537.79 per kilogram, underscoring the potential to transform low-value industrial by-products into commercially valuable construction materials. These financial indicators affirmed the project's viability and its potential contribution to both economic and environmental sustainability in the construction sector.

Liapis & Kantianis (2015) highlighted that integrating depreciation methods into Lifecycle Costing (LCC) proved crucial for accurately assessing an asset's total financial impact over its lifespan. Depreciation systematically allocates an asset's cost, directly affecting cash flow, taxes, and investment choices. Different depreciation methods, such as straight-line and declining balance, created distinct financial outcomes by altering the timing and amount of cost recovery. Inclusion of these methods in the LCC framework enabled organizations to estimate long-term ownership costs more precisely, helping stakeholders make informed decisions about economic viability. This combined approach optimized capital budgeting, asset utilization, and financial forecasting by accounting for initial investment and final residual value, yielding a complete assessment of asset cost-effectiveness.

Saediman et al. (2014) evaluated the financial feasibility of traditional small-scale brick-making enterprises in Southeast Sulawesi, Indonesia, using key investment criteria, including Net Present Value (NPV), Internal Rate of Return (IRR), Benefit-Cost Ratio (BCR), and Payback Period (PBP). Analysis revealed that with an initial investment of $2,006.7 and annual operational costs of $2,957.4, the enterprises generated average annual revenue of $4,445.9, resulting in a net cash flow of $920.6 after taxes. Financial indicators were notably strong: NPV was $1,710, IRR was 57.69%, BCR was 1.85, and PBP was 2.4 years, all confirming the business model's profitability and viability. Sensitivity analysis confirmed the enterprise's robustness to moderate fluctuations in revenue and variable costs. Access to microcredit significantly enhanced the financial sustainability of these enterprises, enabling timely loan repayments and improving producers' livelihoods. These findings underscore the potential of small-scale brick-making as a viable economic activity and advocate increased financial support from formal institutions to strengthen the sector.

Huang et al. (2013) primarily focused on the environmental and mechanical benefits of using iron ore tailings (IOTs) in engineered cementitious composites (ECC). However, they offered insights relevant to financial considerations in sustainable construction. Partial replacement of cement with IOTs—an industrial waste—demonstrated a significant reduction in material costs and environmental impact. Mixtures containing IOTs achieved 10–32% lower energy consumption and 29–63% lower carbon dioxide emissions compared to conventional ECC, resulting in reduced lifecycle costs. Cement content in these green ECC mixtures was lowered to as little as 117.2 kg/m³, while maintaining high compressive strength (up to 57 MPa) and tensile ductility (2.3–3.3%), indicating that less expensive, more sustainable materials delivered comparable performance. Abundant, non-hazardous waste materials like IOTs implied substantial savings in raw material procurement and waste management, making the approach financially attractive for large-scale infrastructure applications. These findings supported the economic viability of green ECC as a cost-effective and durable alternative to traditional concrete systems.

2.6 Critical Summary

Cement production's 26% CO_2 emissions and 15% industrial energy use drove the adoption of supplementary cementitious materials (SCMs) and industrial by-products in

construction. Iron ore tailings (IOT), despite environmental challenges such as heavy metal contamination and habitat destruction, offered viable alternatives as construction materials. Two decades of research established IOT's viability, though site-specific characterization remained essential due to variable composition.

GGBS, a pig iron by-product, enhanced concrete through C-S-H gel formation at 40–45% replacement, improving strength, durability, and reducing CO_2 emissions. Fly ash (Class F or C) at 20–30% replacement enhanced pozzolanic reactions, improved durability, and provided sustainable cement substitution. Limestone powder (10–15% replacement) enhanced cement performance through filler and nucleation effects, improving strength and reducing CO_2 emissions. Ceramic waste (15–30% of tile production) contained pozzolanic silica and alumina, offering cost savings despite modest reductions in strength. Crushed stone sand (CSS), replacing sand up to 50% in M20/M30 grades, maintained mechanical integrity while reducing construction costs and environmental impact.

Iron ore tailings (IOT) served as partial replacements for fine aggregates in Portland cement mortars and concrete, showing significant improvements in compressive strength (up to 22.9% at 40% replacement) and tensile strength. Workability remained acceptable up to 40% IOT, with enhanced particle packing contributing to durability through lowered water absorption and drying shrinkage. Optimal replacement ranged from 20% to 40% across various concrete grades. Alkali-activated, kiln-free geopolymer bricks incorporating IOT and industrial wastes (such as red mud and GGBS) demonstrated promising strengths and water resistance, meeting Indian standards, with compressive strengths ranging from 16.68 to 28.23 N/mm². Recycled aggregate pavers and sustainable cement tiles made with IOT-substituted aggregates offered improved mechanical properties, along with drainage and aesthetic benefits. Advances in fiber-reinforced concretes and prefabricated claddings cemented IOT's role as an eco-friendly building material, with coconut coir fibers reinforcing enhanced strength and insulation. Despite successes, most research has focused on fresh tailings, leaving gaps in understanding long-term oxidation effects, secondary mineralization, and behaviour under tropical weather cycles. Ultrafine tailings (<75 μm) remain under-studied, limiting the predictive power of models.

Long-term durability protocols must quantify the environmental stability and mechanical performance of aging tailings integrated into composite systems.

Literature primarily focused on fresh iron ore tailings, with limited studies on long-term oxidation, mineralization, and their effects on composites. The stability of ultrafine tailings (<75 μm), especially under tropical cycles, has been under-researched. Most studies remained at the laboratory scale, lacking data on scale-up, production consistency, and quality control. Experiments for optimal replacement lacked the rigor of a design-of-experiments approach. Durability issues, such as freeze-thaw resistance and heavy metal leaching, remained inadequately addressed. The absence of international standards and the scarcity of economic and pilot-scale studies hindered broader adoption and applicability, especially in tropical and developing regions.

Proposed research addressed gaps by creating sustainable composite building materials from iron ore tailings (IOT) in Goa, India, combined with cement, fly ash, and GGBS. Development of five products progressed from lab to pilot scale, using rigorous experiments, advanced characterization, and extensive durability assessments beyond standard 28-day tests. A cost-benefit analysis determined the economic feasibility.

Integrated analytical techniques quantified the inherent compositional heterogeneity of the iron ore tailings. Comprehensive mechanical, durability, and environmental safety testing, including leaching, ensured long-term performance. Pilot production and monitoring bridged scale-up gaps for practical adoption.

CHAPTER 3
EXPERIMENTAL INVESTIGATIONS

3.1 General

This chapter established the experimental framework for the development and evaluation of composite construction materials incorporating Iron Ore Tailings (IOTs) derived from mine waste. Systematic physicochemical characterization and binder optimization converted IOTs from overburden dumps into construction composites. The integrated framework simultaneously mitigated environmental burdens, extracted latent economic value, reduced reliance on landfilling, and generated sustainable building products. At the same time, a cost-benefit evaluation demonstrated manufacturing feasibility and potential scalability within a circular-economy model for a resource-constrained region. The experimental program characterized the raw constituents (IOTs, supplementary binders, and aggregates), designed and manufactured a series of IOTs-based composite products, such as bricks, blocks, pavers, tiles, and cladding panels, and evaluated their performance and economic viability.

3.2 Physical properties of materials

The constituent materials underwent systematic physical characterization to verify their suitability for application in IOTs-based composites.

3.2.1 Iron Ore Tailings

IOTs from a mine site in Dharbandora Taluka, South Goa, served as the primary waste-derived constituent. Figure 3.1 shows the sampling site at latitude 15.3366411°N and longitude 74.2472719°E. Figure 3.2 depicts the tailings stored at the site, while Figure 3.3 illustrates the IOTs sample collected from the mine.

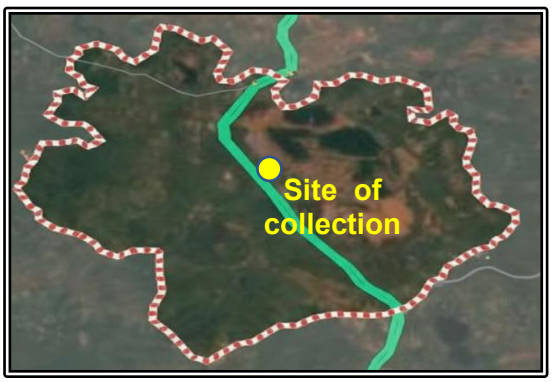


Figure 3.1: Location of mine



Figure 3.2: Tailing dump

A 200 kg IOTs sample served as the base for a systematic characterization program, in which laboratory protocols defined the physical and chemical properties. Table 3.1 summarizes the parameters analysed in this study.



Figure 3.3: Iron Ore Tailing sample

Table 3.1: Physical properties of Iron Ore Tailings

Sr. No.	Test	IS Code details
1	Specific Gravity	IS 2386 (Part 3):1963 -reaffirmed in 2021
2	Water absorption	
3	Density	
4	Sieve Analysis	IS 12550 :1988 -reaffirmed in 2024

3.2.2 Cement

Ordinary Portland Cement (OPC) of 53-grade illustrated in Figure 3.4 functioned as the primary binder in the IOTs based composite mix which is summarized in Table 3.2. Standard Physical and Chemical testing verified the properties of the locally sourced Cement.



Figure 3.4: OPC -53 grade sample

Table 3.2: Physical properties of Cement

Sr. No.	Test	IS Code details
1	Fineness (Blaine air-permeability)	IS 4031 (Part 2):1999 -reaffirmed in 2018
2	Soundness (Le Chatelier method)	IS 4031 (Part 3):1999 -reaffirmed in 2019

Sr. No.	Test	IS Code details
3	Setting Times	IS 4031 (Part 5):1988 -reaffirmed in 2019
4	Standard Consistency (Vicat apparatus)	IS 4031 (Part 4):1988 -reaffirmed in 2019
5	Specific Gravity	IS 4031 (Part 11):1988 -reaffirmed in 2019
6	Density	

3.2.3 Ground-Granulated Blast-Furnace Slag (GGBS)

Ground-Granulated Blast-Furnace Slag (GGBS) served as a supplementary cementitious material in the IOTs-based composite, enhancing durability, mitigating the heat of hydration, and augmenting long-term strength (Ganesh & Murthy, 2019). GGBS, shown in Figure 3.5, originated as an industrial by-product obtained by rapid quenching of molten blast-furnace slag in water. Subsequent mechanical milling yielded the high-fineness powder required for cementitious reactivity.



Figure 3.5: GGBS sample

A 50 kg GGBS sample from the JSW division facilitated the preliminary testing phase. Table 3.3 lists the tests performed on GGBS used in an IOT-based composite.

Table 3.3: Physical properties of GGBS

Sr. No.	Test	IS Code details
1	Fineness	IS 4031 (Part 2):1999 -reaffirmed in 2018
2	Specific Gravity	IS 4031 (Part 11):1988 -reaffirmed in 2019
3	Density	IS 4031 (Part 11):1988 -reaffirmed in 2019
4	Residue by wet basis on 45µ	IS 4031 (Part 1):1996 -reaffirmed in 2021

3.2.4 Fly ash

Fly ash, a pozzolanic by-product of coal combustion, illustrated in Figure 3.6, served as a supplementary cementitious component in the IOTs composite matrix.



Figure 3.6: Fly ash sample

Adherence to IS 3812 (Part 1): 2013 - Reaffirmed in 2022 standards defined the chemical and physical parameters of the Class F (low-calcium) fly ash. The spherical particle morphology and fine particle size distribution promoted dense particle packing, reduced water demand, and improved workability, thereby refining the pore structure and lowering permeability. These microstructural modifications enhanced the long-term strength and durability of the composite system (Yao et al., 2015). Table 3.4 outlines the tests performed on the fly ash sample.

Table 3.4: Physical properties of Fly ash

Sr. No.	Test	IS Code details
1	Fineness	IS: 1727 - 1967 reaffirmed in 2018
2	Residue by wet basis on 45μ	
3	Specific Gravity	
4	Moisture Content	
5	Density	
6	Soundness by Autoclave	

3.2.5 Lime powder

Lime functioned as an alkaline activator within the blended binder system. In high-pH conditions, lime dissolved reactive silica and alumina phases present in GGBS, fly ash, and IOTs, thereby precipitating calcium silicate hydrate and calcium aluminate hydrate gels (Sedira et al., 2017). Figure 3.7 presents the lime sample, while Table 3.5 outlines the physical properties.



Figure 3.7: Lime powder sample

As a cost-effective activator, lime enhanced workability and durability, facilitated greater utilization of industrial by-products, and reduced overall cement consumption.

Table 3.5: Physical properties of lime

Sr. No.	Test	IS Code details
1	Specific Gravity	IS : 1540 (Part I)- 1980 Reaffirmed in 2024
2	Specific surface area, in m^2/kg	

3.2.6 Ceramic waste

A laboratory jaw crusher processed broken ceramic waste sourced from a local vendor, yielding a 5 kg sample. The ceramic waste partially replaces conventional aggregates. This substitution reduces landfill disposal, conserves resources, and promotes environmental sustainability through circular-economy practices. Table 3.6 outlines tests performed on the ceramic waste.

Table 3.6: Physical properties of ceramic waste

Sr. No.	Test	IS Code details
1	Specific Gravity	IS 2386 (Part 3):1963 -reaffirmed in 2021
2	Water absorption	
3	Uncompacted Bulk density	
4	Compacted Bulk density	

3.2.7 Fine and coarse aggregates

Crushed stone aggregates, procured from a local metal quarry, provided the granular structure of the composite products. Mechanical crushing produced angular, rough-textured particles that provided better mechanical interlock than naturally rounded gravel. The supply of fine and coarse aggregates, each at 5 kg, facilitated the characterization procedures.

The production of crushed stone aggregate comprised two principal stages:(i) extraction and primary processing, and (ii) secondary and tertiary processing, which graded the material into specified size fractions. Particle size distribution governed the classification of aggregates into fine and coarse fractions.

Figure 3.8 displays fine aggregates i.e. crushed stone sand with particle sizes below 4.75 mm, while Figure 3.9 illustrates coarse aggregates of 10 mm.



Figure 3.8: Crushed stone sand sample



Figure 3.9: 10 mm aggregate sample

Typical coarse aggregates range in size from 4.75 mm to 37.5 mm. Tables 3.7 and 3.8 present the physical properties of the fine and coarse aggregates, respectively.

Table 3.7: Physical properties of fine aggregate

Sr. No.	Test	IS Code details
1	Bulk Density	IS 2386 (Part 3):1963 -reaffirmed in 2021
2	Specific Gravity	
3	Water Absorption	
4	Silt Clay & Fine Dust	IS 2386 (Part 2):1963 -reaffirmed in 2021
5	Sieve Analysis	IS 2386 (Part 1):1963 -reaffirmed in 2021

Table 3.8: Physical properties of coarse aggregate

Sr. No.	Test	IS Code details
1	Bulk Density	IS 2386 (Part 3):1963 -reaffirmed in 2021
2	Specific Gravity	
3	Water Absorption	
4	Combined Flakiness & Elongation Index	IS 2386 (Part 1):1963 -reaffirmed in 2021
5	Flakiness Index,	
6	Elongation Index	
7	Sieve Analysis	IS 2386 (Part 1):1963 -reaffirmed in 2021
8	Aggregate Crushing Value	
9	Aggregate Impact Value	IS 2386 (Part 4):1963 -reaffirmed in 2021
10	Aggregate Abrasion Value	

3.3 Chemical properties of material

The ARL X-Ray Fluorescence (XRF) spectrometer shown in Figure 3.10 quantifies the chemical constituents of IOTs, OPC, GGBS, fly ash, lime, fine aggregate, coarse aggregate, and ceramic powder.



Figure 3.10: X-Ray Fluorescence (XRF) spectrometer

The high-power X-ray tube of the instrument excited atoms within each sample and induced emission of characteristic secondary X-rays during electronic relaxation to the ground state. A wavelength-dispersive detection system then separated and quantified these emissions, thereby resolving both major and minor oxides simultaneously.

A combination of non-destructive multi-element analysis, rigorous calibration protocols, controlled sample preparation (pellet pressing and glass-bead fusion), and optimized measurement parameters enabled the ARL XRF system to generate rapid, accurate oxide profiles. These profiles supported quality control of constituents, optimization of binder–filler blends, and systematic evaluation of alternative construction materials.

3.4 X-ray diffractometer analysis

The Rigaku Smart Lab X-ray diffractometer shown in Figure 3.11 identified crystalline phases, quantified mineral compositions, and assessed structural properties in materials such as mining waste and construction composite. This multipurpose diffractometer executed powder XRD, grazing-incidence XRD, X-ray reflectivity, and high-resolution

XRD to elucidate atomic arrangements, phase purity, and residual stress in iron ore tailings.



Figure 3.11: X-ray diffractometer setup

Standard mounting techniques consolidated the powdered samples onto zero-background holders or low-background slides. SmartLab Studio II software directed automatic alignment in Bragg-Brentano or parallel-beam geometry. X-rays irradiated the sample during goniometer scans (typically 5–80° 2θ at 0.02–0.05° steps). HyPix-3000 detectors acquired diffracted intensities. Post-acquisition software refined peak positions, correlated phases with ICDD databases, and performed quantitative phase analysis quantification.

3.5 FE-SEM with EDX analysis

The ZEISS Sigma 360 FE-SEM with EDX illustrated in Figure 3.12 reveals the surface morphology and elemental composition of materials such as mining waste and construction composites at nanoscale resolution. This instrument delivers high-resolution imaging alongside EDX mapping to delineate microstructures, phases, and impurities within iron ore tailings. Sample preparation mounted specimens on stubs, sputter-coated non-conductive surfaces, and verified that the sample height remained below the instrument's maximum limit.

The airlock vented to enable insertion of the sample via the transfer rod, after which the chamber was pumped down to high vacuum ($< 2\times10^{-5}$ torr).



Figure 3.12: FE-SEM with EDX setup

Imaging conditions established through activation of the electron high tension (EHT) at 3–15 kV, engagement of detectors such as SE2 or InLens, optimization of working distance and stage position, and beam focusing with stigmation. SEM images captured microstructures. EDX conducted point, line, or map scans to quantify elemental distributions. Shutdown proceeded through deactivation of the EHT, venting of the airlock for sample exchange, system logout, and final cleaning.

3.6 Mix proportion for bricks

Conventional bricks available in the market typically use clay or bottom ash as their primary constituent. In contrast, the present Brick manufacturing employed a composite blend of industrial by-products and binders comprising IOTs, GGBS, fly ash, cement, and lime powder. Earlier studies (Kumar et al., 2017; Kuranchie et al., 2015) helped decide the mix proportions. All trial mixes maintained a fixed IOTs content of 50% by mass to maximize waste utilization.

The study utilizes a TxxFxxGxx naming convention to classify brick compositions based on the percentages (xx) of IOTs (T), fly ash (F), and GGBS (G). For example, T50F05G35 represents a mixture comprising 50% IOTs, 5% fly ash, 35% GGBS, 5% cement, and 5% lime.

The experimental program examined the influence of varying the relative contribution of pozzolanic constituents. The mix design matrix increased the fly ash content in 5% increments (5% to 35%) while simultaneously reducing GGBS in corresponding steps (35% to 5%). Cement and lime remained at a constant dosage of 5% each. Following

the procedures reported by Almada et al. (2022) and Thejas & Hossiney (2022), the mixing protocol subjected all dry constituents to mechanical blending until the mix achieved homogeneity. Preliminary workability trials established the required water content.

Cube moulds received freshly prepared mixes directly from the mixer, followed by mechanical vibration for 2 minutes at 12,000 ± 400 vibrations per minute. Table 3.9 summarizes all seven laboratory-scale mixtures evaluated before transitioning to industrial-scale casting.

Table 3.9: Mix proportions for bricks (all values in %)

Trial	A	B			
	IOT	Cement	GGBS	Fly Ash	Lime
T50F05G35	50	5	35	5	5
T50F10G30	50	5	30	10	5
T50F15G25	50	5	25	15	5
T50F20G20	50	5	20	20	5
T50F25G15	50	5	15	25	5
T50F30G10	50	5	10	30	5
T50F35G05	50	5	5	35	5

This compaction process expelled entrapped air and enhanced density. After demoulding, six cubes from each mix were water-cured and subsequently tested for compressive strength at 7 and 28 days. Compressive strength tests employed a controlled loading rate in accordance with IS 4031 (Part 6 – 1988).

3.7 Casting of bricks

The casting process produced brick specimens with nominal dimensions of 0.23 m × 0.10 m × 0.07 m, corresponding to a unit volume of 0.00161 m³. The study determined the mass of each constituent per brick from its percentage by mass and its dry loose bulk density.

Following the approach of Rao (2020), Equation 3.1 governed the estimation of material quantities: Quantity of material (kg) =

Volume of the brick (m³) × raw material percentage (%) × density (kg/m³)..… **(Eq. 3.1)**

Careful blending of the materials produced bricks with an even mix and colour. Equation 3.1 generated precise quantities of IOTs, cement, GGBS, fly ash, and lime, and the calculated constituents subsequently followed the mix design specified in result section, Table 4.9.

A mechanical mixer blended the components for approximately 5 minutes, producing a uniform colour and absence of visible segregation.

Preliminary workability assessments determined the precise water dosage required to ensure optimal consolidation during hydraulic pressing. The workable mix advanced into a hydraulic brick-manufacturing press, where a 40-tonne compactive load densified the material and enhanced its structural integrity. Standard water curing for 28 days optimized the hydration process and subsequent strength development. Production yielded 60 specimens per mix proportion, providing a comprehensive dataset for mechanical characterization.

3.8 Laboratory investigations on cast brick

Laboratory investigations evaluated brick quality in accordance with Bureau of Indian Standards (BIS) specifications. After curing, the bricks underwent mechanical and durability testing, including compressive strength and water absorption tests. An efflorescence test assessed suitability for applications requiring sustained aesthetic appearance of masonry surfaces. Table 3.10 lists all tests conducted on the cast bricks.

Table 3.10: List of tests carried out on cast brick

Test	Source	Sample Size (In Nos.)	Curing Age
Dimension	IS 1077: 2025	20	28 days
Water Absorption	IS 3495 (Part 2) : 2019	5	28 days
Bulk Density	IS 3495 (Part 1) : 2019	5	28 days
Brick Ageing	Thejas & Hossiney (2022)	3	28 days
Efflorescence	IS 3495 (Part 3) : 2019	3	28 days
Electrical Resistivity	Kuranchie et al. (2015)	3	28 days
Falling Test	Kumar et al. 2020	3	28 days
Soundness	Kumar et al. 2020	3	28 days
Hardness	Kumar et al. 2020	3	28 days

3.8.1 Dimension test

The dimensional assessment followed IS 1077: 2025. The procedure selected 20 bricks at random, arranged them in rows, and aligned them along a straight line. A steel tape measured overall lengths, widths, and depths to the nearest millimetre, and the recorded values enabled evaluation of dimensional accuracy and consistency. Figure 3.13 shows the cast brick along with dimensions.

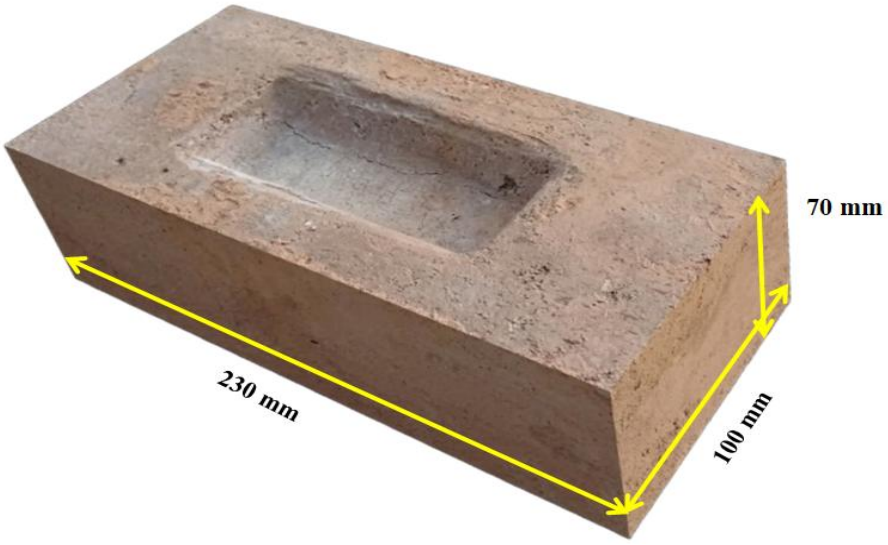


Figure 3.13: Cast brick with dimensions

3.8.2 Compressive strength and dry bulk density

A digital compression testing machine measured the compressive strength in accordance with IS 3495 (Part 1): 2019. Prior to testing, each specimen underwent conditioning by immersion in water at room temperature for 24 hours, followed by removal of surface moisture with a damp cloth. The digital compression testing machine applied an axial load at a uniform rate of 14 ± 1 N/mm^2/min until structural failure. The final indicator reading marked the maximum load where the specimen no longer offered resistance. The compressive strength, expressed in N/mm^2, was obtained by dividing the maximum load at failure (N) by the average net area of the loaded faces (mm^2):

$$\text{Compressive strength, in N/mm}^2 = \frac{\text{Maximum load at failure,in N}}{\text{Average area of the bed faces,in mm}^2} \quad \text{..... (Eq. 3.2)}$$

Bulk density measurement for each specimen also followed IS 3495 (Part 1): 2019. Bricks were dried in an oven at 110°C for 24 hours, cooled to room temperature, and weighed. Length, width, and thickness measured at three points, and average

dimensions calculated defined the specimen volume. The computed mass and corresponding volume then yielded the bulk density as:

$$\text{Dry bulk density (kg/m}^3\text{)} = \frac{\text{Dry weight ,in kg}}{\text{length (m)} \times \text{width (m)} \times \text{thickness (m)}} \quad \text{..... (Eq. 3.3)}$$

3.8.3 Water absorption and wet bulk density

Adherence to IS 3495 (Part 2): 2019 protocols governed the quantification of water absorption properties. An oven operating at 110°C dried the brick specimens for 24 hours, establishing the dry mass (M1) after the samples returned to room temperature. Clean water at 27 ± 2°C saturated the completely dried specimen for 24 hours. Removal of superficial moisture via a dry cloth achieved a saturated surface-dry condition without removing absorbed water from the specimen interior, before the balance registered the saturated mass (M2). The equations mentioned below determines water absorption and bulk density respectively.

$$\text{Water Absorption (\%): } = \frac{(M2 - M1)X100}{M1} \quad \text{..... (Eq. 3.4)}$$

M1 = Weight of brick in dry condition

M2 = Weight of brick after immersion in water

$$\text{Wet bulk density (kg/m}^3\text{)} = \frac{\text{Wet weight ,in kg}}{\text{length (m)} \times \text{width (m)} \times \text{thickness (m)}} \quad \text{..... (Eq. 3.5)}$$

3.8.4 Brick ageing

The methodology outlined by Thejas & Hossiney (2022) governed the accelerated ageing protocol and the subsequent durability assessment. Seven cycles of wetting and drying simulated harsh weathering. Each cycle consisted of complete immersion in clean water for 5 hours (wetting cycle) followed by oven drying at 70°C for 42 hours (drying cycle). Equation 3.2 yielded the compressive strength values necessary to evaluate the durability performance of three bricks following each cycle.

3.8.5 Efflorescence

IS 3495 (Part 3): 2019 standards specified the characterization of efflorescence. A shallow dish subjected the vertically oriented specimens to a 25 mm immersion depth, driving capillary uptake to complete saturation. After absorption and drying, the reintroduction of an equivalent volume of water initiated a secondary saturation cycle. Upon completion of the second evaporation phase, a visual assessment identified

efflorescence as perceptible surface deposits. Visual inspection then categorized any resulting surficial salt crystallization as Nil, Slight, Moderate, Heavy, or Very Heavy.

3.8.6 Electrical resistivity

The methodological framework established by Kuranchie et al. (2015) guided the electrical resistivity measurements. Conductive probes attached to the specimen terminals interfaced with a multimeter as shown in Figure 3.14 captured the resistance data. Controlled environmental parameters maintained the samples in a dry state during testing to minimize moisture interference.

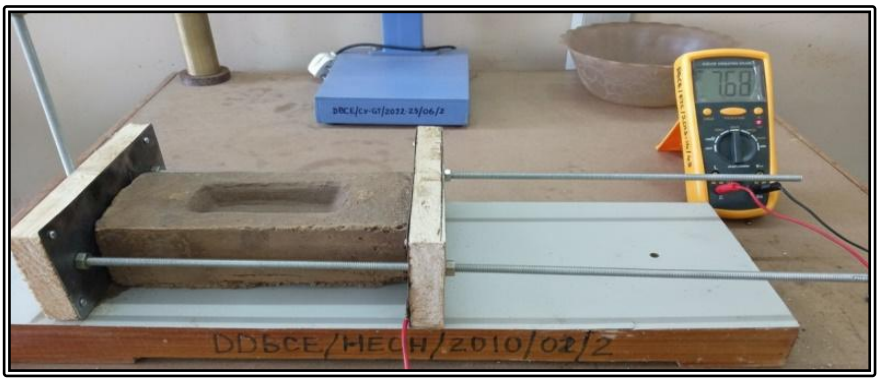


Figure 3.14: Electrical resistivity of brick

The computation of resistivity relied on the recorded resistance value and the specimen geometry:

$$\text{Electrical resistivity } (\Omega \cdot \text{m}) = \frac{R\ XA}{L} \qquad \text{…….. (Eq. 3.6)}$$

Where R is the electrical resistance (Ω),

A is the surface area (m^2) through which current flows, and

L is the length of the brick (m).

3.8.7 Falling test

Upon curing, the dried bricks were dropped from a height of 1 m onto firm, levelled ground to assess the material's fracture resistance. Specific cracking patterns determined the failure mode, with standard practice deeming moderate edge failure acceptable.

3.8.8 Soundness test

Mechanical shock delivered by striking two bricks together or via a hammer impact, induced an acoustic response to assess soundness. A distinct metallic ring characterized bricks possessing adequate density and structural integrity.

3.8.9 Hardness test

Surface scratch resistance established the metric for hardness. The bricks' resistance to perceptible indentation under manual fingernail pressure substantiated their suitability for construction applications.

3.9 Mix proportion for blocks

The growing demand for construction materials in the sector necessitated exploring a novel approach using IOTs in masonry units. Masonry blocks incorporated IOT as Fine aggregate replacement and ceramic waste as partial substitution for 10 mm conventional aggregates.

The block casting process utilizes an AxxCWxx nomenclature to specify mix proportions, assigning A to aggregate and CW to ceramic waste. Accordingly, A70CW30 denotes a formulation comprising 70% coarse aggregate of size 10 mm and 30% ceramic waste, alongside IOTs and supplementary cementitious materials.

Four distinct mix design trials comprising a baseline formulation with conventional 10 mm aggregate and three experimental variations incorporating ceramic waste as a partial coarse aggregate replacement constituted the experimental framework. Table 3.11 gives the aggregate distribution percentages within the matrix

Table 3.11: Percentage breakdown of aggregates in the mix (all values in %)

Trial	10 mm Aggregate	4.75 mm Ceramic Waste
A100CW00	100	---
A090CW10	90	10
A080CW20	80	20
A070CW30	70	30

IS 10262:2019 protocols governed the mix design optimization. The methodological sequence commenced with the derivation of the target mean strength, calculated as the sum of the characteristic compressive strength (f_{ck} and 1.65 times the standard deviation, as mandated by IS 10262:2019. Subsequently, durability requirements outlined in Table 5 of IS 456:2000 - Reaffirmed in 2021 governed the selection of the water-cement ratio. Table 2 of IS 10262:2019 determined the maximum water content based on the nominal maximum aggregate size.

These parameters formed the basis for the cement content calculation, while Table 3 of IS 10262:2019 guided the estimation of coarse aggregate proportions. This systematic quantification facilitated precise material estimation for each constituent, with necessary adjustments to correct for aggregate moisture content.

Table 3.12 details the specific mix proportions, which dictated the mixing protocol for full-scale industrial implementation. Furthermore, Table 4.21 of results section enumerates the material quantities required to cast a 1 m^3 volume.

Dry constituents mixed thoroughly to achieve homogeneity, while controlled water addition produced a cohesive paste with no air voids; standardised mixing parameters optimised both workability and uniformity. The mixture comprises three distinct fractions: Part A contains the cementitious materials; Part B consists exclusively of iron ore tailings (IOTs) as the fine aggregate; and Part C incorporates 10 mm coarse aggregates besides ceramic waste.

Table 3.12: Mix Proportions for Blocks (all values in %)

Trial	Cementitious Material				Fine Aggregate	Coarse Aggregate	
	A= 100%				B=100%	C=100%	
	Cement	GGBS	Fly Ash	Lime	IOTs	10mm	Ceramic Waste
A100CW00	15.00	65.00	10.00	10.00	100.00	100.00	--
A090CW10	15.00	65.00	10.00	10.00	100.00	90.00	10.00
A080CW20	15.00	65.00	10.00	10.00	100.00	80.00	20.00
A070CW30	15.00	65.00	10.00	10.00	100.00	70.00	30.00

Controlled curing conditions were maintained for six 150 mm × 150 mm × 150 mm cubes for each trial mix at ambient temperature. IS 516: 2021 protocols directed the compressive strength evaluation at 7 and 28 days. A 200-tonne-capacity compression-testing machine applied the load at a gradual rate of approximately 14 N/mm²/min until specimen failure.

3.10 Casting of blocks

An industrial facility within the Kakoda Industrial Estate (Goa, India) executed the full-scale synthesis of experimental blocks, systematically converting raw constituents into construction blocks for commercial validation.

The manufacturing sequence commenced with the introduction of IOTs into a pan mixer, followed by the sequential addition of GGBS, fly ash, cement, and lime, in the proportions specified in the results section. A 5-minute operation cycle ensured the uniform blending of all cementitious materials; this homogenization phase proved critical for consistent block properties and structural integrity.

Following the complete homogenization of fines, the process incorporated 10 mm basaltic aggregate and ceramic waste into the mix. Controlled addition of water achieved the optimal consistency for block manufacturing, ensuring adequate workability while preventing segregation or bleeding.

The hydraulic block-making unit subjected the mix to a compressive force of 80 tonnes, transforming the granular material into cohesive, high-density blocks with precise geometry. Figure 3.15 illustrates the block-making machine, while Figure 3.16 displays the resulting block.



Figure 3.15: Block making machine

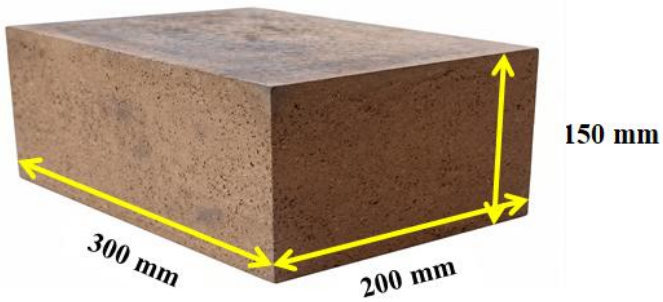


Figure 3.16: Cast block with dimensions

The newly formed blocks underwent immediate surface finishing and were subsequently cured under controlled conditions to facilitate proper hydration and

strength development. The cast blocks were initially maintained under ambient conditions for 24 hours to allow initial setting, followed by water curing at 27 ± 2°C for the specified duration. Comprehensive testing on representative samples from each production batch verified quality and performance consistency.

3.11 Laboratory investigations on cast block

IS 2185(Part 1):2005 –Reaffirmed in 2020 standards framed the quality assessment of manufactured blocks, and Table 3.13 presents the tests carried out on cast blocks. The experimental protocol incorporated dimensional verification, mechanical property evaluation, and durability assessment to validate compliance with construction specifications. Standard requirements dictated the sample sizes, while controlled laboratory conditions governed all testing procedures.

Table 3.13: List of tests carried out on cast block

Test	Source	Sample Size (In Nos.)	Curing Age
Dimension	IS 2185(Part 1):2005 – Reaffirmed in 2020	20	28 days
Compressive Strength		8	7, 28 days
Water Absorption		3	28 days
Bulk Density		3	28 days
Efflorescence	IS 3495 (Part 3) : 2019	3	28 days

3.11.1 Dimension test

To evaluate dimensional accuracy, 20 blocks were randomly selected and arranged systematically in rows. Precise measurements of length, width, and height were recorded to the nearest millimeter using a calibrated steel tape. Straight reference lines facilitated the measurement of overall dimensions, ensuring strict adherence to dimensional conformity.

3.11.2 Compressive strength and bulk density

A digital compression testing machine, shown in Figure 3.17, was used to measure the compressive strength of the specimens. The apparatus applied axial loads at a uniform rate of 14 N/mm²/min, increasing pressure incrementally until definitive specimen failure. Equation 3.2 yielded the compressive strength.



Figure 3.17: Compression testing of block

For bulk density determination, oven drying at 100°C for 24 hours removed moisture, after which a calibrated balance recorded the mass of the cooled specimens. Dimensional measurements taken at three locations provided average values of all three dimensions, and Equation 3.3 determined the bulk density of the block.

3.11.3 Water absorption

A 24-hour immersion protocol at ambient temperature ensured complete saturation of the test specimens. Hydrostatic weighing, using a metal-wire suspension system, determined the submerged mass. Following removal, a one-minute drainage period on 10 mm wire mesh, combined with surface blotting, established the saturated surface-dry condition for immediate weighing

A ventilated oven operating between 100 -115°C dries the saturated specimens for a minimum of 24 hours. This heating period continues until successive mass readings at 2-hour intervals indicate a loss increment below 0.2 percent.

$$\text{Water Absorption (\%)}: = \frac{(A-B)X100}{B} \quad \text{…….. } \textbf{(Eq. 3.7)}$$

A = Weight of block in wet condition, in kg

B = Weight of block in dry condition, in kg

3.11.4 Efflorescence test

The test followed IS 3495 (Part 3): 2019. A flat dish held the sample upright in 25 mm of distilled water. Controlled room conditions managed evaporation, while a glass cover ensured water moved only through the material's pores rather than evaporating from the dish. The block absorbed the water completely before drying. Adding the same amount of water started a second cycle. Finally, visible salt deposits on the surface determined the level of efflorescence.

3.12 Mix design for pavers and tiles

The paver specifications classify the paver into five distinct classes. The composition of the mix depends on various parameters, such as specific gravity, water absorption, and other factors. This investigation employed a novel approach that incorporated IOTs into paver and tile casting. M30 concrete mix design comprised eighteen formulations based on three cement replacement sets: Set 1 (100% cement), Set 2 (80% cement + 20% GGBS), and Set 3 (60% cement + 40% GGBS). Within each set, IOT replaced crushed stone sand at 0%, 10%, 20%, 30%, 40%, and 50%, enabling a comprehensive evaluation of the effects of IOT incorporation on concrete properties, and with a constant 10 mm coarse aggregate, creating a structured matrix (C100Tx, C080Tx, and C060Tx).

Table 3.14 governed the proportions of material fractions for casting test cubes to determine the optimal mix. 10 mm aggregate was used to 100% in the mix. In the case of Pavers and Tiles, the concrete composition consisted of a CxxTx mix, where "C" denotes the percentage of Cement and "T" denotes the percentage of Tailing. The mix designation C080T10 indicates 80% cement within the total 100% cementitious content and 10% replacement of the total fine aggregate with IOTs. The mix design used 10 mm coarse aggregate in all 18 trials.

Table 3.14: Mix proportions for pavers and tiles (all values in %)

Trial	100%		100%		
	Cementitious Content		Fine Aggregate		Admixture
	Cement	GGBS	IOT	Crushed Stone Sand	
C100T00	100	-	0	100	0.3
C100T10	100	-	10	90	0.3

Trial	100% Cementitious Content		100% Fine Aggregate		Admixture
	Cement	GGBS	IOT	Crushed Stone Sand	
C100T20	100	-	20	80	0.35
C100T30	100	-	30	70	0.40
C100T40	100	-	40	60	0.50
C100T50	100	-	50	50	0.70
C080T00	80	20	0	100	0.3
C080T10	80	20	10	90	0.3
C080T20	80	20	20	80	0.35
C080T30	80	20	30	70	0.40
C080T40	80	20	40	60	0.50
C080T50	80	20	50	50	0.70
C060T00	60	40	0	100	0.3
C060T10	60	40	10	90	0.3
C060T20	60	40	20	80	0.35
C060T30	60	40	30	70	0.40
C060T40	60	40	40	60	0.50
C060T50	60	40	50	50	0.70

The concrete mix design process adhered to established guidelines for grade M30 concrete as per IS 10262:2019. Target mean strength determination involved adding 1.65 times the standard deviation of concrete strength to the characteristic compressive strength (fck) as specified in IS 10262:2019.

The water-cement ratio was carefully selected in accordance with IS 456:2000-Reaffirmed in 2021, while nominal maximum aggregate size specifications as per IS 10262:2019 determined the maximum water content. These parameters enabled the calculation of cement content, followed by coarse aggregate proportion estimation in accordance with IS 10262:2019. Table 4.28 in results sections presents the quantities of each constituent material required per cubic meter of paver casting. The evaluation of trial mixes validated and refined the predicted mix proportions.

A drum mixer performed concrete mixing with controlled parameters, ensuring consistency and homogeneity. Constituent materials, including IOTs, cement, GGBS, crushed stone sand, coarse aggregates, superplasticizer, and water, were manually

loaded in accordance with the mix design. A mixing duration of 2–3 minutes after material addition ensured homogeneous concrete development, immediate transfer to casting trays, followed by mixing completion.

Standard cube moulds (150 mm × 150 mm × 150 mm) were filled in three equal layers, with mechanical compaction of 35 blows per layer, as per IS 516: 2021 specifications. Vibrating tables provided additional compaction, eliminating air voids and ensuring adequate consolidation. Completion of the 24-hour setting time allowed the demoulding and the relocation of specimens to curing tanks. Three replicate cubes per mix design were cured for 7 and 28 days, enabling the establishment of strength development patterns prior to compressive strength determination.

A 200-tonne capacity digital compression testing machine conducted compressive strength testing in accordance with IS 516: 2021. Horizontal positioning of test specimens between compression platens ensured proper alignment and uniform load distribution. Controlled axial loading without shock application proceeded at a uniform rate of approximately 14 N/mm^2/min until specimen failure occurred.

Sustained loading through observable structural failure, including cracking and ultimate collapse, yielded the compressive strength calculation as per Equation 3.2. Paver casting (dimensions: 200 mm × 100 mm × 60 mm) and tile casting (dimensions: 300 mm × 300 mm × 25 mm) proceeded on all trial combinations selected based on compressive strength performance.

3.13 Casting of pavers and tiles

A pan mixer initiated the manufacturing process by systematically loading materials. IOTs underwent initial loading, followed by sequential addition of cement, GGBS, crushed stone sand, and 10 mm aggregate in proportions specified in Table 3.14. Approximately 2 minutes of dry mixing achieved uniform material distribution prior to controlled water addition as per design calculations. Figure 3.18 illustrates the paver and tile casting process.

A hydraulic paver manufacturing machine received the homogeneous mix and formed specimens under controlled compaction pressure for paver production. Tile production transferred the mix to tile moulds (25 mm thickness), with moulds advancing on vibrating conveyor belts to ensure adequate compaction and surface finishing.

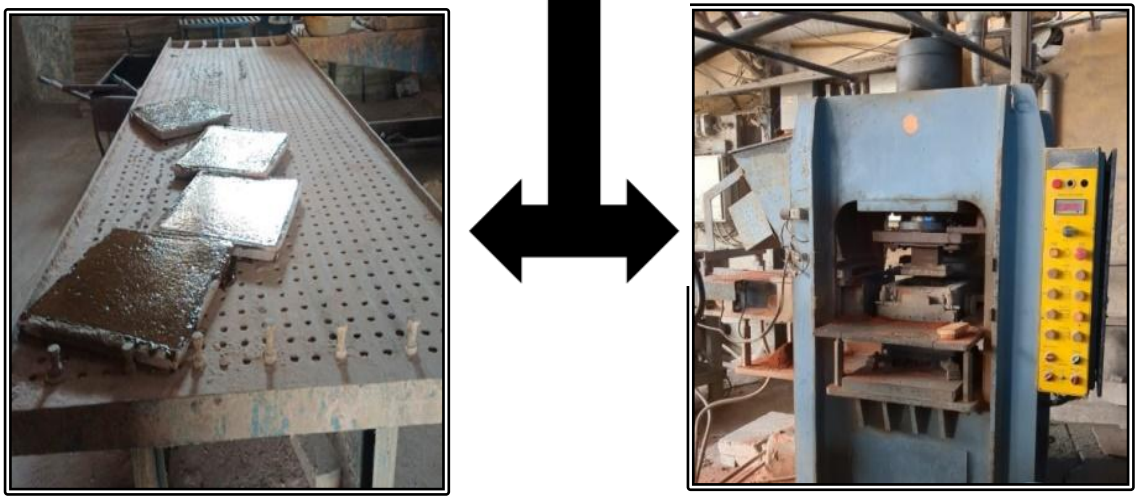


IOT Cement GGBS Crushed Stone Sand Aggregate

Material for paver and tiles



Mixing of material



Pressing mechanism for pavers **Vibration mechanism for tiles**

Figure 3.18: Process of casting paving blocks and tiles

Cool storage facility maintained freshly cast pavers and tiles prior to further processing. Demoulding of tiles occurred after 24 hours. Controlled curing by water immersion at

27 ± 2°C conditioned both pavers and tiles. Predetermined intervals (7 and 28 days) determined removal timing for the testing program. Figure 3.19 shows the cast paver with dimensions while Figure 3.20 shows the cast tile with dimensions.

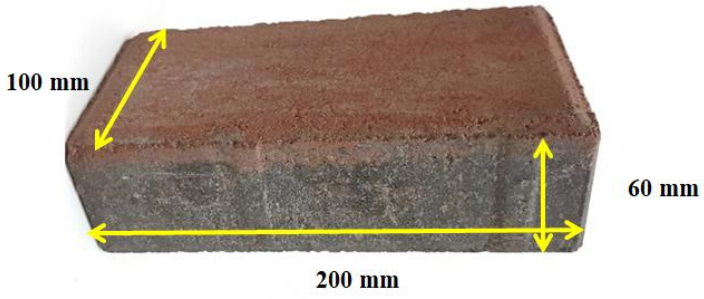


Figure 3.19: Cast paver with dimensions

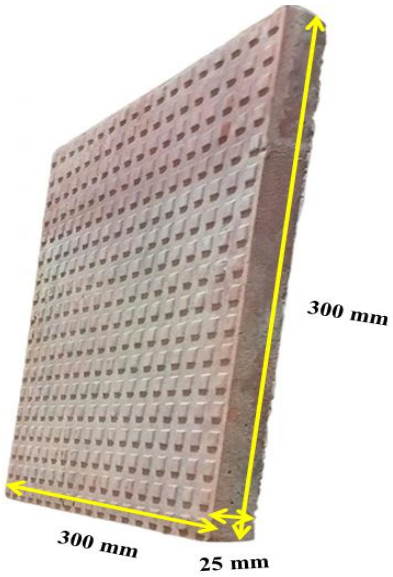


Figure 3.20: Cast tile with dimensions

3.14 Laboratory Investigations on Pavers

Relevant Indian Standards governed the comprehensive quality assessment of the manufactured pavers and tiles. The testing program encompassed dimensional verification, mechanical property evaluation, and durability assessment to ensure compliance with construction use requirements. Table 3.15 presents the list of tests carried out on cast paver samples.

Table 3.15: List of tests carried out on cast pavers

Test	Source	Sample Size (In Nos.)	Curing Age
Dimension	IS 15658 : 2021	4	28 days
Water Absorption		3	28 days
Compressive Strength		4	7, 28 days
Flexural Strength		4	28 days
Tensile Splitting Strength		4	28 days
Acid resistance test	Djamaluddin et al. (2020)	3	28

Controlled laboratory conditions at 23 ± 2°C maintained standardization throughout testing. Standard requirements determined sample sizes.

3.14.1 Length, width, and thickness measurement

Calibrated steel callipers performed dimensional measurements following systematic procedures. Length measurements across two opposite faces at two representative positions, and width measurements at three locations, were recorded. The digital callipers measured the thickness at four different positions to account for dimensional variations. Mean values were calculated and reported to the nearest 1mm for statistical analysis.

3.14.2 Water absorption

IS 15658:2021 procedures governed water absorption testing with systematic specimen preparation and testing protocols. Complete immersion in clean water at room temperature for 24 ± 2 hours achieved saturation. Following immersion, 10 mm wire-mesh drainage for exactly 1 minute, and standardized surface water removal. Careful removal of visible surface water using a damp cloth preserved absorbed water within the specimen's interior. Immediate weighing provided saturated mass (M2) to the nearest 0.01 N. Subsequently, oven-drying at 107 ± 7°C for a minimum of 24 hours continued until consecutive weighing at 2-hour intervals showed mass variation not exceeding 0.2% of previously determined specimen mass (M1). Equation 3.4 enabled water absorption calculation.

3.14.3 Compressive strength

IS 15658:2021 specifications guided the determination of compressive strength through proper specimen conditioning and testing procedures. Accurate determination of specimen area preceded testing. Specimens were stored in water at 20 ± 5°C for 24 ± 4 hours prior to testing. The specimen was aligned correctly to ensure uniform load distribution. Controlled axial loading without shock was applied at 15 ± 3 N/mm²/min until the maximum sustainable load or delamination occurred. Accurate recording of maximum applied load enabled strength calculations as per Equation 3.2.

3.14.4 Tensile splitting strength

The experimental configuration positioned the specimen to establish direct contact between the bearers and the packing pieces on the upper and bed faces, rigidly aligning the mechanical axes with the splitting section. A strict hierarchical protocol governed the identification of the fracture plane. The methodology primarily targeted the longest

splitting section parallel and symmetrical to the edges, necessitating that the lateral distance to any side face exceed 0.5 times the specimen thickness across 75 percent of the area. Figure 3.21(a) and (b) shows the testing setup.



(a) (b)

Figure 3.21: Tensile splitting strength of paver

The testing apparatus exerted a smooth, progressive load, strictly controlling the rate of stress increase to 0.05 ± 0.01 MPa. Recording of failure load (P) to the nearest 0.01 N enabled failure plane area calculation using:

$S = l \times t$ **..... (Eq. 3.8)**

Where: S = failure area (mm^2),

l = mean of two measurements of the failure length, one at the top and one at the bottom of the specimen, (mm)

t = mean of three measurements of thickness at failure plane (mm)

Tensile splitting strength calculation:

$T = 0.637 \times k \times (P/S)$ **..... (Eq. 3.9)**

Where: k: Shape/size correction factor

T = tensile splitting strength (MPa),

P = failure load (N)

3.14.5 Flexural strength

A three-point loading configuration employed in flexural strength testing positioned the specimen as a simple beam with mid-span loading through a roller placed between

supporting rollers. The load application without shock proceeded at a uniform rate of 6 kN/min until specimen failure occurred.

Recording of maximum applied load to the nearest N enabled breaking load determination and flexural strength calculation using:

$$\text{Flexural strength}, f_b = \frac{3Pl}{2bd^2} \quad \text{..... (Eq. 3.10)}$$

Where: f_b = flexural strength (N/mm²),

P = maximum load (N),

l = distance between centrelines of supporting rollers (mm),

b = average specimen width (mm),

d = average thickness at fracture line (mm).

3.14.6 Acid resistance test

Immersion in a 3% H_2SO_4 solution for 56 days evaluated the acid resistance of the 28-day-old paving blocks, following the method of Djamaluddin et al. (2020). Tap water washing removed the acid residues, while subsequent open-air drying brought the specimens to a constant weight. Finally, a compression testing machine quantified the compressive strength.

3.15 Laboratory investigations on tiles

Relevant Indian Standards governed the comprehensive quality assessment of the manufactured product. The testing program encompassed water absorption and wet transverse strength evaluation. Table 3.16 presents the list of tests carried out on cast tile.

Table 3.16: List of tests carried out on cast tiles

Test	Source	Sample Size (In Nos.)	Curing Age
Water Absorption	IS 13801 : 2013 Reaffirmed in 2021	4	28 days
Wet Transverse strength		3	28 days

3.15.1 Water absorption

Selecting six full-size tiles enabled water-absorption testing in accordance with standardized procedures. Immersion in clean water for 24 hours preceded removal and surface-drying with a clean cloth. Immediate weighing provided saturated mass measurements.

Subsequent oven-drying at 110 ± 5°C to constant mass, cooling to room temperature, and reweighing enabled the determination of the dry mass. Equation 3.4 enabled individual specimen water absorption calculation.

3.15.2 Wet Transverse Strength

A three-point loading configuration used in wet transverse strength testing positioned the specimens on two support rods, with the textured surfaces facing upward. Figure 3.22 illustrates the testing process. The projection of length 'l' beyond each support rod, with the central loading rod positioned equidistant between the supports, characterised the specimen's positioning.

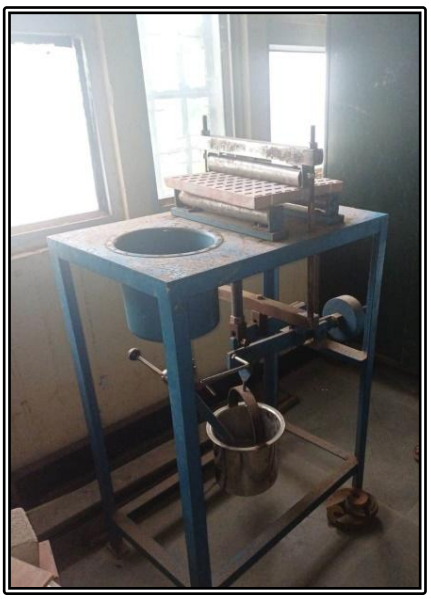


Figure 3.22: Wet transverse strength of tile

Controlled load application achieved a stress increase rate of 1 ± 0.2 N/mm²/s until specimen fracture occurred within the central portion equivalent to the loading rod diameter. Averaging of five acceptable test results provided the final strength determination.

The wet transverse strength f, calculation:

$$\text{Modulus of rupture } (\text{N/mm}^2)\text{ , f} = \frac{3\text{Pl}}{2\text{bt}^2} \qquad \textbf{..... (Eq. 3.11)}$$

Where:

P = Failure load (N),

l = Span between support (mm),

b = Tile width (mm),

t = Fracture thickness of the tiles measured from the fracture line (mm)

3.16 Mix design for cladding panels

The study explored an innovative approach that used IOTs as a sustainable, viable construction material for wall cladding. Mix proportions presented in Table 3.17 use mine waste to enhance the performance of cladding panels.

Table 3.17: Mix composition for wall cladding panels (all values in %)

Trial	Cementitious Content		Fine Aggregate		Fiber
	Cement	GGBS	IOT	Crushed Stone Sand	10 mm
C100G00T50F0	100	0	50	50	0
C080G20T50F0	80	20	50	50	0
C060G40T50F0	60	40	50	50	0
C100G00T50F1	100	0	50	50	1
C080G20T50F1	80	20	50	50	1
C060G40T50F1	60	40	50	50	1

*Note: Trial nomenclature indicates component percentages (C: Cement, G: GGBS, T: IOT, F: Fiber)

Cladding panel formulations varied in cement and GGBS contents while maintaining constant IOT and crushed stone sand fractions at 50% each by mass. The cement content decreased from 100% to 60% as the GGBS content increased from 0% to 40%. Cladding panel compositions follow the notation CxxGxxTxxFx, where C denotes Cement content, G denotes GGBS content, T denotes IOTs, and F denotes Fiber content.

Six trial mixes comprised the investigation: three without fiber (C100G00T50F0, C080G20T50F0, C060G40T50F0) and three with 1% fiber (C100G00T50F1, C080G20T50F1, C060G40T50F1).

Based on the material proportions, the process involved making standard 70.6 mm test cubes and cladding panels (0.25 m × 0.25 m × 0.01 m).

Dry mixing of cement, GGBS, IOT, crushed stone sand, and fiber was performed for 1 minute, followed by a gradual addition of water over 3–4 minutes. Moulds coated with a release agent receive a fresh mix, followed by vibration at 12,000 ± 400 rpm for 2 minutes, to eliminate entrapped air voids per IS 4031 (Part 6):1988 - Reaffirmed in 2019. Demoulding occurs after 24 hours, followed by immersion curing. The experimental casting phase generated 90 cubes across all mix designs and systematically distributed the specimens for testing at different ages. Compressive strength testing carried out as per IS 2250:1981- Reaffirmed in 2020, with strength

derived according to Equation 3.2. Systematic testing of three specimens per composition at 7, 28, and 56 days captures strength development patterns. Data from acid-resistance and water-absorption tests on specimens complete the product characterization.

3.17 Casting of cladding panels

A manufacturing facility executed the full-scale cladding panel casting upon the conclusion of cube testing, a process detailed in Figure 3.23. Controlled manufacturing conditions and specialized equipment at the facility enabled the production of panel cladding. Equation 3.1 determined the quantity of material required per cladding panel and the calculated constituents subsequently followed the mix design specified in result section, Table 4.40.

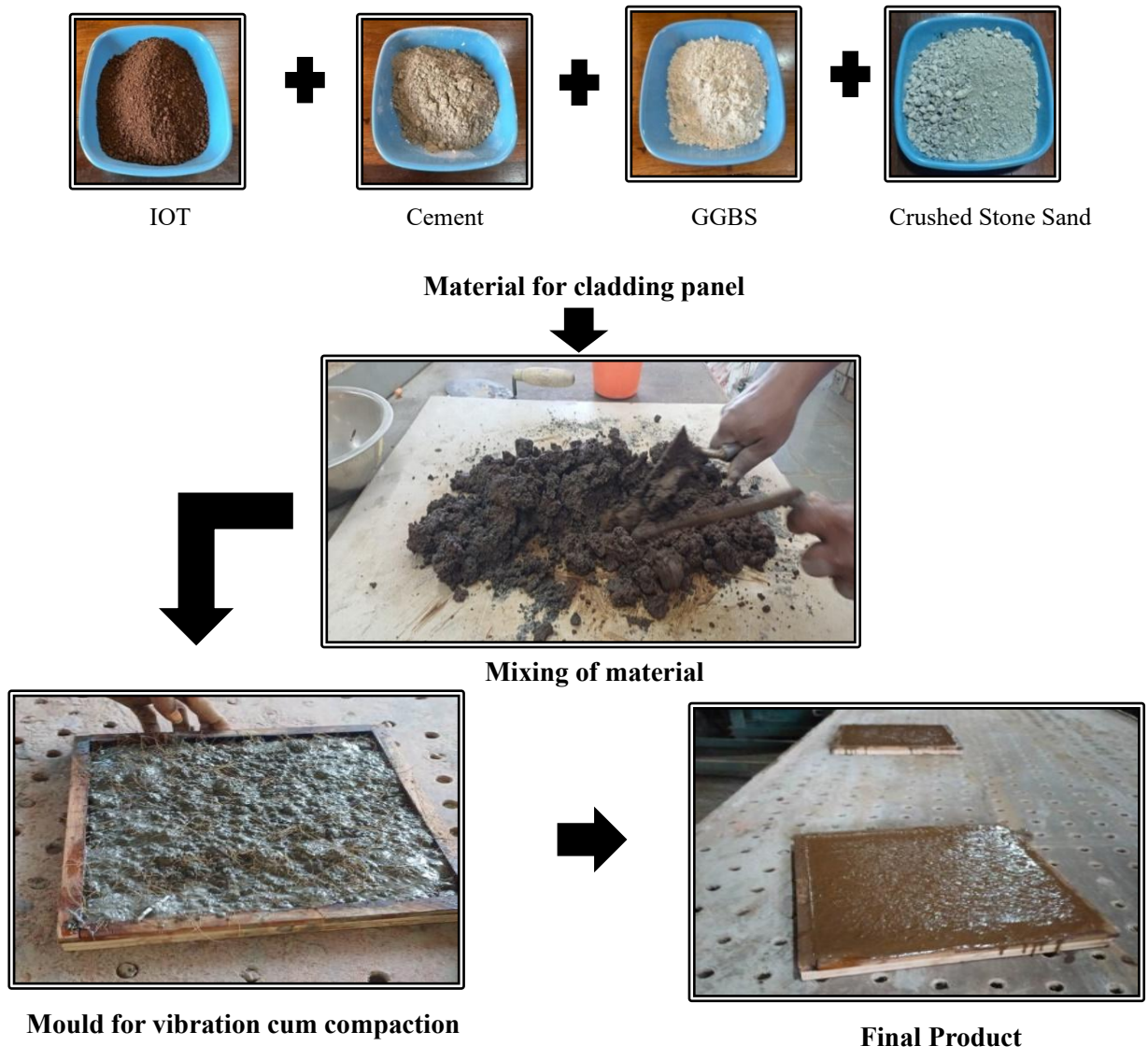


Figure 3.23: Cladding panel manufacturing process

The homogeneous mixture filled the pre-treated panel moulds to meet the dimensional requirements of wall cladding applications. Moulds were treated with demoulding agents to ensure smooth panel extraction and a high-quality surface finish.

The vibrating table, which operates at a consistent frequency of 3000 vibrations per minute, consolidates the cast panels. This controlled-vibration process eliminated air voids and achieved a uniform density distribution, producing a smooth surface finish.

Demoulding occurred after 24 hours, followed by controlled water curing at room temperature. This systematic curing protocol facilitated proper hydration and strength development, ensuring optimal mechanical properties and dimensional stability.

3.18 Laboratory investigations on cladding panel

Comprehensive quality assessment of manufactured cladding panels, following relevant testing standards, encompassed mechanical property determination, durability assessment, and thermal performance characterization to ensure suitability for construction applications.

Controlled laboratory conditions maintained standardization and characterization, with proper specimen conditioning and standardized procedures governing all evaluations. Cladding panel preparation included appropriate drying, conditioning, and handling protocols to ensure reliable, reproducible results. Table 3.18 presents the list of tests carried out on cast cladding panel

Table 3.18: List of tests carried out on cast cladding panel

Test	Source	Sample Size (In Nos.)	Curing Age
Compressive Strength	IS 2250: 1981 - Reaffirmed in 2020	3	28 days
Breaking Strength and Modulus of Rupture	IS 13630-Part 6: 2019	3	28 days
Thermal Conductivity		3	28 days
Rate of water absorption	Raj et al., 2021 & Aravind et al., 2019	3	28 days
Acid resistance		3	28 days

3.18.1 Thermal conductivity test

The QTM-710 portable thermal conductivity instrument performed thermal conductivity measurements after 28 days of curing, as shown in Figure 3.24. Oven-drying specimens prior to testing removed all moisture, ensuring accurate measurements.

The QTM-710 used a non-constant-heater wire method to determine thermal conductivity. Constant electrical power supplied to the probe caused the heater wire to heat exponentially. The logarithmic temperature-rise pattern indicates the thermal-conductivity characteristics of the sample: low-conductivity materials exhibit large temperature-rise angles, while high-conductivity materials exhibit smaller angles.



Figure 3.24: Thermal conductivity of cladding panel

Placement of the probe on the cladding specimen surface (dimensions: 250 mm × 250 mm) enabled recording thermal conductivity in W/m·K units. Four measurements taken at different locations on each panel accounted for potential variation, and the calculated mean served as the final value.

3.18.2 Breaking strength and modulus of rupture

A three-point loading test, configured in accordance with IS 13630 (Part 6): 2019, quantified the modulus of rupture and breaking strength. The experimental setup positioned the central rod equidistant from the support rods, ensuring direct contact with the panel surface. Simultaneously, the loading mechanism applied force at a stress increment of $1 \pm 0.2 N/mm^2$ Equations 3.12 and 3.13 define the calculations for breaking strength and modulus of rupture, respectively.

$$\text{Breaking strength} = \frac{FL}{b} \qquad \textbf{..... (Eq. 3.12)}$$

$$\text{Modulus of rupture} = \frac{3FL}{2bh^2} \qquad \textbf{..... (Eq. 3.13)}$$

3.18.3 Water absorption

The specimens underwent water absorption characterization after completing 28 days of curing and a minimum 24-hour drying phase at 110°C. A wax coating applied to all sides of the cubes, except the bottom surface, sealed the cubes, preventing air ingress

into the void during immersion. Initial cube weights were measured, with placement in containers ensuring that the top faces (as cast) made contact with water. Weight measurements at 15, 60, 240, and 1440 minutes documented the progression of water absorption. Equation 3.14 enabled calculation of average water absorption rate (A_T) in grams/100 cm²:

$$A_T = \frac{W_T - W_0 \times 10{,}000}{L_1 \times L_2} \quad \text{..... (Eq. 3.14)}$$

Where:

L_1 = average length of the test surface of the cube in mm

L_2 = average width of the test surface of the cube in mm

W_T= Weight of cube at time T in grams.

W_0 = Initial weight of cube in grams.

3.18.4 Acid resistance test

The acid resistance test employed 7.06 cm cubes following 28 days of curing. Immersion in 1% H_2SO_4 for 90 days preceded compressive strength testing. Strength attainment following acid immersion was calculated and compared with that of control specimens to assess material durability. Figure 3.25 shows the cube after undergoing acid resistance test.



Figure 3.25: Cube after undergoing acid test

3.19 Statistical analysis of cast products

The statistical analysis evaluated the physical, mechanical, and durability properties of various sustainable cast products, including bricks, blocks, pavers, tiles, and cladding panels. A systematic statistical methodology quantified experimental scatter, ensured reproducibility, and validated the significance of performance enhancements across different mix proportions.

3.19.1Experimental design and variables

A structured experimental matrix evaluated the individual and interactive effects of various binder and filler replacements on material properties. A structured experimental matrix was utilized to evaluate the individual and interactive effects of various binder and filler replacements on material properties. Systematic variations in binder systems and aggregate replacements, such as iron ore tailings (IOTs), are standard practice for optimizing sustainable concrete mixtures (Zhao et al., 2021).

- **Independent variables:** Systematic variations in binder systems and aggregate replacements drove the experimental design. For example, the paver mix design used a factorial design with three distinct cement dosage levels (100%, 80%, and 60%) and six IOTs replacement rates ranging from 0% to 50% in 10% increments. The tile investigation employed a similarly systematic matrix encompassing 18 distinct mix proportions.
- **Dependent variables:** Performance metrics quantified across the cast products encompassed 7-day and 28-day compressive strength, bulk/dry/wet density, water absorption, electrical resistivity, flexural strength, splitting tensile strength, wet transverse strength, thermal conductivity, breaking strength, modulus of rupture, and acid resistance.

3.19.2 Descriptive statistics and dispersion metrics

A comprehensive suite of descriptive statistics quantified the reliability and homogeneity of the experimental data across each test parameter. The methodology derived the following statistical indicators:

- **Mean and Standard Deviation (SD):** These metrics established the central tendency and the absolute dispersion of the test results for each mix proportion.
- **Standard Error of the Mean (SE):** This metric indicates the accuracy of the mean estimates; consistently low SE values ensure the sample means accurately reflect the broader population behavior.
- **Coefficient of Variation (COV):** As a primary indicator of material homogeneity and manufacturing consistency, the COV enables comparison of relative variability across diverse test parameters. Low COV values served as the benchmark, confirming robust quality control and reproducible production processes (Masi et al., 2019).

- **95% Confidence Intervals (CI):** Upper and lower 95% confidence bounds indicate the statistical reliability of the sample means.

3.19.3 Correlation and Regression Analysis

Bivariate correlation and linear regression analyses modelled relationships among different physical and mechanical properties. Applying statistical regression is a proven method for predicting the mechanical performance (such as compressive strength) of cementitious composites based on physical properties like water absorption (Okafor & Egbe, 2017).

- **Linear regression modelling:** Simple linear regression quantified the predictive relationship between independent and dependent performance variables. For example, regression equations in the form of $y = a + bx$ modelled the impact of water absorption on the wet transverse strength of tiles across different cement dosages .
- **Correlation Coefficients:** Pearson's correlation coefficient (r) and the Coefficient of Determination (R^2) assessed the strength and direction of these linear relationships. These metrics evaluated predictive accuracy and confirmed how variations in physical properties systematically compromised or enhanced mechanical strength (Reis et al., 2024).

3.19.4 Criteria for evaluating statistical significance and optimization

The derived statistical parameters guided the identification of optimal mix designs, alongside summarizing the data:

- **Statistical Significance:** Confidence intervals determined the statistical significance of competing mix designs. Specifically, non-overlapping confidence intervals for key performance metrics confirmed statistically meaningful differences and robust enhancements in material behavior (Revilla-Cuesta et al., 2020).
- **Material Optimization:** The optimal balance of materials (e.g., iron ore tailings, fly ash, and GGBS) emerged in mix compositions that exhibited superior mean performance metrics and minimal statistical variability (Gayana & Chandar, 2018).

3.20 Financial analysis of manufacturing of composite material

This section presents the methodology adopted to determine the manufacturing cost of the developed construction materials and to evaluate the overall economic feasibility of their production. A systematic, two-step approach estimated the cost of the

manufactured products, placing primary emphasis on raw material expenditure (Joyner & McGowan, 2024; Sitompul, 2019).

This structured framework enabled a comprehensive analysis of the financial dimensions involved, beginning with the assessment of raw material costs and culminating in an evaluation of the business viability of the proposed manufacturing unit (Saediman et al., 2014; Iqbal, 2016).

The production costs of the cast products, which varied by size and specifications, were calculated (Tempa et al., 2022; Sitompul, 2019). A business model evaluated the financial viability of the manufacturing process by incorporating key financial indicators derived from a projected income statement (Tarigan et al., 2018 ; Iqbal, 2016).The production costs were determined using data generated directly from experimental trials, thereby ensuring that the cost estimates reflected realistic operating conditions (Tempa et al., 2022 ; Sitompul, 2019).

The analysis relied on fundamental financial metrics that provide a quantitative basis for assessing a manufacturing operation's financial health and potential (Iqbal, 2016; Saediman et al., 2014). These metrics included revenue, operating expenses, profit margins, and return on investment (Saediman et al., 2014). A critical element of the financial analysis was the appropriate accounting of depreciation (Joyner & McGowan, 2024; Saediman et al., 2014). Although depreciation is a non-cash expense, it plays an essential role in accounting for the reduction in the value of assets over time. It thereby influences reported profits, tax liabilities, and other key financial indicators (Youssef et al., 2019).

Consequently, the assessment framework incorporated depreciation methods and their implications (Joyner and McGowan, 2024; Youssef et al., 2019). Furthermore, the described analytical framework dictates an annual implementation cycle (Saediman et al., 2014).

This periodic review enabled performance tracking against projections, identification of economic trends, and timely adjustment of operational and strategic decisions (Tarigan et al., 2018; Saediman et al., 2014). The primary data source for the financial analysis was the income statement, which provides a concise summary of revenues, expenditures, and earnings over a defined fiscal period (Joyner & McGowan, 2024).

It served as the central financial document for evaluating the manufacturing unit's economic performance and as the basis for all cost and payback period calculations.

3.20.1 Data collection framework

A comprehensive data-collection and analysis framework estimated the production costs of various products (brick, block, paver, tile, and cladding) (Tempa et al., 2022; Saediman et al., 2014). The methodology integrated primary and secondary data sources to capture the factors influencing cost, subsequently classifying the collected data into the following categories:

Direct material costs: Expenditures related to specific raw materials used in production, including both the quantity of each material required per unit of product and the corresponding unit cost (Joyner & McGowan, 2024; Sitompul, 2019).

Direct labour costs: Labour hours allocated to each stage of production, along with the associated wage rates (Joyner & McGowan, 2024; Sitompul, 2019).

Indirect manufacturing costs (overheads): A range of indirect expenses, including indirect materials (e.g., fuel), indirect labour (e.g., wages of support staff such as supervisors and maintenance personnel), and other indirect costs (e.g., utilities, rent, depreciation, property taxes, insurance, maintenance, administrative expenses, and regulatory permits) (Hafez et al., 2017; Iqbal, 2016).

The data collection protocol utilized a mixed-methods approach:

Direct observation (primary data): On-site facility inspections captured the manufacturing processes, documented material flows, assessed labour utilization and equipment operation, and revealed opportunities for cost optimization (Tempa et al., 2022 ;Sitompul, 2019).

Document review (secondary data): Existing company and project records were examined, including invoices for raw materials and services, employee payroll data, utility bills, daily production logs, and detailed financial statements (Iqbal, 2016;Saediman et al., 2014). Document analysis segregated fixed costs (e.g., rent, salaries, and equipment depreciation) from the variable costs (e.g., raw material consumption and energy usage) that fluctuate with production volume (Hafez et al., 2017).

A rigorous data validation procedure ensured the reliability of the results .The protocol cross-checked multiple data sources to verify consistency and reconciled plant log production volumes with financial record cost data (Sitompul, 2019; Saediman et al., 2014).Subsequent system reviews and financial audits validated the calculated unit costs.

3.20.2 Cost evaluation process for manufactured products

A two-step cost evaluation procedure established both the final production cost of the manufactured products and the specific cost contribution of raw materials.

Step 1: Product formulation and reference data

The first phase examined existing product formulations and characterized the constituent raw materials. Understanding the physical and chemical properties of the raw materials and their influence on the final product performance was essential. This step also involved compiling and documenting the specific mix designs of the developed products. The detailed understanding of material behaviour and interactions established the technical basis for subsequent cost calculations (Tempa et al., 2022).

Step 2: Calculation of initial cost

The second phase quantified raw material costs, initially establishing the unit price for each constituent (Joyner & McGowan, 2024). Subsequent calculations determined the direct material cost per cast product by multiplying the material quantities consumed during casting by their respective unit prices (Sitompul, 2019). The methodology subsequently accounted for actual labour costs and, finally, incorporated miscellaneous expenses (Saediman et al., 2014). By integrating detailed material characterization with precise cost estimation, the proposed framework simultaneously evaluated the technical and financial dimensions of each product component (Tempa et al., 2022).

3.20.3 Estimation of manufacturing unit setup costs

This phase systematically estimated all expenditures associated with establishing the manufacturing. A rigorous assessment was necessary to avoid underestimation of the total investment required.

The principal components considered were as follows:

1. Land and building costs

Land-related costs included the purchase price of the land and associated expenses such as legal fees, registration charges, and stamp duty. Site preparation costs, including levelling, clearing, and other essential groundwork, were also incorporated (Saediman et al., 2014).Building-related costs comprised the construction or acquisition of the factory building, including materials, construction labour, architect and consultancy fees, and renovation or modification expenses required to adapt the structure to operational requirements (Iqbal, 2016).

2. Machinery and equipment

Classification schemes divide capital expenditures on machinery and equipment into standard and specialized manufacturing categories (Saediman et al., 2014).Total costs comprise purchase prices of machines, tools, and auxiliary equipment, plus installation and commissioning expenses. Transportation charges and transit insurance augment the overall machinery and equipment investment (Iqbal, 2016).

3. Working capital

The initial working capital requirement extended beyond fixed capital investments and encompassed several critical components. Raw material and inventory costs covered the initial stock of raw materials, intermediate goods, and finished products, as well as storage and handling expenses (Saediman et al., 2014). Utilities and basic infrastructure costs included the connection and installation of essential services such as electricity, water, and communication facilities; labour-related costs comprised initial recruitment, training, and early-stage administrative and production salaries (Saediman et al., 2014; Tarigan et al., 2018).

3.20.4 Financial viability and payback period analysis

The payback period method assesses the financial soundness of the proposed investment (Tarigan et al., 2018).The payback period measures the time required for net cash inflows from operations to recover the initial investment (Youssef et al., 2019 ; Saediman et al., 2014). This method delivers simple, practical financial viability metrics and supports preliminary project evaluation.

1. Calculation of annual cash inflows

The annual net cash inflow was determined by estimating the expected annual sales revenue and subtracting the corresponding annual operating expenses, excluding depreciation. Net cash from core business activities generates this value annually and the expression derived from Youssef et al. (2019), adopts the form:

Annual Net Cash Inflow = Annual Sales Revenue − Annual Operating Expenses (excluding depreciation)

2. Payback period calculation

Constant annual net cash inflows prompt the calculation of the payback period by dividing the initial investment by the annual net cash inflow (Tarigan et al., 2018; Saediman et al., 2014).When projected annual cash inflows varied over time, the

payback period was determined by cumulatively summing the annual cash inflows until the total equalled the initial investment (Saediman et al., 2014). Partial-year recovery divides the year-start balance that remains unrecovered by that year's cash inflows to estimate the fractional period required for complete recovery (Youssef et al., 2019; Tarigan et al., 2018).

CHAPTER 4
RESULTS AND DISCUSSION

4.1 General

This chapter presents the experimental evaluation of utilizing iron ore tailings (IOT) integrated with ground granulated blast-furnace slag (GGBS), fly ash, cement, lime, ceramic waste, and aggregates. The experimental framework focused on the manufacture of composite products with enhanced properties for sustainable use in the construction industry. Detailed characterizations of the physical, chemical, mechanical, and durability properties of these materials guided the mix design optimization. The casting process utilized these formulated mixes to produce bricks, blocks, pavers, tiles, and cladding panels. Subsequent testing evaluated their compressive strength, water absorption, bulk density, and thermal conductivity. The analytical results confirm the feasibility of incorporating iron ore tailings as a primary component, support the establishment of quality standards and production protocols, and highlight the commercial viability of these sustainable materials for industrial applications.

The experimental mix design combined constituent materials, including Iron Ore Tailings (IOTs), Portland Cement, GGBS, Fly Ash, Lime, Ceramic Waste, Crushed Stone Aggregate, and 10 mm Basaltic Aggregates, to synthesize the final composite matrix. The subsequent sections explain the characterization and properties of each material constituent utilized in the casting of these construction products.

4.2 Materials used in casting of composites

Comprehensive analysis evaluated the constituent materials of the IOT composite products, and this section presents the corresponding characterization results.

4.2.1 Iron Ore Tailing (IOTs): A mining facility located in Dharbandora Taluka, South Goa district (latitude 15.3366411°N, longitude 74.2472719°E) provided the Iron Ore Tailings. A systematic analytical framework quantified the physical and chemical properties of the collected samples, resulting in the data presented in Table 4.1. The tested IOTs exhibited a specific gravity of 3.25, which is significantly higher than that of natural fine aggregates. Atterberg limits (liquid limit: 52.42%, plastic limit: 48.45%, shrinkage limit: 35.70%) indicated low plasticity and minimal volumetric changes upon

drying, providing favourable conditions for aggregate replacement. The testing apparatus recorded a water absorption rate of 22.00%, a metric that required careful consideration during the mix design phase.

Table 4.1: Physical and chemical properties of Iron Ore Tailings

Sr. No.	Parameter	Value
1	Specific gravity	3.25
2	Liquid limit, in %	52.42
3	Plastic limit, in %	48.45
4	Shrinkage limit, in %	35.70
5	Water absorption, in %	22.00
6	Fe, % by mass	44.12
7	SiO_2, % by mass	17.90
8	Al_2O_3, % by mass	5.80
9	MnO, % by mass	1.40
10	P, % by mass	0.04
11	TiO_2, % by mass	0.27
12	Na_2O, % by mass	0.02
13	K_2O, % by mass	0.17
14	CaO, % by mass	0.02
15	MgO, % by mass	0.13
16	S, % by mass	0.02
17	LOI, % by mass	11.66

The particle size distribution curve of iron ore tailings shows an extremely fine material, with particle sizes predominantly in the micron range and very low coarser fractions. The logarithmic x-axis scales in micrometres, while the distribution curve shows a gradual increase in the finer percentage up to approximately 1 μm. The passing fraction then increases steeply from roughly 1 to 5 μm, ultimately reaching a 100% finer threshold near 8 to 10 μm. Figure 4.1 illustrates the particle size distribution of IOTs used in this study.

At very small sizes (below approximately 0.5 μm), only a small fraction of the material is finer, indicating a limited colloidal-size content. Beyond this, there is a continuous increase in the cumulative percentage finer, suggesting a well-graded but ultra-fine

distribution within the silt and clay-size range, which is consistent with tailings generated from the beneficiation of iron ore.

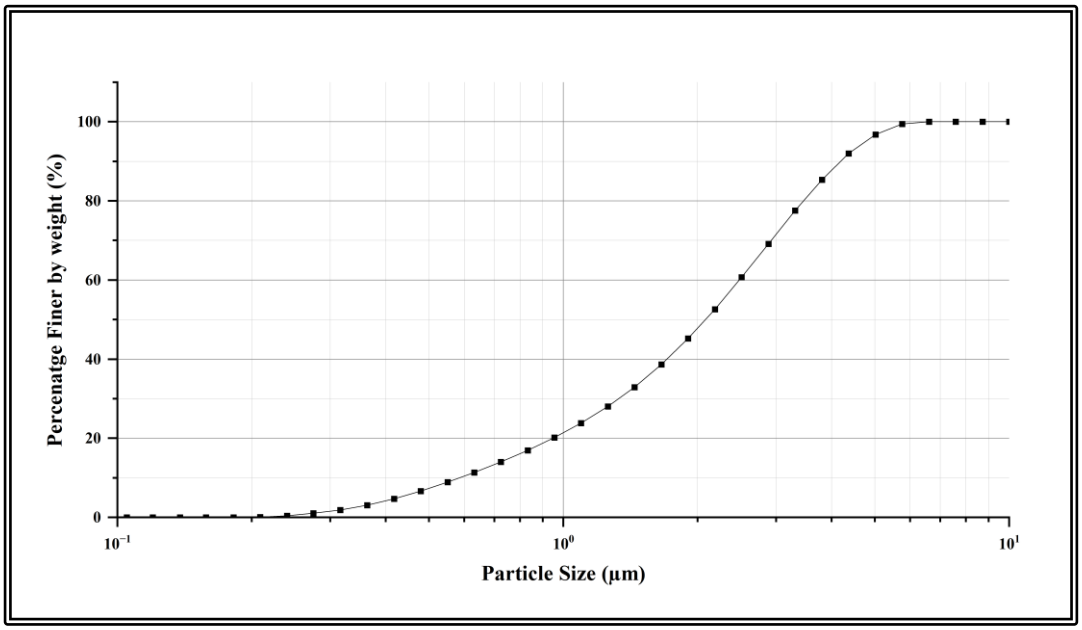


Figure 4.1: Particle size distribution of IOTs

XRF analysis revealed iron (44.12%) and silicon dioxide (17.90%) as the primary constituents, alongside alumina (5.80%) and manganese oxide (1.40%) as secondary phases. The compositional analysis determined the Fe_2O_3 content to be 63.09%. Trace elements, including phosphorus, titanium dioxide, alkali oxides, and sulphur, appeared in negligible concentrations. The Loss on Ignition (LOI) value of 11.66% reflected hygroscopic moisture and residual organic material. The low sulphur content (0.02%) and the absence of deleterious substances confirmed the IOTs chemical stability and suitability for concrete applications.

These analytical findings align with existing literature. Previous investigations (George, 2023) examining IOT as a partial fine aggregate replacement in M20-grade concrete had a specific gravity of 2.65, indicating a denser, finer material than natural sand. The material's particle-size distribution showed a higher proportion of fine particles, which reduced workability but increased packing density. Chemically, the prior composition contained significant proportions of iron oxide (Fe_2O_3:57.57%) and silica (SiO_2: 9.59%), with minor amounts of alumina and magnesia influencing the hydration reaction and strength development. Similarly, related compositional studies (Fontes et al., 2018) identified iron, silica, and alumina as the dominant oxides in IOTs (Fe_2O_3: 49.0%, SiO_2:

40.1%, Al_2O_3: 8.9%), with negligible levels of sulphates (0.1%). Historical data (Aruna & Kumar, 2010) show that specific tailings exhibit a specific gravity of 2.95 and consist predominantly of silica (SiO_2: 68.61%) and iron oxide (Fe_2O_3: 25.88%), alongside minor constituents such as alumina, magnesia, and calcium oxide. These characteristics contributed to improved compressive strength in modified mixes. Furthermore, crystallographic assessments (Filho et al., 2017) identified IOT as fine, dense, and crystalline, composed mainly of silica (63 ± 9%), iron (35 ± 5%), and alumina (1.2 ± 0.9%). Figure 4.2 illustrates the XRD diffractogram of IOTs.

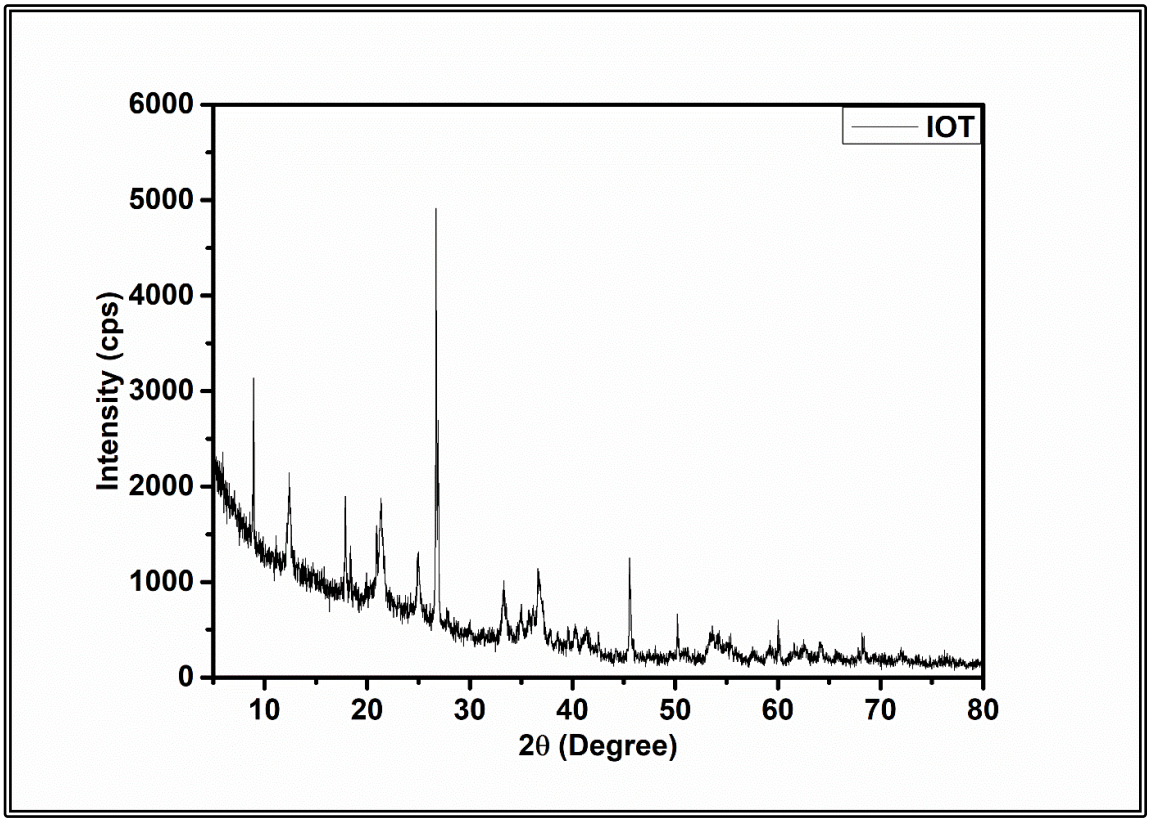


Figure 4.2: XRD diffractogram of IOTs

X-ray diffraction (XRD) analysis, using Cu Kα radiation, was performed on the IOTs over a 2θ range of 10° to 80°. The resulting diffractogram yields a mixed crystalline-amorphous profile, characterizing typical mining by-products generated during iron extraction processes. A high-crystalline Quartz fraction, coupled with low baseline noise, denotes a low-reactivity material. These specific material characteristics restrict optimal IOT application to non-structural fills or partial aggregate replacement (up to 20–30% substitution) in mortars, thereby averting significant strength degradation.

A broad amorphous hump spanning ~20° to 35° 2θ (intensity ~2000–3000 cps) delineates the siliceous and aluminosilicate glassy residues produced during ore processing. This disordered structure (FWHM ~10°–15°) accounts for approximately 30–50% of the sample volume. The inherent amorphous phase drives the material's potential reactivity within alkali-activated systems or geopolymers via pozzolanic or filler effects.

Sharp crystalline peaks, primarily originating from siliceous gangue minerals and iron oxides, superimpose the amorphous baseline. A dominant, sharp reflection at ~26.6° 2θ (~5000 cps) confirms the presence of α-quartz (trigonal, JCPDS 46-1045), constituting ~40–60% of the sample. Secondary quartz reflections manifest at ~20.8° (100 plane, ~1500 cps), ~36.5° (110 plane, ~1000 cps), ~39.5° (102 plane, ~800 cps), ~50.1° (112 plane, ~1000 cps), ~59.9° (211 plane, ~600 cps), and ~68.3° (203 plane, ~500 cps). Distinct peaks located at ~33.1° (104 plane, ~1500 cps, trigonal, JCPDS 33-0664) and ~53.5° (116 plane, ~500 cps) establish the presence of hematite.

Reflections emerging at ~35.4° (311 plane, ~1200 cps, cubic, JCPDS 19-0629), ~43.1° (400 plane, ~600 cps), and ~62.6° (440 plane, ~400 cps) verify magnetite constituents.

Low-intensity signals indicate minor contributions from mullite, resolving as a shoulder at ~16.4° 2θ, alongside Kaolinite remnants at ~12.4° 2θ (<500 cps).While the qualitative profile identifies the primary phases governing the IOT's mechanical value and environmental behaviour (e.g., leaching potential), advanced phase quantification necessitates Rietveld refinement. This methodology precisely determines exact phase compositions (e.g., Quartz ~50%, Hematite ~15%, Magnetite ~10%, Glass ~20%, trace others ~5%). Furthermore, these quantitative metrics facilitate direct correlation with toxicity assessments (such as TCLP) and mechanical tests, thereby optimizing IOT utilization within sustainable composites. XRD analysis confirmed the presence of quartz, Hematite, and Kaolinite, demonstrating that IOT typically exhibits low water absorption, high density, and stable, non-hazardous chemistry.

4.2.2 Cement: A local supplier provided 53-grade Ordinary Portland cement (OPC). Standardized testing protocols evaluated various parameters and presented the final results in Table 4.2. The utilized cement exhibited physical and chemical properties falling well within the prescribed limits set by the relevant Indian Standard Codes. These metrics consistently align with values reported in contemporary literature.

Table 4.2: Physical and chemical properties of Cement

Sr. No.	Parameter	Value
1	Fineness in m^2/kg (Blaine air-permeability)	323
2	Soundness in mm (Le Chatelier method)	1.0
3	Setting Times in min	Initial : 125 Final: 210
4	Standard Consistency in % (Vicat apparatus)	29
5	Specific Gravity	3.14
6	Density in g/cc	3.14
7	CaO,% by mass	62.5
8	Lime Saturation Factor $\frac{CaO - 0.7\,SO_3}{2.8\,SiO_2 + 1.2\,Al_2O_3 + 0.65\,Fe_2O_3}$	0.89
9	$Al_2O_3$to Fe_2O_3 Ratio	1.09
10	Insoluble Residue, % by mass	1.24
11	Magnesia (MgO), % by mass	1.21
12	Total Sulphur Content (SO_3), % by mass	2.40
13	Loss on Ignition, % by mass	2.99
14	Chloride (Cl), % by mass	0.015
15	Alkali Content (as Na_2O), % by mass	0.36

For example, corresponding chemical analyses (Farooq et al., 2023) indicate a CaO content of 62.5%, an Al_2O_3 to Fe_2O_3 ratio of 1.55, and a standard consistency of 30%. Similarly, physical property evaluations (Kumar et al., 2019) observed a specific gravity of 3.12, an initial setting time of 110 minutes, a final setting time of 220 minutes, and a standard consistency of 30%. Further compositional documentation (Mendes et al., 2021) indicates an Al_2O_3:Fe_2O_3 ratio of 1.44, a CaO content of 61.99%, and a specific gravity of 3.12. These comparative metrics reinforce that the cement used in this research meets both regulatory standards and contemporary literature benchmarks, ensuring the reliability and validity of the assessed material characteristics. Figure 4.3 presents the XRD diffractogram of Cement.

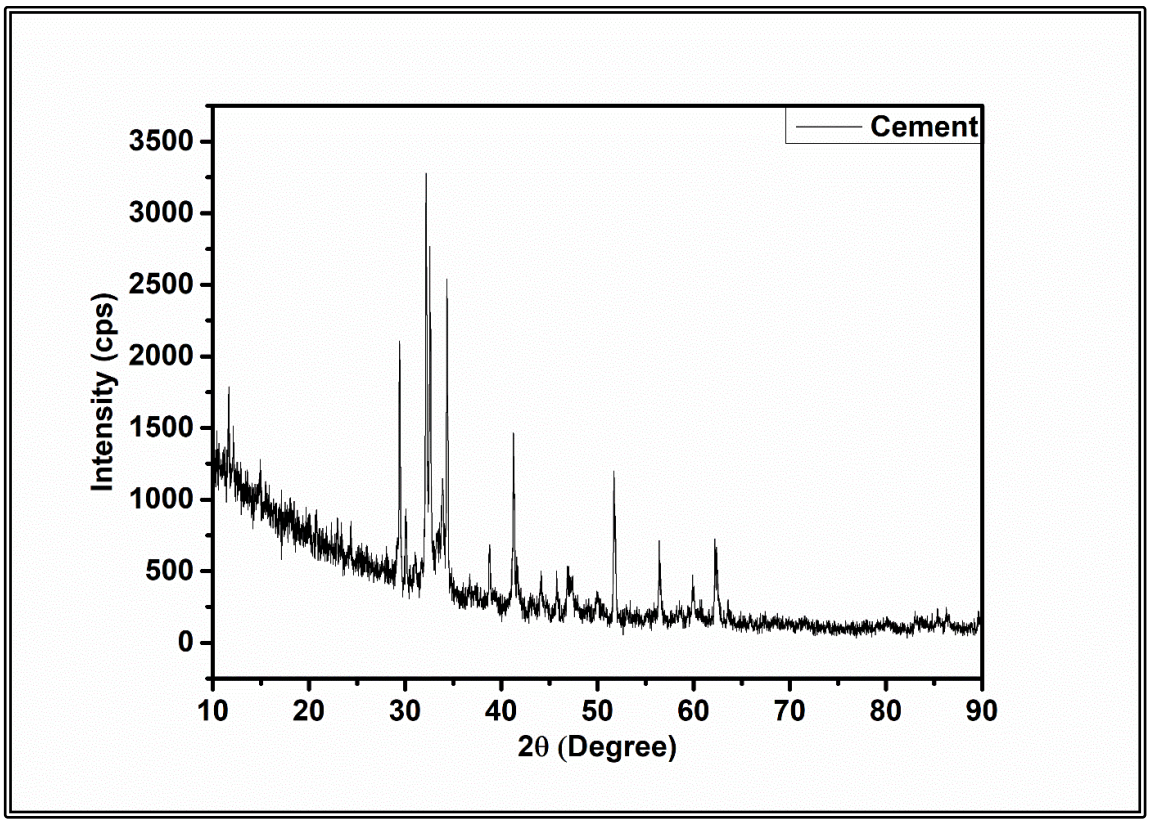


Figure 4.3: XRD diffractogram of Cement

The X-ray diffraction (XRD) pattern of the cement, recorded over a 2θ range of 10° to 90° using Cu Kα radiation, exhibited characteristic peaks indicative of an ordinary Portland cement (OPC) composition. The analyzed Cement sample primarily comprised clinker phases such as tricalcium silicate (alite, C_3S), dicalcium silicate (belite, C_2S), tricalcium aluminate (C_3A), tetracalcium aluminoferrite (brownmillerite, C_4AF), and minor sulfate phases, such as gypsum.

The most prominent peak, observed at approximately 29.5° 2θ (intensity ~3200 cps), corresponded to the overlapping (211) and (300) reflections of alite, with additional contributions from the (021) plane of gypsum. Adjacent shoulders and peaks at ~32.2° (alite and belite), 34.4° (alite), and 51.7° (alite) further confirmed the dominance of alite. As is well established, alite typically accounts for 50–70% of OPC clinker and imparts early strength development.

Peaks at ~33.2° and 33.8° correspond to the cubic aluminate and orthorhombic ferrite phases, respectively, which dictate setting behaviour and durability. Furthermore, lower-intensity peaks at ~11.6° (gypsum, (020)) and 20.7° (gypsum, (021)), alongside scattered minor reflections between 18°–28° and 40°–60°, indicate the presence of bassanite or anhydrite sulfates and potential trace impurities such as Quartz or Calcite.

Overall, the pattern displayed relatively low baseline noise, indicating good crystallinity, with no evidence of amorphous humps or unreacted raw materials, which **is** consistent with a well-burned clinker.

4.2.3 Ground Granulated Blast-Furnace Slag (GGBS): The composite design incorporated GGBS as a supplementary cementitious material to enhance durability, reduce the heat of hydration, and improve the long-term strength of the final products. Table 4.3 presents the test results for the GGBS used in this study.

Table 4.3: Physical and chemical properties of GGBS

Sr. No.	Parameter	Values
1	Fineness m^2/kg	397
2	Specific Gravity	2.81
3	Calcium Oxide (CaO) %,% by mass	37.63
4	Silicon dioxide (SiO_2)% ,% by mass	34.81
5	Aluminum Oxide (Al_2O_3) ,% by mass	17.92
6	Manganese Oxide (MnO),% by mass	0.12
7	Magnesium Oxide (MgO) %,% by mass	7.83
8	Sulphide Sulphur,% by mass	0.51
9	Sulphate,% by mass	0.24
10	Insoluble Residue,% by mass	0.29
11	Chloride content,% by mass	0.009
12	Glass content,% by mass	92.00
13	Loss on ignition,% by mass	0.18
14	$\frac{CaO+MgO+1/3\ Al_2O_3}{SiO_2+2/3\ Al_2O_3}$	1.11
15	$\frac{CaO+MgO+Al_2O_3}{SiO_2}$	1.94

Physical and chemical testing thoroughly characterized the GGBS, confirming its conformity with Indian Standard IS 16714:2018. The material exhibited a fineness of 397 m^2/kg and a specific gravity of 2.81; both values provide favourable conditions for supplementary cementitious applications and support elevated replacement ratios. Chemical analysis revealed an optimal composition, with CaO (37.63%) and SiO_2 (34.81%) acting as the primary reactive components, while Al_2O_3 (17.92%) and MgO (7.83%) remained within standard limits. Deleterious constituents registered at

negligible levels, with sulphide sulphur (0.51%), sulphate (0.24%), insoluble residue (0.29%), chloride (0.009%), and LOI (0.18%) all falling substantially below the IS limits.

The measured glass content of 92.00% ensures optimal pozzolanic activity for the formation of secondary calcium silicate hydrate (C-S-H). The measured fineness of 397 m^2/kg substantially exceeds the IS 16714:2018 minimum requirement of 320 m^2/kg, driving superior reactivity. Although the theoretical framework confirms that increased fineness yields higher strength (Fathollah & Hashim, 2011), real-world manufacturing constraints often prevent the commercial realization of this optimal fineness. Microstructural assessments (Jinpeng et al., 2019) indicated that composite particle structures, in which finer particles surround larger ones, enhance strength development. Figure 4.4 presents the XRD diffractogram of GGBS.

X-ray diffractometry captured the diffraction (XRD) pattern of the ground granulated blast furnace slag (GGBFS) sample over a 2θ range of 10° to 80°. The resulting diffractogram shows a predominantly amorphous structure, characteristic of rapidly quenched slag from iron production. This low-crystalline fraction and minimal baseline noise indicate a high-quality GGBFS that aligns with ASTM C989 standards (Grade 100 or 120). These material characteristics validate the slag's suitability for partial cement replacement (20–50% by mass) in sustainable concrete applications.

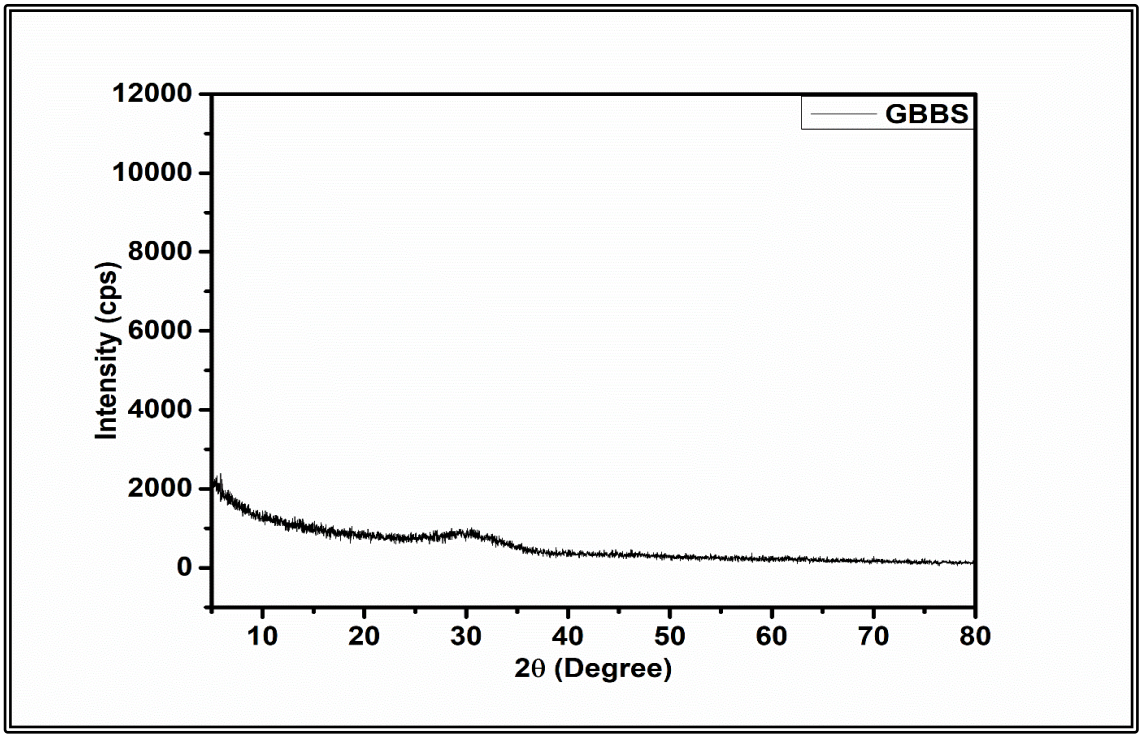


Figure 4.4: XRD diffractogram of GGBS

A broad, diffuse hump spanning approximately 20° to 40° 2θ, with a peak intensity of ~3000 cps centered at ~30°, dominates the profile. This feature represents the amorphous vitreous phase, comprising the glassy aluminosilicate matrix (~80–95% by volume). The disordered short-range order of this phase (FWHM ~15°–20°) drives the hydraulic reactivity of the slag upon alkali or portlandite activation in blended cement matrices.

Several minor crystalline peaks punctuate the amorphous halo, signalling the presence of trace residual phases typical of blast furnace processes. A sharp, prominent reflection at ~26.6° 2θ (~2000 cps) indicates residual α-quartz (SiO_2, trigonal, JCPDS 46-1045), constituting approximately 5–10% of the sample due to silica impurities. Secondary, low-intensity quartz peaks emerge at ~50.1° (112 plane, ~400 cps), ~59.9° (211 plane, ~300 cps), and ~68.3° (203 plane, ~200 cps). A minor peak at ~36.5° 2θ (~500 cps) exhibits overlapping reflections from Quartz (110) and Mullite (210) ($3Al_2O_3 \cdot 2SiO_2$, orthorhombic, JCPDS 15-0776). A minor shoulder defining the ~31°–32° 2θ region suggests trace amounts of akermanite ($Ca_2MgSi_2O_7$, tetragonal, JCPDS 35-0755).

While the qualitative XRD profile confirms the material's viability as a supplementary cementitious material, precise phase quantification necessitates a Rietveld refinement. This advanced analytical step establishes accurate assessments of the glass content (~90%), Quartz (~5%), and mullite (~3–5%) fractions. Correlating these exact fractions with reactivity indices (e.g., ASTM C1073) directly optimizes mix designs for geopolymers or high-volume slag blends.

4.2.4 Fly ash: The IOT composite mixes incorporated fly ash, a pozzolanic by-product from coal combustion in thermal power plants.

The tested fly ash exhibited an average fineness of 325 m²/kg, exceeding the minimum requirement of 320 m²/kg as specified in IS 3812 (Part 1): 2013 - Reaffirmed in 2022 and demonstrating an adequate specific surface area for effective pozzolanic reactions. This fineness value aligns with the 368 m²/kg value reported by Moghaddam et al. (2019). At this fineness, the fly ash exhibited negligible impact on early-age calcium hydroxide consumption (at 1 and 7 days), while driving a significant enhancement by 28 days. Table 4.4 summarizes the fly ash characterization test results.

Table 4.4: Physical and chemical properties of Fly ash

Sr. No.	Parameter	Value
1	Fineness , m^2/kg	325
2	Residue by wet basis on 45µ ,% by mass	23.1
3	Specific Gravity	2.6
4	Soundness by Autoclave ,% by mass	0.08
5	Loss on Ignition, % by mass	3.10
6	Insoluble Residue, % by mass	72.00
7	SiO_2+Al_2O_3+Fe_2O_3 (Min), % by mass	88.95
8	SiO_2 (min), ,% by mass	56.61
9	Al_2O_3 ,% by mass	27.54
10	Fe_2O_3 ,% by mass	4.80
11	CaO (Max), ,% by mass	5.00
12	MgO (Max), ,% by mass	0.60
13	SO_3 (Max), ,% by mass	0.40
14	Na_2O (Max), ,% by mass	0.70
15	Total Chlorides,% by mass	0.02

Khushal et al. (2017) identified fineness as the most critical parameter governing fly ash performance characteristics, including workability, bleeding, and segregation, emphasizing the importance of consistent fineness values for reliable concrete quality control and commercial viability.

The present sieve analysis yielded a 45-µm sieve residue of 23.1%, falling substantially below the IS 3812 (Part 1): 2013 - Reaffirmed in 2022 maximum permissible limit of 34%. Such a retention rate positions the utilized fly ash within the lower end of the classified material variability range (5–34%). Furthermore, the measured 23.1% residue closely aligns with the 17.66% retention value reported by Elmrabet et al. (2019); consequently, both values demonstrate robust compliance with standard specifications.

The lower residue value of 23.1% indicates superior particle fineness and a higher proportion of spherical particles, thereby enhancing workability and optimizing filler effects within the cement matrix. The utilized fly ash exhibited an average LOI value of 3.10%, demonstrating full compliance with the IS 3812 maximum permissible limit of 5%. This value establishes a substantial margin below the upper threshold and sits

significantly lower than the international specification range of 3–6%, confirming superior quality characteristics.

Chen et al. (2019) recorded LOI values of 4.62% and 7.78%, revealing considerable variability in fly ash LOI across different sources. Concurrently, researchers examined fly ash with LOI values of 5% and 8%, establishing relationships between LOI variation and corresponding changes in concrete properties across multiple cement replacement levels. In contrast, according to Ngo et al. (2018), durability assessments of high-LOI fly ash (15.8%, exceeding ASTM standards) demonstrate that substantially elevated LOI does not severely compromise long-term concrete performance under sulfate exposure. Consequently, the utilized low-LOI fly ash (3.10%) curtails adverse effects on admixture efficiency and strength development, thereby facilitating a reliable assessment of its intrinsic pozzolanic contributions to the cementitious system.

The fly ash exhibited a soundness value of 0.08%, substantially lower than the IS 3812 maximum permissible limit of 0.2%, indicating excellent dimensional stability and minimal risk of expansive reactions. This value is marginally lower than comparable data reported by Aaron et al. (2018), which reported a soundness value of 0.1% in investigating the free lime (CaO), sulfates, and periclase (MgO) constituents responsible for undesirable volumetric changes in hardened concrete. The significantly low soundness value of 0.08% demonstrates superior material stability, ensuring that undesirable volumetric changes are highly unlikely during the extended service life of concrete incorporating this specific fly ash.

The evaluated fly ash exhibited a combined content of $SiO_2 + Al_2O_3 + Fe_2O_3$ of 88.95%, significantly exceeding the IS 3812 minimum requirement of 70% for Class F fly ash and confirming strong pozzolanic characteristics. This compositional value falls within the ranges recorded in mechanical property studies by Young et al. (2019) investigating Class F fly ash with combined contents ranging from 80.6% to 89.7% (with corresponding CaO contents of 2.5% to 6.2%), which yielded 28-day compressive strengths of 41.1 to 51.5 MPa. The present CaO content of 5.00% aligns with this same range, classifying the material as low-calcium (Class F) fly ash with excellent long-term pozzolanic activity potential.

In a comparative chemical analysis by Gyu et al. (2016), which documented SiO_2 of 53.0%, Al_2O_3 of 20.7%, Fe_2O_3 of 6.94%, CaO of 6.17%, and LOI of 4.93%, yielding a 28-day compressive strength of 51.5 MPa, the present fly ash composition demonstrates

similar reactivity potential. The present silica content of 56.61% and alumina content of 27.54% indicate comparable glass content and hydraulic properties.

Chemical composition parameters intrinsically govern long-term (91-day) strength development more decisively than early-age (28-day) strength. This time-dependent correlation corroborates the established literature on the kinetics of the progressive pozzolanic reaction. Figure 4.5 shows the XRD diffractogram of Fly ash.

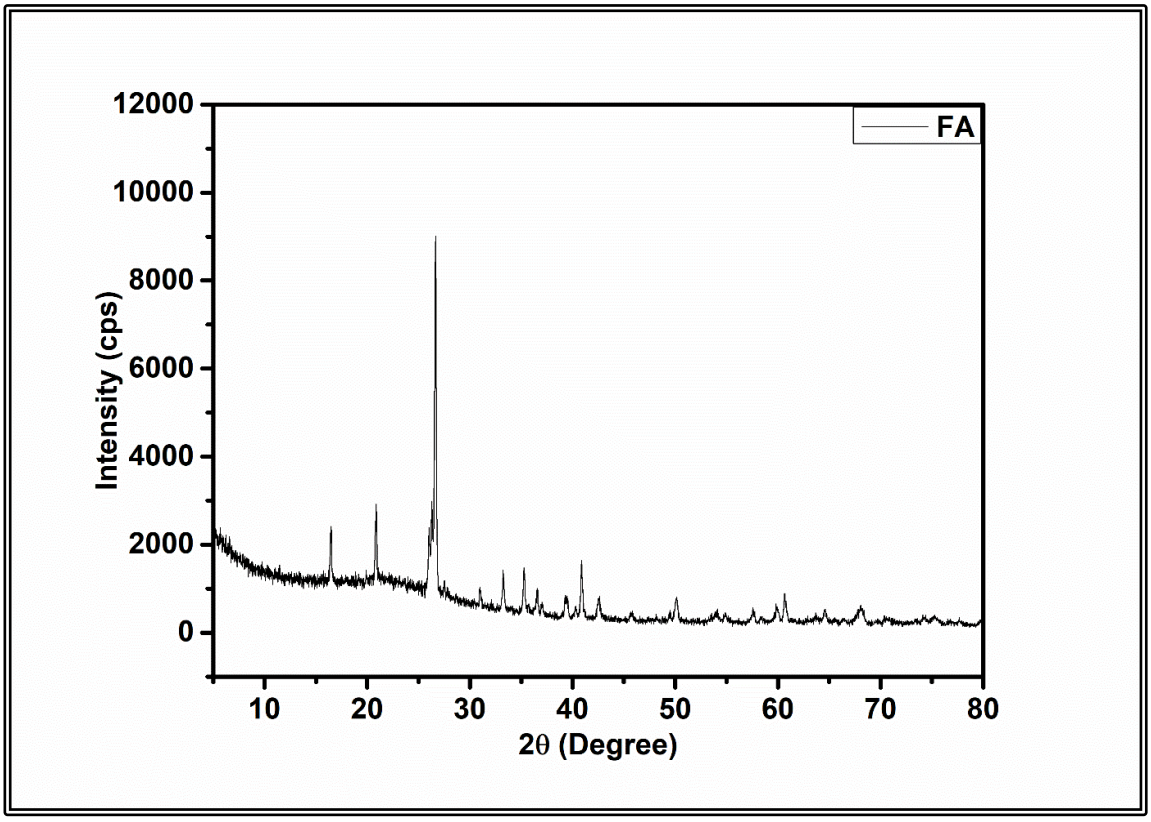


Figure 4.5: XRD diffractogram of Fly Ash

The X-ray diffraction (XRD) pattern of the fly ash (FA) sample, obtained over a 2θ range of 10° to 80°**,** exhibited a predominantly amorphous structure typical of Class F fly ash (a low-calcium, siliceous type derived from bituminous coal combustion). The construction industry widely uses this supplementary cementitious material to enhance concrete durability, reduce permeability, and promote sustainability by mitigating alkali-silica reactions and sulfate attack through its pozzolanic activity.

A broad, diffuse hump centered at approximately 20°–35° 2θ (peak intensity ~4000–6000 cps, labeled as Amorphous Glassy Phase) dominated the spectral profile. This prominent feature indicated the presence of vitreous aluminosilicate glass (~60–80% by volume), which drives the material's reactive potential during hydraulic binding with

calcium hydroxide to form secondary calcium silicate hydrate (C-S-H) gels. Furthermore, this amorphous feature, characterized by a full width at half maximum (FWHM) of ~10°–15°, underscores small crystallite domains and a disordered structure that contribute to long-term strength gain in blended cements.

Superimposed sharp crystalline peaks further characterized the XRD profile. The Quartz (101) crystallographic plane produced the most prominent peak at ~26.6° 2θ (~11,000 cps), confirming α-quartz (SiO_2, trigonal, JCPDS 46-1045) as a major inert phase (~10–20%). Secondary reflections at ~20.8° (Quartz (100), ~2000 cps), ~39.5° (Quartz (102), ~1000 cps), ~42.5° (Quartz (200), ~800 cps), ~50.1° (Quartz (112), ~1200 cps), and ~68.3° (Quartz (203), ~600 cps) provided additional confirmation of this quartz content. Overlapping reflections occurred at ~36.5° (~1500 cps) due to the coincident Quartz (110) and Mullite (210) planes ($3Al_2O_3 \cdot 2SiO_2$, orthorhombic, JCPDS 15-0776), and at ~59.9° (~800 cps) due to the Quartz (211) and Hematite (110) planes (minor hematite Fe_2O_3, trigonal, JCPDS 33-0664).

These minor peaks suggested the presence of additional trace minerals, such as magnetite (Fe_3O_4 at ~35.5° if resolved) or unburned carbon residues. However, the low intensity of these trace peaks, combined with the absence of broad organic humps**,** implied a high-quality, low-LOI (loss on ignition) fly ash suitable for partial cement replacement (up to 30–50% by mass) without compromising workability.

Ultimately, the pattern's low baseline noise and the calculated crystalline fraction (~20–30%) aligned with ASTM C618 standards for pozzolans. Utilizing such compliant materials enhances environmental benefits by diverting coal combustion by-products from landfills. Moving forward, precise determination of phase proportions (e.g., glass ~70%, Quartz ~15%, mullite ~10%, oxides ~5%) necessitates quantitative Rietveld refinement. These quantitative refinements will ultimately correlate with reactivity tests (e.g., Chapelle or ASTM C311) to inform optimized mix designs for sustainable concretes or geopolymers.

4.2.5 Lime: Lime performs an essential function in composite design by activating pozzolanic materials, accelerating hydration, improving microstructure, enhancing durability, reducing overall binder cost, and optimizing the reactivity of constituent materials, including the iron ore tailings.

The tested lime demonstrated a specific gravity of 2.2, indicating a relatively low density compared to OPC, which benefits lightweight brick production. The specific surface area of 147 m^2/kg reflects the lime powder's high fineness, providing sufficient surface area for hydration reactions and pozzolanic interactions with supplementary cementitious materials. Table 4.5 presents the chemical composition and physical properties of the lime powder used in this study.

Table 4.5: Physical and chemical Properties of Lime

Sr. No.	Parameter	Value
1	Specific Gravity	2.2
2	SiO_2, in %	0.27
3	CaO , in %	57.19
4	MgO , in %	1.50
5	Al_2O_3 , in %	0.23
6	Fe_2O_3, in %	0.35
7	Loss on ignition , in %	41.65
8	Specific surface area, in m^2/kg	147

Chemical composition analysis revealed calcium oxide (CaO) as the predominant constituent, accounting for 57.19% of the total mass and serving as the primary reactive component. The silica content (SiO_2) was 0.27%, confirming the lime's high purity and minimal siliceous impurities. Magnesium oxide (MgO) constituted 1.50%, contributing marginally to the cementitious properties of the material. The alumina content (Al_2O_3) registered at 0.23%, while iron oxide (Fe_2O_3) accounted for 0.35%. A Loss on Ignition (LOI) value of 41.65% indicates the presence of residual hydroxides and carbonates, typical of lime powder derived from limestone calcination. This LOI aligns with hydrated lime ($Ca(OH)_2$) rather than quick lime (CaO), suggesting the lime underwent partial hydration prior to testing.

The lime powder's low specific gravity, high LOI, and predominant CaO content render it an effective alkali source for pozzolanic activation while maintaining the chemical purity requisite for sustainable brick manufacturing with industrial waste materials. The characterized properties align well with values reported in the existing literature, particularly confirming the structural and chemical parameters established by Jung et al.

(2018), Mageed et al. (2012), and Algin &Turgut (2008), thereby validating the quality of the material used in this research.

X-ray diffractometry analysis characterized the lime sample over a 2θ range of 10° to 80° is presented in Figure 4.6. The resulting diffractogram exhibits sharp crystalline peaks that confirm the predominant presence of quicklime (calcium oxide, CaO, cubic structure, space group Fm-3m, JCPDS 37-1497).

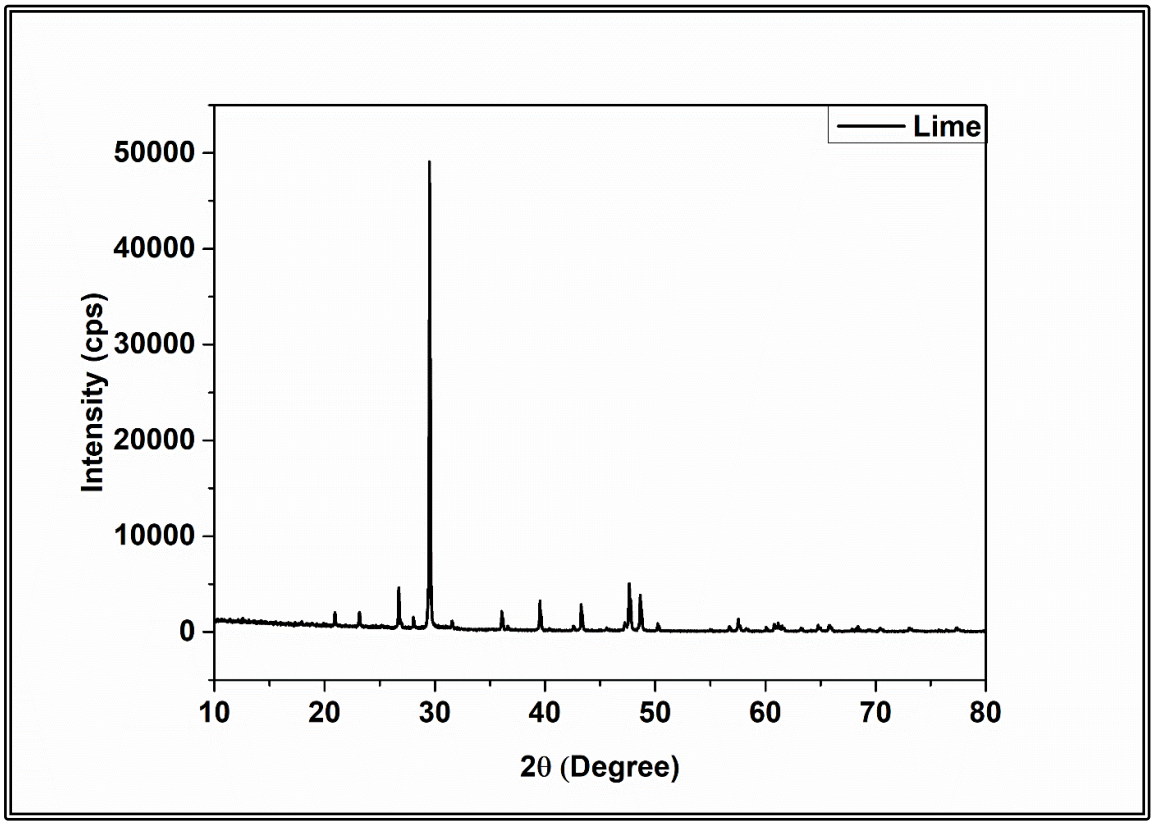


Figure 4.6: XRD diffractogram of Lime

Narrow peak widths signify large crystallite sizes, directly validating high phase purity and excellent material crystallinity. These fundamental structural characteristics render the sample a highly reactive precursor for construction materials (e.g., mortar, plaster, and soil stabilization). Within these applications, the CaO phase undergoes exothermic hydration to precipitate hydrated lime ($Ca(OH)_2$). The diffractogram precisely resolves characteristic CaO reflections, dominated by high-intensity crystallographic signals. A dominant peak at ~37.4° 2θ (intensity ~48,000 cps) corresponds directly to the (200) crystallographic plane. Additional sharp peaks manifest at ~32.2° (111 plane), ~53.9° (220 plane), ~64.2° (311 plane), ~67.4° (222 plane), and ~79.5° (400 plane). Low-intensity minor peaks and structural shoulders at ~18° and ~34° 2θ signal trace

impurities within the predominantly pure (~95% CaO) matrix. These minor diffractogram signals isolate two specific trace constituents: Distinct reflections at 18.1° (001 plane) and 34.1° (101 plane) evidence partial hydration. Ambient atmospheric moisture exposure during sample handling or storage drives this localized phase transformation.

Residual signals expose trace remnants of unreacted calcite. Incomplete calcination of the initial limestone feedstock accounts for this surviving mineral fraction. High phase purity, operating in tandem with a minimal trace impurity profile, directly governs the material's functional performance. These defined phase characteristics strongly dictate subsequent slaking reactivity, carbonation resistance, and ultimate mechanical property evolution within synthesized mortars or concretes.

4.2.6 Ceramic Waste: Ceramic waste, derived from discarded tiles during construction and industrial manufacturing processes, presents a significant environmental challenge due to its extremely slow degradation rate. However, using ceramic waste as a concrete aggregate replacement diverts material from landfills while conserving natural resources through circular-economy applications. Table 4.6 provides the characterization test results for the ceramic waste.

Table 4.6: Physical and chemical properties of ceramic waste

Sr. No.	Parameter	Value
1	Specific Gravity	2.25
2	Average Water absorption, in %	9.00
3	Uncompacted Bulk density, in kg/m^3	1090
4	Compacted Bulk density, in kg/m^3	1265
5	Loss on Ignition, % by mass	1.80
6	SO_3, % by mass	0.40
7	SiO_2, % by mass	60.30
8	Al_2O_3, % by mass	17.60
9	Fe_2O_3 , % by mass	4.00
10	CaO , % by mass	2.40
11	MgO, % by mass	4.20

The evaluated ceramic waste demonstrated substantial promise as a lightweight, sustainable constituent for composite concrete development. Testing established a specific gravity of 2.25, significantly lower than that of conventional mineral aggregates

such as granite (2.65–2.75). This measurement of 2.25 closely aligns with the findings of Pincha &Arnon (2010), who reported a specific gravity of 2.31 for similar ceramic waste aggregates. At a 50% replacement level, this reduced density directly translates to a 3.1–3.4% lower unit weight in the finished composites. This reduction lowers the structural dead load, enabling more economical design solutions without compromising mechanical performance.

Workability assessments substantiate the practical implementation viability of this material. Pincha & Arnon (2010) established, based on prior workability tests, that a 50% ceramic waste substitution maintains an acceptable slump of 110 mm (comparable to the control Portland cement concrete). In contrast, a 100% replacement triggers severe degradation, resulting in a 5 mm slump.

The rough, angular morphology of the ceramic particles significantly increases inter-particle friction and water demand. Consequently, a 50% substitution threshold serves as a practical upper limit t maintain workability while still harnessing the material's lightweight properties and strength-enhancing benefits. The bulk density measurements obtained in this study validate the reliability of the ceramic waste characterization. The uncompacted density of 1.09 g/cm³ and compacted density of 1.265 g/cm^3 align closely with literature benchmarks as evaluated by Yiosese et al., (2018) who reported an uncompacted density of 1.042 g/cm^3 and a compacted density of 1.217 g/cm^3, while studies by Daniyal & Ahmad, (2015) documented a compacted density of 1.325 g/cm³. The approximately 175 kg/m³ difference between the uncompacted and compacted densities reflects the particle void structure and packing efficiency, critical parameters that influence water demand and rheological properties.

Ceramic tile waste exhibits higher water absorption than natural aggregates, with 9% in the present study compared to 12.12% reported by Bikash et al. (2020). While this porosity necessitates a proportionally higher water-to-cement ratio to meet the increased water demand, the retained moisture provides beneficial internal curing during binder hydration. This internal curing helps reduce drying shrinkage and enhances early-age strength, offering a crucial advantage for the IOT-integrated mixes evaluated in this study. Supporting this performance benefit, Awoyera et al. (2018) demonstrated that substituting 100% of the fine aggregate with ceramic waste increases overall compressive strength by 22.1%. Chemical analysis revealed that the ceramic waste is a silica-dominant pozzolanic material. The 60.30% silica content reacts with the calcium

hydroxide produced during OPC hydration, generating C-S-H gels that elevate long-term strength and durability. A complementary alumina content of 17.60% further enhances reactivity by forming calcium aluminate hydrate. The combined pozzolanic constituents (SiO_2 + Al_2O_3 + Fe_2O_3 = 81.90%) substantially exceed the 80% minimum threshold specified by regulatory guidelines (Valéria & Ana, 2011), confirming the material's suitability for cementitious applications.

The secondary components present in the ceramic waste pose minimal risk as magnesium oxide (4.20%) remains within safe limits; calcium oxide (2.40%) contributes marginally to reactivity; a critically low sulfate content (SO_3 = 0.40%) eliminates the risk of delayed ettringite formation; and a low LOI (1.80%) confirms minimal organic matter presence. Figure 4.7 shows the XRD diffractogram of Ceramic waste.

The X-ray diffraction (XRD) pattern of the ceramic waste (CW) sample, scanned over a 2θ range of 10° to 80°, exhibited predominantly sharp crystalline peaks. These peaks indicated Quartz (α-SiO_2, trigonal structure, space group $P3_221$, JCPDS 46-1045) as the primary phase. Such silica-rich components likely originate from discarded tiles, bricks, or pottery, which the construction industry commonly recycles as partial cement replacements or aggregate fillers to enhance sustainability and reduce landfill waste.

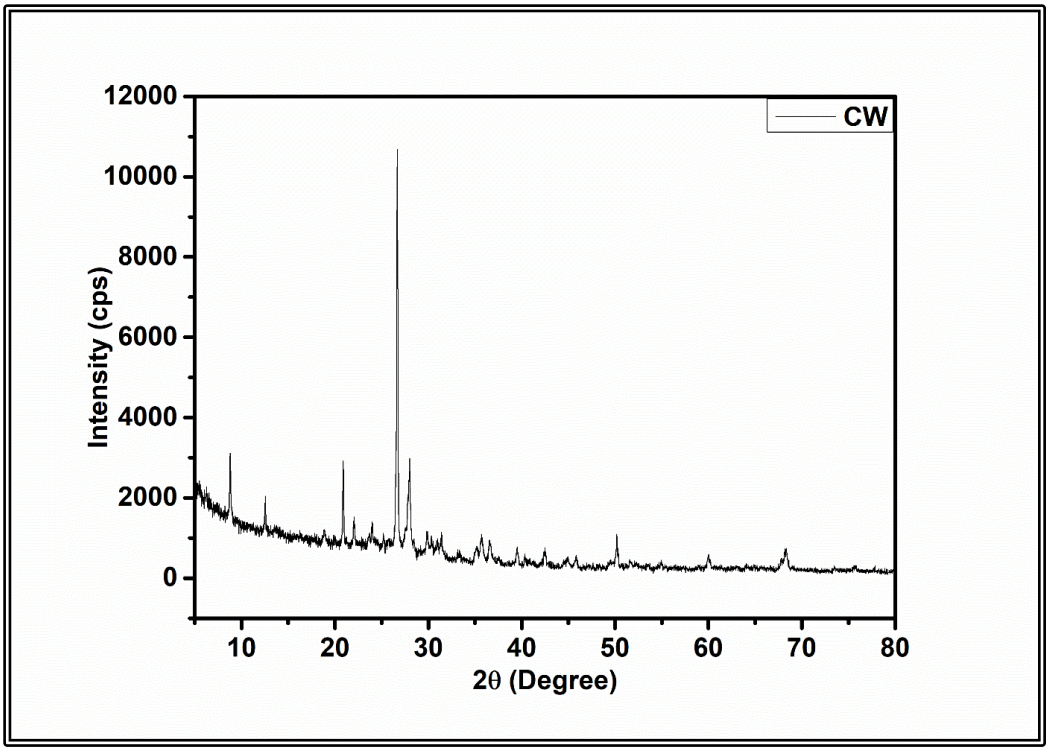


Figure 4.7: XRD diffractogram of Ceramic waste

The (101) crystallographic plane produced the most intense peak at approximately 26.6° 2θ (intensity ~11,000 cps), which dominated the spectral profile. Furthermore, secondary reflections at ~20.8° (Quartz (100), ~8000 cps), ~36.5° (Quartz (110), ~2000 cps), ~39.5° (Quartz (102), ~1500 cps), ~42.5° (Quartz (200), ~1000 cps), ~45.8° (Quartz (111), ~800 cps), ~50.1° (Quartz (112), ~1500 cps), ~59.9° (Quartz (211), ~1000 cps), and ~68.3° (Quartz (203), ~800 cps) confirmed a high quartz content, estimated at >90%. Narrow peak widths reflected excellent crystallinity and, through the Scherrer approximation, suggested crystallite sizes of 50–100 nm, alongside minimal amorphous phases from vitrified ceramics. Minor peaks or shoulders around 27°–28° (such as the potential feldspar (002) reflection at ~27.5°, ~500 cps) and scattered low-intensity reflections (e.g., ~54.9° for Quartz (202), ~400 cps) indicated trace impurities. These impurities include alkali feldspars, such as orthoclase or albite derived from clay raw materials, or trace mullite ($3Al_2O_3 \cdot 2SiO_2$), although the characteristic (110) reflection at ~16.4° remained absent in this specific profile. The presence of such components, typical in ceramic waste from fired kaolinitic clays, can influence pozzolanic reactivity when ground and incorporated into cementitious matrices, thereby improving compressive strength and reducing permeability. Ultimately, the low baseline noise and the absence of broad humps implied a well-crystallized, low-glass-content waste suitable for value-added reuse in eco-friendly concretes or mortars. However, precise phase quantification (e.g., Quartz ~95%, feldspar ~3–5%) and the assessment of potential leaching risks or hydration contributions necessitate quantitative Rietveld refinement. Future refinements will then correlate with mechanical tests to generate optimized mix designs.

4.2.7 Fine and Coarse Aggregates: Crushed stone aggregate, produced through the mechanical crushing of quarried rocks, behaves distinctly differently from naturally weathered gravel. Its angular, rough-edged particles facilitate superior mechanical interlocking, thereby enhancing the structural performance of composite matrices.

Particle size distribution classified the crushed stone aggregates used in this study into two distinct categories: (i) fine aggregates comprising particles smaller than 4.75 mm, and (ii) coarse aggregates retained on a 4.75 mm sieve.

Systematic testing procedures characterized and evaluated these aggregates, detailing the results in Tables 4.7 and 4.8.

Table 4.7: Physical and chemical properties of fine aggregates

Sr. No.	Parameter	Value
1	Bulk Density, Kg/m^3	1630 (Loose) 1860 (Compacted)
2	Specific Gravity	2.78
3	Water Absorption, in %	3.50
4	Silt clay & fine dust, in % by mass	2.36
5	Soundness (after 5 Cycles) , % Loss in wt. (With Sodium Sulphate)	3.10
6	Alkali Aggregate Reactivity	
a)	Dissolved Silica, in millimoles/litre	23.53
b)	Reduction in Alkalinity, in millimoles/litre	123.24
7	Water soluble Chloride (as Cl^-), in % by mass	0.009
8	Sulphate (as SO_3), in % by mass	0.017

Table 4.8: Physical properties of coarse aggregates

Sr. No.	Parameter	Values
1	Bulk Density	1450 (Loose) 1580 (Compacted)
2	Specific Gravity	2.80
3	Water Absorption, in %	0.80
4	Combined Flakiness & Elongation Index,	16.20
5	Flakiness Index, in %	8.05
6	Elongation, in %	8.15
7	Aggregate Crushing Value, in %	13.1
8	Aggregate Impact Value, in %	8.5
9	Aggregate Abrasion Value, in %	17.7

Figure 4.8 and 4.9 illustrates the particle size distribution curves of crushed stone sand and 10mm coarse aggregate

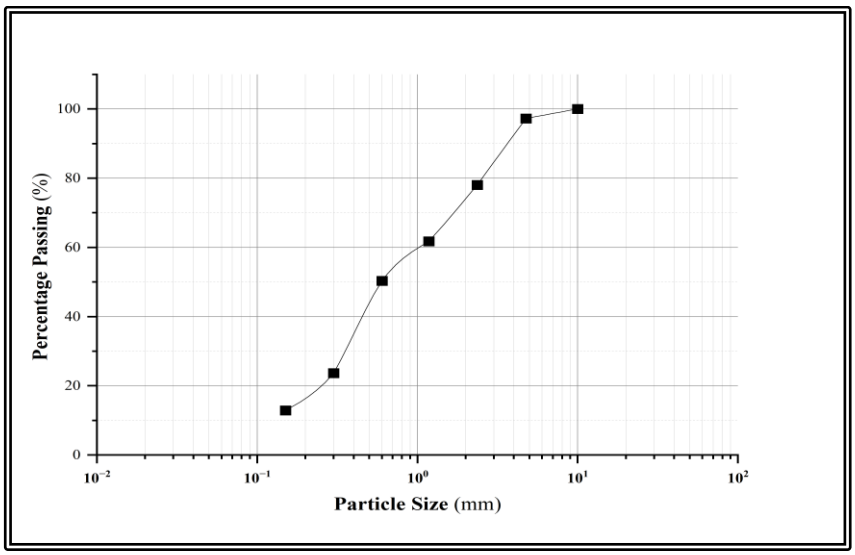


Figure 4.8: Particle size distribution of crushed stone sand

A semi-logarithmic plot illustrates the particle-size distribution of crushed stone sand, mapping particle diameter (mm) on a logarithmic axis against passing percentage on a linear axis. The measured gradation spans approximately 0.075 to 10 mm. Within this spectrum, the cumulative passing fraction steadily increases from a baseline of 12.9% at the 0.15 mm to 100% at the upper boundary. The intermediate points on the curve show about 23.7%, 50.3%, 61.8%, 78.1%, and 97–100% passing at successively larger sieve sizes, reflecting a continuous, relatively well-graded sand. The absence of abrupt steps in the curve indicates that the CSS does not exhibit pronounced gap grading, and the material contains a balanced proportion of fine and coarse sand fractions, which is favourable for achieving a dense particle packing in mortar and concrete mixes.

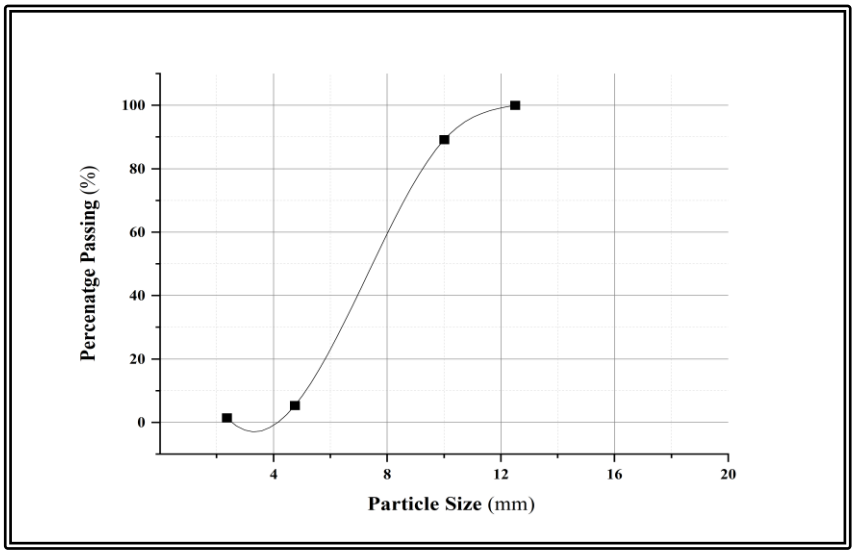


Figure 4.9: Particle size distribution of 10 mm aggregate

The data points indicate that only a small fraction passes the lower sieve (around 4.75 mm). In contrast, about 60–90% passes through the intermediate sieves before the curve flattens near full passing at the nominal maximum size. This behaviour is typical of a single-sized coarse aggregate with a 10 mm nominal maximum size, limited fines, and a narrow size band, which supports good workability control and predictable packing when combined with finer fractions.

The tested coarse aggregate exhibited bulk density values of 1450 kg/m^3 in the loose state and 1580 kg/m^3 in the compacted state, while the fine aggregate displayed values of 1630 kg/m^3 and 1860 kg/m^3, respectively. Hydrometer analysis determined specific gravities of 2.80 for the coarse aggregate and 2.78 for the fine aggregate. The density differential between the loose and compacted conditions reached 130 kg/m³ for the coarse aggregate and 230 kg/m³ for the fine aggregate, indicating superior packing efficiency in the finer fraction. These parameters serve a critical function in mix design optimization, as they directly influence void content and particle distribution. Favourable packing characteristics drive the strength development and durability of concrete composites.

The coarse aggregate exhibited water absorption of 0.80%, indicating superior durability. The fine aggregate demonstrated water absorption of 3.50%, with a silt, clay, and fine dust content of 2.36% by mass; both values comply with IS 383 limits. These characteristics ensure acceptable workability and require minimal adjustments to water demand during composite production.

The fine aggregate demonstrated structural soundness, with a 3.10% mass loss after five sodium sulphate cycles, indicating excellent resistance to weathering and freeze-thaw degradation. An alkali-aggregate reactivity assessment revealed a dissolved silica content of 23.53 millimoles per litre and an alkalinity reduction of 123.24 millimoles per litre.

Chemical characterization showed a chloride concentration of 0.009% by mass and a sulphate content of 0.017% by mass, both remaining significantly below the IS 383 limits of 0.05%. These analytical values confirm that the aggregate lacks deleterious compounds, ensuring structural durability and corrosion resistance in chloride and sulphate-exposed environments.

The coarse aggregate exhibited a combined flakiness and elongation index of 16.20%, with individual flakiness and elongation indices of 8.05% and 8.15%, respectively.

These results indicate favourable morphological properties, characterized by a minimal presence of flat and elongated particles. Mechanical strength assessments revealed aggregate crushing values of 13.1%, impact values of 8.5%, and abrasion values of 17.7%, demonstrating excellent resistance to mechanical stress and environmental degradation. These low values further confirm superior durability and packing efficiency.

All tested physical and mechanical properties of the aggregates comply with the requirements specified in Indian Standard IS 2386 (Methods of test for aggregates for concrete) and IS 383 (Coarse and fine aggregates from natural sources for concrete). The aggregates thus meet all quality criteria for utilization in the production of the experimental composites. Figure 4.10 shows the XRD diffractogram of Crushed Stone Sand.

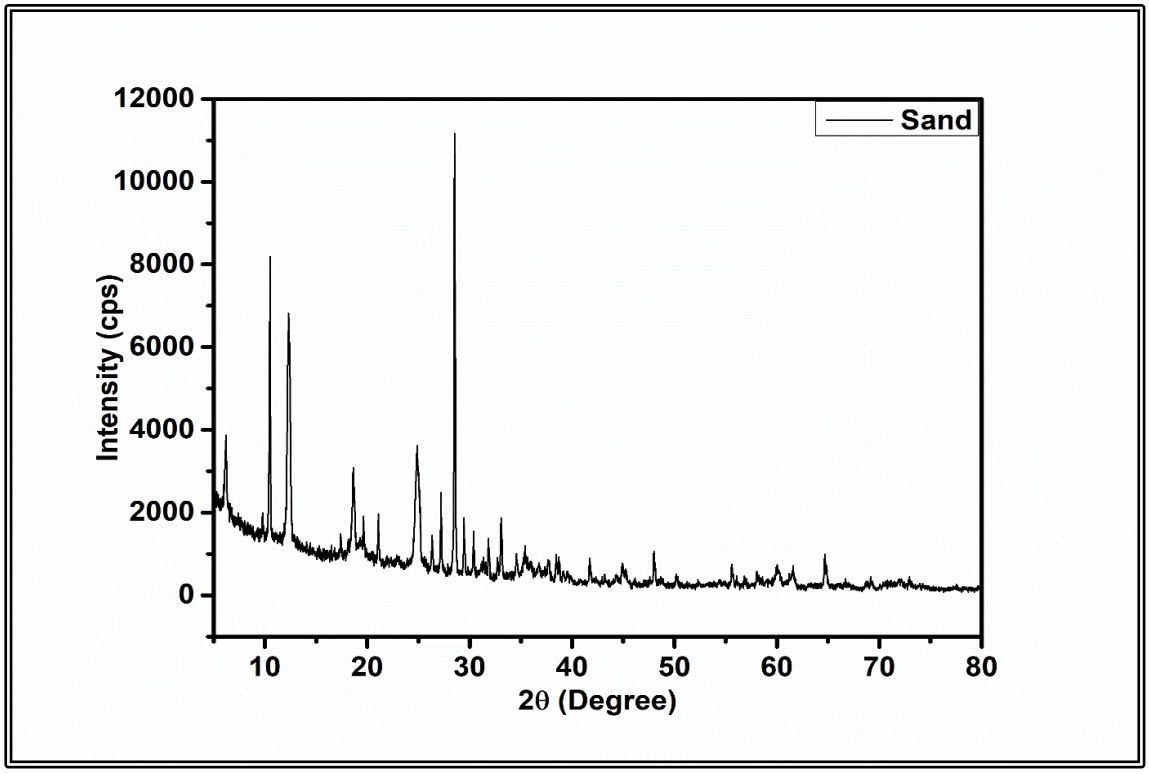


Figure 4.10: XRD diffractogram of Crushed Stone Sand

X-ray diffraction (XRD) analysis characterized the Crushed Stone Sand (CSS) sample across a 2θ range of 10° to 80°. The resulting diffractogram predominantly features sharp, high-intensity peaks defining crystalline Quartz (α-SiO_2, trigonal structure, space group $P3_221$, JCPDS 46-1045). This dominant mineralogical profile reflects the aggregate's direct derivation from crushed granitic or quartzitic source rocks.

Functioning as a fine aggregate replacement for river sand, this high-purity M-sand inherently enhances concrete durability and workability, simultaneously mitigating the environmental impacts of natural sand extraction.

The Scherrer equation yields crystallite sizes of 50–100 nm, directly validating the material's excellent crystallinity and high quartz purity (>95%). The most prominent peak at approximately 26.6° 2θ (intensity ~11,000 cps) corresponds directly to the (101) crystallographic plane. Additional distinct reflections manifest at ~20.8° (100 plane), ~36.5° (110 plane), ~39.5° (102 plane), ~42.5° (200 plane), ~45.8° (111 plane), ~50.1° (112 plane), ~59.9° (211 plane), and ~68.3° (203 plane), alongside minor high-angle signals. The complete absence of broad amorphous humps or significant impurity peaks (e.g., the absence of feldspar signals at ~27.8° 2θ and mica signals at ~8.8° 2θ) verifies a well-processed M-sand devoid of substantial clay, silt, or carbonate contaminants. This refined state optimizes the material's capacity to enhance compressive strength and reduce shrinkage in cementitious matrices. However, trace structural shoulders emerging around 27°–28° 2θ denote minor orthoclase or plagioclase feldspar remnants inherited from the parent rock.

While the qualitative XRD profile establishes the aggregate's robust baseline quality, precise phase composition and gradation analysis dictate a quantitative Rietveld refinement. Correlating these exact phase metrics with aggregate performance directly optimizes subsequent mix designs for high-performance, sustainable concrete applications.

4.2.8 Coconut fiber: The coconut fiber used as reinforcing media in cladding panel was also subjected to XRD. The X-ray diffraction (XRD) pattern of the coconut fiber (coir) sample, acquired over a 2θ range of 10° to 80° using Cu Kα radiation, exhibited a predominantly amorphous structure characteristic of lignocellulosic natural fibers. Broad humps in the pattern indicated semi-crystalline cellulose domains embedded within an amorphous matrix of hemicellulose, lignin, and pectin. The (002) crystallographic plane of cellulose I (native cellulose allomorph) produced the most intense broad peak, centered at approximately 22° 2θ (intensity ~3800 cps). This specific reflection demonstrated the ordered packing of cellulose chains along the fiber axis, a structural feature that contributes to the mechanical strength and tensile properties of coir. Furthermore, the (040) plane generated a secondary, less intense

broad hump around 34°–36° 2θ (~1000 cps), confirming the presence of crystalline cellulose. Concurrently, a subtle shoulder or broadening in the 15°–18° region aligned with the (101) plane; such overlapping frequently occurs due to the low degree of crystallinity typically found in untreated coir (30–50%). Figure 4.11 shows the XRD diffractogram of Coconut fiber.

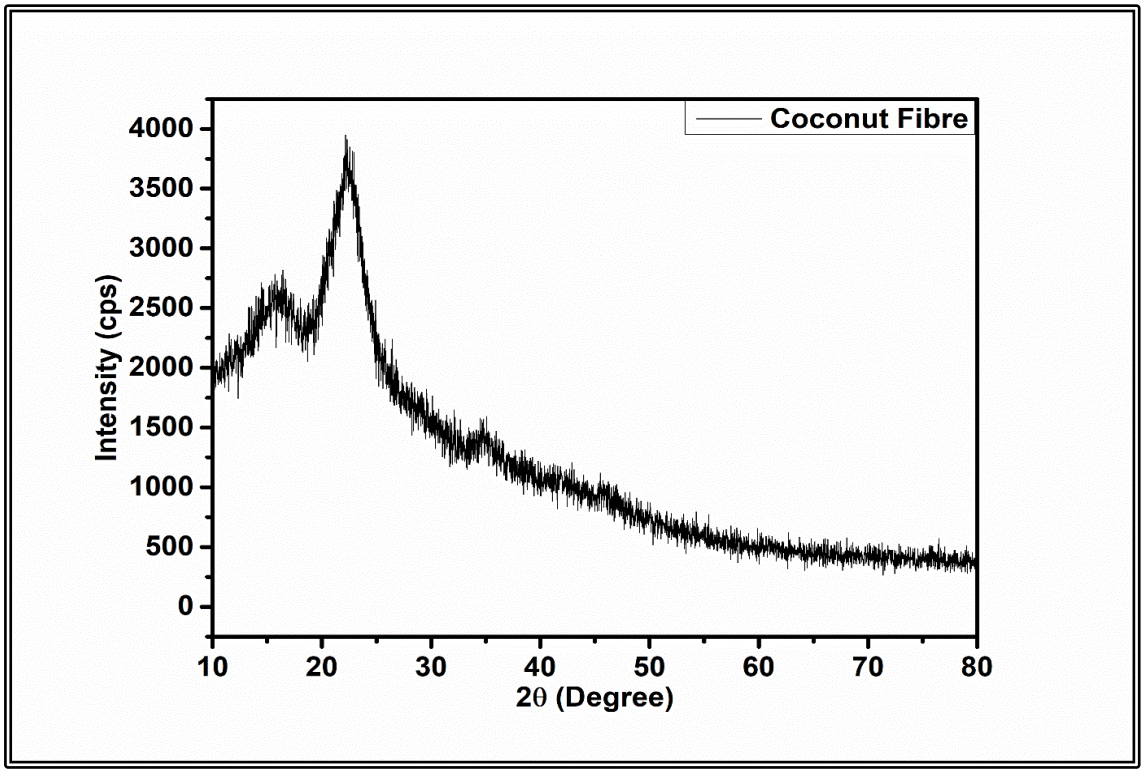


Figure 4.11: XRD diffractogram of Coconut fiber

The absence of sharp, high-intensity peaks suggested minimal inorganic impurities, such as silica or mineral residues common in certain agro-wastes, thereby highlighting the fiber's organic, polymeric nature. Additionally, the broad peak widths (FWHM ~5°–10°) indicated small crystallite sizes (~2–5 nm) and structural disorder driven by the heterogeneous composition of coir (lignin ~45%, cellulose ~43%, hemicellulose ~12%). The overall decreasing baseline intensity with increasing 2θ was consistent with scattering from amorphous regions, and the lack of significant peaks beyond 40° implied limited long-range order. In the context of construction materials, the acquired XRD profile underscores the potential of coir as a sustainable reinforcement in cementitious composites. In these applications, the fiber's inherent low crystallinity may enhance interfacial bonding and toughness. However, surface treatments (e.g., alkali or

silane) could sharpen the crystalline peaks and improve matrix compatibility by reducing the amorphous lignin content.

4.3 Performance assessment and insights of bricks

The subsequent sections detail the brick mix proportions and outline the various tests conducted on the cast bricks.

4.3.1 Mix proportion for bricks

The casting program produced bricks using the mix proportions provided in Table 3.9, and Table 4.9 reports the corresponding material quantities by weight.

Table 4.9: Material quantities used per brick (all values in kgs.)

Brick Composition	IOT	Fly Ash	GGBS	Cement	Lime
T50F05G35	1.89	0.09	0.71	0.12	0.06
T50F10G30	1.89	0.18	0.61	0.12	0.06
T50F15G25	1.89	0.27	0.51	0.12	0.06
T50F20G20	1.89	0.35	0.41	0.12	0.06
T50F25G15	1.89	0.44	0.30	0.12	0.06
T50F30G10	1.89	0.53	0.20	0.12	0.06
T50F35G05	1.89	0.62	0.10	0.12	0.06

The experimental programme prepared various trial batches with differing mix ratios. It evaluated their performance primarily through compressive strength testing of 70.6 mm × 70.6 mm × 70.6 mm cubes, with the results at 7 and 28 days of curing compiled in Table 4.10.

Table 4.10: Compressive strength measured on cube specimens for various mixes (all values in N/mm^2)

Brick Composition	Average compressive strength	
	7D	28D
T50F05G35	6.96	10.70
T50F10G30	7.26	11.15
T50F15G25	5.31	8.86
T50F20G20	4.92	8.10
T50F25G15	3.60	6.90
T50F30G10	2.41	5.28
T50F35G05	1.82	5.06

Figure 4.12 shows that Trial 2, comprising 50% iron ore tailings, 10% fly ash, and 30% GGBS, attained the highest compressive strength of 11.15 N/mm² at 28 days and 7.26 N/mm² at 7 days, thereby exceeding all IS code thresholds.

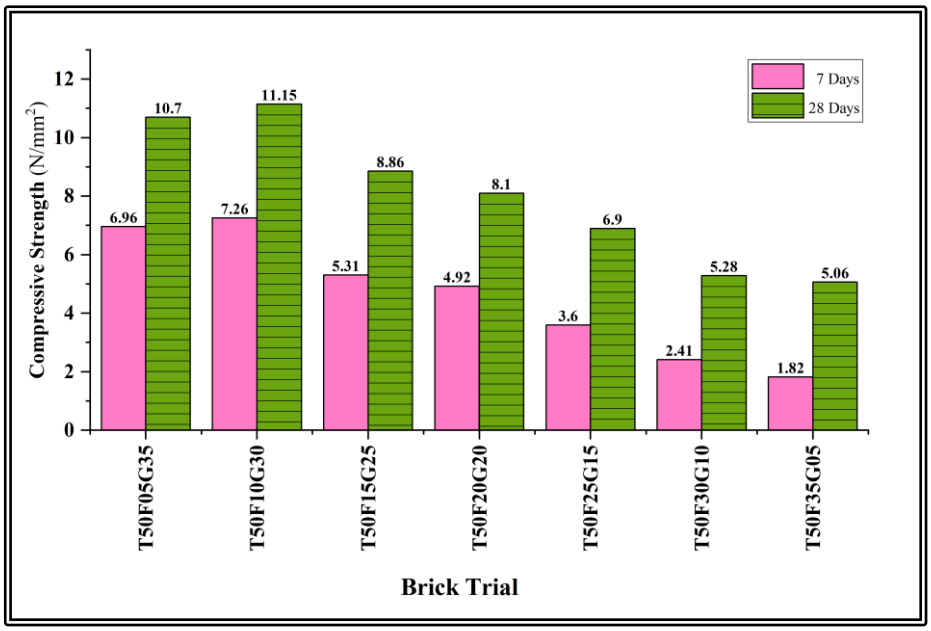


Figure 4.12: Compressive strengths of different trial mixes

Results reported by Yang et al. (2014) indicate a decline in strength with increasing fly ash content, yet maintain values above the minimum performance criteria, and the current mix behaviour aligns with this trend. In contrast, formulations reported by Thejas and Hossiney (2022) yielded a compressive strength of 7.7 N/mm² for blocks containing 44% GGBS, 42% iron ore tailings, and 4% lime, representing the mix with the highest GGBS content and the lowest tailings content, similarly the compressive strength was 18.45N/mm^2 when the GGBS was highest in case of bricks.

The present mix achieved superior performance despite incorporating the second-highest GGBS proportion, owing to optimized particle packing and synergistic pozzolanic and latent hydraulic reactions among GGBS, lime, and iron ore tailings, which enhanced matrix densification and reduced capillary porosity. These mechanisms collectively improved density, mechanical durability, and long-term service life, enabling the developed composites to conform to IS 1077 specifications.

4.3.2 Tests on bricks

The cast bricks underwent a series of tests to quantify key quality parameters, and this section presents the corresponding results.

4.3.2.1 Dimension test

IS 1077:2025 governed the dimensional test procedures, and Table 4.11 summarizes the subsequent evaluation of the brick specimens. All seven cast trials achieved identical dimensional conformity, indicating consistent geometric stability across the mixes.

Table 4.11: Dimensions of bricks (all values in mm)

Details	No. of units	Dimension	Average dimension	Code recommendations
L	20	230	230	4600 ± 80 mm
B		100	102	2000±40 mm
H		70	68	1400±40 mm

4.3.2.2 Compressive strength and bulk density

The compressive strength of the bricks governs resistance to compressive forces and reflects the effectiveness of reactions between the alkali source and the solid aluminosilicates, so higher resistance indicates a refined microstructure and improved durability. Table 4.12 reports the compressive strengths obtained for the different brick trial mixes.

Table 4.12: Compressive strength results of different brick trial mixes (all values in N/mm^2)

Brick Composition	Average compressive strength	
	7D	28D
T50F05G35	9.85	13.03
T50F10G30	10.47	13.58
T50F15G25	7.66	10.67
T50F20G20	7.10	10.09
T50F25G15	5.19	8.62
T50F30G10	3.48	6.43
T50F35G05	2.62	6.16

The brick mix designated T50F10G30—containing 50% iron ore tailings (IOTs), 30% GGBS, 10% fly ash, and 5% each of cement and lime—achieved 10.47 N/mm^2 at 7 days and 13.58 N/mm^2 at 28 days, thereby exceeding the minimum requirements prescribed in IS 1077:2025 and confirming suitability for construction applications.

The T50F10G30 mix demonstrated superior performance relative to other trial compositions, underscoring the critical role of balanced supplementary cementitious

materials (SCMs). Figures 4.13 and 4.14 show that all compressive strengths from the current experimental matrix exceeded the values specified in the Indian Standard code.

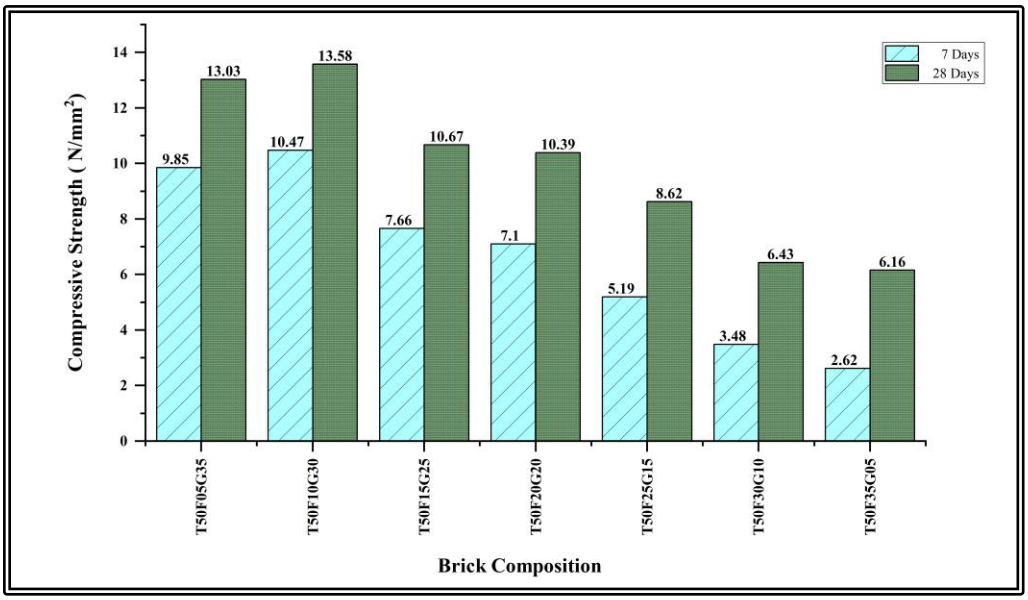


Figure 4.13: Compressive strength of different bricks at 7 and 28 days

Comparative analysis with prior studies further validates the effectiveness of this mix design despite the absence of aggressive alkali activators used in specific geopolymer systems, as evidenced by Beulah et al. (2021), who attained 28 N/mm² using 8 M NaOH and sodium silicate activators to form strong geopolymeric bonds at the cost of more complex input systems.

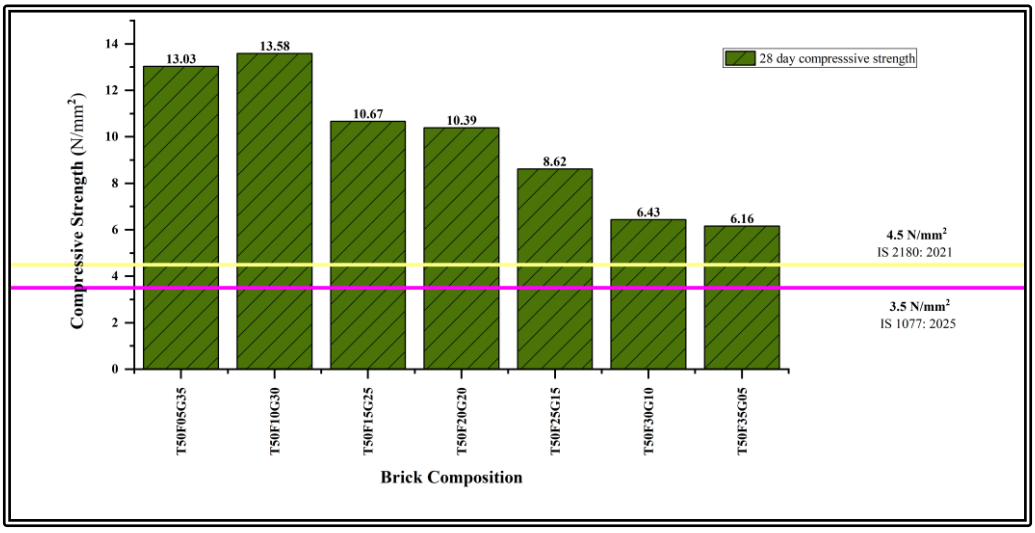


Figure 4.14: Compressive strengths of bricks with IS code limits

Likewise, mixes reported by Kumar et al. (2017, 2020) achieved strengths exceeding 25 N/mm² via high-alkali activation strategies. In contrast, the present bricks achieved

competitive compressive strengths (>13 N/mm² at 28 days) under ambient curing without such activation, thereby offering a more simplified and potentially more economical process.

Compared with ordinary Portland cement (OPC)-reliant mixes, such as those reported by Singh et al. (2021) with 8.58 N/mm² for blends containing 20% OPC and 80% IOTs, the current formulation surpassed this performance through synergistic pozzolanic and latent hydraulic reactions among IOTs, fly ash, and GGBS, while simultaneously avoiding the environmental and cost implications associated with OPC usage. Further, results from Freitas et al. (2018) showed compressive strengths of only around 3 N/mm² for mixes with high GGBS content, thereby emphasizing the necessity of a balanced reactive phase composition such as that achieved in T50F10G30 for matrix densification. The balanced silica-to-alumina ratio in T50F10G30, maintained by limiting fly ash content to 10%, effectively addressed the strength decline reported by Thejas & Hossiney (2022) in mixes with higher IOTs and imbalanced SCM content by mitigating the deleterious effect of the typically high Fe_2O_3 content in IOTs on polymerization and strength development.

The T50F10G30 mix, therefore, exhibited optimal synergy among iron ore tailings, fly ash, and GGBS, enabling ambient curing to yield sustainable bricks whose compressive strengths exceeded relevant standards and remained competitive with geopolymers and OPC-based mixes, thereby reducing reliance on energy-intensive activation methods and OPC and advancing cost-effective, eco-friendly construction materials.

Bulk density, defined as brick mass per unit volume and expressed in kilograms per cubic meter (kg/m³), critically influences strength, durability, and unit weight. The present study recorded values ranging from 1495 to 1839 kg/m^3 (dry) and 1575 to 1932 kg/m^3 (wet) across different mix proportions. Table 4.13 lists the dry and wet bulk densities for the brick mix trials.

Table 4.13: Dry and wet bulk densities for various brick mix trials (all values in kg/m^3)

Brick **Composition**	**Average Dry density**	**Average Wet density**
T50F05G35	1787	1860
T50F10G30	1839	1932
T50F15G25	1755	1840
T50F20G20	1710	1800
T50F25G15	1650	1740
T50F30G10	1570	1690
T50F35G05	1495	1575

This bulk density variation primarily reflected the influence of IOTs content and its interaction with SCMs on particle packing efficiency and overall mass per unit volume, as illustrated in Figure 4.15.

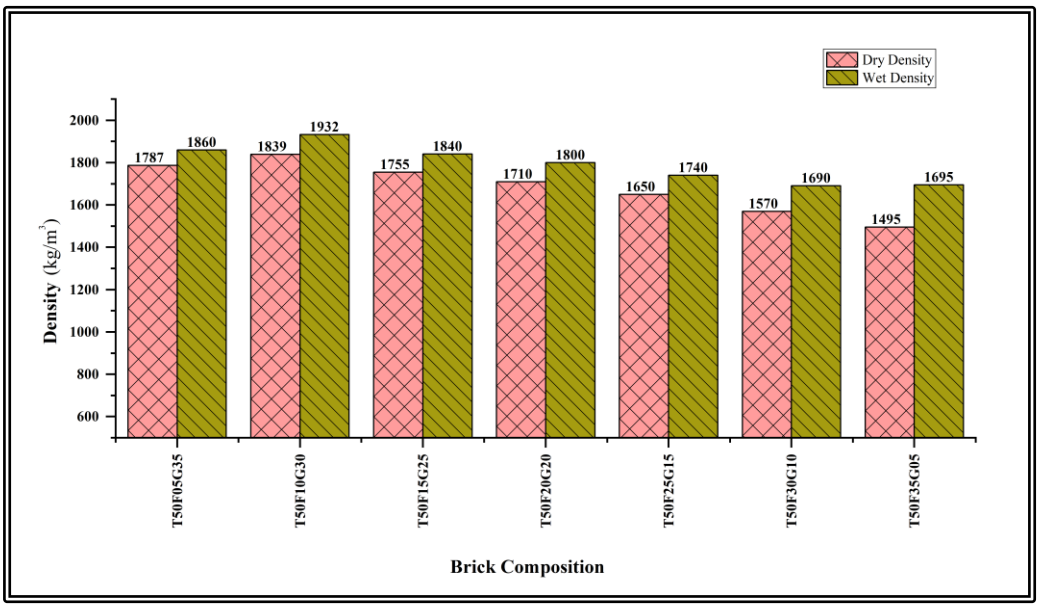


Figure 4.15: Dry and wet densities of brick

Comparable bulk densities documented in the literature substantiate these observations wherein Thejas & Hossiney (2022) reported densities between 2000 and 2400 kg/m^3 for IOT-containing bricks, highlighting the densification effect of tailings with high specific gravity; Beulah et al. (2021) documented values between 970 and 1260 kg/m^3; Singh et al. (2021) showed that increasing cement content enhanced densification, delivering bulk densities between 1880 and 2120 kg/m^3 in iron tailings–cement–sand mixes; and Freitas et al. (2017) recorded densities up to 2430 kg/m^3 for slag–IOT combinations, underscoring the key role of IOT fine particle size and iron oxide content in promoting density and packing efficiency.

Geopolymer bricks incorporating IOT and other industrial by-products, as reported by Kumar et al. (2020), exhibited dry bulk densities between 1978 and 2120 kg/m^3 and wet densities up to 2180 kg/m^3, while density values in Kuranchie et al. (2015) ranged from approximately 1990 to 2130 kg/m^3 depending on initial setting time, curing temperature, curing duration, and activator content, collectively indicating that optimized IOT content and appropriate activation enhanced compactness and reduced porosity.

The angular morphology and high specific gravity of IOTs optimize particle packing and minimize void spaces; this densification mechanism validates IOTs as effective constituents for producing structurally dense, standard-compliant bricks. The bulk density results from the present experimental program demonstrated that IOT, in combination with GGBS, fly ash, cement, and lime, yielded bricks with densities comparable to traditional fired bricks, thereby reinforcing their suitability for sustainable construction applications.

4.3.2.3 Water absorption and wet bulk density

Water absorption served as a key indicator of brick porosity and durability, and brick mixes containing 50% IOT combined with GGBS, fly ash, cement, and lime consistently registered water absorption values below the 15% limit specified in IS 1077:2025.

Within these mixes, trial T50F10G30 produced the lowest water absorption of 5.05%, demonstrating that optimized reactive precursor ratios can offset the naturally low reactivity and coarse particle texture of IOT, which typically increases pore volume and water ingress.

These observations aligned with those reported by Thejas & Hossiney (2022), where AABI40 (40% IOT, 21% fly ash, 21% GGBS) achieved 12.6% water absorption and qualified as first-class bricks under IS 1077:2025,whereas bricks with higher IOT content (e.g., AABI90) exhibited increased absorption up to 18% due to larger pore structures arising from insufficient binder phases. Fly ash and GGBS collectively enhanced packing density and promoted reaction formation, filling capillary pores and reducing water uptake. Table 4.14 shows water absorption of various brick mix trials.

Table 4.14: Water absorption of various brick mix trials (all values in %)

Brick Composition	Average Water Absorption
T50F05G35	5.32
T50F10G30	5.05
T50F15G25	6.50
T50F20G20	6.85
T50F25G15	7.03
T50F30G10	8.72
T50F35G05	8.90

Relative to the behaviour reported by Kumar et al. (2020), where geopolymer bricks with 20–40% IOT absorbed 2.83–6.67% water under 10 M NaOH activation and elevated GGBS content, the current bricks attained comparable performance under ambient curing without aggressive alkali dosing, while Kuranchie et al. (2015) documented absorption as low as 7.18% for bricks with 100% IOT activated by sodium silicate and optimized curing. Figure 4.16 depicts the water absorption of various trials alongside the IS code limits.

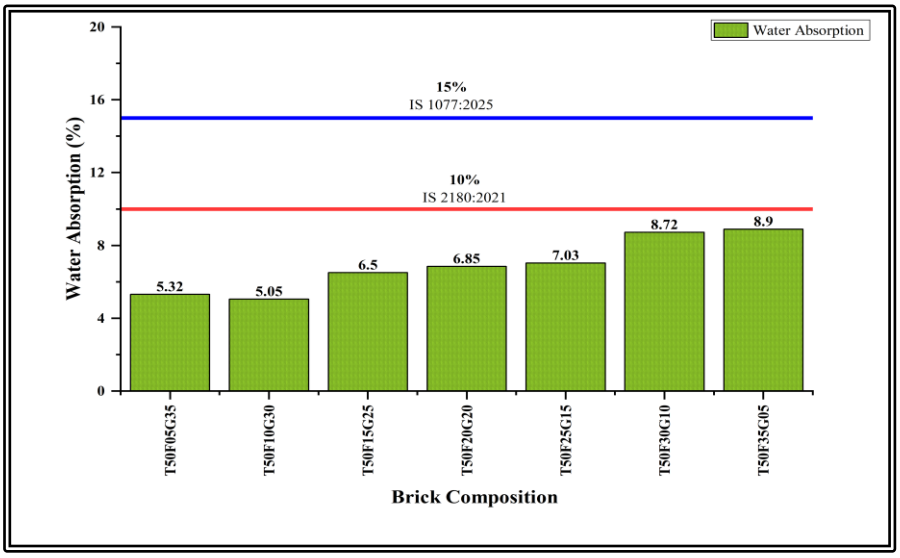


Figure 4.16: Water absorption of bricks with IS code limits

Similar trends arose in the work of Singh et al. (2021), who observed absorption between 5.50% in IOT–cement mixes and 21% in IOT–sodium silicate blends, thereby emphasizing cement's role in matrix densification, while Beulah et al. (2021) showed that appropriate GGBS ratios in IOT–GGBS bricks consistently maintained absorption below 7.58%, with a minimum of 3.78% for high IOT mixes. Collectively, the evaluated mixes met or surpassed these benchmarks, achieving low water absorption, refined pore structures, and enhanced durability, thereby confirming the potential of the developed bricks as sustainable construction materials.

Figure 4.17 plots compressive strength against water absorption for the bricks and reveal an inverse relationship based on seven experimental data pairs.

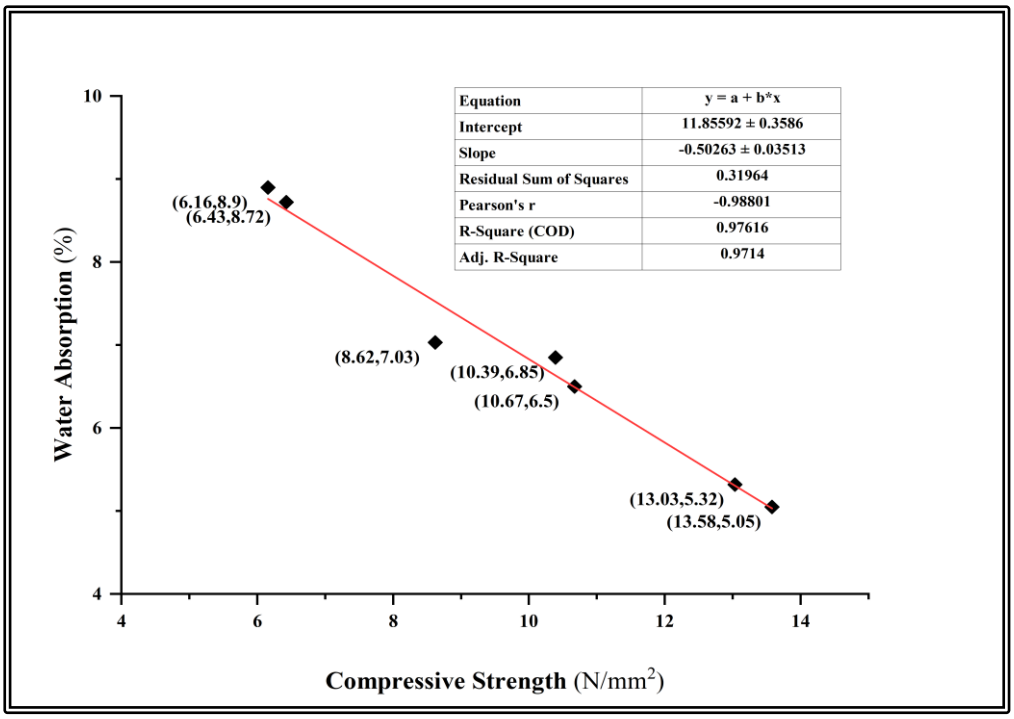


Figure 4.17: Relationship between compressive strength and water absorption

The regression model (Water absorption) = 11.8559 - 0.5026 x (strength) showed a strong negative correlation, with Pearson's r = -0.9880 and R^2= 0.9762, indicating that each 1 N/mm² increase in strength reduced water absorption by approximately 0.5%. At the same time, the intercept (11.8559 ± 0.3586) represented the extrapolated absorption at zero strength.

The residual sum of squares of 0.3196 and the adjusted R^2 of 0.9714 confirmed the excellent fit of the model.

4.3.2.4 Brick ageing

The accelerated ageing tests that subjected composite bricks with 50% IOT and varying fly ash and GGBS proportions to cyclic wet–dry conditions recorded an average compressive strength loss of 24.55% over seven cycles, a reduction that remained within the 20–30% range considered acceptable for masonry in harsh weathering environments.

Among the mixes, T50F10G30 exhibited the highest initial strength of 13.60 N/mm^2. It retained 10.67 N/mm^2 after ageing, corresponding to a 21.56% reduction. In contrast, mixes containing 20–30% GGBS, such as T50F20G20 (21.20% loss) and T50F25G15 (20.83% loss), showed the least strength degradation, indicating that moderate GGBS contents enhance microstructural densification and moisture resistance.

In contrast, mixes with high fly ash contents (30–35%) exhibited increased porosity and greater strength losses (30.33–30.40%), as shown in Table 4.15 and illustrated in Figure 4.18.

Table 4.15: Compressive strength at various cycles of brick ageing
(all values in N/mm^2)

Cycle	1	2	3	4	5	6	7
Brick Composition							
T50F05G35	13.09	12.45	11.55	11.00	10.65	10.35	10.14
T50F10G30	13.60	12.90	12.00	11.48	11.10	10.85	10.67
T50F15G25	11.10	10.53	9.80	9.38	9.02	8.85	8.61
T50F20G20	12.50	11.90	11.05	10.59	10.23	10.00	9.85
T50F25G15	9.60	9.15	8.60	8.25	7.98	7.78	7.40
T50F30G10	6.25	5.92	5.50	5.28	5.00	4.65	4.35
T50F35G05	6.00	5.70	5.35	5.05	4.82	4.50	4.15

Mid-range formulations such as T50F05G35 and T50F15G25 showed intermediate durability, with strength losses around 22.5%, behaviour consistent with the known influence of SCMs: GGBS refines the pore structure and reduces permeability, whereas excessive fly ash increases pore connectivity and facilitates water ingress, accelerating deterioration.

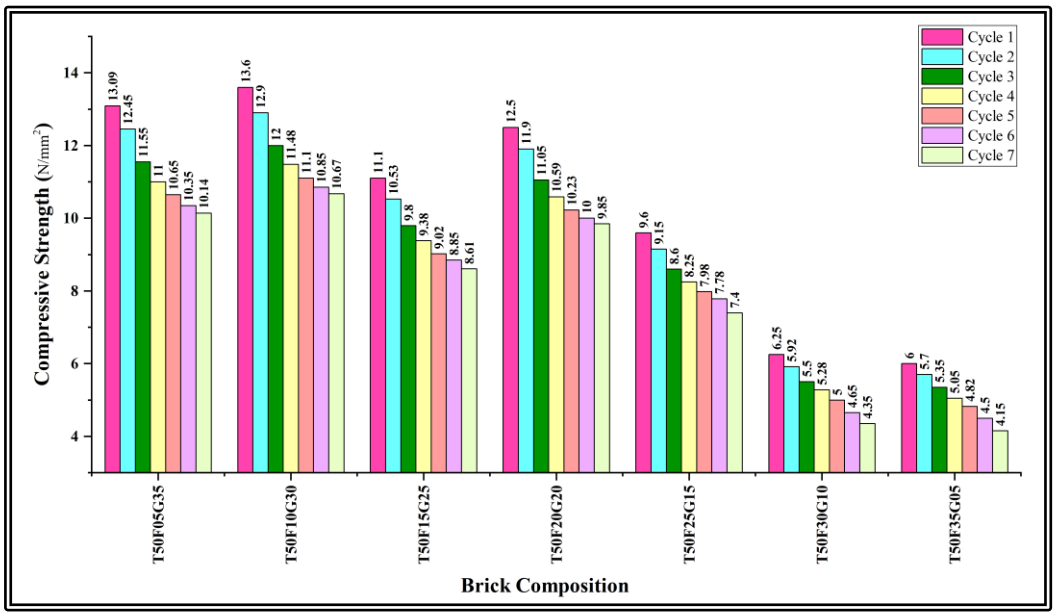


Figure 4.18: Variation in compressive strength over different cycles of wetting and drying

Data from Thejas and Hossiney (2022) provided a relevant benchmark, with alkali-activated bricks at lower IOT content (40% IOT, 21% fly ash, 21% GGBS) exhibiting the least strength reduction at 14.69% and bricks with 90% IOT showing a substantial

48.03% loss; that work attributed poorer durability at high IOT levels to low reactivity and enlarged pore structures that promote water movement during wet–dry cycling.

The positive contribution of fly ash and GGBS to reactive gel formation and microstructural densification in that study aligned with the current ageing results, in which balanced GGBS and fly ash contents enabled high IOT utilization while maintaining durability.

Overall, the formulated mixes either outperformed or matched established compositions by optimizing the synergistic effects of GGBS and fly ash to resist ageing while maximizing iron ore tailings content, thereby providing sustainable, durable bricks suitable for diverse climatic conditions and confirming the advantages of the tailored mix designs.

4.3.2.5 Electrical resistivity

Electrical resistivity testing assessed composite bricks containing IOT to quantify the risk of electrical conduction arising from high iron content, as elevated Fe_2O_3 levels can enhance conductivity and raise safety concerns in construction. Table 4.16 summarizes the electrical resistivity results for the brick trials. The measured resistivity values ranged from 266.43 to 471.734 kΩ·m, spanning both the conventional safe range of 450–700 kΩ·m cited by Thejas & Hossiney (2022) and > 682 kΩ·m reported by Kuranchie et al. (2015).

Table 4.16: Electrical resistivity of bricks (all values in kΩ·m)

Brick Designation	Electrical Resistivity
T50F05G35	452.56
T50F10G30	471.73
T50F15G25	442.66
T50F20G20	376.50
T50F25G15	347.39
T50F30G10	272.01
T50F35G05	266.43

Although current measurements yield slightly lower values, even the minimum resistivity exceeds fundamental insulation requirements, thereby confirming the continued safety of these materials for construction use. These moderate reductions in resistivity remained practically insignificant from a safety standpoint, and the results collectively confirmed that bricks with high IOT dosages did not become sufficiently

conductive to pose electrical hazards in typical service conditions, thereby supporting the safe, sustainable utilization of IOT in brick production and broadening industrial waste valorization without introducing risk to workers or end-users. Figure 4.19 plots compressive strength against electrical resistivity for IOT-based bricks.

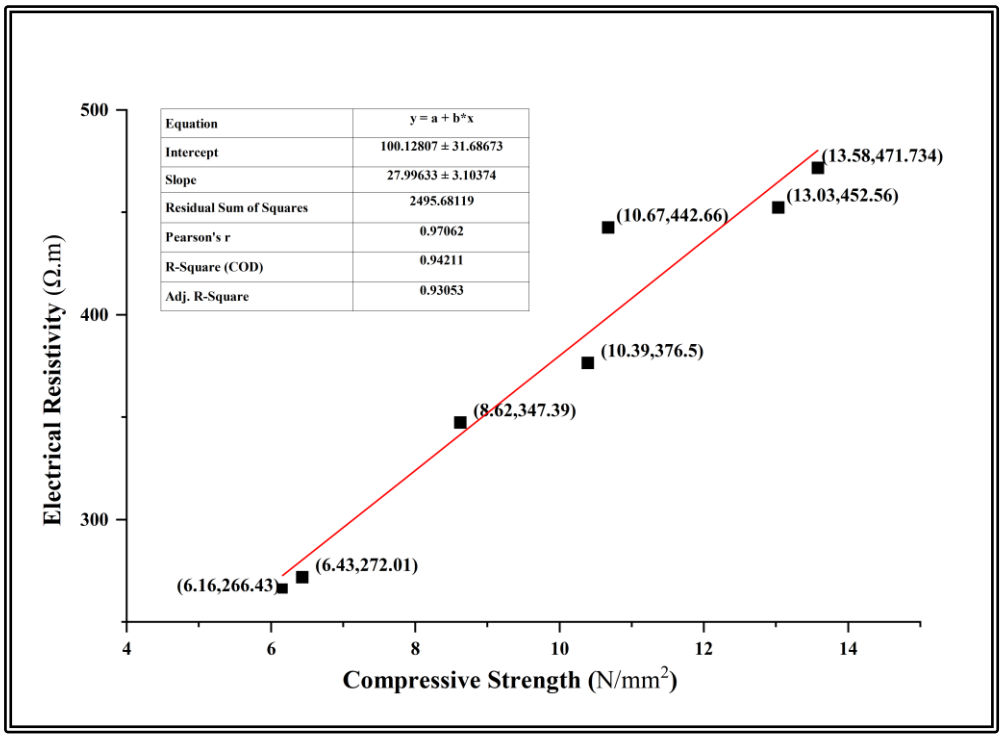


Figure 4.19: Relationship between compressive strength and electrical resistivity

The figure reveals a clear positive correlation, whereby increasing compressive strength coincides with increasing electrical resistivity, captured by the regression equation y = 100.13 + 27.99x with Pearson's correlation coefficient, r = 0.97 and R^2 = 0.94, indicating an excellent linear fit.

This relationship suggests that optimized mixes simultaneously yielded structurally stronger bricks and higher resistance to electrical conduction, a favourable outcome for construction safety because higher resistivity reduces the risk of electrical hazards; higher-strength specimens exceeded 470 kΩ·m, thereby confirming the safe and robust application of IOT-based bricks in practice.

4.3.2.6 Efflorescence

Efflorescence occurs when soluble salts are deposited on brick surfaces. It commonly occurs when water-soluble salts, moisture, and a porous medium coexist within the brick, thereby posing risks of wall plaster damage, paint degradation, and aesthetic

impairment, particularly in unplastered masonry. IS 3495 (Part 3) defines efflorescence classes based on the amount of salt deposited on the brick surface, and the efflorescence tests in the present work showed that composite bricks with 50% IOT developed only slight efflorescence, with approximately 10% of the surface covered by thin salt deposits after two evaporation cycles.

This performance compared favourably with the bricks containing 40% IOT reported by Tejas and Hossiney, (2022) which exhibited no efflorescence and therefore highlighted the additional challenge posed by the higher tailings content in the current composites.

The slight salt migration observed in the present bricks likely reflected residual alkali mobility from unreacted IOT, yet the overall severity remained within acceptable limits for masonry aesthetics and durability.

Comparison with the geopolymer bricks investigated by Kumar et al. (2020), which incorporated fly ash, slag sand, and GGBS and achieved very slight efflorescence (Class AA under IS 3495 Part 3) through effective alkali immobilization within a dense geopolymer matrix, further underscores the importance of binder chemistry.

Similarly, the work of Singh et al. (2021) showed that bricks made with IOT and cement alone exhibited no efflorescence, whereas sodium silicate–rich mixes experienced moderate to heavy salt crystallization due to high alkali content and porous microstructures, collectively indicating that binder chemistry and pore structure critically control efflorescence.

Despite the higher IOT content, the composite bricks in the present matrix exhibited only slight efflorescence, comparable to industry benchmarks. They ensured minimal surface discolouration while avoiding the micro-cracking and strength reduction associated with heavy salt deposits.

Overall, the mixes achieved a sustainable balance between maximizing IOT utilization and minimizing efflorescence, thereby matching or surpassing existing formulations in both aesthetic and durability performance.

4.3.2.7 Falling test

Specimens T50F05G35, T50F10G30, T50F15G25, and T50F20G20 exhibited only mild edge failure, indicating superior impact resistance, whereas T50F25G15, T50F30G10, and T50F35G05 sustained moderate failure. Table 4.17 summarizes the falling test results. Optimized GGBS levels drive this structural resilience by densifying the internal

matrix and reducing pore volume; this refined microstructure strengthens inter-particle bonding and improves energy dissipation upon impact.

Table 4.17: Falling test results of bricks

Brick composition	1st Specimen	2nd Specimen	3rd Specimen
T50F05G35	Mild Edge Failure	Mild Edge Failure	Mild Edge Failure
T50F10G30	Mild Edge Failure	Mild Edge Failure	Mild Edge Failure
T50F15G25	Mild Edge Failure	Mild Edge Failure	Mild Edge
T50F20G20	Mild Edge Failure	Mild Edge Failure	Mild Edge
T50F25G15	Moderate Edge Failure	Moderate Edge Failure	Moderate Edge Failure
T50F30G10	Moderate Edge Failure	Moderate Edge Failure	Moderate Edge Failure
T50F35G05	Moderate Edge Failure	Moderate Edge Failure	Moderate Edge Failure

These findings substantiate those of Kumar et al. (2020), who found that higher slag content (mixes GB-4 to GB-6) restricted damage to mild failures through enhanced energy dissipation, while lower slag and higher iron ore tailings (IOT) content (mixes GB-1 to GB-3) induced moderate failures. Ultimately, strategically proportioning slag and tailings yields geopolymer units that surpass conventional clay bricks in impact resistance, effectively valorizing industrial waste for sustainable construction applications.

4.3.2.8 Soundness test

Striking the brick specimens together generated a clear metallic ring without fracturing, verifying high density, strong internal bonding, and overall durability. Table 4.18 summarizes the soundness test data.

Table 4.18: Soundness test results of bricks

Brick composition	Soundness
T50F05G35	Heavy and Good
T50F10G30	Heavy and Good
T50F15G25	Heavy and Good
T50F20G20	Heavy and Good
T50F25G15	Heavy and Good
T50F30G10	Heavy and Good
T50F35G05	Heavy and Good

This acoustic response confirms the physical integrity of all tested samples for load-bearing applications. These results align with observations by Kumar et al. (2017, 2020), who reported that comparable metallic sounds correlated with solid brick fabrication. Consequently, these metrics demonstrate that the engineered mix proportions deliver the mechanical integrity and dimensional stability required for dependable performance in structural masonry.

4.3.2.9 Hardness test

A sharp object created an impression on the brick surfaces, evaluating material rigidity; the complete absence of residual indentations across all trials verified sufficient hardness for construction applications. Table 4.19 presents the hardness test results.

Table 4.19: Test results of hardness test on bricks

Brick composition	Test results	Hardness
T50F05G35	No impression left	Sufficiently hard
T50F10G30	No impression left	Sufficiently hard
T50F15G25	No impression left	Sufficiently hard
T50F20G20	No impression left	Sufficiently hard
T50F25G15	No impression left	Sufficiently hard
T50F30G10	No impression left	Sufficiently hard
T50F35G05	No impression left	Sufficiently hard

This performance surpassed the findings of Kumar et al. (2017, 2020), in which slight indentations were acceptable. The total lack of surface yielding indicates a highly dense, well-bonded microstructure driven by the effective synergy of iron ore tailings (IOT), fly ash, and GGBS within the binder matrix. Achieving consistent hardness across varying precursor ratios demonstrates mix design versatility. Combined with other strength and durability metrics, this structural resilience establishes these 50% IOT geopolymer mixes as superior, sustainable alternatives to conventional clay bricks.

Ultimately, the composite mix T50F10G30 (50% IOT, 30% GGBS, 10% fly ash, and 5% each of cement and lime) exhibited optimal overall performance, achieving maximum compressive strength and electrical resistivity while maintaining relatively low water absorption.

4.4 SEM-EDX characterization of bricks

Combined SEM-EDX analysis detailed the microstructural morphology and elemental composition of the brick samples. The SEM imaging process resolved surface texture, grain size, and porosity, while the EDX system quantified and mapped the distribution of primary elements, including silicon, aluminum, and calcium. Together, these analytical techniques provided the parameters necessary to evaluate the source raw materials, structural quality, and long-term durability of the bricks. Scanning electron microscopy (SEM) reveals the microstructural morphology of the two brick compositions.

a) Brick composition: T50F10G30

High-resolution FESEM analysis of T50F10G30 reveals a finely textured microstructure characteristic of a synthesized brick composite. This morphology confirms the structural integration of pozzolanic or cementitious binders with waste-derived aggregates. Spherical-to-angular particles, ranging from sub-micron to 2–5 μm, densely agglomerate to generate a highly compact matrix. The restricted inter-particle void network (5–15% apparent porosity) dictates highly effective compaction and advanced geopolymerization mechanisms during fabrication. Consequently, this densified architecture drives the high compressive strength and low water absorption strictly required for load-bearing, eco-friendly masonry. Figure 4.20 shows an SEM micrograph illustrating the microstructural morphology of T50F10G30, while Figure 4.21 shows an EDX spectrum illustrating the relative abundance of the principal elements detected within T50F10G30.

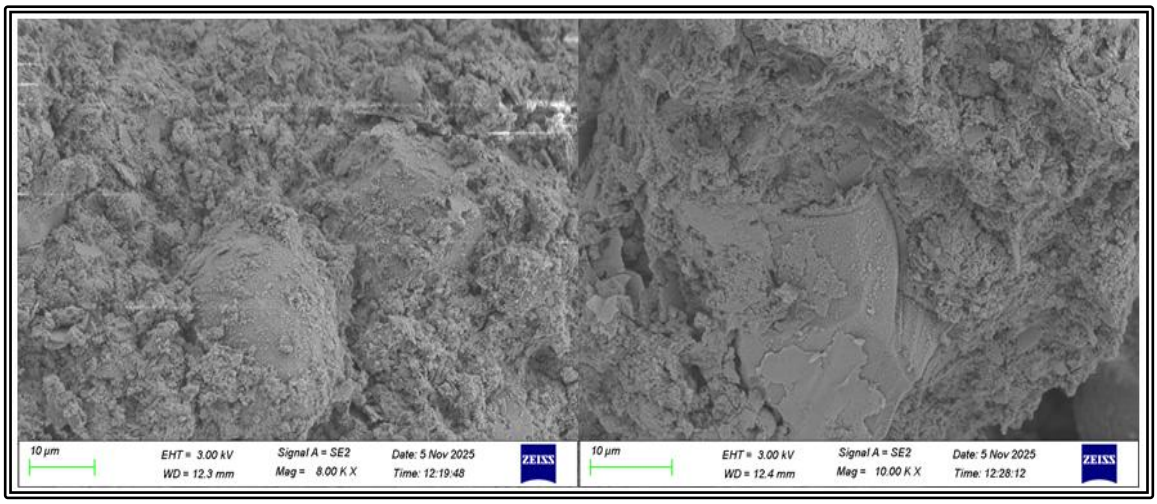


Figure 4.20: SEM micrograph of brick composition T50F10G30

Concurrent EDX mapping resolves the elemental architecture across this densified matrix. Oxygen (green) saturates the material, constructing the foundational oxide framework. Silicon (red) dominates the core regions, indicating the formation of stable siliceous structures such as quartz or C-S-H phases. Aluminum (cyan) co-precipitates with silicon, generating distinct aluminosilicate domains from the reactive precursors. Calcium (pink) concentrates in localized zones, marking the precipitation of calcareous hydration products. Iron (brown) isolates into spotty concentrations, characterizing distinct oxide inclusions.

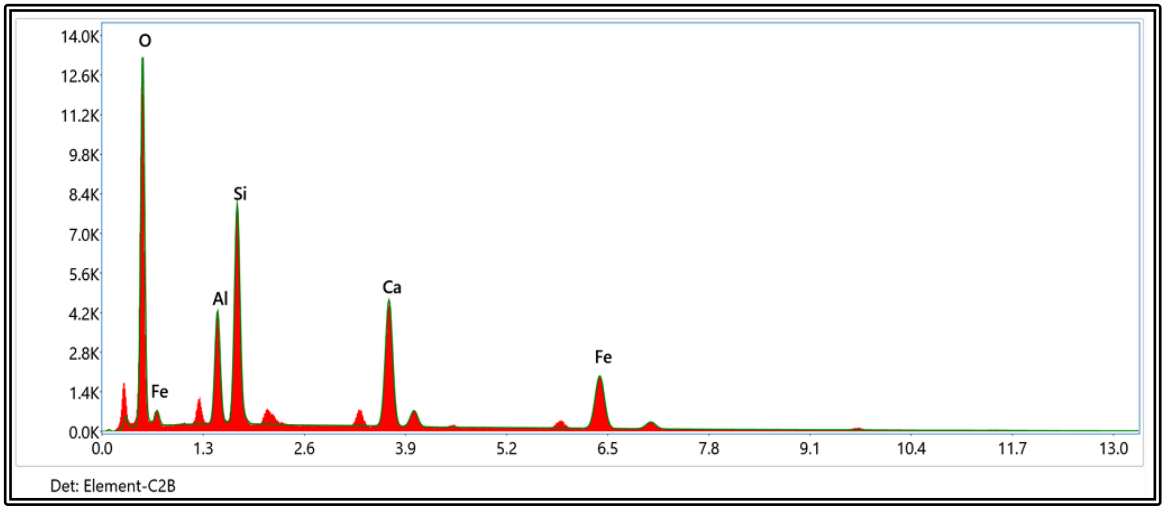


Figure 4.21: EDX spectrum detailing of principal elements for brick composition T50F10G30

This pronounced elemental homogeneity accelerates chemical bonding and fortifies material durability within alkaline environments. Collectively, these microstructural properties position T50F10G30 as a robust brick for sustainable construction applications, specifically low-emission units incorporating 20–40% industrial byproducts. Future quantitative EDX evaluation (e.g., atomic ratios: O ~50–60%, Si ~25–35%, Al ~10–15%, Ca ~5–10%, Fe ~3–5%) and digital porosity analysis will evaluate material performance and direct ongoing material optimization**.**

b) **Brick composition: T50F35G05**

The field emission scanning electron microscopy (FESEM) images of T50F35G05, illustrate a compact yet textured microstructure typical of a synthesized brick composite, likely utilizing cementitious or geopolymeric binders with fine aggregates, displaying 1-8 µm sub-rounded particles densely interlocked with limited porosity (~10-20%) and smooth surface facets, indicative of effective mixing or curing processes that could promote structural integrity and thermal resistance in masonry units for building

applications. Figure 4.22 shows SEM micrograph illustrating the microstructural morphology of the T50F35G05 while Figure 4.23 shows EDX spectrum illustrating the relative abundance of the principal elements detected within T50F35G05.

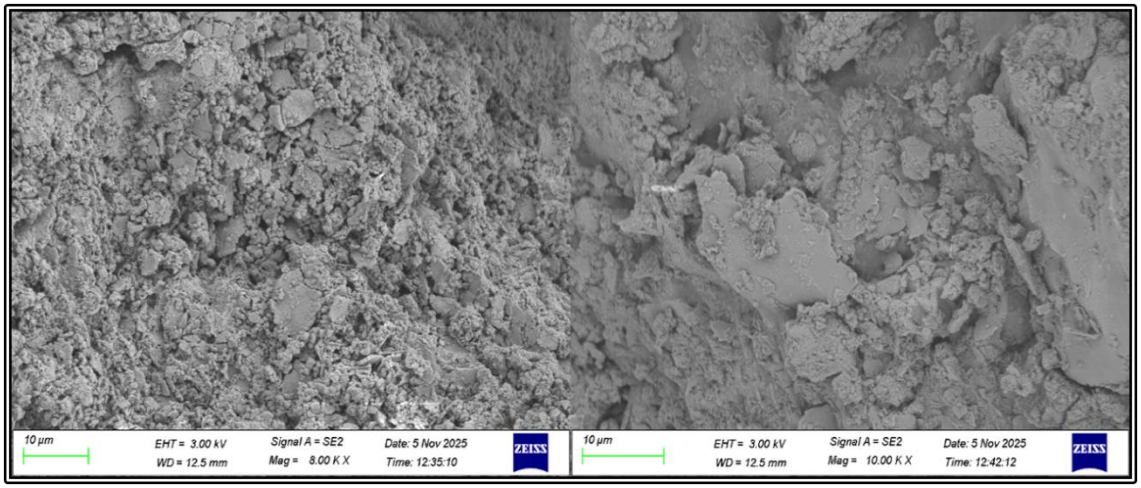


Figure 4.22: SEM micrograph of brick composition T50F35G05

The EDX map reveals oxygen (O K, green, pervasive as the oxide framework), with silicon (Si K, red, uniformly in matrix cores suggesting siliceous phases), aluminum (Al K, cyan, co-distributed with Si in aluminosilicate regions), calcium (Ca K, pink, in clustered hydraulic domains), and iron (Fe K, brown, in isolated iron oxide clusters); this elemental arrangement implies a balanced formulation for enhanced compressive strength and environmental stability in bricks with potential 15-25% supplementary materials, though quantitative EDX (e.g., atomic ratios: O ~50-60%, Si ~25-35%, Al ~5-15%, Ca ~5-10%, Fe ~3-7%) or fracture mechanics evaluation would further assess suitability on material durability.

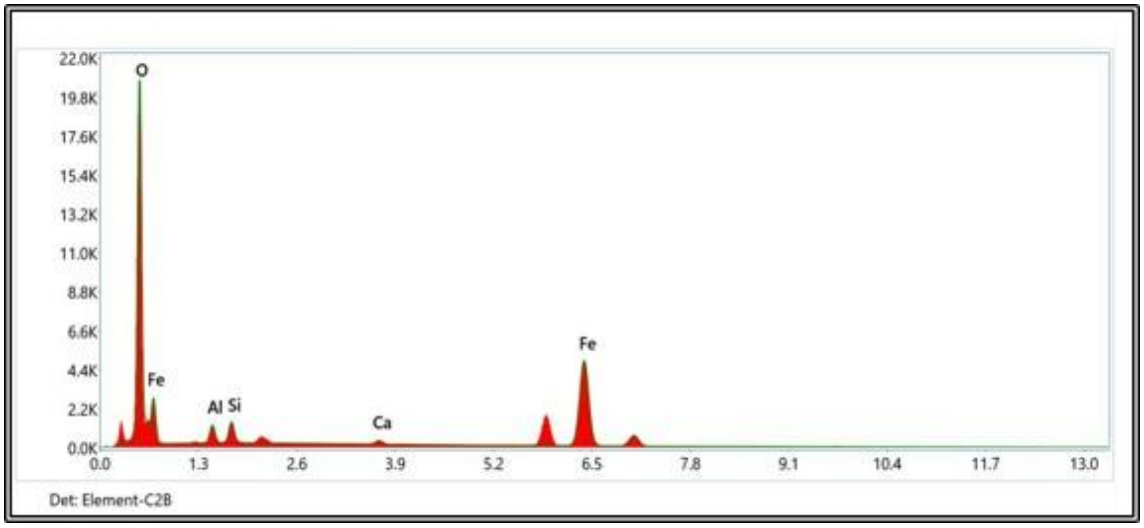


Figure 4.23: EDX spectrum detailing of principal elements for brick composition T50F35G05

4.5 Statistical analysis of various parameters of cast bricks

A comprehensive statistical analysis of the test results is presented in Table 4.20. At 7 days, the T50F10G30 mix attained a mean compressive strength of 10.47 N/mm² (95% CI: 10.05–10.89 N/mm²; COV = 3.3%), significantly exceeding mixes with higher proportions of fly ash or GGBS, and the non-overlapping confidence intervals between T50F10G30 and other mixes (e.g., T50F15G25, T50F20G20) indicated statistically meaningful differences in early-age strength.

Table 4.20: Statistics of various parameters of brick

Brick composition	Mean	Standard Deviation	Lower 95% CI of Mean	Upper 95% CI of Mean	SE of mean	Coefficient of Variation
7 days Compressive Strength						
T50F05G35	9.852	0.463	9.278	10.426	0.207	0.047
T50F10G30	10.470	0.342	10.046	10.894	0.153	0.033
T50F15G25	7.660	0.092	7.546	7.774	0.041	0.012
T50F20G20	7.100	0.074	7.008	7.192	0.033	0.010
T50F25G15	5.190	0.065	5.109	5.271	0.029	0.013
T50F30G10	3.480	0.032	3.441	3.519	0.014	0.009
T50F35G05	2.620	0.045	2.564	2.676	0.020	0.017
28 days Compressive Strength						
T50F05G35	13.026	0.094	12.910	13.142	0.042	0.007
T50F10G30	13.582	0.035	13.539	13.625	0.016	0.003
T50F15G25	10.674	0.358	10.230	11.118	0.160	0.034
T50F20G20	10.386	0.233	10.097	10.675	0.104	0.022
T50F25G15	8.624	0.046	8.567	8.681	0.020	0.005
T50F30G10	6.428	0.048	6.368	6.488	0.022	0.007
T50F35G05	6.156	0.055	6.087	6.225	0.025	0.009
Dry Density						
T50F05G35	1787	24.197	1756.955	1817.045	10.821	0.014
T50F10G30	1839	49.341	1777.735	1900.265	22.066	0.027
T50F15G25	1755	33.369	1713.567	1796.433	14.923	0.019
T50F20G20	1710	9.975	1697.614	1722.386	4.461	0.006
T50F25G15	1650	11.769	1635.387	1664.613	5.263	0.007
T50F30G10	1570	9.028	1558.791	1581.209	4.037	0.006
T50F35G05	1495	11.467	1480.761	1509.239	5.128	0.008
Wet Density						
T50F05G35	1860	23.854	1830.382	1889.618	10.668	0.013
T50F10G30	1932	60.947	1856.325	2007.675	27.256	0.032
T50F15G25	1840	78.163	1742.947	1937.053	34.956	0.042
T50F20G20	1800	34.293	1757.42	1842.58	15.336	0.019

Brick composition	Mean	Standard Deviation	Lower 95% CI of Mean	Upper 95% CI of Mean	SE of mean	Coefficient of Variation
Wet Density						
T50F25G15	1740	26.926	1706.567	1773.433	12.042	0.015
T50F30G10	1690	26.363	1657.266	1722.734	11.790	0.016
T50F35G05	1695	32.749	1654.337	1735.663	14.646	0.019
Water Absorption						
T50F05G35	5.32	0.112	5.181	5.459	0.050	0.021
T50F10G30	5.05	0.178	4.829	5.271	0.080	0.035
T50F15G25	6.50	0.139	6.327	6.673	0.062	0.021
T50F20G20	6.85	0.467	6.271	7.429	0.209	0.068
T50F25G15	7.03	0.207	6.773	7.287	0.093	0.029
T50F30G10	8.72	0.201	8.471	8.969	0.090	0.023
T50F35G05	8.90	0.324	8.498	9.302	0.145	0.036
Electrical Resistivity						
T50F05G35	452.56	17.670	430.619	474.501	7.902	0.039
T50F10G30	471.73	15.215	452.842	490.626	6.804	0.032
T50F15G25	442.66	14.511	424.643	460.677	6.489	0.033
T50F20G20	376.50	19.809	351.904	401.096	8.859	0.053
T50F25G15	347.39	21.426	320.786	373.994	9.582	0.062
T50F30G10	272.01	23.303	243.075	300.945	10.421	0.086
T50F35G05	266.43	22.017	239.092	293.768	9.846	0.083

By 28 days, strength gains became more pronounced, with T50F10G30 reaching 13.58 N/mm² (95% CI: 13.54–13.63 N/mm²; COV = 0.3%), again outperforming all mixes, and the narrow standard error (0.016 N/mm²) together with the minimal coefficient of variation emphasized the high consistency of this mix.

Mixes containing ≥15% fly ash exhibited progressively lower strengths, thereby confirming that excessive fly ash content diminished later-age performance.

Dry density decreased monotonically with increasing fly ash content, falling from 1787 kg/m³ at T50F05G35 to 1495 kg/m³ at T50F35G05. This trend reflected the lower specific gravity of fly ash relative to GGBS. At the same time, wet densities followed a similar pattern but showed greater variation at intermediate GGBS proportions (e.g., COV = 4.2% for T50F15G25), suggesting more connected pore networks and higher moisture retention in these mixes.

The optimal T50F10G30 mix combined a high dry density of 1839 kg/m³ (95% CI: 1777–1900 kg/m³; COV = 2.7%) with the highest wet density of 1932 kg/m³ (95% CI:

1856–2008 kg/m³; COV = 3.2%), thereby indicating a dense microstructure that is less susceptible to moisture ingress.

Water absorption increased with higher fly ash content, rising from 5.05% for T50F10G30 (COV = 3.5%) to 8.90% for T50F35G05 (COV = 3.6%). The relatively low absorption recorded for T50F10G30 demonstrated effective pore refinement driven by pozzolanic reactions. In contrast, mixes with more than 15% fly ash developed more connected porosity and therefore exhibited greater water uptake.

Electrical resistivity peaked for T50F10G30 at 471.73 kΩ·m (95% CI: 452.84–490.63 Ω·m; COV = 3.2%), signalling a more impermeable and less conductive matrix, while resistivity declined sharply in mixes with more than 20% fly ash (e.g., 376.50 Ω·m for T50F20G20; COV = 5.3%), corroborating the trend of increased pore continuity and ionic mobility once fly ash content exceeded the optimal level.

The combined statistical indicators, including means, standard deviations, 95% confidence intervals, and coefficients of variation, collectively showed that the T50F10G30 composition exhibited superior structural and durability characteristics compared with the alternative mixes.

The non-overlapping confidence intervals for key performance metrics confirmed that the enhancements observed for this mix were statistically robust, and T50F10G30 therefore emerged as the optimal balance of iron ore tailings, fly ash, and GGBS for high-performance sustainable brick production.

4.6 Performance assessment and insights of blocks

The subsequent sections present the mix proportions for blocks and the various tests conducted on the cast blocks.

4.6.1 Mix proportion for blocks

To produce an effective and cost-efficient mix, the mix proportioning followed the guidelines of IS 10262:2019, after which the mix design procedure directed the casting of test cubes. Cube casting established the optimal material blend, with the materials mixed according to the percentages listed in Table 3.12.

Table 4.21 details the final material breakdown adopted for the mix design, and Table 4.22 presents the resulting compressive strengths obtained from the cast cubes. The table reports the average compressive strength values for various mix trials at 7 and 28 days of curing.

Table 4.21: Materials and their proportions for IOT mix design
(Without correction for water absorption and moisture content) (all values in kgs.)

Block Composition	Cementitious Material				IOT	Coarse Aggregate	Ceramic Waste	Remark
	GGBS	Fly Ash	Cement	Lime				
A100CW00	300.95	46.3	69.45	46.3	905.28	939.64	--	100%
A090CW10	300.95	46.3	69.45	46.3	905.28	830.35	92.26	90%+10%
A080CW20	300.95	46.3	69.45	46.3	905.28	716.30	179.07	80%+20%
A070CW30	300.95	46.3	69.45	46.3	905.28	621.99	266.57	70%+30%

Table 4.22: Compressive strength obtained on cubes(all values in N/mm^2)

Block Composition	Average Compressive Strength	
	7days	28 days
A100CW00	7.76	8.53
A090CW10	7.20	7.92
A080CW20	7.32	8.05
A070CW30	7.43	8.16

The control mix A100CW00 exhibited the highest compressive strength, with values of 7.76 N/mm² at 7 days and 8.53 N/mm^2 at 28 days. Other trials with partial replacement displayed slightly lower strengths at 7 days but showed a marginally converging trend at 28 days, with A070CW30 attaining 8.16 N/ mm^2. Figure 4.24 presents the compressive strengths of different trial mixes designed for block.

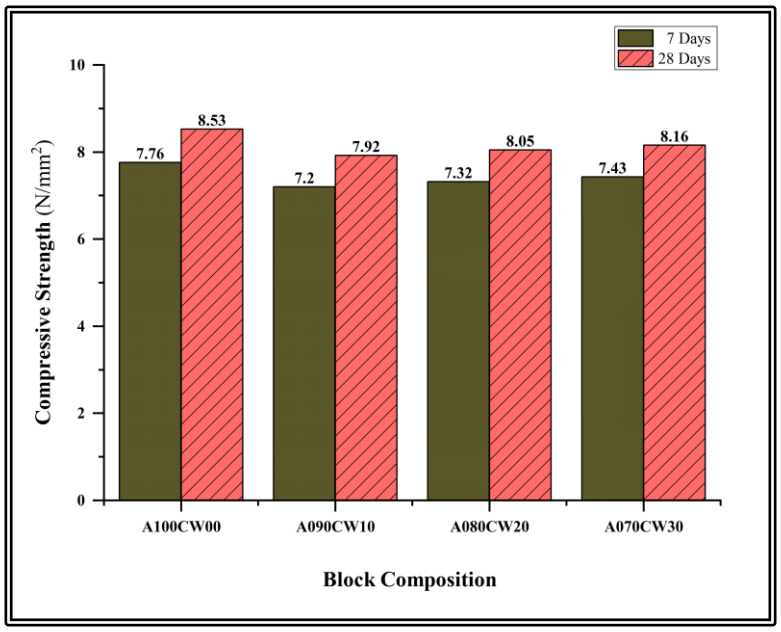


Figure 4.24: Compressive strength of cast cubes at 7 and 28 days

This behaviour indicated that increasing the replacement content did not drastically reduce long-term strength, thereby demonstrating strong potential for sustainable substitutions without significant compromise in compressive performance. Given the importance of compressive strength as a measure of resistance to applied forces (Castillo et al., 2021), masonry blocks emerged as a suitable alternative due to their adherence to IS codes and the substantial demand for such units in construction applications.

4.6.2 Tests on blocks

Various tests evaluated the suitability of the block as a construction material, and this section presents the results.

4.6.2.1 Dimension Test

The dimension test arranged the blocks lengthwise and measured their dimensions. The procedure was repeated this step three times, each time rearranging the blocks and recording the average length. A similar procedure evaluated width and thickness to ensure consistent dimensional assessment. Table 4.23 presents the results of the Dimension Test on the blocks.

Table 4.23: Dimensions of blocks (all values in mm)

Details	No. of units	Dimensions	Average Dimensions	Code recommendations	
L	20	290	295	5680	5920
B		190	192	3720	3880
H		140	142	2740	2860

4.6.2.2 Compressive strength and density of the cast block

The blocks exhibited strong behaviour under compression but remained vulnerable under tension, so the selection of blocks for load-bearing structures critically depends on their capacity to resist compressive stress. Table 4.24 summarizes the compressive strength of blocks for different trials after 7 and 28 days of curing.

The control mix A100CW00 achieved the highest values, with 10.91 N/mm^2 at 7 days and 15.92 N/mm^2 at 28 days. Blends with partial replacement (up to 30%) also developed robust strengths; for instance, A070CW30 reached 15.50 N/mm^2 at 28 days.

Table 4.24: Compressive strength obtained on blocks (all values in N/mm^2)

Block Composition	Average Compressive Strength	
	7days	28 days
A100CW00	10.91	15.92
A090CW10	10.15	14.89
A080CW20	10.39	15.13
A070CW30	10.55	15.50

These results demonstrated that incorporating alternative materials did not significantly diminish compressive strength over time, thereby supporting the feasibility of using such blends in construction while maintaining structural performance. Figure 4.25 illustrates the graphical representation of the compressive strength of the blocks.

Thejas and Hossiney (2022) performed five different block trials and reported a maximum average compressive strength of 7.7 N/mm^2 in a trial incorporating 42% IOTs and 44% GGBS. Such enhancements arose from the intricate reaction mechanisms of GGBS and Lime with IOTs. The complex reaction mechanisms between GGBS, Lime, and IOTs played an important role, as GGBS and Lime interacted with IOTs through two primary pathways: an exothermic reaction accompanied by rapid ion exchange, and a slower, progressive chemical reaction between calcium hydroxide and pozzolanic materials. Furthermore, the extended chemical reaction between calcium and the silica–alumina compounds in IOTs produced highly stable silicates and aluminates, providing stronger bonds and enhanced resistance to deterioration over time. These findings aligned with those of Oti et al. (2009), who observed similar reactions of GGBS and Lime that improved soil properties for construction applications.

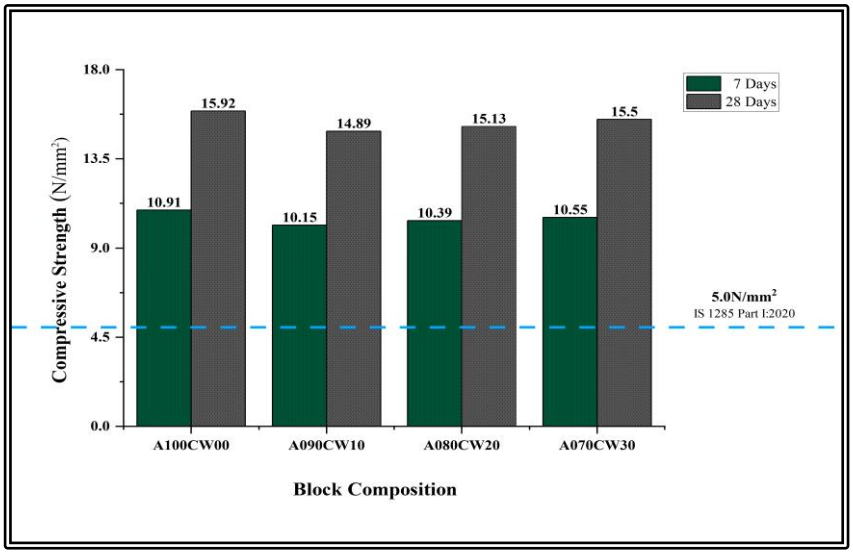


Figure 4.25: Compressive strength of blocks with IS code limits

Elahi et al. (2021) reported that a mixture containing 21% Fly Ash, soil, and Cement exhibited an average compressive stress capacity of 4.4 N/mm^2.

Nagaraja & Shreyasvi (2017) employed Cement, quarry dust, and Lime, along with mining waste materials, and observed that at 40% replacement with mining waste, the compressive strength reached 3.5 N/mm^2. Sekhar and Nayak (2018) manufactured blocks using 75% fine-grained sedimentary rock, 25% GGBS, and 12% Cement, and recorded a compressive strength of 5.5 N/mm^2 at 28 days.

The influence of IOTs on block density, a crucial parameter in masonry design, was systematically investigated. The incorporation of IOTs resulted in a marginally higher density, ranging from 1860 to 2200 kg/m^3 across different block samples. Table 4.25 presents the average bulk densities for the various block mix trials.

Table 4.25: Average bulk densities for various block mix trials (all values in kg/m^3)

Block Composition	Bulk density
A100CW00	2200
A090CW10	2030
A080CW20	1980
A070CW30	1860

This trend was consistent with Abdulrahman's (2015) observations, who reported an increase in density in Sand Crete Blocks (SCB) when IOTs replaced sand (10% to 30%) in a Cement-to-sand mix of 1:6, attributing this behaviour to the denser nature of IOTs compared with sand. Similarly, James et al. (2016) observed a bulk density of 1.85 g/cm^3.

The density enhancements observed in the present block mixes may be associated with the tighter packing of fine IOT particles and their marginally greater specific gravity compared with conventional earthen blocks, which typically exhibit densities of 1.8-1.9 g/cm^3.

Figure 4.26 presents the graphical representation of the bulk densities for the various block trials.

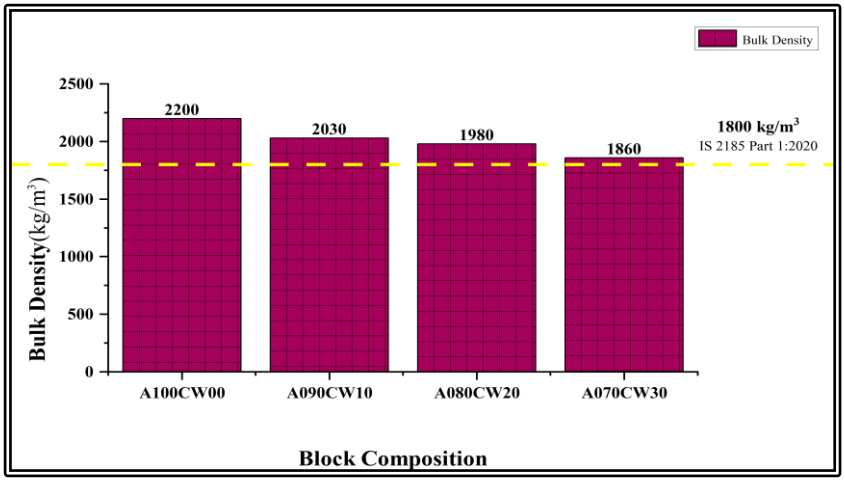


Figure 4.26: Densities of Blocks with IS code limits

4.6.2.3 Water absorption

Water absorption of masonry units plays a crucial role in durability, particularly in resistance to freeze–thaw damage. Lower water absorption indicates a smaller pore volume within the unit, thereby enhancing frost resistance. Typically, standards recommend that the water absorption rate for clay bricks and blocks remain below 20%. Table 4.26 summarizes the water absorption data for the cast blocks.

Table 4.26: Water absorption of various block mix trials (all values in %)

Block Composition	Water Absorption
A100CW00	4.64
A090CW10	5.30
A080CW20	5.10
A070CW30	4.91

In the present study, the mix employing 100% IOTs as fine aggregate, constituting 35% of the total volume, achieved a favourable water absorption range of 4.64-5.30%. The control mix A100CW00 exhibited water absorption of 4.64%. With 10% and 20% replacement of coarse aggregate (A090CW10 and A080CW20), absorption slightly increased to 5.30% and 5.10%, respectively. However, with 30% replacement (A070CW30), absorption decreased to 4.91%. These results indicated that although some mixes showed a marginal increase in water absorption, the effect remained limited, and higher replacement levels could still maintain absorption values close to those of the control, thereby supporting the applicability of these mixes in construction. Figure 4.27 graphically represents the water absorption of blocks.

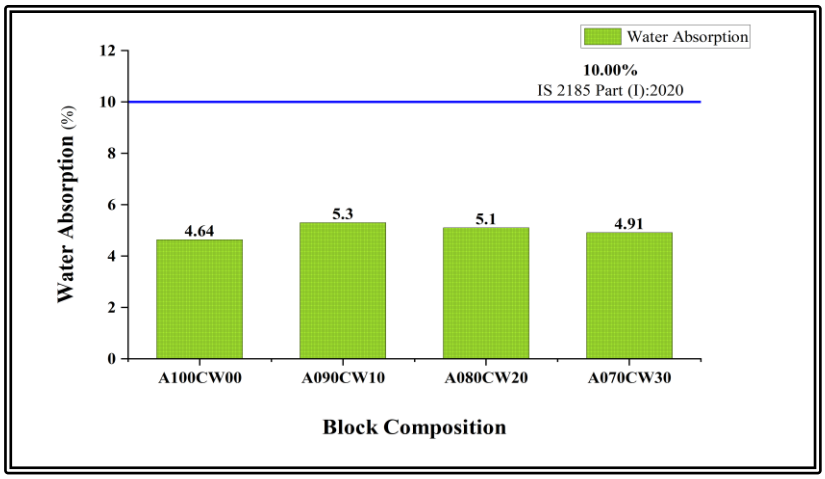


Figure 4.27: Water absorption results of blocks with IS code limits

Thejas and Hossiney (2022) reported optimal performance for 42I-44G blocks (42% IOTs, 44% GGBS) with a water absorption of 13%, and they observed a correlation between increased IOTs content and higher water absorption. Nagaraj et al. (2014) studied compressed stabilized earth blocks (CSEB) incorporating Lime and Cement, achieving a minimum water absorption of 7% for a mixture of 92% soil, 4% Cement, and 4% Lime. Kumar and Surendra (2020) reported water absorption below 18% in all tests with varying Cement percentages.

4.6.2.4 Efflorescence

Block efflorescence arises from the deposition of soluble salts on the block surface. This phenomenon readily occurs in the concurrent presence of three key elements: water-soluble salts, moisture, and a porous block medium. In particular, severe efflorescence can compromise wall plaster and paint adhesion and can negatively affect aesthetics even on unplastered surfaces. Consequently, construction practice favours efflorescence-free blocks. IS 3495 – Part 3: 2019 establishes an efflorescence classification system based on the quantity of salt deposits on the block surface.

Thejas and Hossiney (2022) observed a correlation between increased IOTs content and higher efflorescence, with their 82% IOTs block exhibiting significant salt deposition compared with their other trials, which did not show visible deposits. This observation suggested that a higher IOTs content potentially facilitated salt migration. In contrast, incorporating GGBS and Fly Ash into blocks can increase alumina content, promote stronger cross-linking within the binder phase, and restrict alkali movement, thereby

mitigating efflorescence. In this study, the IOTs content did not produce efflorescence, possibly due to the aforementioned mechanisms.

4.7 SEM-EDX characterization of blocks

Combined SEM-EDX analysis characterized the microstructural morphology and elemental composition of the two block samples. SEM imaging highlighted surface texture, grain size, and porosity, whereas the EDX system quantified and mapped the distribution of primary elements, such as silicon, aluminum, and calcium. Collectively, these analytical methods provided the data required to evaluate the raw source materials, structural quality, and long-term durability of two block compositions.

a) Block composition : A100CW00

The field-emission scanning electron microscopy (FESEM) image and the accompanying energy-dispersive X-ray (EDX) elemental mapping overlay of A100CW00 (analyzed using Zeiss SmartEDX software) depict a heterogeneous microstructure. This morphology and elemental profile were consistent with a synthesized construction material, likely a geopolymer or cementitious composite incorporating industrial by-products such as iron ore tailings, fly ash, or slag.

Figure 4.28 shows SEM micrograph illustrating the microstructural morphology of A100CW00 while Figure 4.29 shows EDX spectrum illustrating the relative abundance of the principal elements detected within A100CW00.

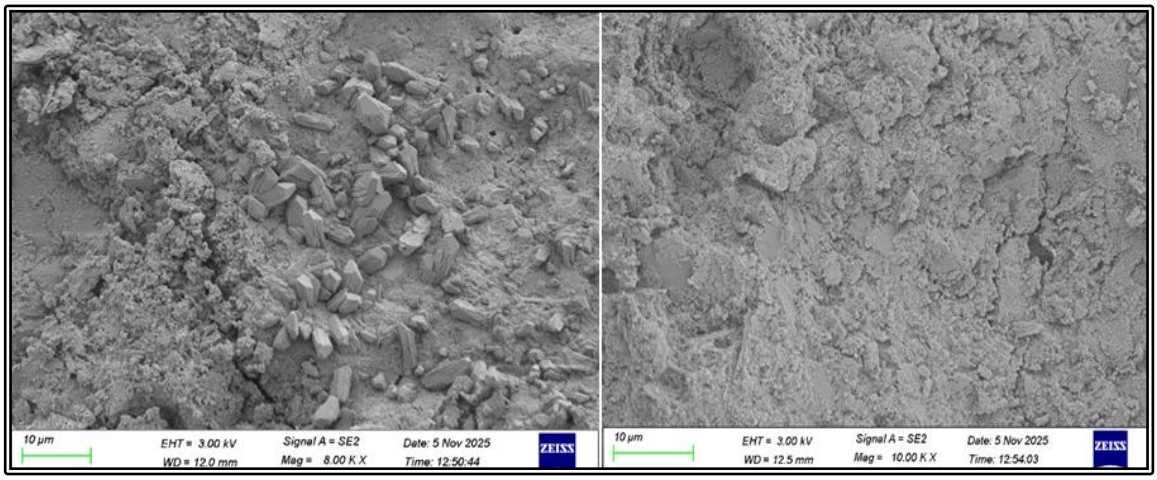


Figure 4.28: SEM micrograph of block composition A100CW00

The FESEM micrograph (~50 µm scale) reveals irregularly shaped, angular aggregates ranging in size from 1 to 10 µm. These particles were clustered, with evident interparticle voids, and exhibited a rough, fractured surface texture, suggesting

mechanical grinding or incomplete densification during synthesis. This porous architecture (approximately 20–30% apparent porosity) could enhance water absorption and permeability in applications such as bricks or stabilized blocks. However, it may compromise early compressive strength while simultaneously promoting long-term durability through secondary hydration or geopolymerization reactions.

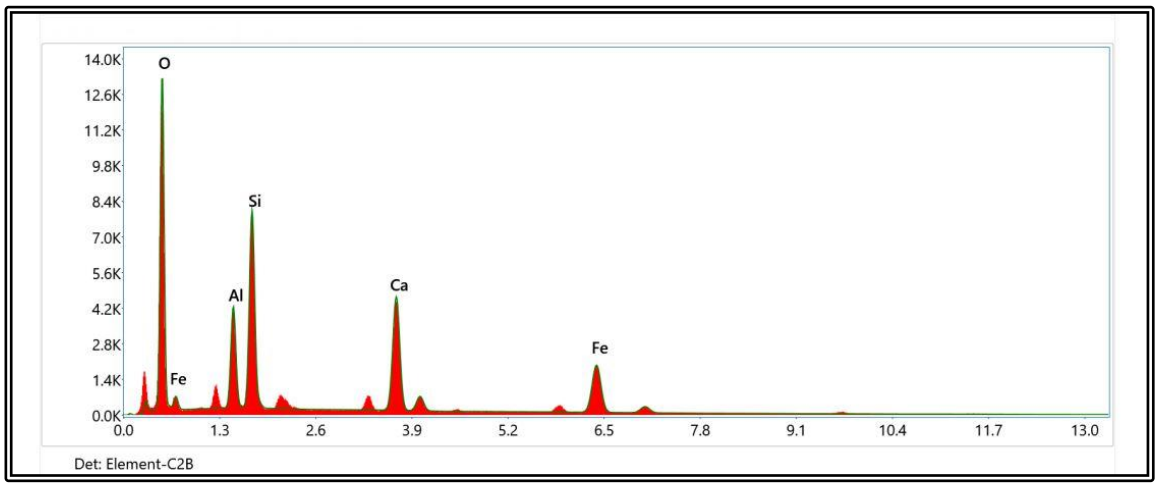


Figure 4.29: EDX spectrum detailing of principal elements for block composition A100CW00

The 20-µm scale EDX overlay map illustrates the spatial distribution of key elements across the matrix. Oxygen (O, green) uniformly pervades the matrix, acting as the primary oxide component. Silicon (Si, red) dominates the particle cores, indicating siliceous phases such as quartz or aluminosilicates. Aluminum (Al, cyan) co-locates with Si in patchy regions, implying the presence of kaolinitic or mullite-derived structures originating from pozzolanic precursors. Calcium (Ca, pink) aggregates in discrete clusters, likely deriving from hydraulic binders (e.g., lime or slag) to form C-S-H gels. Finally, iron (Fe, brown) occupies spotty domains, consistent with hematite or magnetite residues from the tailings; this distinct localization potentially imparts magnetic properties or coloration to the material.

Ultimately, this spatial segregation highlights the sample's phase heterogeneity. The Si-Al-rich zones suggest the formation of geopolymeric networks, whereas the Ca-Fe enrichments point to cementitious inclusions or iron oxides. Overall, these microstructural findings support the potential of A100CW00 for eco-friendly construction applications, such as low-carbon concretes utilizing 20–40% waste substitution. However, further optimization—such as the use of chemical activators to

mitigate porosity—is recommended to correlate these morphological features with improved mechanical performance effectively.

b) Block composition: A90CW10

FESEM and EDX mapping of A90CW10 reveal a compact, heterogeneous microstructure characteristic of a synthesized construction composite. This morphology indicates the successful incorporation of pozzolanic wastes—such as fly ash, slag, or tailings—within an alkali-activated or blended cement matrix. Figure 4.30 shows SEM micrograph illustrating the microstructural morphology of A90CW10 while Figure 4.31 shows EDX spectrum illustrating the relative abundance of the principal elements detected within A90CW10.

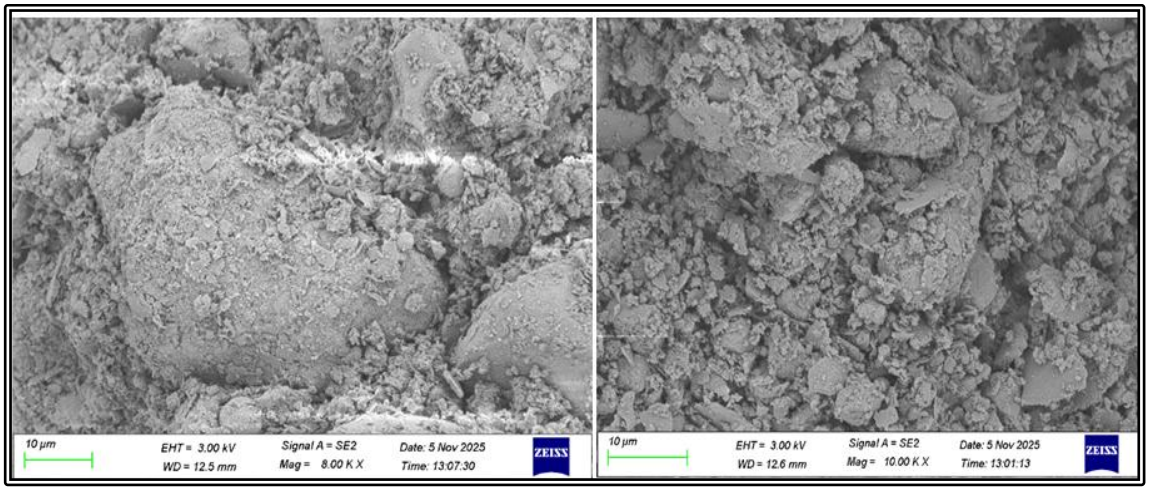


Figure 4.30: SEM micrograph of block composition A90CW10

A100CW00 achieves finer particle aggregation and substantially lower visible porosity than A090CW10. Densely packed, angular grains spanning sub-micron to 5 µm dimensions dominate the matrix. The restricted void network (approximately 10–20% apparent porosity) evidences robust densification, driven by advanced geopolymerization or secondary hydration reactions. This consolidated architecture directly promotes superior mechanical properties, such as compressive strength, while simultaneously restricting permeability—essential traits for sustainable brick or pavement applications.

High-resolution (5-µm) EDX mapping delineates the spatial elemental distribution. Oxygen (green) ubiquitously permeates the material, forming the foundational oxide backbone. Silicon (red) is heavily distributed within the particle cores, reflecting robust siliceous frameworks (e.g., quartz or C-S-H gels). Aluminum (cyan) co-precipitates

with silicon across heterogeneous aluminosilicate domains, originating from the reactive precursors. Calcium (pink) aggregates into discrete clusters, signaling the formation of hydraulic phases from calcareous binders. Iron (brown) segregates into localized, spotty

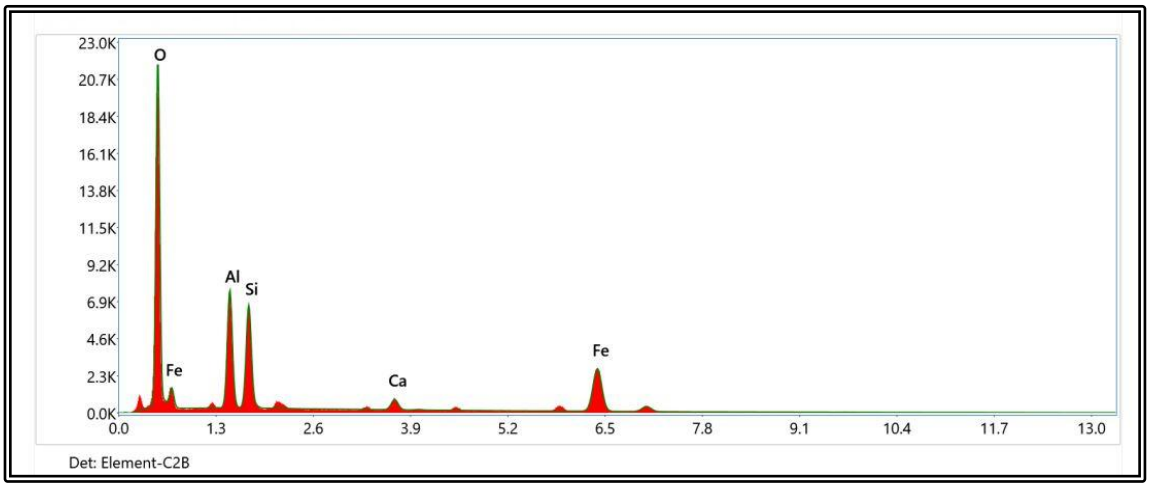


Figure 4.31: EDX spectrum detailing of principal elements for block composition A90CW10

enrichments, representing remnant oxide inclusions (e.g., hematite) from the raw tailings.

Extensive Si-Al networks drive the primary pozzolanic activity, whereas distinct Ca-Fe zones facilitate localized cementitious bonding. Together, these microstructural mechanics validate A90CW10 as a high-performance eco-material capable of incorporating 30–50% waste. Although advanced processing techniques (e.g., finer grinding) stand to optimize uniformity further, the integration of quantitative EDX (e.g., atomic ratios: O ~50–60%, Si ~25–35%, Al ~5–15%, Ca ~5–10%, Fe ~3–8%) and nano indentation data promises to refine the current mechanistic understanding of phase evolution and long-term durability.

4.8 Statistical analysis of various parameters of cast blocks

The statistical data provide a comprehensive analysis of the physical and mechanical properties of the various block mix trials, explicitly focusing on compressive strength, bulk density, and water absorption, as presented in Table 4.27. At 7 days, the compressive strength means ranged from 10.15 N/mm² (A090CW10) to 10.91 N/mm² (A100CW00). The corresponding coefficients of variation indicated reliable consistency across samples, with values not exceeding 0.073.

Table 4.27: Statistics of various parameters of block

Block Composition	Mean	Standard Deviation	Lower 95% CI of Mean	Upper 95% CI of Mean	SE of mean	Coefficient of Variation
7 days Compressive Strength						
A100CW00	10.91	0.344	10.48	11.34	0.154	0.032
A090CW10	10.15	0.626	9.37	10.93	0.280	0.062
A080CW20	10.39	0.757	9.45	11.33	0.338	0.073
A070CW30	10.55	0.459	9.98	11.12	0.205	0.044
28 days Compressive Strength						
A100CW00	15.92	0.359	15.47	16.37	0.161	0.023
A090CW10	14.89	0.282	14.54	15.24	0.126	0.019
A080CW20	15.13	0.443	14.58	15.68	0.198	0.029
A070CW30	15.50	0.500	14.88	16.12	0.224	0.032
Bulk Density						
A100CW00	2200	138.834	2027.64	2372.36	62.089	0.063
A090CW10	2030	81.548	1928.76	2131.24	36.469	0.040
A080CW20	1980	91.992	1865.80	2094.20	41.140	0.046
A070CW30	1860	82.614	1757.44	1962.56	36.946	0.044
Water Absorption						
A100CW00	4.64	0.202	4.39	4.89	0.090	0.043
A090CW10	5.31	0.251	5.00	5.62	0.112	0.047
A080CW20	5.10	0.193	4.86	5.34	0.086	0.038
A070CW30	4.91	0.198	4.67	5.15	0.088	0.040

By 28 days, all mixes registered a notable increase in strength, with the control mix A100CW00 attaining 15.92 N/mm^2 and the alternative mixes maintaining values between 14.89 and 15.50 N/mm^2. These outcomes demonstrated that partial replacement within the binder system did not significantly compromise compressive performance, while low standard deviations and coefficients of variation confirmed reproducibility.

Bulk density declined systematically with increasing substitution, from 2200 kg/m^3 in A100CW00 to 1860 kg/m^3 in A070CW30. The low coefficients of variation (ranging from 0.040 to 0.063) further confirmed the consistency of the block formation process. Water absorption values ranged from 4.64% to 5.31%, with minimal intergroup

differences, indicating satisfactory durability performance even with partial replacement.

4.9 Performance assessment and insights of pavers and tiles

The following section details the mix proportions adopted for pavers and tiles and presents the results of laboratory tests evaluating their properties and assessing their suitability for construction applications.

4.9.1 Mix proportion for pavers and tiles

The mix design for pavers and tiles systematically incorporated IOTs in accordance with IS 10262:2019 specifications to optimize both performance characteristics and economic viability. The mix followed the proportions listed in Table 3.14, and Table 4.28 presents the quantity of material used per m³ of mix.

Table 4.28: Materials and their proportions for IOT mix design
(Without correction for water absorption and moisture content) (all values in kgs.)

Designation	Cementitious Material		Fine aggregate		Coarse Aggregate	Admixture	Remarks
	Cement	GGBS	IOT	Crushed Stone Sand			
C100T00	420	00	0	836	1090	1.26	0% IOT
C100T10	420	00	98	753	1090	1.26	10% IOT
C100T20	420	00	196	669	1089	1.47	20% IOT
C100T30	420	00	293	585	1089	1.68	30% IOT
C100T40	420	00	391	501	1089	2.10	40% IOT
C100T50	420	00	488	417	1087	2.94	50% IOT
C080T00	336	84	0	833	1085	1.26	0% IOT
C080T10	336	84	97	749	1085	1.26	10% IOT
C080T20	336	84	195	666	1085	1.47	20% IOT
C080T30	336	84	292	583	1084	1.68	30% IOT
C080T40	336	84	389	499	1084	2.10	40% IOT
C080T50	336	84	486	415	1082	2.94	50% IOT
C060T00	252	168	0	829	1080	1.26	0% IOT
C060T10	252	168	97	746	1080	1.26	10% IOT
C060T20	252	168	194	663	1080	1.47	20% IOT
C060T30	252	168	291	580	1079	1.68	30% IOT
C060T40	252	168	387	497	1079	2.10	40% IOT
C060T50	252	168	483	413	1077	2.94	50% IOT

The casting procedure molded standard cubic specimens measuring 150 mm × 150 mm × 150 mm for each experimental trial, and subsequent compressive strength tests evaluated their performance. The resulting strength values for all cast cubes are presented in Table 4.29 and illustrated graphically in Figure 4.32.

Table 4.29: Compressive strength of cubes (all values in N/mm^2)

Cementitious Content →	**100% Cement**		**80% Cement +20% GGBS**		**60% Cement +40% GGBS**	
IOT % ↓	7 days	28 days	7 days	28 days	7 days	28 days
0	30.67	46.85	27.38	43.52	26.61	42.30
10	32.73	47.83	29.77	45.37	27.93	43.73
20	30.50	43.55	28.25	43.61	25.51	39.52
30	28.80	39.72	26.01	41.61	23.38	35.97
40	26.65	36.04	25.26	37.71	21.33	33.87
50	24.66	32.65	23.91	35.47	19.48	30.72

The experimental results showed that incorporating IOT up to 10% enhanced both early-age and long-term compressive strength across all binder systems. At 7 days, the strength of pure cement mixes increased from 30.67 N/mm^2 (0% IOT) to 32.73 N/mm^2 (10% IOT), while the 80% cement + 20% GGBS and 60% cement + 40% GGBS blends peaked at 29.77 N/mm^2 and 27.93 N/mm^2, respectively, before declining at higher IOT levels.

By 28 days, the 10% IOT mixes achieved 47.83 N/mm^2 (100% cement), 45.37 N/mm^2 (80/20), and 43.73 N/mm^2 (60/40), reflecting continued hydration and GGBS pozzolanic activity. Of the 18 compositions tested, the 100% cement and 80% cement + 20% GGBS mixes fell below the target strength at 40% and 50% IOT, respectively, whereas the 60% cement + 40% GGBS blend did so at 30%, 40%, and 50% IOT. These findings highlighted the necessity of balancing IOT and GGBS content: up to 10% IOT exploited micro-filler benefits without diluting cementitious material, and GGBS replacements up to 40% yielded sustainable long-term strength gains, provided appropriate mix design managed early-age strength.

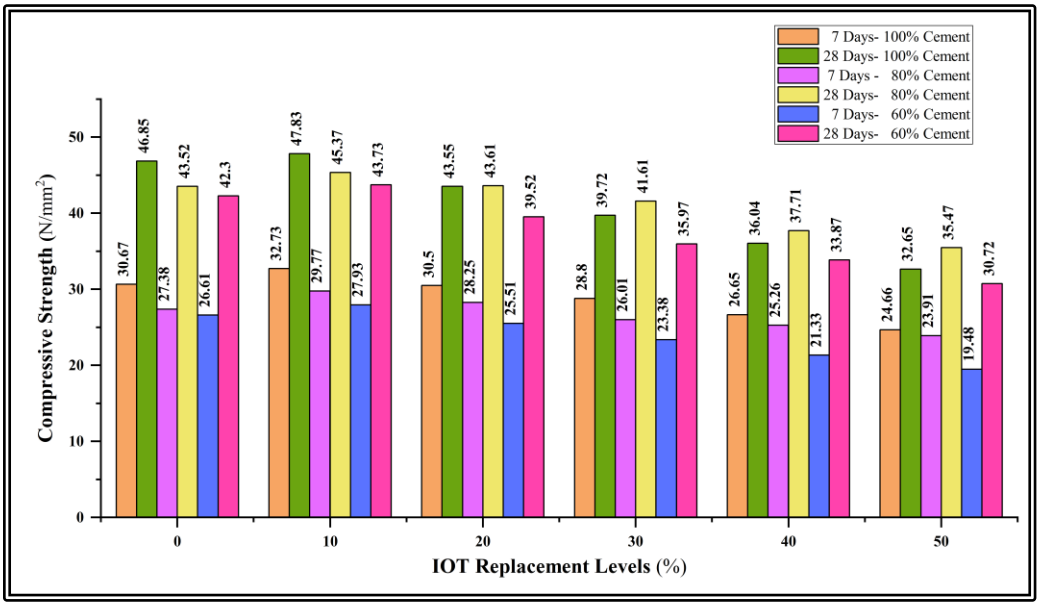


Figure 4.32: Compressive strength of paver mix at 7 and 28 days for various IOT replacement levels

Previous studies reported similar trends, indicating that IOT substitution between 10% and 40% optimizes aggregate performance, while higher replacements impair workability and strength. Adiguzel et al. (2022) identified 10%–40% tailings as the optimal fine-aggregate replacement range, and George (2023) recorded up to an 18.4% strength gain in M20 concrete with 20%–60% IOT. Mendes et al. (2021) reported workability loss at 30% IOT, and the present investigation observed a similar phenomenon at 40% tailings. Chinnappa & Karra (2020) reported compressive strengths around 50 N/mm² at a water–cement ratio of 0.4 with IOT replacements between 10% and 50%, attributing the elevated strength to the incorporation of Alcofine additives, while Jiang et al. (2019) found a peak strength of 42.8 N/mm² at 30% substitution. The measured compressive strengths provided the basis for casting pavers and tiles at an industrial facility, using the identified mixes to translate laboratory performance into production-scale units. The following section details the results of tests conducted on these cast specimens.

4.9.2 Tests on pavers and tiles

4.9.2.1 Dimension test

The dimensional test of pavers served as a critical quality-control procedure that verified compliance with specified design parameters. This evaluation ensured a consistent and aesthetically uniform pavement surface. Uniform dimensions promoted

precise interlocking and seamless alignment of pavers, thereby reducing gaps and surface irregularities. In addition, dimensional accuracy significantly enhanced the structural integrity and load distribution capacity of the pavement assembly. Table 4.30 systematically presents detailed dimensional data for the pavers, emphasizing their importance in the quality assurance process within the manufacturing workflow.

Table 4.30: Dimensions of pavers (all values in mm)

Paver Designation	Average Length	Average Width	Average Thickness
C100T00	201	101	61
C100T10	201	100	61
C100T20	200	100	60
C100T30	200	100	61
C100T40	201	101	61
C100T50	201	100	60
C080T00	200	101	60
C080T10	201	100	61
C080T20	201	101	60
C080T30	201	101	60
C080T40	200	100	60
C080T50	201	101	60
C060T00	200	100	61
C060T10	200	100	61
C060T20	201	101	60
C060T30	201	100	61
C060T40	200	101	60
C060T50	200	100	61

4.9.2.2 Water absorption

Water absorption, as a fundamental material property, governs the durability and performance of pavers and tiles across various environments. This parameter quantified the amount of water a product could absorb, which, in turn, influenced vulnerability to frost damage, efflorescence, and overall service life. Material composition, porosity, and specific manufacturing processes largely dictated the degree of water absorption,

and these factors collectively determined the finished product's density and microstructure.

Tiles and pavers with lower water absorption rates typically exhibited enhanced longevity, greater resistance to mechanical and environmental stresses, and improved performance in moist or frost-prone settings. Understanding water absorption was essential to materials selection and quality control during the manufacture and application of pavers and tiles. Table 4.31 reports the results of water absorption tests carried out on paver samples.

Table 4.31: Water absorption of paver mix trials (all values in %)

Paver Designation	Mean Water Absorption	Paver Designation	Mean Water Absorption	Paver Designation	Mean Water Absorption
C100T00	2.15	C080T00	3.29	C060T00	3.68
C100T10	1.77	C080T10	2.73	C060T10	3.49
C100T20	3.52	C080T20	3.57	C060T20	5.28
C100T30	5.18	C080T30	3.75	C060T30	7.03
C100T40	7.49	C080T40	6.17	C060T40	8.11
C100T50	9.96	C080T50	7.67	C060T50	10.61

The experimental results showed that replacing iron ore tailings (IOT) with crushed sand in paver production produced a marked increase in water absorption as the cement content decreased from 100% to 60%. Pavers made with 100% cement demonstrated water absorption values ranging from 1.77% to 9.96%, conversely, mixtures containing 80% and 60% cement exhibited water absorption values spanning from 2.73% to 7.67% and from 3.49% to 10.61%, respectively, across the 0% to 50% IOT replacement range.

This progressive trend demonstrated that elevating the IOT content increased both porosity and void spaces, driven by the distinct morphological characteristics of the ore tailings compared to standard materials. Furthermore, within specific cement groups, the rising absorption rates proved that combining dense IOT concentrations with modified design parameters significantly intensified matrix permeability. Consequently, these outcomes aligned with previous studies establishing a direct correlation between sustainable IOT utilization and higher water absorption.

Filho et al. (2017) reported that pavers produced with IOT (10%, 20%, and 80%) exhibited reduced water absorption and showed at least a 25% decrease in voids compared with those made with sand alone. Sá et al. (2022) found water absorption values of 8.89% and 9.58% for mixtures containing 10% and 20% IOT, respectively. Figure 4.33 illustrates the water absorption of pavers for various IOT replacement levels.

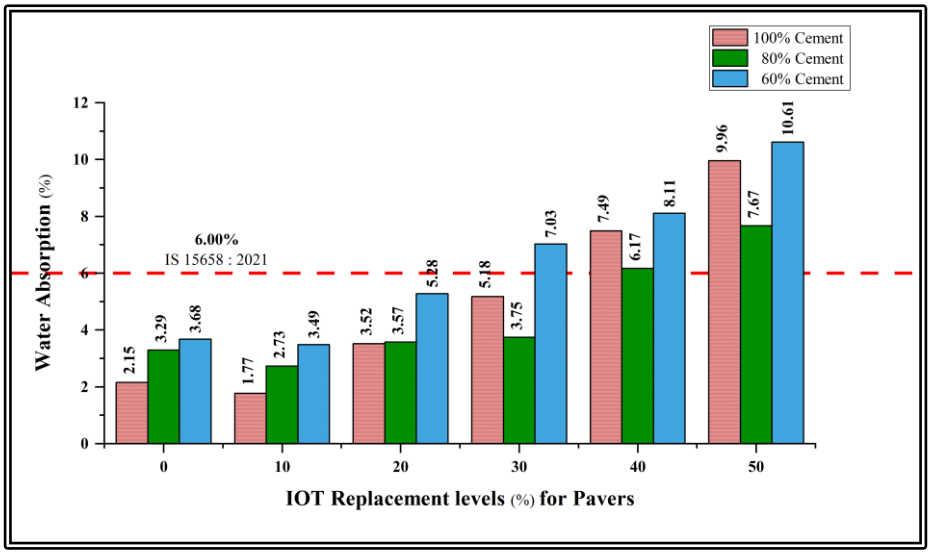


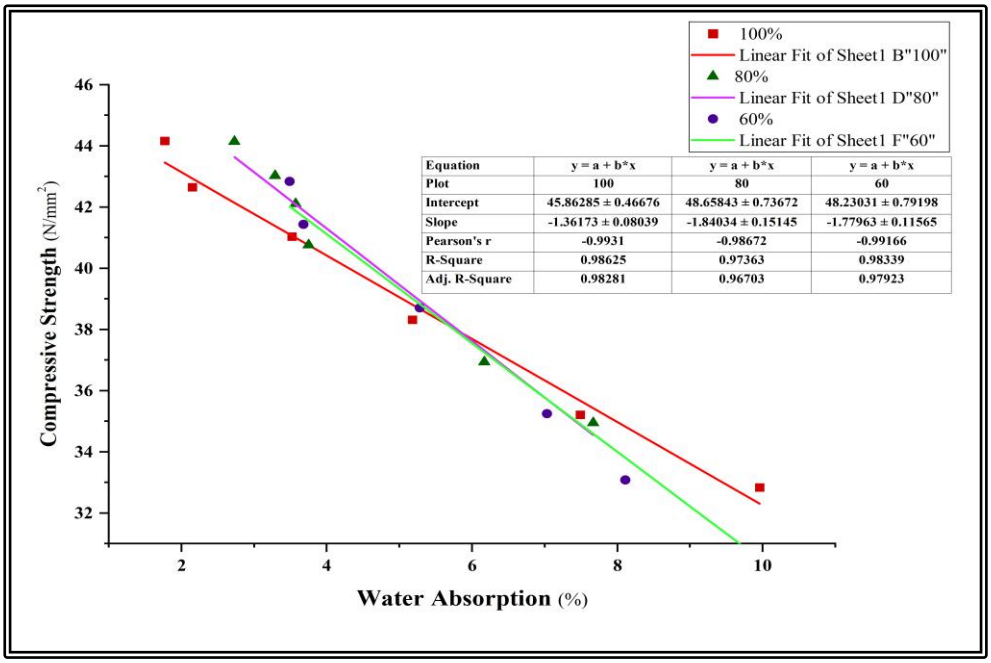
Figure 4.33: Water absorption of pavers with IS code limits

Farooq et al. (2023) reported water absorption values of 6.34% and 5.3% for recycled aggregate concrete pavers with cement dosages of 15% and 20%, respectively. Mtarfi et al. (2023) observed that the water absorption of concrete paving stones increased from 2.3% to 3.8% depending on the water-to-cement ratio when using electric slag, and Ravikumar et al. (2012) reported water absorption values ranging from 2.4% to 2.5% for mixes containing 5% to 25% IOT.

Several mixes developed in the present study exhibited water absorption percentages below the 6% threshold specified by IS 15658:2021 for concrete pavers, thereby indicating compliance with national standards for durability and quality. Furthermore, these values were lower than those reported in comparable literature for similar or lower iron ore tailings (IOT) replacement levels, demonstrating the effectiveness of the mix design strategies implemented in this work.

Figure 4.34 illustrates the relationship between water absorption and compressive strength for composite specimens containing different cement levels (100%, 80%, and 60%). The graph displays three sets of data points, each representing a cement

proportion, along with the corresponding linear regression lines and associated statistical metrics, including intercept, slope, residual sum of squares, Pearson's r, and R-square. The results indicated a strong negative linear correlation between water absorption and compressive strength across all mixes, as confirmed by high absolute values of Pearson's r and R-square, indicating strong model accuracy.



Equation	y = a + b*x	y = a + b*x	y = a + b*x
Plot	100	80	60
Intercept	45.86285 ± 0.46676	48.65843 ± 0.73672	48.23031 ± 0.79198
Slope	-1.36173 ± 0.08039	-1.84034 ± 0.15145	-1.77963 ± 0.11565
Pearson's r	-0.9931	-0.98672	-0.99166
R-Square	0.98625	0.97363	0.98339
Adj. R-Square	0.98281	0.96703	0.97923

Figure 4.34: Relationship between water absorption and compressive strength of pavers

Specimens with lower cement content (60%) exhibited a steeper reduction in compressive strength with increasing water absorption, highlighting the greater impact of water penetration on mechanical properties in these composites. These findings demonstrated that optimizing water absorption was essential to ensure adequate mechanical strength, particularly when implementing higher cement replacement levels in sustainable construction materials, and further reinforced the reliability and relevance of the presented data for evaluating material durability in advanced composite systems.

4.9.2.3 Compressive strength

Compressive strength dictates the structural integrity, load-bearing capacity, and durability of concrete pavers by preventing cracking and deformation under varying conditions. Consequently, specific applications demand strength thresholds tailored to anticipated traffic and environmental exposures.

Table 4.32 details the laboratory-tested compressive strength values for the paver specimens.

Table 4.32: Compressive strength of pavers (all values in N/mm^2)

Paver Composition	Average Compressive Strength		
	7days	**28 days**	**56 days**
C100T00	29.21	42.65	45.63
C100T10	30.89	44.17	46.47
C100T20	28.90	41.04	42.68
C100T30	27.18	38.32	39.48
C100T40	25.15	35.21	36.09
C100T50	23.80	32.84	33.50
C080T00	26.70	43.03	52.41
C080T10	28.10	44.14	53.63
C080T20	26.70	42.11	50.19
C080T30	25.90	40.76	48.21
C080T40	23.80	36.94	43.25
C080T50	21.70	34.95	40.54
C060T00	25.10	41.44	51.8
C060T10	25.50	42.84	53.08
C060T20	24.20	38.71	47.77
C060T30	22.10	35.24	42.99
C060T40	20.10	33.08	40.69
C060T50	18.40	30.09	37.31

The C100Tx series attained compressive strengths of 23.8–30.89 N/mm² at 7 days and 32.84–44.17 N/mm² at 28 days, while the C080Tx and C060Tx series developed slightly lower early-age strengths but comparable or superior values at later ages. At 7 days, the C080Tx and C060Tx mixes achieved 21.70–28.10 N/mm² and 18.40–25.50 N/mm², respectively, with the 28-day strengths increasing to 34.95–44.14 N/mm² for C080Tx and 30.09–42.84 N/mm² for C060Tx across the different IOT replacement levels. Figure 4.35 illustrates the evolution of compressive strength at 7, 28, and 56 days for all IOT dosages, confirming the pronounced strength gain of the C080Tx and C060Tx mixes between 7 and 28 days.

Figure 4.35 presents the compressive strengths at 7, 28, and 56 days while Figure 4.36 highlights compressive strength of paver at 28 and 56 days for various IOT replacement levels.

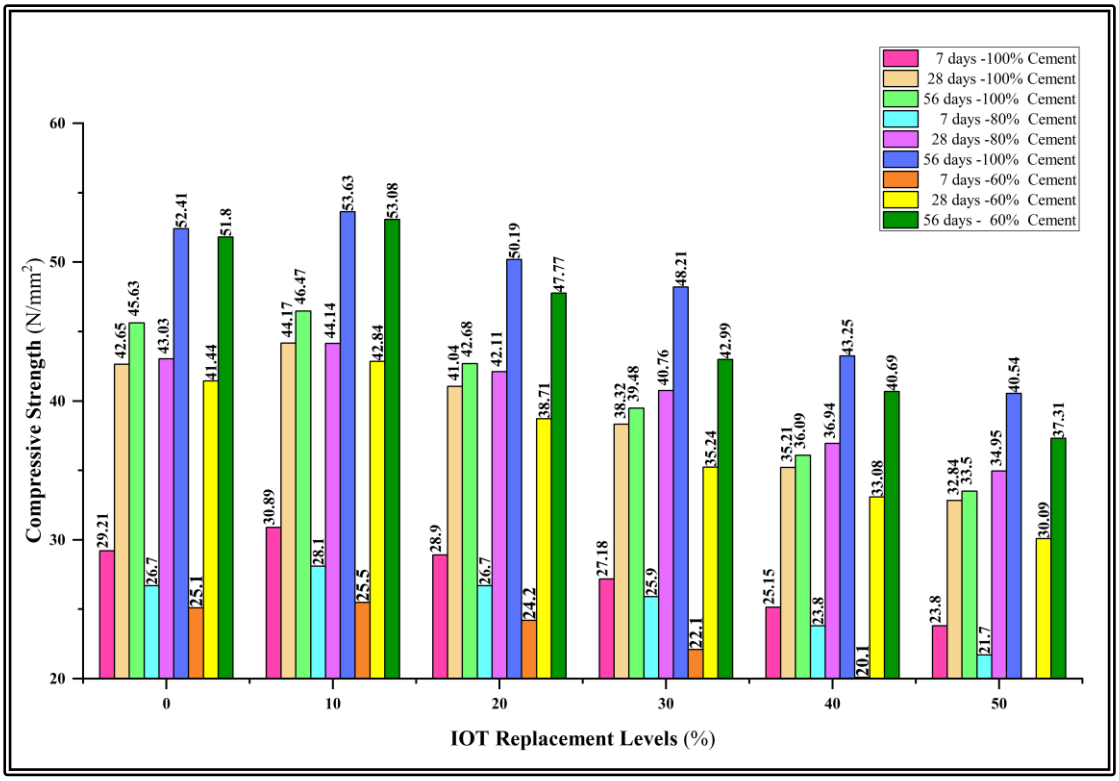


Figure 4.35: Compressive strength of paver at 7, 28 and 56 days for various IOT replacement levels

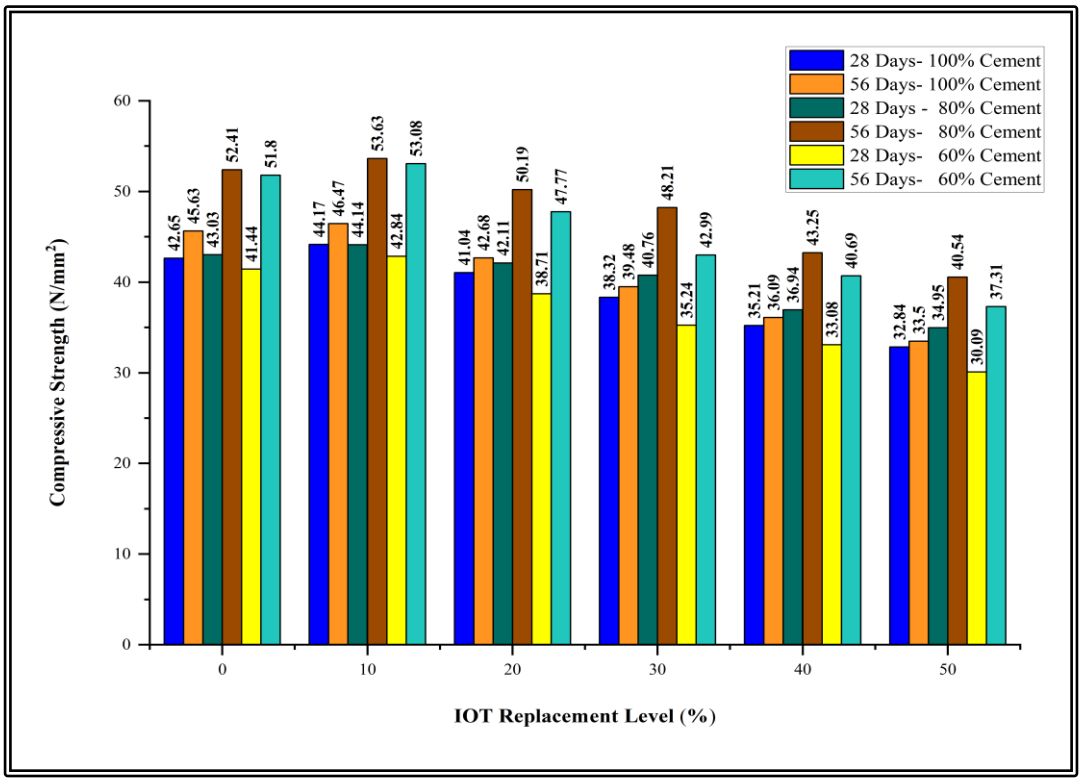


Figure 4.36: Compressive strength of paver at 28 and 56 days for various IOT replacement levels

Incorporation of 10% IOT produced a consistent enhancement in mechanical performance at all cement contents. At 28 days, the 10% IOT mixes reached 44.17 N/mm^2 (C100T10), 44.14 N/mm^2 (C080T10), and 42.84 N/mm^2 (C060T10). The best-performing mixes, C080T10 (53.63 N/mm^2) and C060T10 (53.08 N/mm^2), exceeded the optimum C100 mix by more than 14% at 56 days, attributable to improved particle packing and microstructural densification. Iron ore tailings (IOT) concentrations exceeding 10% progressively reduced compressive strength, indicating that excessive tailings compromised the structural integrity of the binder matrix.

Despite the reduction in cement content and the inclusion of IOT, all 18 paver formulations satisfied the minimum M30 strength requirement. However, seven mixes did not meet the specified target strength at 28 days. Compressive strength, therefore, remains a key design parameter, as it governs pavers ability to resist traffic-induced stresses, control cracking and deformation, and maintain surface regularity under varying loading and environmental conditions. Accordingly, the selection of suitable mix proportions for specific applications must consider anticipated traffic intensity and exposure conditions.

Comparisons with the literature further support the present findings. Ravikumar et al. (2012) reported that 5% IOT replacement to Cement in M25 concrete produced compressive strengths of 28.35 N/mm^2 at 7 days and 37.11 N/mm^2 at 28 days, and considered up to 15% replacement feasible. Kumar et al. (2014) observed 28-day peak strength of 55.10 N/mm^2 with 40% IOT in the absence of GGBS, surpassing the control mix. For high-strength pavers, Filho et al. (2017) achieved 62 N/mm^2 in M50 units with 10% IOT using 150 kg of cement for 108 pavers, whereas the present work achieved comparable strength levels with only 20.16 kg of cement for 50 pavers, demonstrating the binder efficiency of the IOT–GGBS system. Previous studies by Oner and Akyuz (2007), Arivalagan (2014), and Dom et al. (2022) likewise corroborate the strength-enhancing effects of GGBS under prolonged curing, which align with the long-term performance trends observed in this investigation.

Figure 4.37 quantifies the influence of IOT content through linear regression for the 100%, 80%, and 60% cement systems, showing a clear negative correlation between IOT replacement level and compressive strength for all binders.

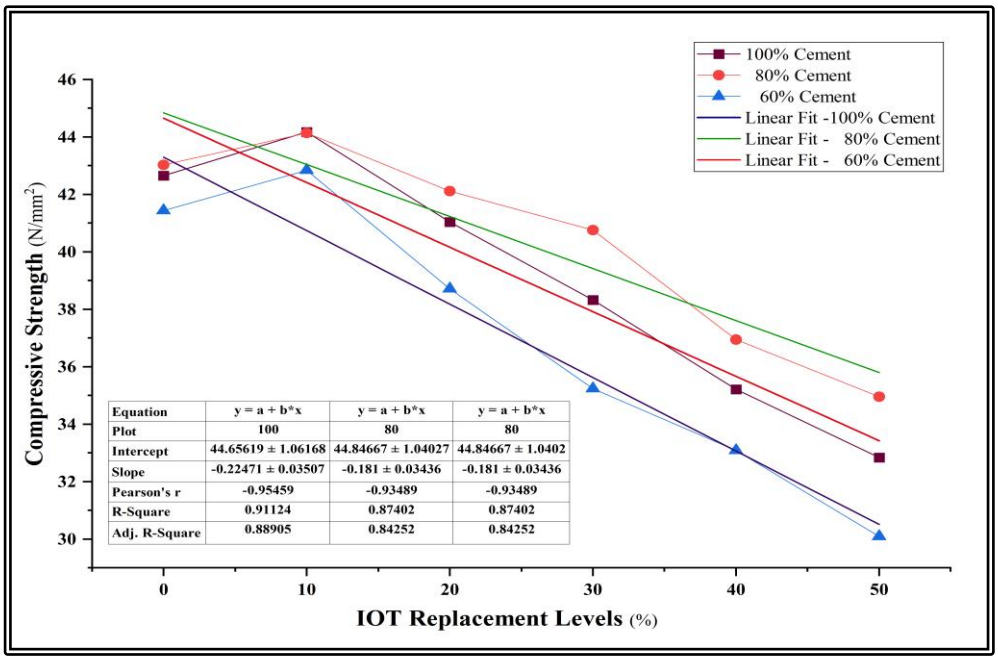


Figure 4.37: Relationship between compressive strength and IOT replacement levels for 100%, 80%, and 60% cement mixes

The regression parameters (slope, intercept, Pearson's r, and R^2) confirm the reliability of this trend, with a steeper reduction in strength observed in the 60% cement mixes compared with the 80% and 100% systems. These results emphasize the need to optimize IOT dosage to balance sustainability with structural performance and demonstrate that 10% replacement represents a practical compromise for green paver production.

4.9.2.4 Tensile splitting strength

Tensile splitting strength served as a key performance indicator for concrete pavers, reflecting their ability to resist crack initiation and propagation under tensile loads. Whereas compressive strength quantified resistance to compressive forces, tensile splitting strength evaluated performance when opposing forces attempted to pull the material apart.

High splitting tensile strength correlated directly with enhanced crack resistance, improved durability, and overall structural integrity of the pavers. Table 4.33 summarizes the measured tensile splitting strengths for all paver mixes. The tensile splitting strength results revealed a clear, consistent trend across all three cement content series (100%, 80%, and 60%) when IOTs were incorporated. Each series attained its peak tensile splitting strength at a 10% IOT replacement level.

Table 4.33: Tensile splitting strength of pavers (all values in N/mm^2)

Paver Designation	Average Tensile Splitting Strength	Paver Designation	Average Tensile Splitting Strength	Paver Designation	Average Tensile Splitting Strength
C100T00	6.59	C080T00	6.10	C060T00	5.83
C100T10	6.79	C080T10	6.36	C060T10	6.02
C100T20	6.09	C080T20	6.16	C060T20	5.54
C100T30	5.67	C080T30	5.73	C060T30	5.35
C100T40	5.26	C080T40	5.23	C060T40	5.06
C100T50	4.90	C080T50	4.88	C060T50	4.85

In the C100 series, tensile splitting strength increased from 6.59 N/mm^2 in the control mix (C100T00) to 6.79 N/mm^2 at 10% IOT (C100T10), before gradually declining to 4.90 N/mm^2 at 50% IOT (C100T50). Similarly, the C080 series recorded an increase from 6.10 N/mm^2 (C080T00) to 6.36 N/mm^2 (C080T10), followed by a reduction to 4.88 N/mm^2 at 50% IOT (C080T50). The C060 series followed the same pattern: strength peaked at 6.02 N/mm^2 for C060T10 (versus 5.83 N/mm^2 for C060T00) and decreased to 4.85 N/mm^2 at the highest IOT level (C060T50). These results demonstrated that reducing the cement content to 80% or 60% did not diminish the benefits of limited IOT substitution, as the gains at 10% IOT remained comparable across all cement contents. A 10% IOT replacement effectively refined the microstructure by improving particle packing and crack resistance while maintaining binder efficiency. Beyond the 10% replacement threshold, tensile splitting strength declined progressively, reflecting the dilution of cementitious phases by the essentially inert tailings and the disruption of binder continuity at higher IOT levels. Consequently, maintaining IOT replacement at or below 10% remained essential for maximizing tensile splitting performance in sustainable paver formulations.

Compared with existing studies, the present investigation achieved significantly improved performance. Srividya et al. (2022) reported a split tensile strength of 3.81 N/mm^2 for alkali-activated binder blocks, and Mtarfi et al. (2023) achieved 4.55 N/mm^2 using electric slag. Ugama et al. (2014) reported splitting tensile strengths ranging from 2.5 N/mm^2 to 2.8 N/mm^2 in concrete with 20% IOT as a replacement for river sand. In contrast, the current investigation reported tensile splitting strengths ranging from 4.85 N/mm^2 to 6.79 N/mm^2 across all mixes, surpassing both these literature values and the

relevant Indian Standard code minimums. This superior performance underscored the dual advantage of IOTs: acting as microstructural enhancers at low replacement levels and contributing to sustainability by valorizing industrial by-products. The optimized blend, particularly at 10% IOT, balances strength enhancement with material efficiency, providing a robust, eco-friendly solution for high-performance concrete pavers.

Figure 4.38 presents the correlation between splitting tensile strength (N/mm^2) and compressive strength (N/mm^2) for composite specimens with varying cement contents (100%, 80%, and 60%, represented as CS 100; CS 80, and CS 60, respectively) that incorporated iron ore tailings (IOT) as a replacement material.

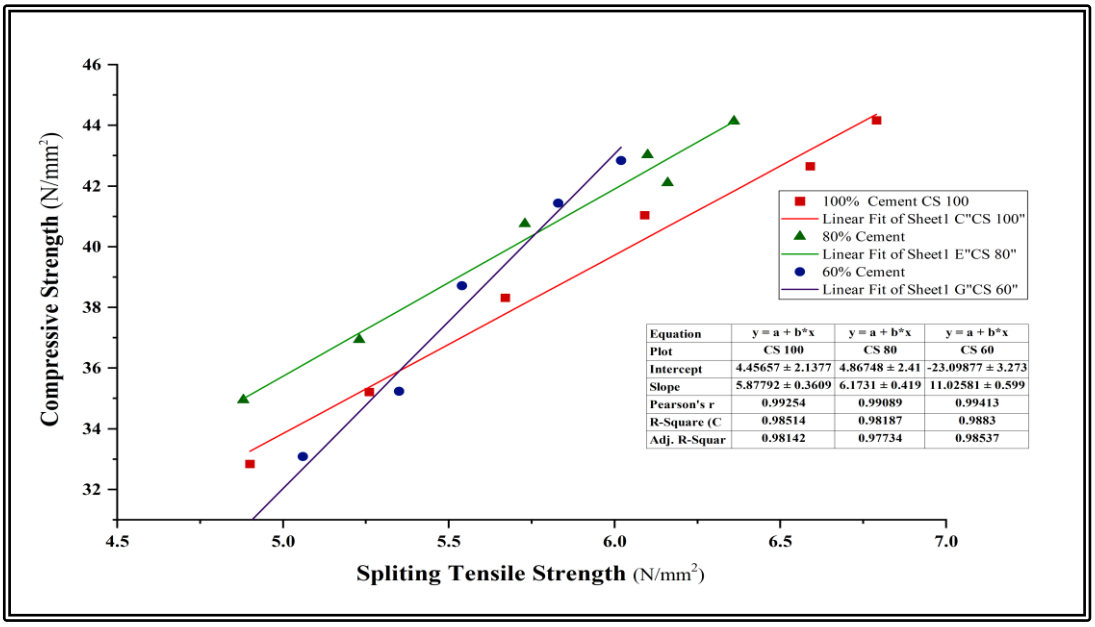


Figure 4.38: Relationship between splitting tensile strength and compressive strength

Three distinct linear regression lines appear, each corresponding to a specific cement content level, with accompanying statistical parameters, including intercept, slope, Pearson's r, R-square, and adjusted R-square, displayed in adjacent tables. The results demonstrated a strong, positive linear relationship between splitting tensile strength and compressive strength across all mixes, with R-square values consistently exceeding 0.98, indicating excellent model fit and predictive power.

The CS 60 mix, with the lowest cement content, shows the steepest regression slope (11.02581) compared with CS 80 (6.1731) and CS 100 (5.87792), indicating greater sensitivity of strength to changes in the splitting tensile–compressive strength relationship at higher levels of cement replacement. This steeper response suggests that

composites with significantly reduced cement exhibit more pronounced microstructural modifications and altered bonding mechanisms due to the lower cement-to-supplementary-material ratio.

These findings emphasize the pivotal role of iron ore tailings in reshaping stress distribution and failure modes within the matrix, thereby influencing both tensile and compressive behaviour concurrently. The strong correlations across all mixes confirm the structural adequacy of IOT as a sustainable replacement material and show that, despite variations in cement content, the fundamental relationship between splitting tensile and compressive strength remains consistent and predictable, which is crucial for design and quality control in practical applications involving waste-derived constituents.

4.9.2.5 Flexural strength

Flexural strength represents a paver's capacity to withstand bending or breaking under external loads, particularly when loads act unevenly or concentrate at single points, such as forces transmitted by vehicle tires or falling heavy objects. This property enables efficient load distribution, minimizing cracking and structural failure. Higher flexural strength better withstands impacts and traffic stresses, extending service life. Table 4.34 presents the measured flexural strength values for all paver mixes.

Table 4.34: Flexural strength of pavers (all values in N/mm^2)

Paver Designation	Average Flexural Strength	Paver Designation	Average Flexural Strength	Paver Designation	Average Flexural Strength
C100T00	9.35	C080T00	8.68	C060T00	8.07
C100T10	9.04	C080T10	9.61	C060T10	8.45
C100T20	8.01	C080T20	8.38	C060T20	7.63
C100T30	7.67	C080T30	8.04	C060T30	6.95
C100T40	6.96	C080T40	7.16	C060T40	6.12
C100T50	6.01	C080T50	6.45	C060T50	5.93

The flexural strength results for the C100, C080, and C060 binder series consistently showed that a 10% replacement of iron ore tailings (IOT) produced the most significant improvement in bending resistance. In contrast, higher replacement levels led to a marked decline in performance.

In the C100 Series, the flexural strength changed marginally from 9.35 N/mm^2(control) to 9.04 N/mm^2 at 10% IOTs, before falling steadily to 6.01 N/mm^2 at 50% IOTs. The C080 Series exhibited a more pronounced enhancement at 10% IOTs, with flexural strength increasing from 8.68 N/mm^2 to 9.61 N/mm^2 and then decreasing to 6.45 N/mm^2 at the maximum IOTs content. At the same time, the C060 Series reached a peak of 8.45 N/mm^2 for C060T10, above the 8.07 N/mm^2 of the control mix, and subsequently declined to 5.93 N/mm^2 at 50% IOTs.

These trends indicate that modest IOT substitution strengthens the matrix by improving load transfer and crack-bridging mechanisms, whereas excessive replacement dilutes the cementitious phase and disrupts binder continuity.

Srividya et al. (2022) reported considerably lower flexural strengths for geopolymer concrete, ranging from 2.24 N/mm^2 to 5.92 N/mm^2, indicating that ordinary geopolymer formulations without optimized tailings incorporation may underperform relative to the titanium-enhanced mixes developed in this investigation. Banupriya et al. (2016) observed a flexural strength of 5.89 N/mm^2 in geopolymer cement concrete. Kumar et al. (2014) showed that their reference mix (no IOTs) reached 10.00 N/mm^2, while mixes with 30%–40% IOT achieved 8.80–9.27 N/mm^2 at 28 and 56 days, values comparable to those of the C060 and C080 series at similar replacement levels. However, the higher-optimum IOT content (30%–40%) in that study contrasts with the present observation that flexural strength diminished markedly beyond 10% IOTs, a discrepancy that may arise from differences in tailings chemical composition, particle fineness, or the use of geopolymer activation, all of which influence hydration kinetics and microstructure development.

Although flexural strength declined beyond a 10% IOTs substitution, none of the trials recorded values below 3.3 N/mm^2, the flexural strength of pavers for M30 grade of concrete as per the Indian Standard code, thereby indicating the feasibility of using higher IOTs percentages while maintaining a practical balance between sustainability and mechanical performance. The sustained strength at elevated IOT levels arose from the filler effect of fine IOTs particles, which promoted additional calcium silicate hydrate formation and enhanced micro-crack bridging. These mechanisms collectively improve ductility under bending stresses and support the practical use of higher IOTs contents in sustainable construction materials without severely compromising flexural capacity.

This replacement level reduces cement usage, lowers the carbon footprint and material costs, and simultaneously improves flexural strength relative to control mixes and many geopolymer systems.

The scatter plot in Figure 4.39 shows the relationship between flexural strength (N/mm^2) and compressive strength (N/mm^2) for composite mortars incorporating IOTs as partial cement replacements at three cement contents—100%, 80%, and 60%—each represented by distinct markers and linear regression lines.

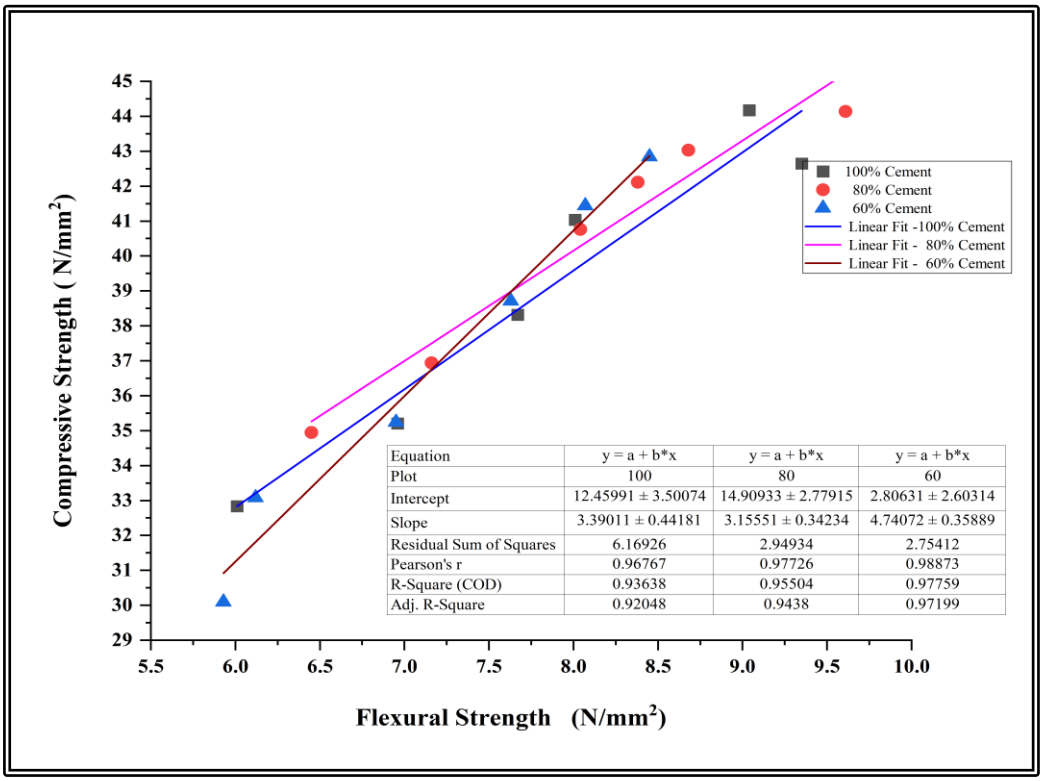


Figure 4.39: Relationship between flexural strength and compressive strength

The regression equations and associated statistical parameters (intercept, slope, Pearson's r, and R^2) demonstrate a consistently strong positive relationship across all mixes, with R^2 values exceeding 0.92 and thereby confirming model robustness.

The CS 60 mix (with the lowest proportion of cement) exhibited the steepest slope (4.74027), compared with CS 80 (3.15551) and CS 100 (3.39011), indicating that IOT-enriched composites amplify the increase in compressive strength per unit gain in flexural strength. This accelerated rate of strength gain likely develops from microstructural densification and improved particle packing, where fine iron ore tailings progressively fill voids within the cement matrix. The data confirm that, although substituting cement with IOTs slightly alters baseline strength, the fundamental

flexural–compressive strength relationship remains highly predictable. Consequently, IOTs serve as a viable, sustainable supplementary material that enhances mechanical performance while reducing cement use, thereby offering substantial potential for green composite design in advanced construction applications.

4.9.2.6 Acid resistance test

The compressive strength detailed in Table 4.35 presents the values of the paving blocks after 56 days of air curing in the laboratory and after 56 days of immersion in a 3% H_2SO_4 solution, revealing distinct patterns of strength development and degradation for the IOT-based composites.

Table 4.35: Compressive strength of pavers at 56 days air drying and acid test (all values in N/mm^2)

Paver Designation	Compressive Strength of air dry sample	Compressive Strength of Acid-Exposed Sample
C100T00	47.61	37.92
C100T10	48.54	39.18
C100T20	43.32	36.36
C100T30	39.64	33.34
C100T40	36.97	30.28
C100T50	33.50	28.24
C080T00	59.74	39.37
C080T10	61.62	39.73
C080T20	56.77	37.77
C080T30	54.16	36.28
C080T40	48.06	32.51
C080T50	44.63	30.76
C060T00	57.67	38.25
C060T10	61.32	39.41
C060T20	54.83	35.42
C060T30	48.15	32.21
C060T40	46.30	29.77
C060T50	42.53	26.93

Figure 4.40 graphically illustrates these trends, highlighting both the substantial strength development under favourable curing and the parallel strength degradation under aggressive chemical attack.

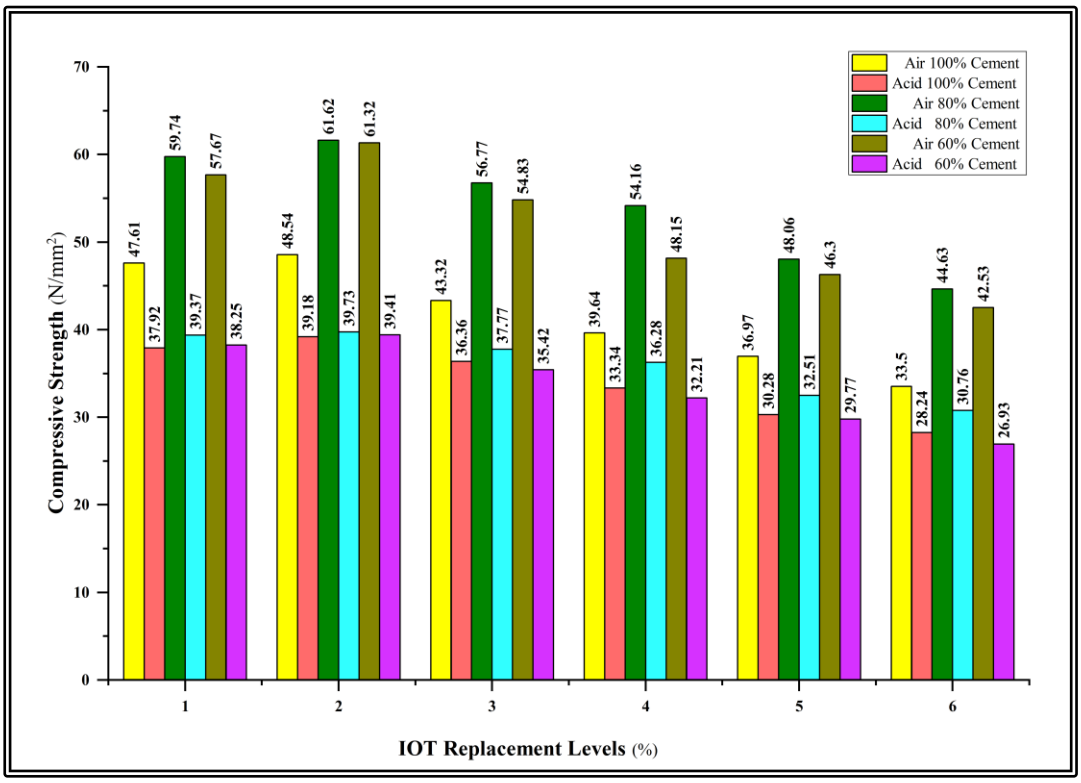


Figure 4.40: Comparison of variation in compressive strength between air dry sample and acid sample

From 28 to 56 days under air curing, the average compressive strength increased from 38.75 N/mm^2 to 49.19 N/mm^2, corresponding to a gain of 10.43 N/mm^2 (26.85%), which is notably higher than the 10–20% post-28-day strength increments typically reported for conventional concretes with mineral additions. The strength increment varied between 2.01% and 43.14% across the 18 mixes, indicating that the kinetics of pozzolanic reactions was strongly influenced by the specific IOT and GGBS proportions.

The 100% cement specimens demonstrated a modest strength increase from 39.04 ± 4.40 N/mm^2 to 41.60 ± 5.97 N/mm^2 (6.26%), indicating that the higher-clinker-content mixtures achieved near-complete hydration by 28 days.

In contrast, the 80% cement + 20% GGBS group exhibited a pronounced increase of 33.99% (40.32 ± 3.62 N/mm^2 to 54.16 ± 6.66 N/mm^2), while the 60% cement + 40% GGBS group achieved the highest gain of 40.31% (36.90 ± 4.96 N/mm^2 to 51.80 ± 7.26 N/mm^2). These results are consistent with the behaviour of pozzolanic systems, in which the continued reaction of supplementary cementitious materials with calcium hydroxide drives extended-age strength. The enhanced late-age performance of the 80 and 60 series, relative to typical strength gains in ordinary concrete, suggests that iron-

bearing phases in the IOT may have contributed to both accelerated early hydration and sustained pozzolanic activity.

Specimens exposed to 3% H_2SO_4 for 56 days developed an average compressive strength of 34.65 N/mm^2, lower than their air-cured counterparts at both 28 and 56 days. When compared with the 28-day air-cured reference, acid exposure resulted in an average strength loss of 4.10 N/mm^2 (10.66%), with reductions ranging from 7.70% to 14.01%; relative to the 56-day air-cured baseline, the mean loss increased to 14.54 N/mm^2 (28.62%), with individual values between 15.70% and 36.68%. Established sulfuric acid attack mechanisms drive this degradation; the acid leaches calcium hydroxide, forming soluble salts and that exposes surfaces and inflicts damage.

The extent of strength loss depended on binder composition: the 100% cement group showed a 12.47% reduction, the 80% cement + 20% GGBS group a 10.63% reduction, and the 60% cement + 40% GGBS group the lowest loss at 8.88%. This inverse relationship between GGBS/IOT content and acid-induced strength deterioration indicates that higher replacement levels improve chemical resistance by lowering calcium hydroxide content and producing a denser, less permeable microstructure that limits acid ingress and leaching. Overall, the 26.85% average gain in compressive strength from 28 to 56 days under air curing, coupled with the relatively modest 10.66% average loss after 56 days in 3% H_2SO_4, demonstrates that the IOT–GGBS composites possess a favourable balance between long-term strength development and acid resistance. Mixes exhibiting 30%–40% strength gains over this period likely contain near-optimal IOT and GGBS proportions that maximise pozzolanic activity without unduly compromising early-age performance. The dual role of iron-rich IOT—enhancing early hydration and contributing to secondary C–S–H formation at later ages—supports its use as a sustainable, performance-enhancing component in paving applications requiring high long-term strength and moderate chemical resistance.

These findings, which align with the durability improvements reported for other pozzolan-bearing concretes by Maria & Prabha (2022) and Djamaluddin et al. (2020), confirm that appropriately designed IOT composites can enable reductions in cement content while still achieving required design strengths at extended ages, thereby advancing both economic and environmental objectives in pavement construction.

4.9.2.7 Water absorption of tiles

In the C100 series (100% cement dosage), the control tile, C100T00, had a baseline water absorption of 3.12%. The incorporation of 10% IOT (C100T10) improved performance, with reduced absorption of 2.52%, representing a 19.2% enhancement compared with the control. However, progressive increases in IOT content beyond 10% led to systematic increases in water absorption, with values rising from 4.44% at 20% replacement to 11.80% at 50% replacement. Table 4.36 presents the water absorption test on tiles while Figure 4.41 presents the graph showing variation in water absorption levels across different IOT replacement levels.

Table 4.36: Water absorption test on tiles (all values in%)

Tile Designation	Mean Water Absorption	Tile Designation	Mean Water Absorption	Tile Designation	Mean Water Absorption
C100T00	3.12	C080T00	4.16	C060T00	4.63
C100T10	2.52	C080T10	3.46	C060T10	4.40
C100T20	4.44	C080T20	4.50	C060T20	6.61
C100T30	6.39	C080T30	4.59	C060T30	8.79
C100T40	8.73	C080T40	7.71	C060T40	9.85
C100T50	11.80	C080T50	8.97	C060T50	12.96

In the C080 series (80% cement dosage), the tiles manufactured with this dosage displayed remarkable consistency in water absorption across the IOT replacement spectrum.

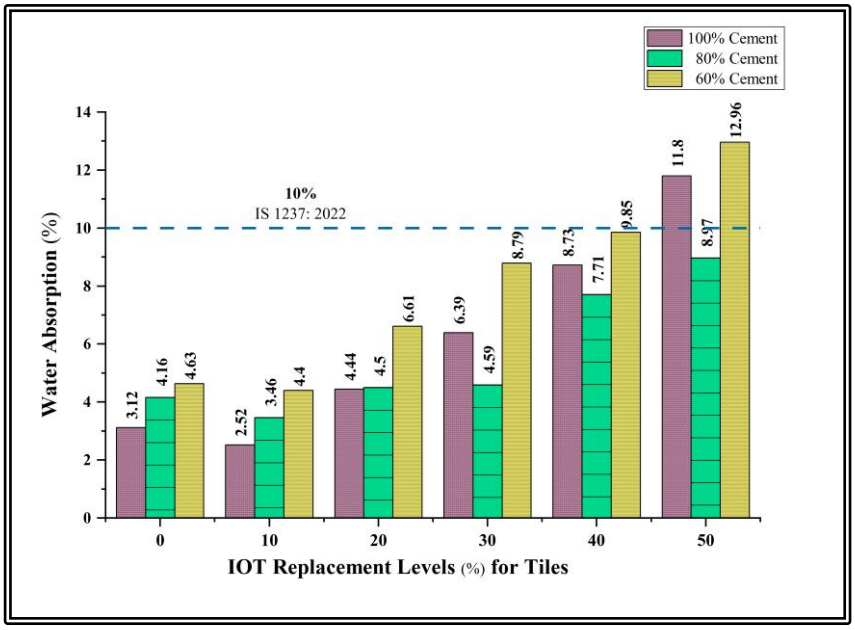


Figure 4.41: Variation in water absorption levels over various IOT replacement levels

The control mix C080T00 recorded 4.16% absorption, while IOT additions of 10% and 20% maintained relatively stable values of 3.46% and 4.50%, respectively.

Even at higher replacement levels of 30% and 40%, the absorption remained within an acceptable range of 4.59% to 7.71%. The C080T50 composition achieved 8.97% absorption, demonstrating superior performance compared with its C100T50 counterpart despite the reduced cement content.

In the C060 series (60% cement dosage), as anticipated, tiles with the lowest cement dosage exhibited the highest water absorption values across all IOT replacement levels. The control mix C060T00 showed 4.63% absorption, with values progressively increasing to 12.96% at 50% IOT replacement. The substantial increases observed at higher replacement levels—8.79% at 30%, 9.85% at 40%, and 12.96% at 50%—indicated insufficient binder content to synthesize the IOT particles effectively and minimize inter-particle voids. Nevertheless, the C060T10 composition (4.40% absorption) performed comparably to the control, indicating that minimal IOT additions remained viable even with reduced cement content.

The experimental data established distinct performance rankings among tile compositions. The C100T10 mix achieved optimal water absorption of 2.52%, demonstrating that strategic IOT incorporation enhanced rather than compromised material properties. The C080 series exhibited superior stability, maintaining absorption below 9% even at maximum replacement and thereby offering a favourable balance between sustainability and performance. Tiles with 10%–20% IOT replacement (3.46%–4.50% absorption) satisfied stringent durability requirements for construction applications, whereas compositions exceeding 30% IOT showed elevated absorption, limiting suitability for exterior applications. Fontes et al. (2021) examined hydraulic tiles manufactured with fine aggregates and pigments recovered from iron ore tailings and reported water absorption values ranging from 14.8% to 18.72%. In contrast, Mendes et al. (2021) demonstrated that the substitution of 30% fine aggregate with iron ore tailings reduced the absorption capacity of conventional concrete from 5.56% to 4.46% (Mendes et al., 2021).

Shettima et al. (2016) similarly observed absorption values of 4.4% for complete aggregate replacement and 3.3% for 25% replacement levels. Cicek et al. (2018) achieved exceptionally low absorption (0.49%) with 5.66 wt.% boron tailing incorporation, and Pati & Sahu (2020) reported 4.17%–6.10% absorption when

replacing 0%–40% fine aggregate with fly ash. These findings collectively underscored the potential of industrial by-products to regulate porosity and performance in cementitious composites.

4.9.2.8 Wet transverse strength on tiles

The wet transverse strength value quantifies each tile's resistance to fracture under a perpendicular load when fully saturated, making this parameter essential for tiles exposed to wet environments. The data in Table 4.37 summarize the average wet transverse strength values for tiles produced with three cement dosages—100%, 80%, and 60%—each blended with iron ore tailings (IOT) at replacement levels of 0%, 10%, 20%, 30%, 40%, and 50% while Figure 4.42 presents the graphical representation of wet transverse strength as a function of IOT replacement level.

Table 4.37: Wet transverse strength on tiles (all values in N/mm^2)

Tile Designation	Average Wet Transverse Strength	Tile Designation	Average Wet Transverse Strength	Tile Designation	Average Wet Transverse Strength
C100T00	9.67	C080T00	8.51	C060T00	8.39
C100T10	8.96	C080T10	8.73	C060T10	8.47
C100T20	8.44	C080T20	8.03	C060T20	7.45
C100T30	7.19	C080T30	8.06	C060T30	6.97
C100T40	6.68	C080T40	7.3	C060T40	6.04
C100T50	6.12	C080T50	6.56	C060T50	5.7

At full cement dosage, the control tile (C100T00) exhibited the highest mean strength of 9.67 N/mm^2. Incorporation of 10% IOT (C100T10) induced a modest reduction to 8.96 N/mm^2, representing a 7.3% decrease while still maintaining structural performance above typical load-bearing requirements. Progressive increases in tailings content caused further strength declines: 8.44 N/mm^2 at 20% replacement, 7.19 N/mm^2 at 30%, 6.68 N/mm^2 at 40%, and 6.12 N/mm^2 at 50%. This trend indicates that iron ore tailings can partially substitute cement without catastrophic strength loss, but excessive replacement compromises binder matrix cohesion and reduces tile load capacity.

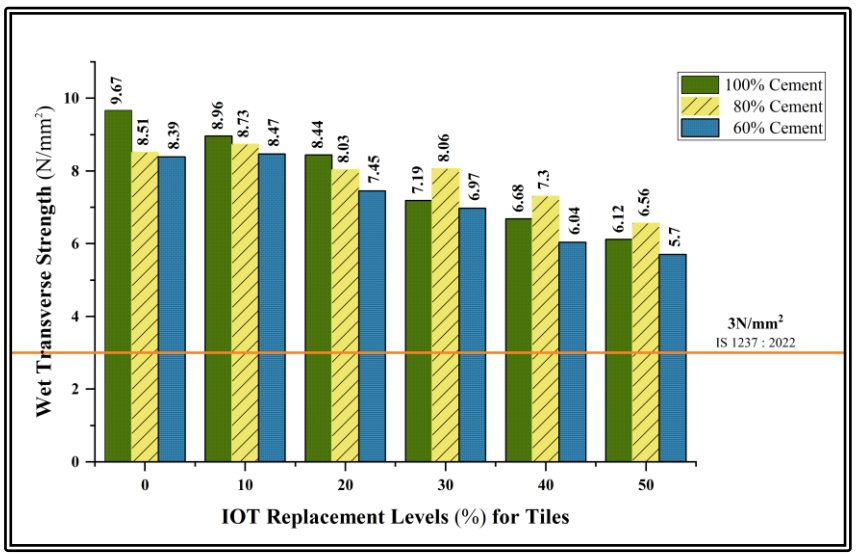


Figure 4.42: Wet transverse strength of tiles with IS code limits

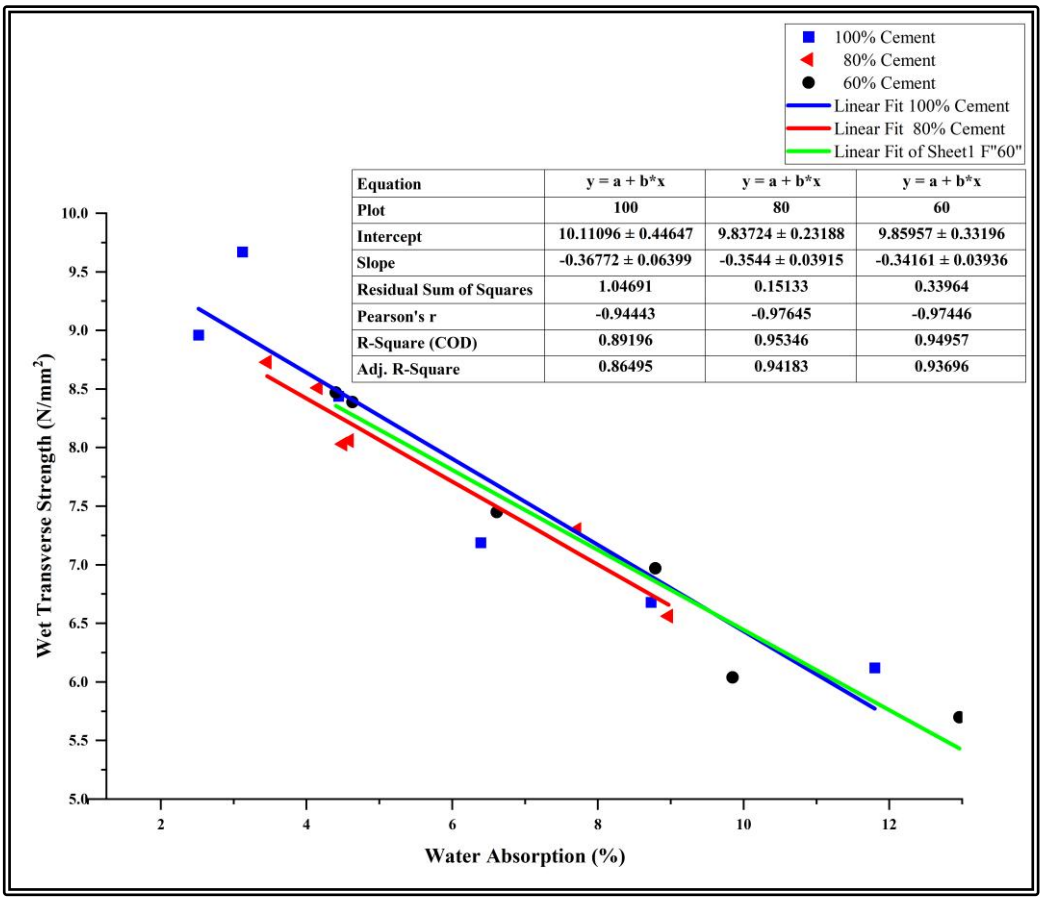
Reducing the cement dosage to 80% yielded control strength of 8.51 N/mm^2. The introduction of 10% IOT (C080T10) enhanced the strength to 8.73 N/mm^2, a 2.6% gain over the C080 control. This improvement suggests that IOTs act as micro-fillers, refining the pore structure and facilitating more uniform stress distribution. At 20% IOT, strength remained acceptable at 8.03 N/mm^2; at 30%, 8.06 N/mm^2; at 40%, 7.30 N/mm^2; and at 50%, 6.56 N/mm^2. The C080 series thus demonstrates robust tolerance to IOT incorporation up to 30%, with minimal strength loss and even slight enhancement at low replacement levels.

In the 60% cement series, the control tile achieved 8.39 N/mm^2. The introduction of 10% IOT (C060T10) marginally increased strength to 8.47 N/mm^2, indicating that an optimized binder-to-tailings ratio can offset reduced cement content. Higher tailings proportions, however, induced notable performance declines: 7.45 N/mm^2 at 20% replacement, 6.97 N/mm^2 at 30%, 6.04 N/mm^2 at 40%, and 5.70 N/mm^2 at 50%.

Collectively, the data reveal that IOTs function as valuable supplementary materials in composite tile production. The fine particle size and inherent iron oxide content of IOTs promote filler effects, thereby enhancing or maintaining mechanical performance. Specifically, both C080T10 and C060T10 surpassed their respective controls, demonstrating that 10% IOT replacement optimizes particle packing and interfacial bonding. Conversely, replacement levels above 30% produce diminishing returns, as excessive tailings overload the binder system, introduce weak interparticle interfaces, and elevate porosity. In the present study, the composite tiles achieved average wet

transverse strengths of 5.7–9.67 N/mm^2, values that markedly exceed those reported in comparable research and the minimum strength specified as 3N/mm^2 as in the relevant IS code. A 15% substitution of cement with red mud yielded a strength of only 3.9 N/mm² (Deshmukh et al., 2021), and Pati & Sahu (2020) reported strengths ranging from 4.6 N/mm^2 to 5.57 N/mm^2 with 0%–40% fly ash replacement of fine aggregate. These comparisons highlight the superior mechanical performance and durability of tiles incorporating iron ore tailings in this investigation and emphasize their effectiveness as a sustainable alternative to conventional and other industrial by-product-based formulations.

The scatter plot in Figure 4.43 illustrates a strong inverse relationship between water absorption and wet transverse strength for tiles containing 100%, 80%, and 60% cement dosages, each partially replaced with iron ore tailings.



Equation	y = a + b*x	y = a + b*x	y = a + b*x
Plot	100	80	60
Intercept	10.11096 ± 0.44647	9.83724 ± 0.23188	9.85957 ± 0.33196
Slope	-0.36772 ± 0.06399	-0.3544 ± 0.03915	-0.34161 ± 0.03936
Residual Sum of Squares	1.04691	0.15133	0.33964
Pearson's r	-0.94443	-0.97645	-0.97446
R-Square (COD)	0.89196	0.95346	0.94957
Adj. R-Square	0.86495	0.94183	0.93696

Figure 4.43: Relationship between water absorption and wet transverse strength

Linear regression of the 100% cement series yielded the equation y = 10.11096 - 0.36772x with R^2 = 0.89196 and Pearson's r = -0.94443, which indicated that each 1% increase in absorption corresponds to a 0.368 N/mm^2 decrease in strength. The 80%

cement series showed a similar trend, y = 9.83724 - 0.35444x, with R^2 = 0.95346 and r = -0.97645, thereby demonstrating the highest predictive accuracy and sensitivity to absorption changes. For the 60% cement series, the generated equation y = 9.85957 - 0.34161x, with R^2 = 0.94957 and r = -0.97446, signified slightly lower strength reduction per unit absorption while still maintaining a robust linear fit. These results confirm that increasing porosity, as reflected by higher water absorption, systematically compromises tile strength, and the consistently high coefficients of determination and correlation underscore the reliability of this relationship across diverse cement-to-tailings ratios.

4.10 SEM-EDX characterization of concrete for paver and tiles

Scanning electron microscopy (SEM) and energy-dispersive X-ray (EDX) spectroscopy characterized the microstructural morphology and elemental composition of the concrete for pavers and tile. SEM imaging elucidated the surface texture, grain size, and porosity, while the EDX system mapped and quantified the spatial distribution of key elements, including silicon, aluminum, and calcium. Collectively, these analytical methods yielded the essential data required to assess the raw materials, structural integrity, and long-term durability of pavers and tiles, and analysed two concrete compositions.

a) **Composition: C080T30**

High-resolution FESEM micrographs of C80T30 expose a fractured, heterogeneous microstructure, definitively establishing the morphological signature of a synthesized paver composite. This structural configuration inherently dictates physical suitability for permeable pavement or interlocking block architectures. Figure 4.44 shows SEM micrograph illustrating the microstructural morphology of C80T30. Figure 4.45 shows EDX spectrum illustrating the relative abundance of the principal elements detected within C80T30.

Irregular particles spanning 2–15 μm microcracks formed during curing, generating deep fissures and a pronounced void network (~25–35% apparent porosity). This interconnected pore volume clearly indicates either an inherent structural permeability driving water infiltration or an incomplete hydration. Consequently, although this extensive void architecture maximizes urban drainage capacity, the interconnected porosity inherently degrades vehicular load resistance, necessitating the integration of structural reinforcement to achieve mechanical stability.

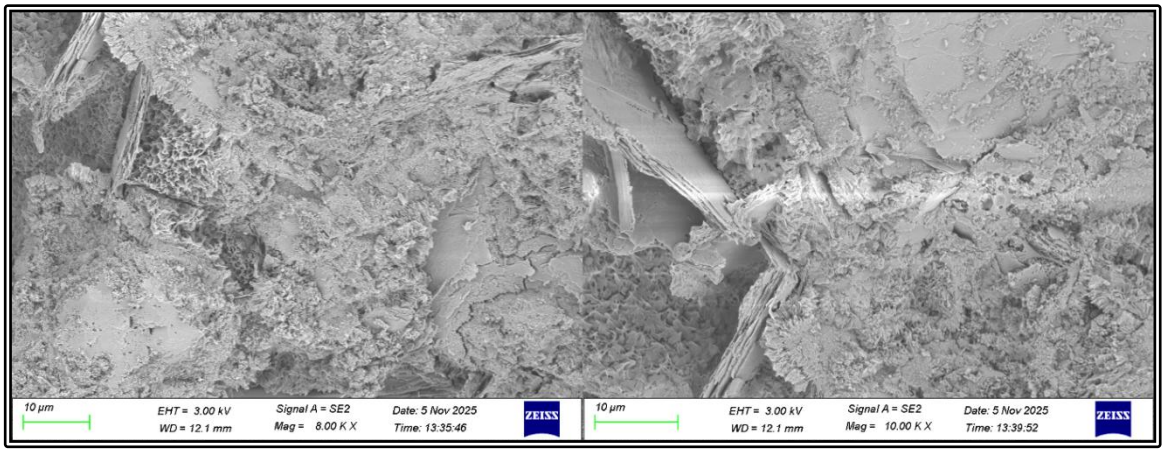


Figure 4.44: SEM micrograph of concrete for pavers and tiles with composition C80T30

Concurrent EDX mapping definitively resolves the spatial elemental distribution across this fractured matrix. Oxygen (O K, green) saturates the material ubiquitously, forming the foundational oxide framework. Silicon (Si K, red) broadly diffuses throughout the particle interiors, reflecting the structural integration of siliceous aggregates or binders. Aluminum (Al K, cyan) sparsely segregates into discrete aluminosilicate domains. Calcium (Ca K, pink) aggregates strictly within minor clustered regions, marking the precipitation of calcareous phases; concurrently, iron (Fe K, brown) segregates into distinct metallic oxide pockets.

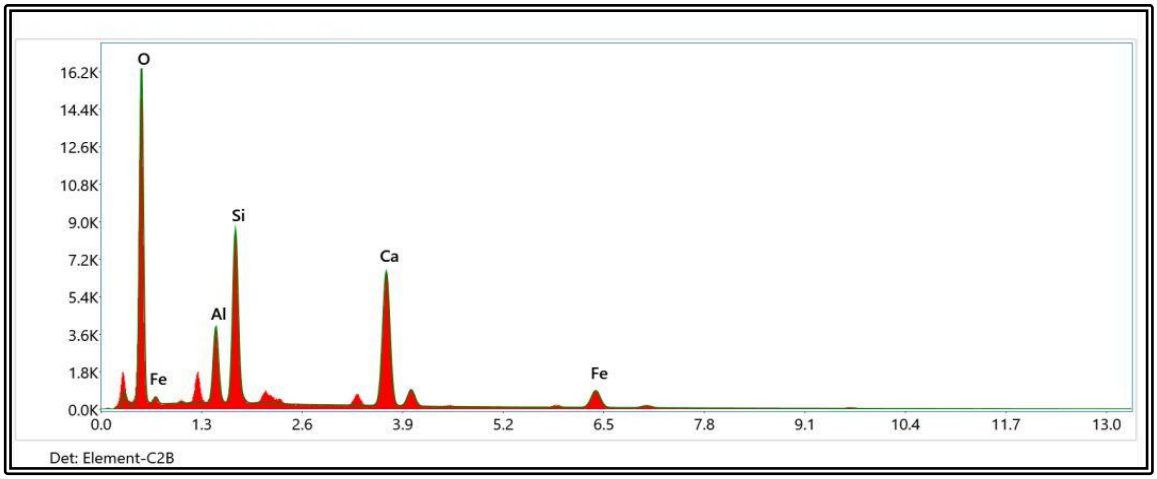


Figure 4.45: EDX spectrum detailing of principal elements for concrete for pavers and tiles with composition C80T30

This specific elemental architecture directly establishes robust physicochemical stability against environmental weathering, structurally qualifying C080T30 for eco-pavement matrices incorporating 15–30% additive volumes. Moving forward, quantitative EDX evaluation (e.g., atomic ratios: O ~55–65%, Si ~20–30%, Al ~5–10%, Ca ~3–8%, Fe

~2–5%) and rigorous hydraulic conductivity assessments will definitively quantify in-service drainage mechanics and strictly govern the thermodynamic and mechanical optimization of future formulations.

b) **Composition: C060T50**

High-resolution FESEM micrographs of C060T50 reveal a highly porous, uneven microstructure that definitively characterizes a synthesized paver composite. This morphological signature typifies a permeable concrete or geopolymer-based interlocking block structurally optimized for pavement applications. Figure 4.46 shows SEM micrograph illustrating the microstructural morphology of C60T50.

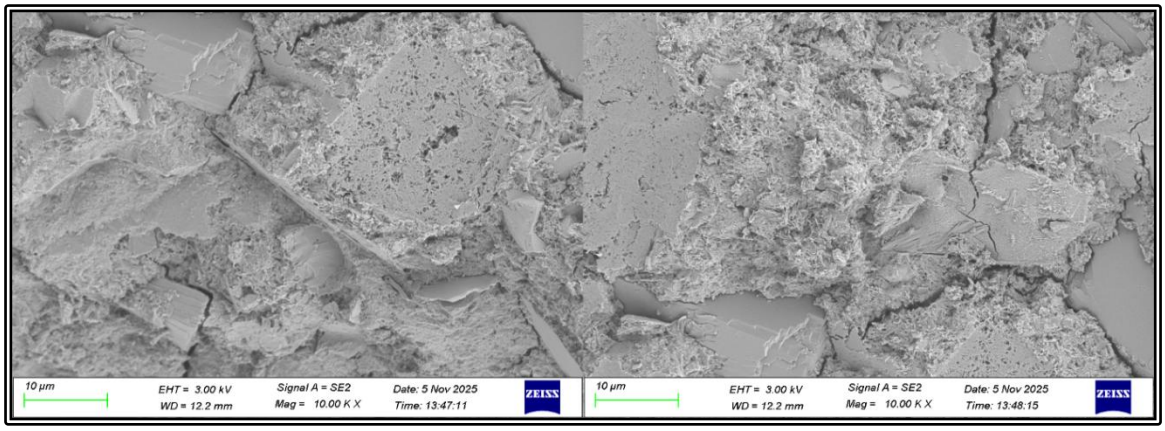


Figure 4.46: SEM micrograph of concrete for pavers and tiles with composition C60T50

Angular aggregates spanning 5–20 µm interlock to form a matrix that sustains extensive surface fissures and an interconnected void network (~30–40% apparent porosity). This interconnected pore volume directly indicates either an inherent permeability profile optimized for stormwater management or a structural compaction deficit during fabrication. Consequently, although this extensive void architecture strongly promotes superior urban drainage, the interconnected porosity inherently compromises the overall load-bearing capacity.

Concurrent EDX mapping definitively resolves the spatial elemental distribution across this highly porous matrix. Oxygen (O K, green) saturates the material ubiquitously, forming the foundational oxide framework. Silicon (Si K, red) is broadly distributed throughout the aggregate cores, indicating the successful integration of siliceous fillers or binders. Aluminum (Al K, cyan) segregates exclusively into scattered patches, reflecting the localized formation of an aluminosilicate phase. Calcium (Ca K, pink) concentrates strictly within fibrous or gel-like regions, marking the precipitation of

hydraulic phases; concurrently, iron (Fe K, brown) segregates into discrete metallic oxide clusters. Figure 4.47 shows EDX spectrum illustrating the relative abundance of the principal elements detected within C60T50.

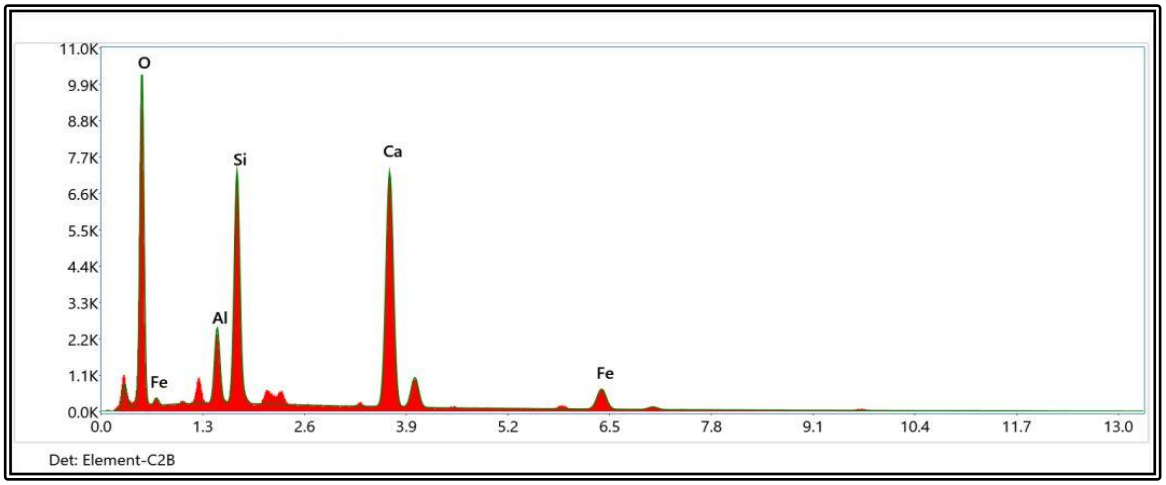


Figure 4.47: EDX spectrum detailing of principal elements for concrete for pavers and tiles with composition C60T50

This specific elemental architecture inherently establishes robust chemical stability against environmental weathering, effectively validating C060T50 as a highly viable for eco-paver applications incorporating 20–30% recycled content. To definitively constrain in-service performance, subsequent quantitative EDX evaluation (e.g., atomic ratios: O ~50–60%, Si ~25–35%, Al ~5–15%, Ca ~5–10%, Fe ~3–8%) and standardized permeability testing will rigorously quantify drainage metrics and strictly govern the formulation of future durable surface materials.

4.11 Statistical analysis of various parameters of pavers

A comprehensive statistical evaluation of the concrete paver mixes detailed in Table 4.38 quantifies water absorption, compressive strength, split tensile strength, and flexural strength across three binder replacement proportions: 100% cement, 80% cement with 20% GGBS, and 60% cement with 40% GGBS.

The experimental program employed a factorial design with three cement levels (100%, 80%, 60%) and six IOTs replacement rates (0%–50%), labelled C100T00 - C060T50, to capture both individual and interaction effects on material properties. Eighteen mixes underwent testing for water absorption, 28-day compressive strength, flexural strength, and splitting tensile strength. For instance, C100T10 yielded a compressive strength of

44.17 N/mm², 3.56% higher than C100T00's 42.65 N/mm², behaviour consistent with the literature, which indicates that 10%–30% IOT can enhance strength.

Table 4.38: Statistics of various parameters of pavers

Paver Composition	Mean	Standard Deviation	Lower 95% CI of Mean	Upper 95% CI of Mean	SE of mean	Coefficient of Variation
Water Absorption						
C100T00	2.15	0.230	1.895	2.405	0.130	10.15
C100T10	1.77	0.110	1.652	1.888	0.060	6.29
C100T20	3.52	0.170	3.324	3.716	0.100	4.93
C100T30	5.18	0.140	5.023	5.337	0.080	2.78
C100T40	7.49	0.220	7.255	7.725	0.120	2.89
C100T50	9.96	0.210	9.725	10.195	0.120	2.12
C080T00	3.29	0.098	3.178	3.402	0.057	2.99
C080T10	2.73	0.219	2.481	2.979	0.127	8.03
C080T20	3.57	0.272	3.262	3.878	0.157	7.61
C080T30	3.75	0.122	3.613	3.887	0.070	3.24
C080T40	6.17	0.145	6.005	6.335	0.084	2.35
C080T50	7.67	0.131	7.521	7.819	0.076	1.71
C060T00	3.68	0.322	3.315	4.045	0.186	8.75
C060T10	3.49	0.330	3.116	3.864	0.191	9.46
C060T20	5.28	0.170	5.088	5.472	0.098	3.22
C060T30	7.03	0.105	6.91	7.15	0.061	1.50
C060T40	8.11	0.180	7.906	8.314	0.104	2.22
C060T50	10.61	0.272	10.302	10.918	0.157	2.56
28 days Compressive Strength						
C100T00	42.65	1.281	41.762	43.538	3.004	0.453
C100T10	44.17	0.897	43.549	44.791	2.031	0.317
C100T20	41.04	1.075	40.295	41.785	2.620	0.380
C100T30	38.32	1.324	37.403	39.237	3.454	0.468
C100T40	35.21	1.193	34.383	36.037	3.388	0.422
C100T50	31.47	3.679	28.92	34.02	11.692	1.301
C080T00	43.03	1.167	42.221	43.84	2.713	0.413
C080T10	44.14	1.223	43.293	44.987	2.770	0.432
C080T20	42.11	0.986	41.426	42.794	2.342	0.349
C080T30	40.76	1.230	39.907	41.613	3.018	0.435
C080T40	36.94	0.726	36.436	37.444	1.964	0.257

Paver Composition	Mean	Standard Deviation	Lower 95% CI of Mean	Upper 95% CI of Mean	SE of mean	Coefficient of Variation
28 days Compressive Strength						
C080T50	34.95	1.125	34.170	35.730	3.218	0.398
C060T00	41.44	0.850	40.852	42.028	2.050	0.300
C060T10	42.84	0.899	42.217	43.463	2.099	0.318
C060T20	38.61	0.881	37.998	39.222	2.283	0.312
C060T30	35.22	1.270	34.340	36.100	3.606	0.449
C060T40	33.08	1.018	32.374	33.786	3.078	0.360
C060T50	30.09	1.017	29.386	30.794	3.378	0.359
Flexural strength						
C100T00	9.35	0.545	8.931	9.769	0.182	0.058
C100T10	9.04	0.355	8.767	9.313	0.118	0.039
C100T20	8.01	0.469	7.650	8.370	0.156	0.059
C100T30	7.67	0.660	7.161	8.176	0.220	0.086
C100T40	6.96	0.366	6.679	7.241	0.122	0.053
C100T50	6.01	0.240	5.826	6.194	0.080	0.040
C080T00	8.68	0.671	8.164	9.196	0.224	0.077
C080T10	9.61	0.976	8.860	10.360	0.325	0.102
C080T20	8.38	0.130	8.279	8.479	0.043	0.016
C080T30	8.04	0.522	7.639	8.441	0.174	0.065
C080T40	7.16	0.540	6.745	7.575	0.180	0.075
C080T50	6.45	0.718	5.897	7.001	0.239	0.111
C060T00	8.07	0.817	7.441	8.697	0.272	0.101
C060T10	8.45	0.339	8.188	8.710	0.113	0.040
C060T20	7.63	0.243	7.444	7.816	0.081	0.032
C060T30	6.95	0.393	6.646	7.251	0.131	0.057
C060T40	6.12	0.333	5.864	6.376	0.111	0.054
C060T50	5.93	0.707	5.387	6.473	0.236	0.119
Splitting Tensile strength						
C100T00	6.59	0.405	6.310	6.870	0.061	0.143
C100T10	6.79	0.813	6.226	7.355	0.120	0.288

Paver Composition	Mean	Standard Deviation	Lower 95% CI of Mean	Upper 95% CI of Mean	SE of mean	Coefficient of Variation
Splitting Tensile strength						
C100T20	6.09	0.656	5.635	6.545	0.108	0.232
C100T30	5.67	0.380	5.407	5.933	0.067	0.134
C100T40	5.26	0.364	5.007	5.513	0.069	0.129
C100T50	4.90	0.335	4.669	5.131	0.068	0.118
C080T00	6.10	0.407	5.818	6.382	0.067	0.144
C080T10	6.36	0.524	5.997	6.723	0.082	0.185
C080T20	6.16	0.298	5.954	6.366	0.048	0.105
C080T30	5.73	0.636	5.289	6.171	0.111	0.225
C080T40	5.23	0.396	4.956	5.504	0.076	0.140
C080T50	4.88	0.258	4.702	5.058	0.053	0.091
C060T00	5.83	0.364	5.577	6.083	0.062	0.129
C060T10	6.02	0.401	5.742	6.298	0.067	0.142
C060T20	5.54	0.284	5.342	5.738	0.051	0.101
C060T30	5.35	0.438	5.046	5.654	0.082	0.155
C060T40	5.05	0.341	4.813	5.287	0.068	0.121
C060T50	4.85	0.241	4.683	5.017	0.050	0.085

Standard deviations for water absorption ranged from 0.098% to 0.330%, and for compressive strength from 0.726 N/mm² to 3.679 N/mm², indicating tightly clustered data. Flexural strength standard deviation ranged from 0.139 N/mm² to 1.044 N/mm², and splitting tensile strength ranged from 0.241 N/mm² to 0.813 N/mm², confirming strong repeatability.

Coefficients of variation (COV) remained uniformly low, 1.50%–10.15% for absorption and 0.257%–1.301% for compressive strength (all <1.5%), demonstrating high precision and homogeneity, with COV values below 3% at 30%–50% IOT. Flexural and tensile COV values consistently remained below 0.4%. Standard errors (SE) for absorption (0.057%–0.191%), compressive strength (1.964–11.692 N/mm²), flexural strength (0.017–0.119 N/mm²), and tensile strength (0.048–0.127 N/mm²) remained small, ensuring accurate mean estimates.

Water absorption rose from 2.15% to 9.96% with IOT content, apart from a minimum of 1.77% at C100T10, indicating optimized particle packing at 10% IOT. Compressive strength peaked at 10% IOT (44.17 N/mm²) and then declined to 31.47 N/mm² at 50% IOT, while the C080 and C060 series exhibited similar optimal trends. Flexural and tensile strengths declined steadily with increasing IOT content because finer particles influenced the interfacial transition zone. Low variability underpinned the reliable identification of optimal mixes (10%–20% IOT) and supports regression modelling and ANOVA to quantify IOT effects and predict composite performance.

4.12 Statistical analysis of various parameters of tiles

A comprehensive set of descriptive statistics quantified the statistical reliability of the experimental results. Table 4.39 details the resulting key parameters, including the mean, standard deviation, coefficient of variation, and standard error.

The systematic investigation examined three cement dosages: 100%, 80%, and 60% (designated C100, C080, and C060), and iron ore tailing replacement levels ranging from 0% to 50% in 10% increments. This experimental matrix encompassed 18 distinct mix proportions, with each performance parameter evaluated using mean values, standard deviation, coefficient of variation (COV), and standard error of the mean.

Table 4.39: Statistical analysis of various parameters of tiles

Tile Composition	Mean	Standard Deviation	Lower 95% CI of Mean	Upper 95% CI of Mean	SE of mean	Coefficient of Variation
Water Absorption						
C100T00	3.12	0.343	2.846	3.394	0.140	0.110
C100T10	2.52	0.211	2.351	2.689	0.086	0.084
C100T20	4.44	0.640	3.928	4.952	0.261	0.144
C100T30	6.39	0.381	6.084	6.696	0.156	0.060
C100T40	8.73	0.418	8.395	9.065	0.171	0.048
C100T50	11.80	1.165	10.869	12.731	0.475	0.099
C080T00	4.16	0.296	3.923	4.397	0.121	0.071
C080T10	3.46	0.534	3.033	3.887	0.218	0.154
C080T20	4.50	0.240	4.308	4.692	0.098	0.053
C080T30	4.59	0.493	4.196	4.984	0.201	0.108
C080T40	7.71	0.382	7.404	8.016	0.156	0.050
C080T50	8.97	0.918	8.235	9.705	0.375	0.102
C060T00	4.63	0.442	4.275	4.985	0.181	0.096

Tile Composition	Mean	Standard Deviation	Lower 95% CI of Mean	Upper 95% CI of Mean	SE of mean	Coefficient of Variation
Water Absorption						
C060T10	4.40	0.198	4.241	4.559	0.081	0.045
C060T20	6.61	0.295	6.375	6.845	0.120	0.045
C060T30	8.79	0.596	8.314	9.266	0.243	0.068
C060T40	9.85	0.527	9.429	10.271	0.215	0.054
C060T50	12.96	0.726	12.378	13.542	0.297	0.056
Wet transverse Strength						
C100T00	9.67	0.457	9.303	10.037	0.187	0.047
C100T10	8.96	0.579	8.497	9.423	0.236	0.065
C100T20	8.44	0.559	7.993	8.887	0.228	0.066
C100T30	7.19	0.518	6.774	7.606	0.212	0.072
C100T40	6.68	0.344	6.406	6.954	0.140	0.051
C100T50	6.12	0.494	5.724	6.516	0.202	0.081
C080T00	8.51	0.599	8.03	8.99	0.245	0.070
C080T10	8.73	0.456	8.365	9.095	0.186	0.052
C080T20	8.03	0.438	7.679	8.381	0.179	0.054
C080T30	8.06	0.378	7.758	8.362	0.154	0.047
C080T40	7.30	0.472	6.922	7.678	0.193	0.065
C080T50	6.56	0.298	6.323	6.797	0.121	0.045
C060T00	8.39	0.733	7.804	8.976	0.299	0.087
C060T10	8.47	0.685	7.921	9.019	0.280	0.081
C060T20	7.45	0.162	7.321	7.579	0.066	0.022
C060T30	6.97	0.421	6.633	7.307	0.172	0.060
C060T40	6.04	0.553	5.597	6.483	0.226	0.092
C060T50	5.70	0.631	5.194	6.206	0.258	0.111

The water absorption analysis yielded critical insights into porosity and durability performance. The control mix C100T00 exhibited a baseline mean absorption of 3.12% with relatively low variability (COV = 0.110).

A 10% replacement of iron ore tailings (IOT) in the C100 series minimized water absorption to an optimal 2.52% (COV = 0.084), reflecting enhanced packing density and reduced porosity. Conversely, elevating the IOT content from 20% to 50% progressively increased water absorption, peaking at 11.80% at the maximum substitution level.

For the C080 series, the water absorption pattern indicated enhanced resistance to porosity development. The control mix C080T00 showed 4.16% absorption, while IOT additions maintained relatively stable values between 3.46% and 4.59% for replacement

levels up to 30%. This performance suggests that combining reduced cement content with moderate IOT incorporation yields a balanced, refined microstructure. The coefficient of variation remained consistently low (0.050–0.154), indicating reproducible results and consistent material behaviour. The C060 series (60% cement) exhibited the highest water absorption values across all IOT replacement levels, with the C060T50 mix reaching 12.96%. Despite higher absorption, the low COV values (0.045–0.096) demonstrated excellent consistency in experimental procedures and material preparation.

The wet transverse strength data describe the structural integrity and load-bearing capacity of the composite tiles under saturated conditions. The C100T00 control mix recorded the highest mean strength of 9.67 N/mm² with minimal variability (COV = 0.047). As iron ore tailings entered the system, a systematic decline in wet transverse strength was observed, with the C100T50 mix attaining 6.12 N/mm², a 36.7% reduction from the control. Nevertheless, all C100 series mixes maintained COV values below 0.081, confirming excellent quality control and material homogeneity. The C080 series demonstrated superior performance stability across IOT replacement levels: the C080T00 mix achieved 8.51 N/mm², and even at 50% IOT replacement, the C080T50 mix retained 6.56 N/mm² strength. Notably, the C080T10 mix (8.73 N/mm²) delivered performance comparable to that of the control, indicating that moderate IOT incorporation with an optimized cement dosage can preserve structural integrity. Consistently low COV values (0.045–0.070) across this series indicate robust manufacturing processes and reliable mechanical performance.

For the C060 series, wet transverse strength values ranged from 8.39 N/mm² to 5.70 N/mm² across the IOT replacement spectrum. Although absolute strength decreased with increasing IOT content, the C060T20 mix exhibited exceptionally low variability (COV = 0.022), demonstrating that specific mix proportions can provide highly predictable performance characteristics. Integration of iron ore tailings into composite construction materials thereby addresses critical environmental, economic, and technical challenges confronting both the mining and construction sectors. The chemical composition and particle size distribution of iron ore tailings impart distinct technical benefits to composite materials, as IOT particles provide a micro-filler effect that enhances packing density and reduces porosity at optimal replacement levels,

exemplified by the improved water absorption of C100T10 (2.52%) compared with the control mix (3.12%).

The statistical parameters reported in the analysis demonstrate rigorous experimental methodology and reliable data collection. Consistently low standard errors of the mean (ranging from 0.066 to 0.475) across all mix proportions indicate measurement precision and adequate sample sizes. Coefficient of variation values predominantly below 15% confirm acceptable variability and reproducible manufacturing processes. The comprehensive dataset offers valuable guidance for optimizing mix designs in commercial production, with the C080 series containing 10%–20% IOT replacement emerging as particularly promising by balancing environmental benefits with structural performance requirements. These findings support the technical feasibility of producing eco-friendly, high-performance construction materials that simultaneously address waste management challenges and respond to the growing demand for sustainable building solutions.

4.13 Performance assessment and insights of cladding panels

The following sections present the mix proportions for the cladding panels and the various tests conducted on the cast cladding panels.

4.13.1 Mix proportion for cladding panels

The mix proportions provided in Table 3.17 governed the casting of the cladding panels, and Table 4.40 presented the corresponding material quantities by weight.

Table 4.40: Material quantities used per cladding panel (all values in kgs.)

Cladding Panel Designation	Cement	GGBS	IOT	Crushed Stone Sand	Fiber
C100G00T50F0	0.65	0.00	0.53	0.37	--
C080G20T50F0	0.52	0.11	0.53	0.37	--
C060G40T50F0	0.39	0.23	0.53	0.37	--
C100G00T50F1	0.65	0.00	0.53	0.37	0.0065
C080G20T50F1	0.52	0.11	0.53	0.37	0.0063
C060G40T50F1	0.39	0.23	0.53	0.37	0.0062

Compressive strength measurements on 70.6 mm × 70.6 mm × 70.6 mm cubes established the mechanical performance of multiple trial batches featuring varying mix

proportions. Table 4.41 provided the compressive strength results after 7 and 28 days of curing, and Figure 4.48 illustrated these trends graphically.

Table 4.41: Compressive strength measured on cube specimens for various mixes (all values in N/mm^2)

Cladding Panel Designation	Average compressive strength	
	7D	28D
C100G00T50F0	14.90	21.31
C080G20T50F0	16.88	25.66
C060G40T50F0	15.30	23.41
C100G00T50F1	15.65	22.69
C080G20T50F1	18.23	28.07
C060G40T50F1	16.49	25.56

The mix composition exerted a critical influence on early and later-age strength development, producing 7-day strengths of 14.9 to 18.23 N/mm^2 and 28-day strengths of 21.31 to 28.07 N/mm^2. The mix C080G20T50F1 (80% Cement, 20% GGBS, 50% iron ore tailings, 1% fiber) achieved the highest 28-day strength of 28.07 N/mm^2. Incorporating 20% GGBS without fiber (C080G20T50F0) increased the 28-day strength by 20.4% relative to the control mix C100G00T50F0 (21.31 N/mm^2), whereas 40% GGBS (C060G40T50F0) produced a smaller gain, thereby confirming an optimal GGBS threshold.

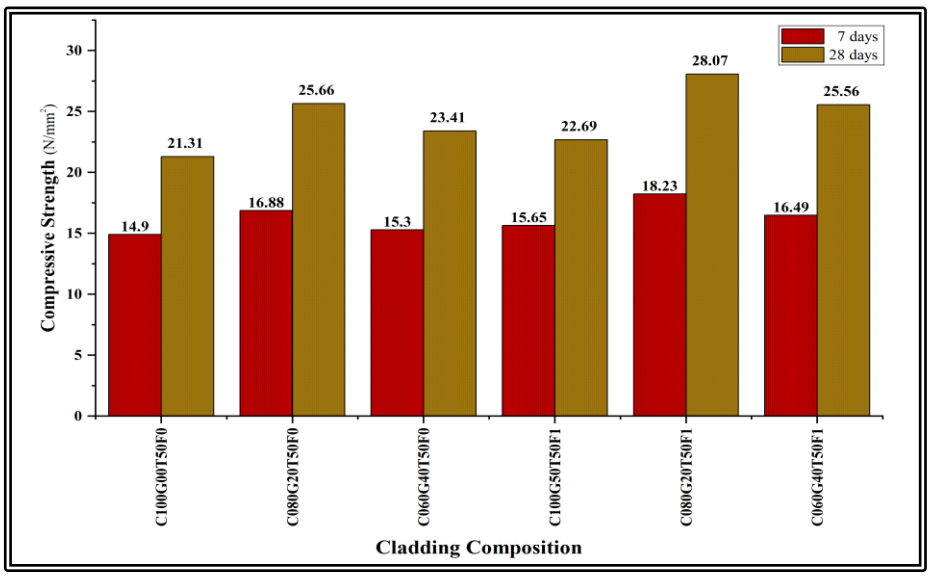


Figure 4.48: Compressive strength of cube obtained at 7 and 28 days

Fiber addition further amplified performance, with C080G20T50F1 exhibiting a 31.7% improvement over the control, which underscored the synergistic contributions of

GGBS pozzolanic activity, iron ore tailing filler effects, and fiber crack-bridging. Figure 4.49 presented the comparison of 7- and 28-day compressive strengths for mixes containing iron ore tailings with and without coir fiber.

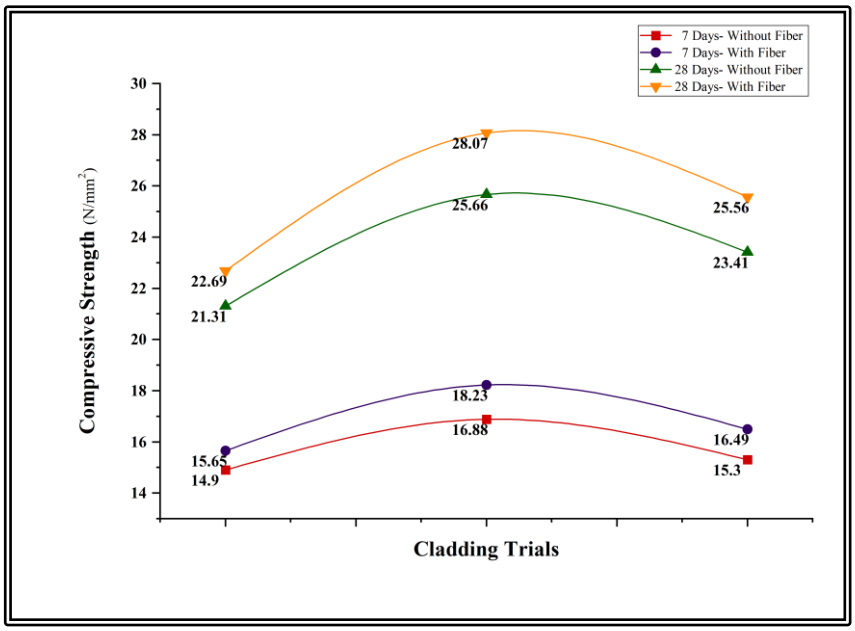


Figure 4.49: Comparison of 7 and 28 days compressive strength in mix with and without coir fiber

Comparisons with previous studies revealed similar interactions between waste materials and supplementary binders. Aravind et al. (2019) reported that rice husk decreased foam concrete strength unless a 60% fly ash content compensated for this loss, resulting in strengths ranging from 2.84 to 3.15 N/mm^2. Andiç-Çakir et al. (2014) demonstrated strength gains of 3.6-14.3% in mortars with untreated coir fibers and 9.0–17.9% with alkali treatment, along with enhanced toughness. These studies collectively confirmed that combining pozzolanic materials with fibers mitigated adverse effects associated with porous inclusions and bolstered mechanical performance. Incorporating GGBS into iron ore tailing–based mixes yielded a 10–20% improvement in 28-day compressive strength, reflecting the pozzolanic enhancement and matrix densification imparted by GGBS. Subsequent fiber addition contributed an additional 6.5–10% increase in strength, thereby demonstrating effective crack-bridging action.

Comparable trends emerged in foam-concrete systems, in which Raj et al. (2021) found that introducing 1% rice straw into a fly ash blend increased 28-day strength by 7.8% over control mixes and by 20.4% relative to mixes without straw. In contrast, higher straw contents reduced strength due to elevated porosity. Similarly, Morsy (2011)

observed that low fiber volumes suppressed crack propagation, whereas excessive fiber contents increased void formation. In the present investigation, mixes containing up to 1% fiber consistently achieved superior compressive performance, thereby confirming the synergistic benefits of pozzolanic binder modification and fiber reinforcement.

4.13.2 Tests on cladding panels

This section summarizes the experimental results obtained from six cladding panel mix designs. The casting and testing programme encompassed compressive strength, breaking load, modulus of rupture, thermal conductivity, and durability performance. Table 4.42 provided a concise overview of these outcomes, followed by a detailed discussion of how each property varied among the different panel specimens.

Table 4.42: Summary of test results

Cladding Panel Designation	Thermal Conductivity	Breaking strength	Modulus of rupture	Acid Resistance
	W/m·K	N	N/mm^2	
C100G00T50F00	1.2483	477.70	5.73	16.62
C080G20T50F00	1.0004	587.14	7.05	20.53
C060G40T50F00	0.9642	544.70	6.54	18.96
C100G00T50F01	1.2448	657.60	7.89	17.02
C080G20T50F01	0.9899	702.72	8.43	21.61
C060G40T50F01	0.9369	662.21	7.95	19.94

The thermal conductivity of the cladding panels decreased as the concentrations of GGBS and iron ore tailings (IOT) increased, and the inclusion of coir fiber further reduced conductivity.

Panels without fibers exhibited conductivities of 1.2483 W/m·K (C100G00T50F00), 1.0004 W/m·K (C080G20T50F00), and 0.9642 W/m·K (C060G40T50F00). Their fiber-reinforced trials showed slightly lower values of 1.2448 W/m·K (C100G00T50F01), 0.9899 W/m·K (C080G20T50F01), and 0.9369 W/m·K (C060G40T50F01).

Figure 4.50 details these variations across the different mix compositions with and without coir fiber.

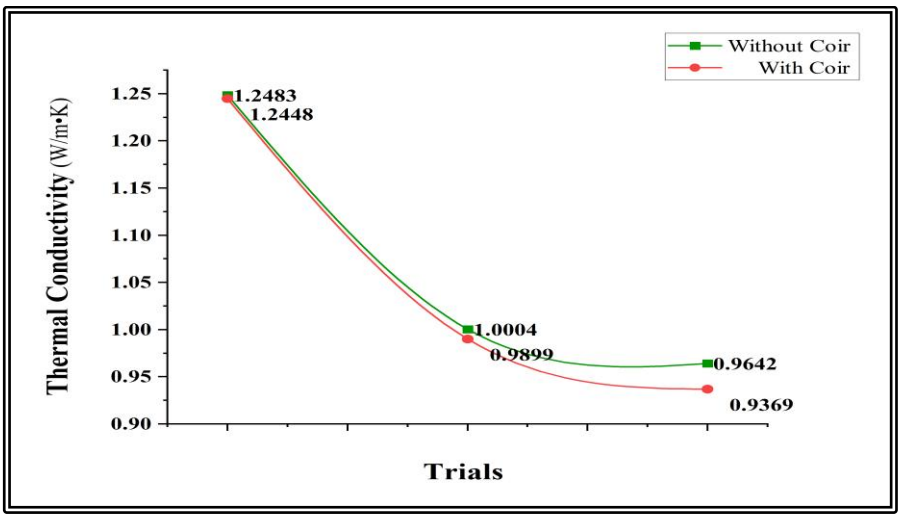


Figure 4.50: Variation in thermal conductivity for different cladding panels

The lowest conductivity, 0.9369 W/m·K, occurred in the mix containing 40% GGBS, 50% IOT, and 1% fiber, thereby demonstrating that supplementary cementitious materials and natural fibers synergistically enhanced insulation performance. When compared with typical wall panel conductivities (0.1–2.10 W/m·K), these results confirmed that optimized GGBS–IOT–fiber combinations significantly improved thermal performance.

Integrating alternative binders and agricultural fibers into foam concretes significantly reduces thermal conductivity, a dynamic corroborated by prior literature (Aravind et al., 2019; Raj et al., 2021). Specifically, substituting conventional cement with fly ash, alongside the addition of rice straw or rice husk, enhances thermal insulation and underscores the viability of these sustainable materials for energy-efficient construction applications.

Figure 4.51 illustrates the effect of coir fiber on the flexural performance of wall cladding panels, with all fiber-reinforced mixes displaying a higher modulus of rupture than their unreinforced trials.

The control mix C100G00T50F00 recorded a modulus of rupture of 5.73 N/mm^2, whereas its fiber-enhanced version C100G00T50F01 increased this value to 7.89 N/mm^2. Incorporating 20% GGBS and 50% IOT further improved flexural capacity, as C080G20T50F00 achieved 7.05 N/mm^2 and C080G20T50F01 peaked at 8.43 N/mm^2. The C060G40T50F00 and C060G40T50F01 mixes followed the same trend, with values rising from 6.54 to 7.95 N/mm^2.

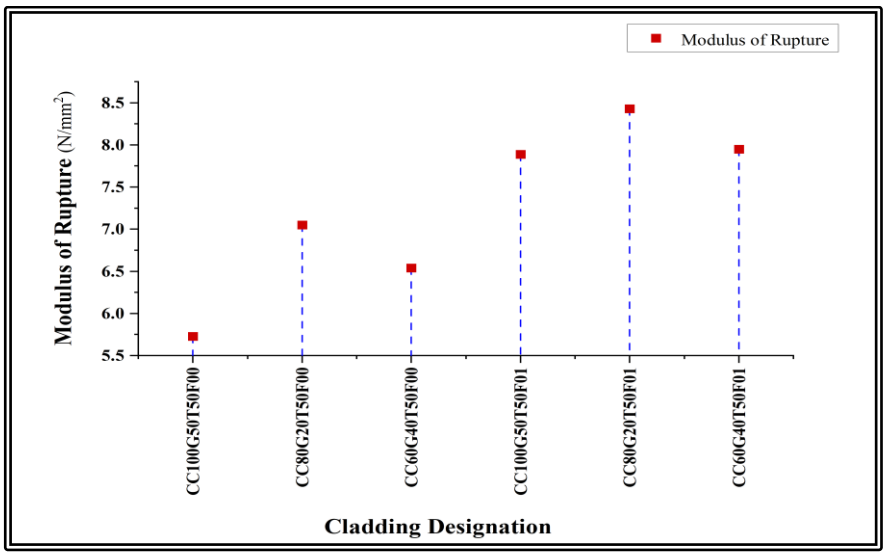


Figure 4.51: Modulus of rupture on cladding panel

The highest modulus of rupture in C080G20T50F01 highlighted the optimal synergy between GGBS pozzolanic activity, the IOT filler effect, and fiber crack-bridging, which collectively enhanced microstructural cohesion and load transfer. These outcomes paralleled the findings of Raj et al. (2021), who reported 5–9% increases in modulus of rupture with 1–2% rice straw and additional gains from fly ash, and those of Aravind et al. (2019), who observed up to 12% flexural strength enhancement when combining rice husk with 60% fly ash. Such consistencies confirmed that natural fibers and supplementary cementitious materials significantly bolstered flexural performance while simultaneously promoting sustainability. The incorporation of coir fiber increased the water absorption capacity compared with the other corresponding mixes, a trend also reported by other studies, as tabulated in the Table 4.43.

Table 4.43: Rate of water absorption over a period of time (all values in grams/100 cm^2)

Cladding Panel Composition	Time Duration in Mins.			
	15	60	240	1440
C100G00T50F00	2.21	3.01	3.41	3.61
C080G20T50F00	1.81	2.41	3.01	3.41
C060G40T50F00	2.01	2.61	3.41	3.81
C100G00T50F01	1.61	2.81	3.81	4.82
C080G20T50F01	2.01	2.61	3.61	4.21
C060G40T50F01	2.41	3.41	4.41	5.22

Figure 4.52 illustrate the water absorption behaviour of the cast cladding panels. Sequential exposure intervals of 15, 60, 240, and 1440 minutes characterized the water absorption behaviour of six composite mixes incorporating iron ore tailings and GGBS.

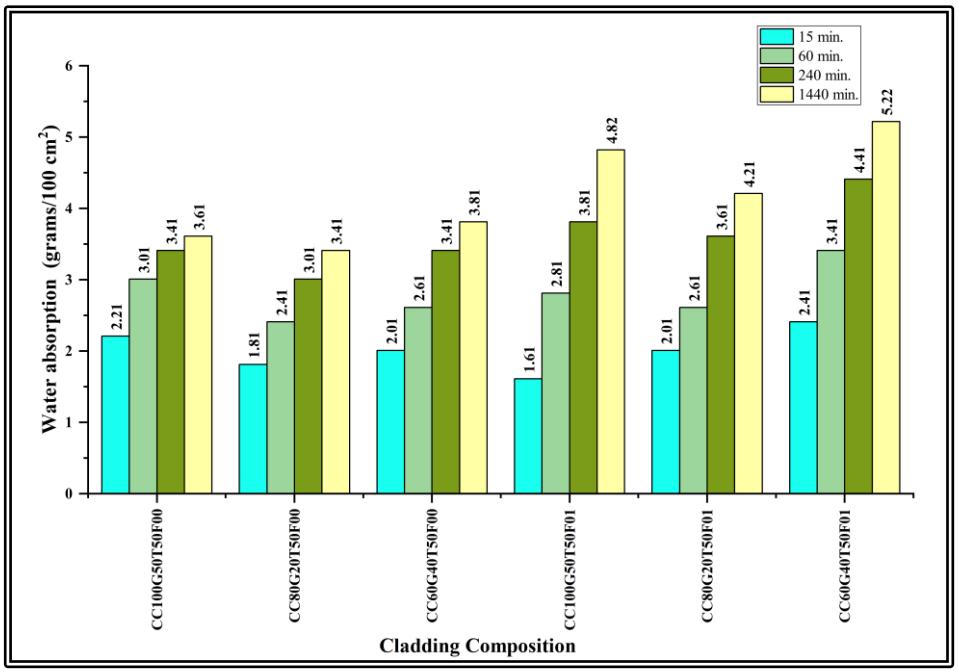


Figure 4.52: Variation of water absorption over a period of time

The mix C060G40T50F01 exhibited the highest water absorption among the cladding panels. The main factors governing water absorption included paste content, pore structure, and void distribution, and the formation of voids and pores varied with different fiber inclusion percentages. Both fibers and voids influenced the rate and magnitude of water uptake.

The mix C080G20T50F00 exhibited the lowest absorption across all intervals, reaching only 3.41% at 24 hours and thereby indicating superior pore refinement and durability. The non-fibrous mixes C100G00T50F00, C080G20T50F00, and C060G40T50F00 showed absorption values ranging from 3.41% to 3.81%, which remained significantly lower than those of the corresponding fiber-reinforced mixes (4.21% to 5.22%). The mix C060G40T50F01 recorded the highest absorption at 5.22%, representing a 53% increase relative to the same mix without fiber.

In acid resistance test, sulphuric acid immersion quantified the acid resistance of the cladding panels; this acidic exposure initiated surface deterioration that progressively advanced inward, ultimately reducing specimen strength relative to the control condition.

Table 4.44 presented the compressive strength of the six cladding panel formulations before and after acid immersion, and Figure 4.53 depicted the corresponding variation in strength. Acid exposure caused significant strength reduction across all mixes, ranging from 26.4% to 27.4%. The mix C080G20T50F1 exhibited the highest strength in both conditions, with 29.75 N/mm^2 before acid immersion and 21.61 N/mm^2 after immersion, thereby demonstrating superior overall performance.

Table 4.44: Compressive strength measured on cube specimens for various mixes (with acid immersion and without acid immersion) (all values in N/mm^2)

Cladding Panel Designation	Average compressive strength	
	Without	With
C100G00T50F0	22.59	16.62
C080G20T50F0	28.23	20.53
C060G40T50F0	26.22	18.96
C100G00T50F1	23.60	17.02
C080G20T50F1	29.75	21.61
C060G40T50F1	26.84	19.94

The mix C100G00T50F0 showed the lowest strength in both states (22.59 N/mm² and 16.62 N/mm², respectively). Fiber-containing mixes consistently outperformed their fiber-free counterparts, with C080G20T50F1 and C100G00T50F1 achieving 29.75 N/mm² and 23.60 N/mm², respectively.

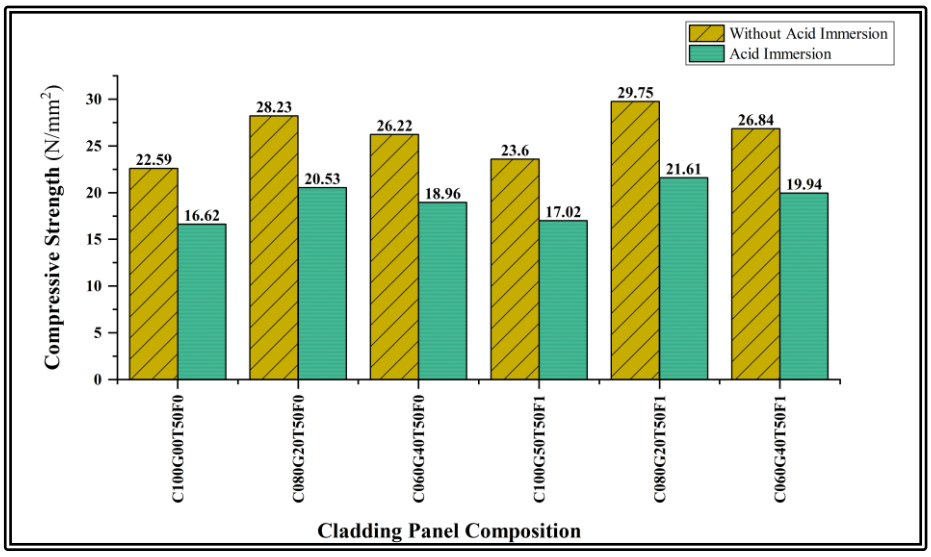


Figure 4.53: Variation in strength due to acid attack

Raj et al. (2021) reported a similar effect, noting that up to 1% rice straw addition, combined with fly ash replacement, increased acid resistance. Aravind et al. (2019) also

found that acid resistance improved with increasing fly ash content and decreased with increasing rice husk content. These parallels reinforced the conclusion that optimally dosed pozzolanic additions and controlled fiber contents enhanced both mechanical performance and durability in aggressive environments.

4.14 SEM-EDX characterization of cladding panels

High-resolution SEM imaging, coupled with EDX spectroscopy, defined the microstructural morphology and elemental profile of the two cladding panel samples. The electron microscope resolved surface texture, grain size, and pore structure, while the EDX system quantified and mapped the distribution of critical elements, such as silicon, aluminum, and calcium. Together, these analytical instruments provided the diagnostic data required to evaluate the raw materials, structural quality, and projected longevity of the two cladding panel compositions.

a) Cladding panel composition : C080G20T50F1

High-resolution FESEM analysis of C080G20T50F1 and concurrent 20-µm EDX elemental mapping reveal a dense, irregular morphology.. This distinct morphology characterizes a fabricated cladding layer, strongly indicating the formation of a polymer-ceramic hybrid or an oxide-based coating engineered for protective construction surfaces. Figure 4.54 shows SEM micrograph illustrating the microstructural morphology of C080G20T50F1.

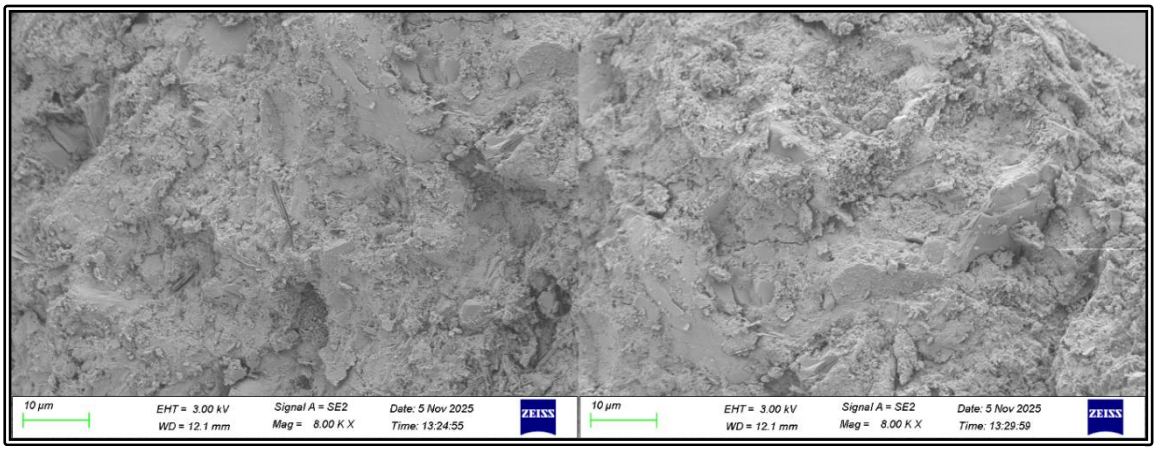


Figure 4.54: SEM micrograph of cladding panel with composition C080G20T50F1

Irregular particles (1–5 µm) actively fuse to form a continuous matrix with moderate porosity (~15–25%) and distinct surface cracks. These structural microfractures clearly record the application of thermal or mechanical stress during the synthesis phase.

Although this roughened topology inherently promotes superior mechanical adhesion to underlying substrates, the interconnected void network inherently compromises weather proofing efficacy, thereby mandating the integration of supplementary sealants for viable façade applications.

The concurrent EDX mapping definitively resolves the spatial elemental architecture, despite a sparse overlay population that potentially arises from imaging artifacts or localized low-density regions. Oxygen (O K, green) saturates the material ubiquitously, forming the foundational oxide framework. Silicon (Si K, red) uniformly permeates the matrix zones, signifying the successful integration of siliceous reinforcements. Aluminum (Al K, cyan) exclusively segregates into distinct patches generated by localized aluminate phases. Calcium (Ca K, pink) aggregates into minor clusters precipitated from calcareous additives, whereas iron (Fe K, brown) isolates into trace spots identifying discrete metallic oxide inclusions. Figure 4.55 shows EDX spectrum illustrating the relative abundance of the principal elements detected within C080G20T50F1.

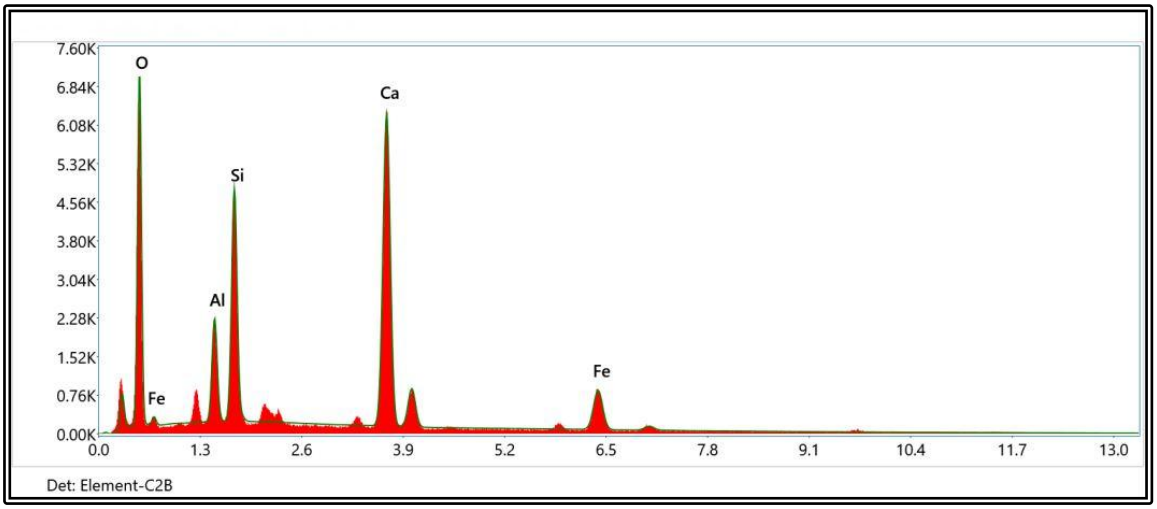


Figure 4.55: EDX spectrum detailing of principal elements for cladding panel with composition C080G20T50F1

This specific elemental architecture inherently yields a durable, corrosion-resistant cladding highly suitable for exterior building environments accommodating 10–20% additive integration. Moving forward, quantitative EDX evaluation (e.g., atomic ratios: O ~50–60%, Si ~20–30%, Al ~5–10%, Ca ~3–8%, Fe ~2–5%) and rigorous cross-sectional analysis will definitively quantify the barrier properties and strictly govern the optimization of future material formulations.

b) Cladding panel composition: C060G40T50F1

High-resolution FESEM analysis of C060G40T50F1 exhibits a highly porous, irregular microstructure, definitively characterizing a synthesized cladding composite. This morphological signature typifies a ceramic or composite coating engineered specifically for exterior construction elements, such as facades or tiles. Clustered aggregates comprising 2–10 µm particles, alongside pronounced void networks and fibrous extensions, heavily dominate the surface architecture. Such interconnected pore volume clearly indicates partial sintering or binder-limited consolidation mechanisms during fabrication. Consequently, while this structural configuration successfully imparts beneficial thermal insulation and aesthetic texturing, the interconnected void network inherently compromises water resistance in the absence of supplementary sealing. Figure 4.56 shows SEM micrograph illustrating the microstructural morphology of C060G40T50F1. Figure 4.57 shows EDX spectrum illustrating the relative abundance of the principal elements detected within C060G40T50F1.

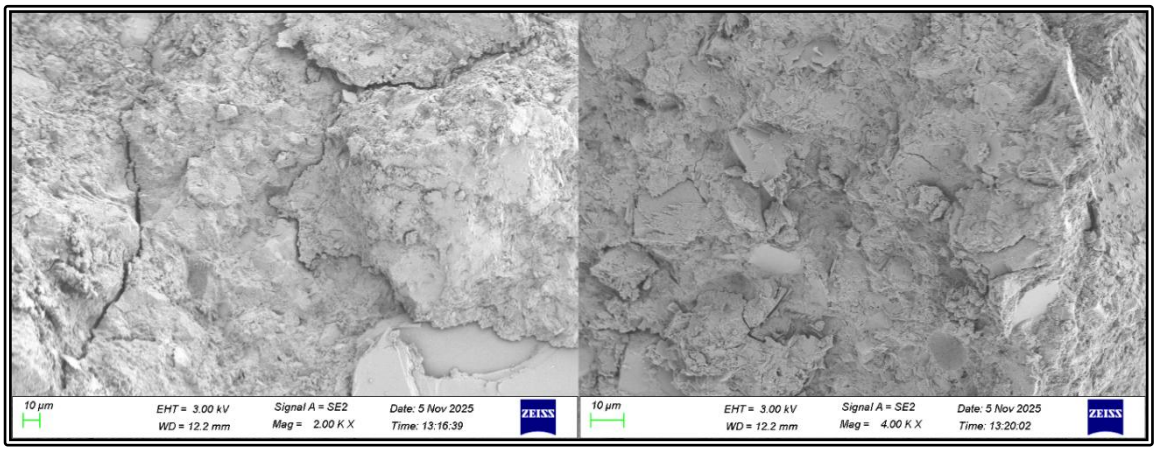


Figure 4.56: SEM micrograph of cladding panel with composition C060G40T50F1

Concurrent EDX mapping precisely resolves the spatial elemental distribution across this porous matrix. Oxygen (O K, green) saturates the material ubiquitously, forming the foundational oxide framework. Silicon (Si K, red) uniformly permeates the interstitial regions, indicating the incorporation of siliceous binders or fillers. Aluminum (Al K, cyan) co-precipitates intimately with silicon, forming distinct aluminosilicate phases.Calcium (Ca K, pink) aggregates into dispersed clusters derived from reactive calcareous components. Iron (Fe K, brown) strictly segregates into localized domains, isolating discrete metallic oxide inclusions.

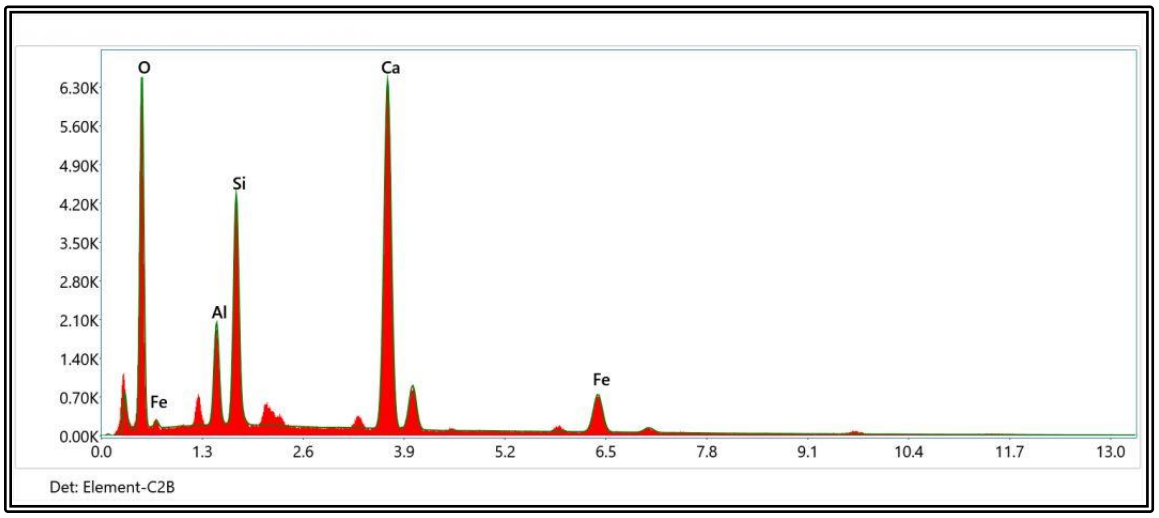


Figure 4.57: EDX spectrum detailing of principal elements for cladding panel with composition C060G40T50F1

This specific elemental architecture successfully establishes a balanced composition, heavily optimizing both durability and adhesion for exterior environments. Collectively, these microstructural and chemical mechanics definitively validate C060G40T50F1 as a highly viable material for eco-friendly building envelopes featuring waste-derived enhancements. Subsequent quantitative EDX evaluation (e.g., atomic ratios: O ~55–65%, Si ~20–30%, Al ~5–10%, Ca ~5–10%, Fe ~2–5%) and surface roughness profiling will definitively quantify material synthesis efficacy and strictly govern future in-service performance predictions.

4.15 Statistical analysis of cladding panels

The statistical analysis of the cladding panel mix presented in Table 4.45 showed consistent behaviour across all response variables, with clear trends associated with GGBS content and fiber addition, and low experimental scatter.

Across all mixtures and tests, the standard deviations and coefficients of variation were very low, generally below 0.02, indicating excellent repeatability of the measurements. The narrow 95% confidence intervals around the means further confirmed that the sample means reliably represented the population behaviour of each cladding mix.

Table 4.45: Statistical analysis of cladding panel

Cladding Panel Composition	Mean	Standard Deviation	Lower 95% CI of Mean	Upper 95% CI of Mean	SE of mean	Coefficient of Variation
7 days Compressive Strength						
C100G00T50F0	14.900	0.070	14.726	15.074	0.040	0.005

Cladding Panel Composition	Mean	Standard Deviation	Lower 95% CI of Mean	Upper 95% CI of Mean	SE of mean	Coefficient of Variation
7 days Compressive Strength						
C080G20T50F0	16.880	0.035	16.794	16.966	0.020	0.002
C060G40T50F0	15.300	0.100	15.052	15.548	0.058	0.007
C100G00T50F1	15.647	0.076	15.457	15.836	0.044	0.005
C080G20T50F1	18.230	0.050	18.106	18.354	0.029	0.003
C060G40T50F1	16.490	0.190	16.018	16.962	0.110	0.012
28 days Compressive Strength						
C100G00T50F0	21.307	0.101	21.057	21.557	0.058	0.005
C080G20T50F0	25.660	0.125	25.350	25.970	0.072	0.005
C060G40T50F0	23.407	0.130	23.083	23.730	0.075	0.006
C100G00T50F1	22.687	0.122	22.383	22.990	0.071	0.005
C080G20T50F1	28.073	0.186	27.612	28.534	0.107	0.007
C060G40T50F1	25.557	0.181	25.106	26.007	0.105	0.007
Thermal Conductivity						
C100G00T50F0	1.248	0.006	1.234	1.263	0.003	0.005
C080G20T50F0	1.000	0.010	0.977	1.024	0.005	0.010
C060G40T50F0	0.964	0.009	0.942	0.986	0.005	0.009
C100G00T50F1	1.245	0.014	1.211	1.279	0.008	0.011
C080G20T50F1	0.990	0.019	0.944	1.036	0.011	0.019
C060G40T50F1	0.937	0.011	0.911	0.963	0.006	0.011
Breaking strength						
C100G00T50F0	477.700	2.364	471.827	483.573	1.365	0.005
C080G20T50F0	587.140	2.647	580.564	593.716	1.528	0.005
C060G40T50F0	544.700	5.027	532.212	557.188	2.902	0.009
C100G00T50F1	657.600	6.729	640.884	674.316	3.885	0.010
C080G20T50F1	702.720	6.371	686.892	718.548	3.679	0.009
C060G40T50F1	662.210	2.550	655.876	668.544	1.472	0.004
Modulus of Rupture						
C100G00T50F0	5.730	0.085	5.518	5.942	0.049	0.015
C080G20T50F0	7.050	0.066	6.887	7.213	0.038	0.009

Cladding Panel Composition	Mean	Standard Deviation	Lower 95% CI of Mean	Upper 95% CI of Mean	SE of mean	Coefficient of Variation
Modulus of Rupture						
C060G40T50F0	6.540	0.082	6.337	6.743	0.047	0.013
C100G00T50F1	7.890	0.062	7.735	8.045	0.036	0.008
C080G20T50F1	8.430	0.062	8.275	8.585	0.036	0.007
C060G40T50F1	7.950	0.066	7.787	8.113	0.038	0.008
Acid Test						
C100G00T50F0	16.620	0.106	16.357	16.883	0.061	0.006
C080G20T50F0	20.530	0.154	20.148	20.912	0.089	0.008
C060G40T50F0	18.960	0.151	18.585	19.335	0.087	0.008
C100G00T50F1	17.020	0.113	16.740	17.300	0.065	0.007
C080G20T50F1	21.610	0.151	21.235	21.985	0.087	0.007
C060G40T50F1	19.940	0.139	19.595	20.285	0.080	0.007

4.16 Cost analysis of construction materials

The construction industry depends on the efficient, cost-effective production of key components such as bricks, blocks, pavers, tiles, and cladding. Effective manufacturing, supply, and overall project management require a clear understanding of production costs. This section explores a detailed breakdown of the expenses involved in producing these fundamental construction materials.

This exploration meticulously examines the factors that contribute to overall production costs. The analysis prioritizes raw material procurement, encompassing the sourcing and pricing of aggregates, cement, pigments, and other essential ingredients. The cost evaluation thoroughly analyzes labour expenses, including wages and operational overhead. Furthermore, the assessment incorporates the impact of energy consumption, machinery maintenance, and depreciation on final production costs.

A comprehensive analysis of cost structures for bricks, blocks, pavers, tiles, and cladding optimizes production, enhances efficiency, and secures competitive pricing. This analytical process ultimately drives informed decisions and fosters sustainable growth within the construction sector.

Data from the most successful trials drive the production cost calculations. A market survey dictates the prevailing material rates, presented in Table 4.46, which form the basis for determining the cost of each item.

Table 4.46: Rates of material used in casting composite construction materials
(Rates are inclusive of delivery charges to the production unit)

Material	Rate per kg in ₹
Cement	7.00
Lime	10.00
GGBS	3.75
Fly Ash	4.00
IOT	0.50
Basaltic Aggregate	1.30
Ceramic Waste	0.50
Manufactured sand	1.40
Coir	14.00

Practical observations from the production process indicate that manufacturing a batch of 1,000 bricks requires a total material input of 2,860 kg, as outlined in Table 4.9. Experimental trials, building upon the study by Kuranchie et al. (2015) and related literature, evaluated varying proportions of Ground Granulated Blast Furnace Slag (GGBS) and Fly Ash. The rate analysis utilizes a selected mix comprising 5% cement, 5% lime, 30% GGBS, 10% fly ash, and 50% iron ore tailings (IOTs).

Casting the trials at the manufacturing facility quantified the labour consumption requirement. The rate analysis shown in Table 4.47 integrates current market rates with the material quantities required to cast 1,000 bricks.

Table 4.47: Rate analysis of brick

Sr. No	Particulars	Qty. (in kg)	Rate (in ₹)	Amount(in ₹)
A)	Material			
1	Cement	132	7.00	924.00
2	Lime	66	10.00	660.00
3	GGBS	671	3.75	2516.25
4	Fly Ash	198	4.00	792.00
5	IOT	2079	0.50	1039.50
			Total	5931.75
B)	Labour	1.00	800.00	800.00
C)	Electricity and Water supply	Lump Sum		200.00
D)	Miscellaneous	Lump Sum		400.00
			Total	**7331.75**

This analysis reveals a total casting cost of ₹7,331.75 per 1,000 bricks, or ₹7.33 per brick.

The rate analysis for concrete blocks uses a mix design trial with a blended cementitious binder comprising 15% cement, 10% lime, 65% GGBS, and 10% fly ash. The mixture incorporates IOTs as fine aggregate and a blend of 70% basaltic aggregate and 30% recycled ceramic waste as coarse aggregate. Table 4.21 presents the material quantities required to produce 1 m³ of the block mix, which serves as the foundation for the subsequent rate analysis.

The casting process directly determined the labour consumption. Table 4.48 presents the rate analysis, derived from prevailing market rates applied to the material quantities required for a 1 m³ block mix.

Table 4.48: Rate analysis of block

Sr. No	Particulars	Qty. (in kg)	Rate (in ₹)	Amount(in ₹)
A)	Material			
1	Cement	71.53	7.00	500.73
2	Lime	47.69	10.00	476.89
3	GGBS	309.98	3.75	1162.42
4	Fly Ash	47.69	4.00	190.76
5	IOT	932.44	0.50	466.22
6	Basaltic Aggregate	640.65	1.30	832.84
7	Ceramic Waste	274.57	0.50	137.28
			Total	3767.15
B)	Labour	0.4	800	320.00
C)	Electricity and Water supply	Lump Sum		100.00
D)	Miscellaneous	Lump Sum		200.00
			Total	**4387.15**

Processing 1 m³ of the mix yields 111 blocks. The 1 m³ volume incurs a total production cost of ₹4,387.15, which translates to ₹39.52 per block (15 cm x 20 cm x 30 cm).

The general casting protocol for pavers and tiles demands cement, GGBS, IOTs, manufactured sand, and 10 mm aggregate. The specific paver mix design dictates a cementitious content of 80% cement and 20% GGBS. The design specifies a fine

aggregate blend of 70% manufactured sand and 30% IOTs, alongside a coarse aggregate consisting entirely of 10 mm basaltic aggregate. Table 4.28 details the material quantities required to cast 1 m³ of the paver mix, which drives the subsequent rate analysis.

As with block production, the casting phase tests established the exact labour consumption. Table 4.49 presents the rate analysis, which integrates prevailing market rates with the material quantities required to cast a 1 m³ mix of pavers.

Table 4.49: Rate analysis of paver

Sr. No	Particulars	Qty. (in kg)	Rate (in ₹)	Amount(in ₹)
A)	Material			
1	Cement	362.88	7.00	2540.16
2	GGBS	90.72	3.75	340.20
3	Crushed Stone Sand	629.64	1.40	881.49
4	IOT	315.36	0.50	157.68
5	Basaltic Aggregate	1170.72	1.30	1521.94
			Total	5441.47
B)	Labour	800.00	1.50	1200.00
C)	Electricity and Water supply	Lump Sum		200.00
D)	Miscellaneous	Lump Sum		400.00
			Total	**7241.47**

Size of pavers: 0.20 m x 0.10 m x 0.06 m

Number of pavers cast from 1 m³ mix: $\frac{1}{0.2\text{m x } 0.1\text{m x } 0.06\text{m}}$ = 833 pavers

Cost of each paver: $\frac{₹\ 7241.47}{833}$ = ₹8.70 per piece

Number of pavers laid per 1 m² area: $\frac{1}{0.2\text{ m x } 0.1\text{ m}}$ =50 pavers

Rate per 1 m² for the pavers: ₹8.70 x 50 = ₹435 per m²

The tile material composition replicates that of the pavers; however, differing manufacturing methodologies alter the required material quantities. Direct observation during the casting process established the labour consumption metrics. Table 4.50

presents the rate analysis, coupling current market rates with the material requirements for casting 1 m³ of the tile mix.

Table 4.50: Rate analysis of tile

Sr. No	Particulars	Qty. (in kg)	Rate (in ₹)	Amount(in ₹)
A)	Material			
1	Cement	349.44	7.00	2446.08
2	GGBS	87.36	3.75	327.60
3	Crushed Stone Sand	606.32	1.40	848.84
4	IOT	303.68	0.50	151.84
5	Basaltic Aggregate	1127.36	1.30	1465.57
			Total	5239.93
B)	Labour	800.00	0.50	400.00
C)	Electricity and Water supply	Lump Sum		200.00
D)	Miscellaneous	Lump Sum		300.00
			Total	6139.93

Size of tiles: 0.30 m x 0.30 m x 0.025 m

Number of tiles cast from 1 m³ mix: $\frac{1}{0.3\text{m x } 0.3\text{m x } 0.025\text{m}}$ = 444 tiles

Cost of each tile: $\frac{6139}{444}$ = ₹13.83 per piece

Number of tiles laid per 1 m² area: $\frac{1}{0.3\text{ m x } 0.3\text{ m}}$ = 11 tiles

Rate per 1 m² for the tiles: ₹13.83 x 11 = ₹152.13 per m²

Trial mix comprising 80% cement and 20% GGBS serves as the basis for the analysis of the cladding panel rate. The mixture incorporates fine aggregate comprising equal parts of manufactured sand and iron ore tailings (IOTs), with a 1% addition of coir fiber. Direct observation during the casting process established labour consumption, consistent with the previously discussed materials. Table 4.51 presents the rate analysis, which applies current market rates to the material quantities needed to cast 1 m³ of the cladding mix.

Table 4.51: Rate analysis of cladding panel

Sr. No	Particulars	Qty. (in kg)	Rate (in ₹)	Amount(in ₹)
A)	Material			
1	Cement	600.83	7.00	4205.81
2	GGBS	127.1	3.75	476.625
3	Crushed Stone sand	427.51	1.40	598.514
4	IOT	612.38	0.50	306.19
5	Coir	7.28	14.00	101.92
			Total	5689.06
B)	Labour	800.00	1	800.00
C)	Electricity and Water supply	Lump Sum		200.00
D)	Miscellaneous	Lump Sum		200.00
			Total	**6889.06**

The 1 m³ cladding volume incurs a total casting cost of ₹6,889.06.

Size of cladding: 0.25 m x 0.25 m x 0.010 m

Number of cladding panels cast from 1 m³ mix: $\frac{1}{0.25\text{m x } 0.25\text{m x } 0.01\text{m}}$ = 1,600 panels

Cost of each cladding panel: $\frac{6889.06}{1600}$ = ₹4.30 per piece

Number of cladding panels laid per 1 m² area: $\frac{1}{0.25\text{ m x } 0.25\text{ m}}$ = 16 panels

Rate per 1 m² for the cladding: ₹4.30 x 16 = ₹68.80 per m²

4.17 Analysis for cost of setting a manufacturing unit

The proposed manufacturing layout incorporates three essential components: a material storage area, an administrative office, and a production shed. The facility design occupies a total area of 1,000 square meters. The storage area design accommodates raw materials for 6 days and includes an additional 3-day buffer to prevent disruptions and ensure uninterrupted operations.

Within this operational workflow, racks support cast-finished construction materials to optimize space utilization during the initial setting and strength-gaining period. Adequate hardening initiates the transfer of these materials to a curing zone for final processing.

The administrative office occupies an allocated area of 20 sq. mts, providing appropriate sizing for small to medium-scale operations.

The production shed, spanning 200 square meters, serves as the primary operational hub. This specific square footage easily accommodates compact, efficient machinery, facilitates all production activities, and enables the smooth handling and movement of finished products. The shed's dimensions offer an optimal blend of functionality, workflow efficiency, and cost-effectiveness, making it ideally suited to micro, small, and medium enterprises.

A quotation from Hanje Hydrotech, Sangli—a reputed local manufacturer of industrial equipment—dictates the cost of the necessary production machinery.

The financial model dictates specific staffing qualifications: the Plant In-Charge role requires a Diploma in Civil Engineering, whereas the Supervisor position necessitates a Higher Secondary School Certificate. Operating requirements mandate that the driver hold a valid Heavy Motor Vehicle (HMV) license, and that multi-tasking personnel possess at least an 8th-grade education.

Prevailing market rates for goods and services dictate the estimation of additional contingency expenses. The financial model categorizes these assumed overhead costs as follows:

Postage and Stationery: Moderate administrative communication needs require envelopes, letterheads, pens, printer paper, and courier/postal charges.

Telecommunications: Standard usage plans dictate the mobile and internet costs for basic communication.

Consumables: Monthly usage rates determine expenditures for printer cartridges, cleaning agents, and lubricants.

Repairs and Maintenance: Preventive maintenance protocols necessitate expenditures for routine servicing, minor machinery/infrastructure repairs, technician fees, spare parts, and lubricants.

Transportation: Material delivery to construction sites—assuming 2 to 3 trips per day within a 25 to 30 km radius—drives the transportation expenses.

Advertisement and Publicity: Digital platforms handle the primary marketing efforts, keeping these expenses modest.

Insurance: Industry norms dictate the premium rates for policies that protect manufacturing machinery and tools, cover worker safety liabilities, and secure stock/premises against fire and theft.

The initial operational stage of the modelled manufacturing unit limits monthly production to the following volumes: 3,000 bricks, 3 m³ of blocks, 8 m³ of pavers, 5 m³ of tiles, and 1 m³ of cladding.

Based on raw material requirements and monthly procurement needs, Table 4.52 presents a detailed analysis of the manufacturing unit setup.

Table 4.52: Manufacturing unit setup cost analysis

A)FIXED CAPITAL			
(i) Land and Building			
Particulars	**Area**	**Rate**	**Amount(in ₹)**
Land	1000.00	2000.00	2000000.00
Office & Store	20.00	20000.00	400000.00
Working Shed	200.00	15000.00	3000000.00
		Total :	**5400000.00**
(ii) Machinery & Equipment Production Unit			
Particulars	**Qty**	**Rate**	**Amount(in ₹)**
Concrete Brick Machine	1	350000.00	350000.00
Concrete Block Machine	1	375000.00	375000.00
Concrete Paver Machine	1	372000.00	372000.00
Electric Mortar (5HP)	4	35000.00	140000.00
Heavy duty Vibration	1	100000.00	100000.00
Colour Pan Mixer	1	70000.00	70000.00
Concrete mixture	1	124000.00	124000.00
Cost of erection and	1	280400.00	280400.00
Mould	1500	400.00	600000.00
Pallet	47	2100.00	98700.00
		Total :	**2510100.00**
		(i+ii)	**7910100.00**
B)WORKING CAPITAL (Per Month)			
(i) Administrative Staff			
Particular	**No**	**Salary**	**Amount(in ₹)**
Plant In charge	1	30000.00	30000.00
Supervisor	1	20000.00	20000.00
Driver	1	18000.00	18000.00
Multi-Tasking Staff	1	12000.00	12000.00
		Total :	**80000.00**
(ii) Tech. Skilled and Semi or Unskilled Personnel			
Particular	**No**	**Wages**	**Amount(in ₹)**
Unskilled Workers	25	800.00	500000.00
		Total :	**500000.00**
		(i+ii)	**580000.00**

(iii) Raw Materials (Per Month)

Particular	Consumption	Rate	Amount(in ₹)
Cement	146645.91	7.00	1026521.35
Lime	8596.13	5.00	42980.63
GGBS	106266.27	3.75	398498.52
Fly Ash	18496.13	4.00	73984.50
IOT	325734.68	0.50	162867.34
Crushed Stone Sand	212405.82	1.40	297368.15
Basaltic Aggregate	423807.10	1.30	550949.23
Ceramic Waste	19229.18	0.50	9614.59
Coir	181.98	14.00	2547.75
		Total :	2565332.05

(iv) Other contingency Expenses (Per Month)

Expense	Amount(in ₹)
Postage and Stationery	2000.00
Mobile and Internet	1000.00
Consumable Stores	2000.00
Repairs and maintenance	5000.00
Transport Charges	30000.00
Advertisement and Publicity	2000.00
Insurance etc.	5000.00
Total :	**47000.00**

Total Recurring Expenditure per month (i+ii+iii) =	**3192332.00**
Total Working Capital (for 3 months) =	**9576996.00**

(C) TOTAL CAPITAL INVESTMENT	
(i) Total Fixed Capital :	**7910100.00**
(ii) Total Working Capital:	**9576996.00**
	17487096.00

4.18 Analysis for payback period

Annual turnover, operating expenses, and financial expenses drive the payback analysis. The newness of the manufacturing facility and the requirement to build customer confidence restrict initial plant operations to 50% capacity, which then scales by 5% each subsequent year. Table 4.53 presents the annual sales report, providing a detailed view of projected sales performance.

Table 4.53: Annual Sales Performances
(Considered With 25 Days of Working per Month)

Material	Unit	Daily production	Rate per unit in ₹	Annual working days	Amount in ₹
Brick	Nos.	3000	12.00	300	10800000.00
Block	Nos.	330	45.00	300	4455000.00
Pavers	M^2	135	550.00	300	22275000.00
Tiles	M^2	200	350.00	300	21000000.00
Cladding	M^2	100	100.00	300	3000000.00
				Total :	61530000.00

The first-year 50% capacity constraint restricts the estimated annual turnover to ₹3,07,65,000 (₹307.65 lakhs). The financial model calculates the annual raw material cost at ₹3,07,83,985 (₹307.84 lakhs). The projection designates 50% of this annual raw material cost (₹153.92 lakhs) as operating expenses. Table 4.54 presents the cash flow statement.

Table 4.54: Cash flow statement (Values in lakhs)

Particulars	Year 1	Year 2	Year 3	Year 4	Year 5
A. INCOME					
Production Capacity (In Lakhs)	615.30	615.30	615.30	615.30	615.30
Capacity utilisation	0.50	0.55	0.60	0.65	0.70
Turnover During the year	307.65	338.42	369.18	399.95	430.71
B. OPERATING EXPENSES					
Raw Material	153.92	169.31	184.70	200.10	215.49
Salary	69.60	69.60	69.60	69.60	69.60
Repair & Maintenance	6.15	6.77	7.38	8.00	8.61
Power & utilities	12.31	13.54	14.77	16.00	17.23
Depreciation	6.72	6.72	6.72	6.72	6.72
Total Operating Expenses	248.70	265.94	283.17	300.41	317.65
Operating Profit (A-B)	58.95	72.48	86.01	99.53	113.06
C. FINANCIAL EXPENSES					
Interest on term loan	10.18	10.56	10.95	11.33	11.72
D. ADMINISTRATIVE EXPENSES					
Office Expenses	5.64	5.64	5.64	5.64	5.64
Total Expenses	264.52	282.14	299.76	317.38	335.01
Profit Before Tax	43.13	56.28	69.42	82.56	95.70
Provision for Tax	10.78	14.07	17.35	20.64	23.93
Profit after Tax (PAT)	32.35	42.21	52.06	61.92	71.78
Dividend Declared	0.00	0.00	0.00	0.00	0.00
Retained Profit	32.35	42.21	52.06	61.92	71.78

The salary component incorporates the actual wages for administrative personnel, technical staff, and both skilled and unskilled workers. The financial projection assumes repair and maintenance costs (classified as operating expenses) equal 2% of annual turnover; these costs increase proportionately with turnover growth. Similarly, the model sets power and utilities expenses at 4% of annual turnover, scaling them with revenue.

The cost analysis applies depreciation of 5% to the building and shed, and 20% to the machinery. Raw material costs, salaries, repair and maintenance, power and utilities, and depreciation constitute the total operating expenses. The difference between annual revenue and total operating expenses determines the operating profit.

The financial model sets the interest on the term loan (secured for land, buildings, and machinery) at 8% and calculates three months of working capital at 10%. Total expenses combine operating expenses and interest on the term loan. Subtracting total expenses from the annual turnover yields the Profit Before Tax (PBT). The projection applies a 25% tax provision to the PBT; after deducting this provision, the result is the Profit After Tax (PAT).

Table 4.55 details the payback period calculation, which cumulatively adds retained earnings until the total matches the initial investment. A proportional calculation in months and days refines the payback period when the investment amount falls between the cumulative cash flows of two consecutive years, determining the exact recovery timeline.

Table 4.55: Pay back calculation (Values in lakhs)

Manufacturing commencement year	Cash Flow	Cumulative
1	32.35	--
2	42.21	74.56
3	52.06	126.62
4	61.92	188.54
5	71.78	260.32

By the end of the third year, cumulative cash flows recover ₹126.62 lakhs of the total investment of ₹174.87 lakhs. Consequently, the fourth-year revenue stream absorbs the outstanding balance of ₹48.25 lakhs.

The fraction of Year 4 required is 0.779.

Total payback period in years: 3+ 0.779 =3.779 years.

Converting the fractional year into months and days:

- 0.779×12=9.3480.779×12=9.348 months (9 months)
- 0.348×30=10.50.348×30=10.5 days (11 days)

Payback period = 3 years, 9 months, 11 days

Establishing a versatile production plant requires significant capital expenditure, primarily for land acquisition, automated machinery, utilities, and working capital. Once a comprehensive market analysis confirms local demand and competitive pricing, financial projections generally indicate a payback period of 2.5 to 4 years; in the present study, it is well justified to set up a full-scale plant having a payback period of less than 4 years. However, the timeframe relies on plant capacity utilization scaling from 50% to 80% over three years, with high-volume foundational products covering fixed overheads while high-margin aesthetic products accelerate overall profitability.

CHAPTER 5
SUMMARY AND CONCLUSIONS

This chapter presents the conclusions derived from the investigation and highlights the scope for further research to build upon these findings.

5.1 Summary

This research successfully validated the sustainable valorization of Goan iron ore tailings (IOTs) into five composite construction product categories: bricks, blocks, pavers, tiles, and cladding panels. Characterized by high specific gravity and chemical stability, IOTs were optimized alongside GGBS, fly ash, and coir fibers to trigger synergistic binding reactions.

Across all applications, the developed composites met or exceeded the requirements of the Indian Standards. Bricks achieved a 28-day compressive strength of 13.58 N/mm² with excellent severe-weather durability, while blocks, tiles, and pavers demonstrated superior mechanical performance and low water absorption. Furthermore, the fiber-reinforced cladding panels provided enhanced thermal insulation and structural integrity.

Financially, the products are highly viable, offering low unit production costs and a commercial payback period of under four years. Ultimately, this study offers a scalable, transferable framework that bridges laboratory waste utilization with regional industrial manufacturing, directly advancing global circular economy objectives.

5.2 Conclusions

Here the research successfully developed and validated a comprehensive range of sustainable composite construction materials derived from iron ore tailings (IOTs), a significant mine waste generated by the Goan mining industry. The work combined rigorous material characterization, mix design optimization across five product categories (bricks, blocks, pavers, tiles, and cladding panels), and extensive durability assessment to provide strong empirical evidence for the valorization of mine waste in the development of composite material. As per the title of this research work, “Development of Composite Material using Mine waste,” and accordingly drafted, all the objectives have been successfully carried out in this research work. Its findings are presented below, along with specific conclusions.

1. With respect to the first objective of analyzing the physicochemical parameters of mine waste, IOTs used in this study exhibited favorable physicochemical characteristics as an ingredient in the development of composite material, with a specific gravity of 3.25, which is higher than natural fine aggregates, and a dominant elemental composition of iron (44.12% by mass) and silicon dioxide (17.90% by mass). Water absorption of 22.00%, very low sulfur content (0.02%), and the absence of deleterious substances confirmed its chemical stability and suitability as a constituent of construction materials.
2. With respect to the other materials, Cement, GGBS, Fly ash, ceramic waste, and lime used in this study for their potential use as a construction material, along with mine waste, indicated that Cement had a fineness of 323 m^2/kg and a specific gravity of 3.14. GGBS with specific gravity 2.81, fineness 397 m^2/kg, glass content 92.00%, and fly ash having specific gravity 2.65 plus combined SiO_2+Al_2O_2+Fe_2O_3 of 88.95% collectively provided synergistic binding and pozzolanic reactions, which help to reduce the content of OPC. The lime used had a specific gravity of 2.2 and a CaO 57.19%. The ceramic waste had a specific gravity of 2.25, an uncompacted bulk density of 1090 kg/m^3, and a compacted bulk density of 1265 kg/m^3. Which are favourable for utilising in appropriate proportions along with mine waste sample for the development of composite material.
3. Various combinations of binding materials with mine waste were evaluated to determine the optimal performance, as per the objective. Compressive strength was the major criterion in determining the optimal mix. It was observed that the values stated in Table 4.10 indicate that the compressive strength of various brick mixes for brick design exceeds the codal requirements. Similarly, the compressive strength values stated in Table 4.22 for the block design were higher than those specified in the IS code. The compressive strength of cubes cast for paver and tile design for M30 grade of concrete was 41.61N/mm2, with 30% mine waste utilized and 20% GGBS as supplementary cementitious material. In the mix for claddings containing 80% cement and 20% GGBS, along with 1% fiber, the compressive strength was 28.07 N/mm2, which was higher than the other designed mixes.
4. The manufacturing of various composite construction materials, such as bricks, blocks, pavers, tiles, and cladding panels was carried as a major part of this reaserch work.

a. For bricks, the optimal mix T50F10G30 (50% IOT, 10% fly ash, 30% GGBS, 5% cement, 5% lime) achieved compressive strengths of 10.47 N/mm² at 7 days and 13.58 N/mm² at 28 days, significantly exceeding the minimum requirement of 3.5 N/mm² as specified in IS 1077:2025. Water absorption remained limited to 5.05%, well below the IS limit of 15%. At the same time, dry and wet bulk densities of 1,839 kg/m³ and 1,932 kg/m³ were comparable to conventional fired bricks, indicating a dense microstructure arising from optimized packing of angular, high-specific-gravity IOT particles.
b. After seven wet–dry cycles, compressive strength of bricks decreased by 21.56% (from 13.60 N/mm² to 10.67 N/mm²), remaining within the acceptable 20–30% reduction range for masonry units in severe weathering conditions.
c. Durability and non-destructive indicators further supported the suitability of IOT bricks. Electrical resistivity ranged from 266.43 to 471.73 Ω·km across mixes, with T50F10G30 achieving 471.73 Ω·km, within the conventional safe range and confirming electrical safety despite high iron content.
d. Efflorescence tests showed only slight salt deposition (approximately 10% surface coverage, Class A), and all bricks exhibited robust impact resistance, metallic ringing in soundness tests, and no surface indentation in hardness tests, confirming structural integrity for load-bearing applications.
e. Statistical analysis revealed a strong inverse correlation between water absorption and compressive strength (Pearson's $r = -0.988$, $R^2 = 0.9762$), indicating that each 1 N/mm² increase in strength reduced water absorption by about 0.5%; conversely, compressive strength and electrical resistivity were strongly positively correlated ($r = 0.97$, $R^2 = 0.94$), showing that optimized mixes can simultaneously enhance strength and electrical safety.
f. Concrete masonry blocks with IOT as coarse aggregate replacement attained 28-day compressive strengths of 15.92 N/mm² in the control mix A100CW00 (100% IOT, 0% ceramic waste) and 15.50 N/mm² in the mix A070CW30 with 30% ceramic waste substitution, demonstrating the feasibility of multi-waste valorization without compromising structural performance.
g. Bulk densities ranged from 1,860–2,200 kg/m³, while water absorption ranged from 4.64% to 5.31%, satisfying requirements for structural masonry blocks.

h. For pavers, mixes with GGBS replacement and limited IOT content delivered outstanding mechanical performance. The C080T10 mix (80% cement and 20% GGBS, 10% IOT) reached compressive strengths of 28.10 N/mm² at 7 days, 44.14 N/mm² at 28 days, and 53.63 N/mm² at 56 days. At 56 days, both C080T10 (53.63 N/mm²) and C060T10 (53.08 N/mm²) exceeded the best 100% cement mixes by more than 14%, confirming that controlled IOT incorporation with high GGBS replacement yields sustainable, high-performance pavements through continued pozzolanic activity.
i. Water absorption of pavers showed optimal performance at 10% IOTs utilisation, with C100T10 at 1.77%, C080T10 at 2.73%, and C060T10 at 3.49%, the lowest at the respective cement replacement levels.
j. Tensile splitting tensile was highest for 10% IOT substitution with a 100% cement mix, at 6.79N/mm², whereas for 80% and 60% cement it was 6.36N/mm² and 6.02N/mm², respectively. Values of all trial mixes exceeded the 2.55 N/mm² minimum threshold mandated by the Indian Standard code for M30 grade concrete pavers.
k. Mixtures containing 10% IOT maximized flexural strength; specifically, the 100% cement formulation yielded 9.04 N/mm², whereas the 80% and 60% cement proportions produced 9.61/mm² and 8.45 N/mm², respectively, which substantially exceeded reported values for comparable materials and demonstrated the effectiveness of the IOT–GGBS system in enhancing crack resistance and bending capacity.
l. The strong positive correlation between splitting tensile and compressive strength ($R^2 > 0.98$) confirmed consistent and predictable mechanical behaviour, enabling reliable engineering design and quality control. Tiles exhibited similarly favourable performance.
m. Water absorption tests in tiles showed optimal performance also at 10% IOT replacement level. The C100T10 mix recorded 2.52% absorption (19.2% lower than the 3.12% of C100T00), and while C080T10 maintained the lowest water absorption at 3.46%, C060T10 had water absorption of 4.40%. Regression confirmed a strong inverse correlation between water absorption and strength.
n. The wet transverse strength of tiles ranged from 5.7 to 9.67 N/mm² across all trials and was much higher than the minimum specified strength of 3N/mm² in the IS

13801 (2013) code. Wet transverse strength reached 8.96 N/mm² for C100T10, 8.73 N/mm² for C080T10, and 8.47 N/mm² for C060T10, which were the maximum for their respective cement substitutions, indicating that IOT-based tiles can meet structural and serviceability requirements.

o. For cladding panels, the study demonstrated that mix composition critically influences both early and long-term strength development. The optimal formulation C080G20T50F1 (80% cement, 20% GGBS, 50% IOT, 1% coir fiber) achieved a 28-day compressive strength of 28.07 N/mm², corresponding to a 31.7% improvement over the control mix C100G00T50F0. Within this increase, 20% GGBS replacement contributed about 20.4% strength enhancement. In comparison, fiber addition provided a further 6.5–10% gain via crack-bridging, confirming the synergistic action of pozzolanic GGBS, IOT filler effects, and coir fiber reinforcement in densifying the matrix and refining the interfacial transition zone.

p. Functional performance indicators of panels also improved with a tailored mix design. Thermal conductivity decreased with increasing GGBS and IOT contents, reaching a minimum of 0.9369 W/m- K for the mix containing 40% GGBS, 50% IOT, and 1% fiber, demonstrating significant insulation enhancement suitable for building envelope use.

q. Water absorption of panels ranged from 2.50% to 6.03%, with fiber-reinforced mixes showing higher uptake due to additional voids around the fibers; however, these composites still maintained superior strength retention under exposure.

r. Acid immersion tests of panels showed strength losses of 26.4–27.4% across all formulations. However, the optimized C080G20T50F1 mix retained the highest absolute strength of 21.61 N/mm², indicating that mix modifications primarily increased the baseline strength rather than fundamentally altering acid-resistance mechanisms.

5. In order to find out the commercial viability, the final objective of the study was to evaluate the cost of setting up a manufacturing unit, calculate the production cost per item, and determine the payback period .

i. Quantified financial metrics confirm the economic viability of the developed composites, as production processes yield unit costs of ₹7.33 per brick, ₹39.52 per block, ₹435 per m² of pavers, ₹152.13 per m² of tiles, and ₹68.20 per m² of cladding panels, achieving a payback period of 3 years, 9 months, and 11 days.

ii. Economic evaluation revealed that IOT-based products achieve significant cost advantages through reduced raw material procurement costs, elimination of disposal expenses, and the use of locally available tailings.

iii. Analyses of setup costs, per-unit production costs, and payback periods confirmed the commercial viability of mine-to-manufacturing integration at a regional scale, making these composites attractive for industrial adoption.

By establishing both technical performance and economic feasibility for large-scale IOTs utilization, this research directly contributes to mitigating the risks associated with Tailings storage across Goa's 154 mining leases.

The standardized characterization protocols, optimized mix designs, and performance evaluation frameworks developed for Goan IOT provide a transferable methodology for other mining regions, demonstrating that mine waste-based composites can match or exceed conventional materials while offering superior environmental and economic profiles. Overall, the study bridges the gap between laboratory-scale waste valorization and industrial-scale implementation and presents a robust, scalable pathway for sustainable construction materials that advance circular-economy objectives.

5.3 Scope for future work

This research has established a robust foundation for the development and characterization of sustainable composite construction materials from iron ore tailings; nevertheless, several promising avenues remain open to extend and enhance the present work. Future studies should address both material innovations and system-level deployment to move from proof-of-concept towards full industrial maturity.

1. Future research should investigate combining lightweight materials with IOT in block production to improve transportability, handling, and cost-efficiency. Testing varying proportions of these aggregates in IOT mixes will quantify their effects on porosity, unit weight reduction, strength retention, and thermal insulation.

2. Paver and tile production requires optimizing ternary binder mix designs of OPC, fly ash, and GGBS. Studies must evaluate replacing OPC with 10–30% fly ash and 20–50% GGBS by mass to identify combinations meeting Indian Standards for compressive and flexural strength, water absorption, and abrasion resistance.

3. Alternative natural fibers beyond coir should be explored for cladding panels and composites. Evaluating surface-modified rice straw and banana fibers at optimized dosages will yield comparative data on strength, toughness, and durability. Additionally, combining multiple fiber types into hybrid reinforcements could leverage complementary mechanical properties.

4. The development of self-compacting concrete (SCC) mixes specifically designed for IOTs incorporation represents a promising approach to improving production efficiency and product quality.

5. Such systems require investigation focusing on mechanical performance, durability, processing parameters, and mix proportion optimization.

Finally, future work should include broader system-level assessments, such as detailed life-cycle assessments of IOTs-based bricks, blocks, pavers, tiles, and cladding panels in real construction projects. These efforts will help quantify environmental benefits relative to conventional materials, validate performance under in-service conditions, and support the formulation of standards, guidelines, and policy instruments that facilitate mainstream adoption of mine waste-derived construction materials.

References

Aaron Fuller, Jörg Maier, Emmanouil Karampinis, Jana Kalivodova, Panagiotis Grammelis, Emmanuel Kakaras and Günter Scheffknecht (2018). “Fly Ash Formation and Characteristics from (co-)Combustion of an Herbaceous Biomass and a Greek Lignite (Low-Rank Coal) in a Pulverized Fuel Pilot-Scale Test Facility”, *Energies* 2018, 11, 1581-1619.

Abdulrahman, H. S. (2015). Potential use of iron ore tailings in sandcrete block making. *International Journal of Research in Engineering and Technology*, *4*(4), 409–414.

Abraham, P., & Gundimeda, H. (2018). 'Greening' the buildings - An analysis of barriers to adoption in India. *Cities and the Environment*, *10*.

Adiguzel, S., Boyaci, H., & Atici, U. (2012). Influence of limestone and fly ash additives on the properties of self-compacting concretes prepared with Portland cement and ground granulated blast furnace slag. *Construction and Building Materials*, *37*, 873–881.

Adiguzel, S., Tayfur, B., & Yazici, H. (2022). Tailings-in-concrete: A comprehensive review on environmental and mechanical aspects. *Construction and Building Materials*, *330*, 127216.

Ahmad, J., Alattyih, W., Jebur, Y. M., Alqurashi, M., & Garcia-Troncoso, N. (2023). A review on ceramic waste-based concrete: A step toward sustainable concrete. *Reviews on Advanced Materials Science*, *62*(1). https://doi.org/10.1515/rams-2023-0346

Akan, E., & Kiraci, K. (2022). A novel depreciation approach in an uncertain environment: Interval type-2 fuzzy sets in the maritime industry. *Soft Computing*, *27*(4), 1941–1969. https://doi.org/10.1007/s00500-022-06778-6

Akan, M. Ö., Dhavale, D. G., & Sarkis, J. (2017). Greenhouse gas emissions in the construction industry: An analysis and evaluation of a concrete supply chain. *Journal of Cleaner Production*, *167*, 1195–1207.

Alexandra, S., & Vitaliy, M. (2024). Approaches for data collection and process standardization in smart manufacturing: Systematic literature review. *Journal of Industrial Information Integration (Online)*, 100578. https://doi.org/10.1016/j.jii.2024.100578

Algin, H. M., & Turgut, P. (2008). Cotton and limestone powder wastes as brick material. *Construction and Building Materials*, *22*(6), 1074–1080. https://doi.org/10.1016/j.conbuildmat.2007.03.006

Ali, B., Loubna, B., & Leila, B. (2021). Impacts of mining activities on soil properties: Case studies from Morocco mine sites. *Soil Science Annual*, *71*(4), 395–407. https://doi.org/10.37501/soilsa/133011

Almada, B. S., Melo, H. S. S., Duarte, M. S., Aguilar, M. T. P., Garcia, D. C. S., Silva, G. J. B., & dos Santos, W. J. (2022). Study of mechanical, durability and microstructural properties of cementitious composite with addition of different iron ore tailings from Brazil. *Journal of Materials Research and Technology*, *18*, 1947–1962.

Almada, J. V., Almeida, N. M., Freitas, D., Dias, M. T., & Alencar, I. N. (2022). Environmental and technical properties of ecological bricks produced with iron ore tailings and recycled ceramic waste. *Journal of Cleaner Production*, *250*, 120020.

Amjad, H., Abd-Elaal, E.-S., Ma, X., Benn, T., & Fisher, M. (2025). A critical review of iron ore tailings as cement and aggregate substitutes for robust infrastructure: Mechanical, durability, eco-economic, and social impacts. *Journal of Cleaner Production*, *492*, 144853. https://doi.org/10.1016/j.jclepro.2025.144853

Andiç-Çakir, Ö., Sarikanat, M., Tüfekçi, H. B., Demirci, C., & Erdoğan, Ü. H. (2014). Physical and mechanical properties of randomly oriented coir fibre-cementitious composites. *Composites Part B: Engineering*, *61*, 49–54. https://doi.org/10.1016/j.compositesb.2014.01.029

Anon (2007). *Base metal and iron ore mining, Pollution Prevention and Abatement Handbook*. World Bank.

Aravind, N., Sathyan, D., & Mini, K. M. (2019). Rice husk incorporated foam concrete wall panels as a thermal insulating material in buildings. *Indoor and Built Environment*, *29*(5), 721–729.

Arbili, M. M., Alqurashi, M., Majdi, A., Ahmad, J., & Deifalla, A. F. (2022). Concrete made with iron ore tailings as a fine aggregate: A step towards sustainable concrete. *Materials*, *15*(18), 6236.

Arivalagan, S. (2014). Sustainable studies on concrete with GGBS as a replacement material in cement. *Jordan Journal of Civil Engineering*, *8*(3), 263–270.

Aruna, M. & Kumar, S. (2010). Studies on iron tailings towards usage for paving blocks manufacture. *International Journal of Earth Sciences and Engineering*, *3*(6), 861–868.

Awoyera, P. O., Ndambuki, J. M., Akinmusuru, J. O., & Omole, D. O. (2018). Characterization of ceramic waste aggregate concrete. *Housing and Building National Research Center*, *14*, 282–287.

Balasubramanian, A. (2017). *Review of an overview of mining methods*. Centre for Advanced Studies in Earth Science, University of Mysore.

Balegamire, C., Nkuba, B., & Dable, P. (2022). Production of gold mine tailings based concrete pavers by substitution of natural river sand in Misisi, Eastern Congo. *Cleaner Engineering and Technology*, *7*, 100427. https://doi.org/10.1016/j.clet.2022.100427

Banupriya, C., John, S., Suresh, R., Divya, E., & Vinitha, D. (2016). Experimental investigations on geopolymer bricks/paver blocks. *Indian Journal of Science and Technology*, *9*(16). https://doi.org/10.17485/ijst/2016/v9i16/92209

Barbhuiya, S., Bhusan Das, B., & Adak, D. (2024). Roadmap to a net-zero carbon cement sector: Strategies, innovations and policy imperatives. *Journal of Environmental Management*, *359*, 121052. https://doi.org/10.1016/j.jenvman.2024.121052

Basavaraj, A. S., & Gettu, R. (2024). Primary life cycle inventory data for cement production, with relevance to sustainability assessment–Indian cases. *Data in Brief*, *54*, 110258. https://doi.org/10.1016/j.dib.2024.110258

Beulah, M., Sudhir, M. R., Mothi Krishna Mohan, Gayathri, G., & Deekshith Jain. (2021). Mine waste-based next generation bricks: A case study of iron ore tailings, red mud and GGBS utilization in bricks. *Advances in Materials Science and Engineering*, 1–10.

Bikash Subedi, Dhurba Kumar Wagle and Keshav Basnet (2020). "Utilization of Crushed Ceramic Tile Wastes as Partial Replacement of Coarse Aggregate in Concrete Production". International Journal of Engineering Research & Technology, 9(7), 1572-1584.

Bini, C., Maleci, L., & Wahsha, M. (2017). Mine waste: Assessment of environmental contamination and restoration. In *Elsevier eBooks* (pp. 89–134).

Borges, P. H. R., Ramos, F. C. R., Caetano, T. R., Panzerra, T. H., & Santos, H. (2019). Reuse of iron ore tailings in the production of geopolymer mortars. *Revista Escola de Minas*, *72*(4), 581–587. https://doi.org/10.1590/0370-44672017720169

Bureau of Indian Standards. (1963a). *Methods of test for aggregates for concrete - Part 1: Particle size and shape* (IS 2386 (Part 1), Reaffirmed 2021).

Bureau of Indian Standards. (1963b). *Methods of test for aggregates for concrete - Part 2: Estimation of deleterious materials and organic impurities* (IS 2386 (Part 2), Reaffirmed 2021).

Bureau of Indian Standards. (1963c). *Methods of test for aggregates for concrete - Part 3: Specific gravity, density, voids, absorption and bulking* (IS 2386 (Part 3), Reaffirmed 2021).

Bureau of Indian Standards. (1963d). *Methods of test for aggregates for concrete - Part 4: Mechanical properties* (IS 2386 (Part 4), Reaffirmed 2021).

Bureau of Indian Standards. (1967). *Methods of test for pozzolanic materials* (IS 1727, Reaffirmed 2018).

Bureau of Indian Standards. (1980). *Quick lime and hydrated lime for chemical industries - Specification - Part 1: Quick lime* (IS 1540 (Part 1), Reaffirmed 2024).

Bureau of Indian Standards. (1981). *Code of practice for preparation and use of masonry mortars* (IS 2250, Reaffirmed 2020).

Bureau of Indian Standards. (1988a). *Cast iron steps for manholes - Specification* (IS 12550, Reaffirmed 2024).

Bureau of Indian Standards. (1988b). *Methods of physical tests for hydraulic cement - Part 4: Determination of consistency of standard cement paste* (IS 4031 (Part 4), Reaffirmed 2019).

Bureau of Indian Standards. (1988c). *Methods of physical tests for hydraulic cement - Part 5: Determination of initial and final setting times* (IS 4031 (Part 5), Reaffirmed 2019).

Bureau of Indian Standards. (1988d). *Methods of physical tests for hydraulic cement - Part 6: Determination of compressive strength of hydraulic cement (other than masonry cement)* (IS 4031 (Part 6), Reaffirmed 2019).

Bureau of Indian Standards. (1988e). *Methods of physical tests for hydraulic cement - Part 11: Determination of density* (IS 4031 (Part 11), Reaffirmed 2019).

Bureau of Indian Standards. (1996). *Methods of physical tests for hydraulic cement - Part 1: Determination of fineness by dry sieving* (IS 4031 (Part 1), Reaffirmed 2021).

Bureau of Indian Standards. (1999a). *Methods of physical tests for hydraulic cement - Part 2: Determination of fineness by specific surface by Blaine air permeability method* (IS 4031 (Part 2), Reaffirmed 2018).

Bureau of Indian Standards. (1999b). *Methods of physical tests for hydraulic cement - Part 3: Determination of soundness* (IS 4031 (Part 3), Reaffirmed 2019).

Bureau of Indian Standards. (2000). *Plain and reinforced concrete - Code of practice* (IS 456, Reaffirmed 2021).

Bureau of Indian Standards. (2005). *Concrete masonry units - Specification - Part 1: Hollow and solid concrete blocks* (IS 2185 (Part 1), Reaffirmed 2020).

Bureau of Indian Standards. (2013a). *Chequered terrazzo tiles - Specification* (IS 13801, Reaffirmed 2021).

Bureau of Indian Standards. (2013b). *Pulverized fuel ash - Specification - Part 1: For use as pozzolana in cement, cement mortar and concrete* (IS 3812 (Part 1), Reaffirmed 2022).

Bureau of Indian Standards. (2019a). *Ceramic tiles — Methods of test, Part 6: Determination of modulus of rupture and breaking strength* (IS 13630 (Part 6)).

Bureau of Indian Standards. (2019b). *Concrete mix proportioning - Guidelines* (IS 10262).

Bureau of Indian Standards. (2019c). *Methods of tests of burnt clay building bricks - Part 1: Determination of compressive strength* (IS 3495 (Part 1)).

Bureau of Indian Standards. (2019d). *Methods of tests of burnt clay building bricks - Part 2: Determination of water absorption* (IS 3495 (Part 2)).

Bureau of Indian Standards. (2019e). *Methods of tests of burnt clay building bricks - Part 3: Determination of efflorescence* (IS 3495 (Part 3)).

Bureau of Indian Standards. (2021a). *Concrete paving blocks — Specification* (IS 15658).

Bureau of Indian Standards. (2021b). *Hardened concrete — Methods of test* (IS 516).

Bureau of Indian Standards. (2025). *Common burnt clay building bricks - Specification* (IS 1077).

Burroughs, J. F., Shannon, J., Rushing, T. S., Yi, K., Gutierrez, Q. B., & Harrelson, D. W. (2017). Potential of finely ground limestone powder to benefit ultra-high performance concrete mixtures. *Construction and Building Materials*, *141*, 335–342. https://doi.org/10.1016/j.conbuildmat.2017.02.073

Castillo, H., Collado, H., Droguett, T., Sánchez, S., Vesely, M., Garrido, P., & Palma, S. (2021). Factors affecting the compressive strength of geopolymers: A review. *Minerals*, *11*(12), 1317.

Chen, H.-J., Shih, N.-H., Wu, C.-H., & Lin, S.-K. (2019). Effects of the loss on ignition of fly ash on the properties of high-volume fly ash concrete. *Sustainability*, *11*(9), 1–15, 2704. https://doi.org/10.3390/su11092704

Chen, L., Yang, M., Chen, Z., Xie, Z., Huang, L., Osman, A. I., Farghali, M., Sandanayake, M., Liu, E., Ahn, Y. H., Al-Muhtaseb, A. H., Rooney, D. W., & Yap, P. (2024). Conversion of waste into sustainable construction materials: A review of recent developments and prospects. *Materials Today Sustainability*, *27*, 100930. https://doi.org/10.1016/j.mtsust.2024.100930

Chen, Y., Zhang, Y., Chen, T., Liu, T., & Huang, J. (2013). Preparation and characterization of red porcelain tiles with hematite tailings. *Construction and Building Materials*, *38*, 1083–1088. https://doi.org/10.1016/j.conbuildmat.2012.06.056

Chen, Y., Zhang, Y., Chen, T., Zhao, Y., & Bao, S. (2011). Preparation of eco-friendly construction bricks from hematite tailings. *Construction and Building Materials*, *25*(4), 2107–2111. https://doi.org/10.1016/j.conbuildmat.2010.11.025

Chinnappa, G. B., & Karra, R. C. (2019). Experimental and Statistical Evaluations of Strength Properties of Concrete with Iron Ore Tailings as Fine Aggregate. *Journal of Hazardous Toxic and Radioactive Waste*, *24*(1). https://doi.org/10.1061/(asce)hz.2153-5515.0000480

Chockalingam, M. P., Palanisamy, N., Padmavathy, S. R., Mohan, E., Winsly, B. W., & Santhappan, J. S. (2021). Techno-economic feasibility study on the application of downdraft gasifier in small-scale red clay bricks industries. *Applied Nanoscience*. https://doi.org/10.1007/s13204-021-01942-0

Choi, H., & Park, J. (2022). Study on mechanical properties of concrete using basalt-based recycled aggregate and varying curing conditions. *Materials*, *15*(13), 4563. https://doi.org/10.3390/ma15134563

Cicek, B., Karadagli, E., & Duman, F. (2018). Valorisation of boron mining wastes in the production of wall and floor tiles. *Construction and Building Materials*, *179*, 232–244. https://doi.org/10.1016/j.conbuildmat.2018.05.182

Collins, R. J., & Ciesielski, S. K. (1994). *Recycling and use of waste materials and by-products in highway construction (NCHRP Synthesis of Highway Practice 199)*. Transportation Research Board, National Research Council.

Cui, X., Geng, Y., Li, T., Zhao, R., Li, X., & Cui, Z. (2021). Field application and effect evaluation of different iron tailings soil utilization technologies. *Resources, Conservation and Recycling*, *173*, 105746.

Da Silva, F. L., Araújo, F. G. S., Castro, C. G., Mendes, J. J., & von Krüger, F. L. (2014). Recycling of concentration tailings of iron ore for the production of concrete block (pavers). *Materials Science Forum*, *775-776*, 631–634. https://doi.org/10.4028/www.scientific.net/msf.775-776.631

Daniyal, M., & Ahmad, S. (2015). Application of waste ceramic tile aggregates in concrete. *International Journal of Innovative Research in Science, Engineering and Technology*, *4*(12), 12808–12815.

Das, M. R., Satapathy, S., & Pothal, L. (2023). A study on waste management in iron mining. *Materials Today: Proceedings*.

Deshmukh, M., Shaikh, S., Iyer, C., & Quadri, A. (2021). Recycling of raw bauxite-residue from alumina industry for production of chequered tile. *International Journal of Engineering Research & Technology (IJERT)*.

Djamaluddin, A. R., Caronge, M. A., Tjaronge, M. W., Lando, A. T., & Irmawaty, R. (2020). Evaluation of sustainable concrete paving blocks incorporating processed waste tea ash. *Case Studies in Construction Materials*, *12*, e00325. https://doi.org/10.1016/j.cscm.2019.e00325

Dom, A. a. M., Jamaluddin, N., Hamid, N. a. A., & Hoon, C. S. (2022). A review: GGBS as a cement replacement in concrete. *IOP Conference Series: Earth and Environmental Science*, *1022*(1), 012044. https://doi.org/10.1088/1755-1315/1022/1/012044

Dong, J., Meng, L., Bian, Z., & Fang, A. (2019). Investigating the characteristics, evolution and restoration modes of mining area ecosystems. *Polish Journal of Environmental Studies*, *28*(5), 3539–3549. https://doi.org/10.15244/pjoes/97390

Dunuweera, S., & Rajapakse, N. (2018). Influence of fly ash on the early strength and setting time of ordinary Portland cement concrete. *IOP Conference Series: Materials Science and Engineering*, *351*(1), 012021.

Elahi, T. E., Shahriar, A. R., & Islam, M. S. (2021). Engineering characteristics of compressed earth blocks stabilized with cement and fly ash. *Construction and Building Materials*, *277*, 122367. https://doi.org/10.1016/j.conbuildmat.2021.122367

Elmrabet, R., El Harfi, A., & El Youbi, M. S. (2019). Study of properties of fly ash cements. *Materials Today: Proceedings*, *13*, 850–856.

Evdokimov, S. I., Maslakov, M. P., & Evdokimov, V. S. (2016). Construction materials based on wastes from mining and metallurgical industries. *Procedia Engineering*, *150*, 1574–1581.

Falagán, C., Grail, B. M., & Johnson, D. B. (2017). New approaches for extracting and recovering metals from mine tailings. *Minerals Engineering*, *106*, 71–78.

Farooq, M. U., Hameed, R., Tahir, M., Sohail, M. G., & Shahzad, S. (2023). Mechanical and durability performance of 100% recycled aggregate concrete pavers made by compression casting. *Journal of Building Engineering*, *73*, 106729. https://doi.org/10.1016/j.jobe.2023.106729

Fathollah Sajedi and Hashim Abdul Razak (2011). “Effects of thermal and mechanical activation methods on compressive strength of ordinary Portland cement–slag mortar”. *Materials and Design*, 32, 984-995.

Filho, J. N. S., Da Silva, S. N., Silva, G. C., Mendes, J. C., & Peixoto, R. A. F. (2017). Technical and environmental feasibility of interlocking concrete pavers with iron ore tailings from tailings dams. *Journal of Materials in Civil Engineering*, *29*(9). https://doi.org/10.1061/(asce)mt.1943-5533.0001937

Fontes, W. C., Fontes, G. G., Costa, E. C. P., Mendes, J. C., Silva, G. J. B., & Peixoto, R. A. F. (2018). Iron ore tailings in the production of cement tiles: A value analysis on building sustainability. *Ambiente Construído*, *18*(4), 395–412.

Fontes, W. C., Franco, M., Keoma Defaveri, Brigolini, G. J., Segadães, A. M., & Ricardo. (2021). Hydraulic tiles produced with fine aggregates and pigments reclaimed

from iron ore tailings. *Journal of Sustainable Metallurgy*, *7*(1), 151–165. https://doi.org/10.1007/s40831-020-00329-9

Franco, J. d. A. B., Domingues, A. M., Africano, N. d. A., Deus, R. M., & Battistelle, R. A. G. (2022). Sustainability in the civil construction sector supported by Industry 4.0 technologies: Challenges and opportunities. *Infrastructures*, *7*(3). https://doi.org/10.3390/infrastructures7030043

Freitas, S. M. A. C., Sousa, L. N., Diniz, P., Martins, M. E., & Assis, P. S. (2018). Steel slag and iron ore tailings to produce solid brick. *Clean Technologies and Environmental Policy*, *20*(5), 1087–1095. https://doi.org/10.1007/s10098-018-1513-7

Gagg, C. R. (2014). Concrete and climate change: A call for responsible development. In *The cement handbook* (pp. 369–393). Springer.

Gairola, S. U., Khanduri, A. K., & Bhuvaneswari, V. (2025). Sustainable mining: Reducing waste and enhancing resource efficiency. *Discover Civil Engineering*, *2*(1). https://doi.org/10.1007/s44290-025-00233-9

Gamage, N., Liyanage, K., Fragomeni, S., & Setunge, S. (2011). Overview of different types of fly ash and their use as a building and construction material. *International Conference of Structural Engineering, Construction and Management*, 1–9.

Ganesh, P., & Murthy, A. R. (2019). Tensile behaviour and durability aspects of sustainable ultra-high performance concrete incorporated with GGBS as cementitious material. *Construction and Building Materials*, *197*, 667–680. https://doi.org/10.1016/j.conbuildmat.2018.11.240

Gayana, B. C., & Chandar, K. R. (2018). Sustainable use of mine waste and tailings with suitable admixture as aggregates in concrete pavements - A review. *Advances in Concrete Construction*, *6*(3), 221–243. https://doi.org/10.12989/acc.2018.6.3.221

George, G. (2023). Replacement of fine aggregate by iron ore tailing (IOT) in concrete for sustainable development. *E3S Web of Conferences*, *387*, 04012.

Ghose, A. K. (2009). Technology vision 2050 for sustainable mining. *Procedia Earth and Planetary Science*, *1*(1), 2–6. https://doi.org/10.1016/j.proeps.2009.09.002

Gong, K., & White, C. E. (2016). Impact of chemical variability of ground granulated blast-furnace slag on the phase formation in alkali-activated slag pastes. *Cement and Concrete Research*, *89*, 310–319. https://doi.org/10.1016/j.cemconres.2016.09.003

Goodland, R. (2012). Responsible mining: The key to profitable resource development. *Sustainability*, *4*(9), 2099–2126.

Gou, M., Zhou, L., & Then, N. W. Y. (2019). Utilization of tailings in cement and concrete: A review. *Science and Engineering of Composite Materials*, *26*(1), 449–464. https://doi.org/10.1515/secm-2019-0029

Government Accounting Standards Advisory Board. (2023). *Natural resource account of Goa for the year 2020-21: Mineral & energy resources*. Comptroller and Auditor General of India.

Government of Goa. (2012). Notification no. 34/10/2012. *Official Gazette*.

Gunson, A., Klein, B., Veiga, M., & Dunbar, S. (2012). Reducing mine water requirements. *Journal of Cleaner Production*, *21*(1), 71–82. https://doi.org/10.1016/j.jclepro.2011.08.020

Guo, Y., Qu, F., & Li, W. (2025). Advancing circular economy and construction sustainability: Transforming mine tailings into high-value cementitious and alkali-activated concrete. *Npj Materials Sustainability*, *3*(1). https://doi.org/10.1038/s44296-025-00049-9

Gyu Don Moon, Sungwoo Oh and Young Cheol Choi (2016). "Effects of the physicochemical properties of fly ash on the compressive strength of high-volume fly ash mortar". Construction and Building Materials, 124, 1072-1080.

Hafez, A. I., Khedr, M. M. A., Mohammed, M. S., Osman, R. M., & Sabry, R. M. (2017). Utilization of rice husk ash and ceramic wastes in manufacturing of developed cement bricks. *ARPN Journal of Engineering and Applied Sciences*, *12*, 2854–2862.

Hafez, A. I., Khedr, M. M. A., Osman, R. M., Sabry, R., & Mohammed, M. S. (2020). A comparative investigation of the unit cost for the preparation of modified sand and clay bricks from rice husk waste. *Journal of Building Engineering*, *32*, 101765. https://doi.org/10.1016/j.jobe.2020.101765

Hake, S. L., Damgir, R. M., & Patankar, S. V. (2018). Temperature effect on lime powder-added geopolymer concrete. *Advances in Civil Engineering*, *2018*. https://doi.org/10.1155/2018/6519754

Hamid, N. B., Azmi, M. A. M., Abdullah, N. H., Mokhtar, M., Prasetijo, J., Muni, M. F. C., Zainudin, M. H. F., & Bakar, A. I. N. A. (2021). A review: Potential of waste materials in tiles production. *Multidisciplinary Applied Research and Innovation*, *2*(1), 91–100.

Hao, X., An, H., Sun, X., & Zhong, W. (2018). The import competition relationship and intensity in the international iron ore trade: From network perspective. *Resources Policy*, *57*, 45–54. https://doi.org/10.1016/j.resourpol.2018.01.005

Hasanbeigi, A., Price, L., & Jessen, P. (2012). Analysis of cement production energy efficiency and CO2 emissions using the clinker production process data for China and India. *Energy*, *42*(1), 227–235.

Hegarty, R. O., Kinnane, O., Newell, J., & West, R. (2021). High performance, low carbon concrete for building cladding applications. *Journal of Building Engineering*, *43*, 102566.

Hota, P., & Behera, B. (2015). Coal mining in Odisha: An analysis of impacts on agricultural production and human health. *The Extractive Industries and Society*, *2*(4), 683–693. https://doi.org/10.1016/j.exis.2015.08.007

Hu, J., & Wang, K. (2011). Effect of coarse aggregate characteristics on concrete rheology. *Construction and Building Materials*, *25*(3), 1196–1204. https://doi.org/10.1016/j.conbuildmat.2010.09.035

Huang, X., Ranade, R., Ni, W., & Li, V. C. (2013). Development of green engineered cementitious composites using iron ore tailings as aggregates. *Construction and Building Materials*, *44*, 757–764. https://doi.org/10.1016/j.conbuildmat.2013.03.088

Humphreys, D. (2018). The mining industry after the boom. *Mineral Economics*, *32*(2), 145–151. https://doi.org/10.1007/s13563-018-0155-x

IBM. (2021). *Iron ore statistics*. Indian Bureau of Mines.

IBM. (2022). *Indian minerals yearbook*. Government of India.

Ikotun, J., Adeyeye, R., & Otieno, M. (2022). Application of mine tailings sand as construction material – A review. *MATEC Web of Conferences*, *364*, 05008. https://doi.org/10.1051/matecconf/202236405008

Indian Institute of Technology (Indian School of Mines). (2019). *Study on impacts of stoppage of mining in Goa on socio-economics*. Dhanabad, Jharkhand.

Inland Waterways Authority of India. (2010). *Development of Mandovi River, Zuari River and Cumberjua Canal in Goa for shipping and navigation, final report* (Vol. I). RITES.

Iqbal, M. A. (2016). Financial feasibility of environment friendly brick manufacturing in the context of Bangladesh, 5–51.

Jackson, S., Poelzer, G., Poelzer, G., & Noble, B. (2022). Mining and Sustainability in the Circumpolar North: The Role of Government in Advancing Corporate Social Responsibility. *Environmental Management*. https://doi.org/10.1007/s00267-022-01680-1

Jakati, D. M. (2021). Development of mining in Goa and its environmental impacts - A geographical perspective. *PalArch's Journal of Archaeology of Egypt/Egyptology*, *18*(7), 2979–2988.

James, J., Pandian, P. K., Deepika, K., Manikanda Venkatesh, J., Manikandan, V., & Manikumaran, P. (2016). Cement stabilized soil blocks admixed with sugarcane bagasse ash. *Journal of Engineering*, *2016*, 1–9. https://doi.org/10.1155/2016/7940239

Jesus, A., & Mendonça, S. (2018). Lost in transition? Drivers and barriers in the eco-innovation road to the circular economy. *Ecological Economics*, *145*, 75–89.

Jhatial, et al. (2019). Eggshell powder as partial cement replacement and its effect on the workability and compressive strength of concrete. *International Journal of Advanced and Applied Sciences*, *6*(9), 71–75. https://doi.org/10.21833/ijaas.2019.09.011

Jiang, Y., Wang, H., Chen, Y., Ruan, M., & Li, W. (2019). Preparations of composite concretes using iron ore tailings as fine aggregates and their mechanical behavior. *Materiali in Tehnologije*, *53*(4), 467–472. https://doi.org/10.17222/mit.2018.222

Jinpeng Dai, Qicai Wang, Chao Xie, Yanjin Xue, Yun Duan and Xiaoning Cui (2019). "The Effect of Fineness on the Hydration Activity Index of Ground Granulated Blast Furnace Slag". *Materials (Basel),* 12,2984-2999.

Jose, S. A., Calhoun, J., Renteria, O. B., Mercado, P., Nakajima, S., Hope, C. N., Sotelo, M., & Menezes, P. L. (2024). Promoting a circular economy in mining practices. *Sustainability*, *16*(24), 11016. https://doi.org/10.3390/su162411016

Joyner, D. T., & Jr., C. B. M. (2024). Determining manufacturing costs using T-accounts and simple mathematics. *Accounting and Finance Research*, *13*(2), 72. https://doi.org/10.5430/afr.v13n2p72

Jung, S.-H., Saraswathy, V., Karthick, S., Kathirvel, P., & Kwon, S.-J. (2018). Microstructure characteristics of fly ash concrete with rice husk ash and lime stone powder. *International Journal of Concrete Structures and Materials*, *12*(1). https://doi.org/10.1186/s40069-018-0257-4

Kakodkar, S. A., & Sawaiker, U. G. (2025). High-performance, eco-friendly blocks from iron ore tailings: A solution for sustainable construction. *Nature Environment and Pollution Technology*, *24*(1), B4220. https://doi.org/10.46488/NEPT.2025.v24i01.B4220

Kalra, M., & Mehmood, G. (2018). A review paper on the effect of different types of coarse aggregate on concrete. *IOP Conference Series: Materials Science and Engineering*, *431*, 082001. https://doi.org/10.1088/1757-899x/431/8/082001

Kapicová, A., Bílý, P., Fládr, J., Šeps, K., Chylík, R., & Trtík, T. (2024). Development of sound-absorbing pervious concrete for interior applications. *Journal of Building Engineering*, *85*, 108697. https://doi.org/10.1016/j.jobe.2024.108697

Karasin, A., Hadzima-Nyarko, M., Işık, E., Doğruyol, M., Karasin, I. B., & Czarnecki, S. (2022). The effect of basalt aggregates and mineral admixtures on the mechanical properties of concrete exposed to sulphate attacks. *Materials*, *15*(4), 1581. https://doi.org/10.3390/ma15041581

Kattoli, R., Brijbhushan, S., Maneeth, P. D., Reddy, S. S., & Siddharth, B. (2018). Effect of partial replacement of cement by ground granulated blast furnace slag and sand by iron ore tailings on properties of concrete. *International Journal of Advanced Technology and Engineering Exploration*, *5*(45), 269–275.

Khushal Chandra Kesharwani, Amit Kumar Biswas, Anesh Chaurasiya and Ahsan Rabbani (2017). "Experimental Study on Use of Fly Ash in Concrete". *International Research Journal of Engineering and Technology,* 4 (9), 1527-1530.

Kinnunen, P., Karhu, M., Yli-Rantala, E., Kivikytö-Reponen, P., & Mäkinen, J. (2022). A review of circular economy strategies for mine tailings. *Cleaner Engineering and Technology*, *8*, 100499.

Kossoff, D., Dubbin, W. E., Alfredsson, M., Edwards, S. J., Macklin, M. G., & Hudson-Edwards, K. A. (2014). Mine tailings dams: Characteristics, failure, environmental impacts, and remediation. *Applied Geochemistry*, *51*, 229–245.

Kumar, B. N. S., Suhas, R., Shet, S. U., & Srishaila, J. M. (2014). Utilization of iron ore tailings as replacement to fine aggregates in cement concrete pavements. *International Journal of Research in Engineering and Technology*, *3*(7), 369–376.

Kumar, G., Shrivastava, S., & Gupta, R. C. (2019). Paver blocks manufactured from construction & demolition waste. *Materials Today: Proceedings*.

Kumar, R., Das, P., Beulah, M., & Arjun, H. R. (2020). Geopolymer bricks using iron ore tailings, slag sand, ground granular blast furnace slag and fly ash. *IntechOpen*, 1–15.

Kumar, R., Das, P., Beulah, M., Arjun, H. R., & Ignatius, G. (2017). Utilization of iron ore tailings for the production of fly ash – GGBS based geopolymer bricks. *Journal of Advanced Manufacturing Systems*, *16*(3), 275–290.

Kumar, V., & Surendra, B. V. (2020). Strength and water absorption characteristics of cement stabilized masonry blocks using brick masonry waste. *Lecture Notes in Civil Engineering*, 131–143. https://doi.org/10.1007/978-981-15-3361-7_10

Kuranchie, F. A., Shukla, S. K., Habibi, D., & Mohyeddin, A. (2015). Utilisation of iron ore tailings as aggregates in concrete. *Cogent Engineering*, *2*(1), 1083137. https://doi.org/10.1080/23311916.2015.1083137

Leyton-Flor, S. A., Sangha, K., & Howey, K. (2024). Assessing environmental liabilities of mining in Northern Australia: A case study of the McArthur River Mine. *The Extractive Industries and Society*, *20*, 101562. https://doi.org/10.1016/j.exis.2024.101562

Li, J., Ren, W., Zhang, A., Li, S., Tan, J., & Liu, H. (2023). Mechanical properties and microstructure analysis of cement mortar mixed with iron ore tailings. *Buildings*, *13*(1), 149. https://doi.org/10.3390/buildings13010149

Li, W., Lei, G., Ya, X., & Qifei, H. (2018). The properties and formation mechanisms of eco-friendly brick building materials fabricated from low-silicon iron ore tailings. *Journal of Cleaner Production*, *204*, 685-692.

Liapis, K. J., & Kantianis, D. D. (2015). Depreciation methods and life-cycle costing (LCC) methodology. *Procedia Economics and Finance*, *19*, 314–324. https://doi.org/10.1016/s2212-5671(15)00032-5

Likhith, N. P., Manjunatha, Siddesh, S. S., Manjunath, K. M., Hadimani, S., & Shivakumara, B. (2017). Manufacturing of building blocks by utilising of iron ore tailings. *International Journal of Engineering Science and Computing*, *7*(5), 12274–12277.

Lin, C. (2021). The role of sustainable building materials in advancing ecological construction. *Journal of Energy and Environmental Policy Options*, *4*(1), 15–21.

Lottermoser, B. (2010). *Mine wastes*. Springer. https://doi.org/10.1007/978-3-642-12419-8

Lumbroso, D., McElroy, C., Goff, C., Collell, M. R., Petkovsek, G., & Wetton, M. (2019). The potential to reduce the risks posed by tailings dams using satellite-based information. *International Journal of Disaster Risk Reduction*, *38*, 101209. https://doi.org/10.1016/j.ijdrr.2019.101209

MacDiarmid, J., Tholana, T., & Musingwini, C. (2018). Analysis of key value drivers for major mining companies for the period 2006–2015. *Resources Policy*, *56*, 16–30. https://doi.org/10.1016/j.resourpol.2017.09.008

Mageed, A. A., & AbdelHaffez, G. S. (2012). Utilization of limestone dust in brick making. *Journal of Engineering Sciences*, *40*(3), 913–922. https://doi.org/10.21608/jesaun.2012.114423

Mantilla, J. N. R., Miranda, D. N., Fuina, J. S., & Carrasco, E. V. M. (2017). Mechanical characteristics of pavers with iron ore tailings. *Applied Mechanics and Materials*, *864*, 330–335.

Maraseni, S. S., Poudel, B., Adhikari, B., Bashyal, M. R., Bhandari, G., Dhakal, S., & Adhikari, B. P. (2025). Eco-friendly paver block: Comparative study by composition review. *OCEM Journal of Management, Technology & Social Sciences*, *4*(1), 144–154. https://doi.org/10.3126/ocemjmtss.v4i1.74757

Maria Vensa, S., & Prabha, G. (2022). Experimental study of hybrid paver blocks engulfed with binary blends. *International Research Journal of Engineering and Technology (IRJET)*, *9*(1), 1565–1570.

Martinelli, F. R. B., Ribeiro, F. R. C., Marvila, M. T., Monteiro, S. N., Filho, F. d. C. G., & Azevedo, A. R. G. d. (2023). A review of the use of coconut fibre in cement composites. *Polymers*, *15*, 1309.

Mascarenhas, A., & Kalavampara, G. (Eds.). (2009). *Natural resources of Goa: A geological perspective*. Geological Society of Goa.

Masi, A., Digrisolo, A., & Santarsiero, G. (2019). Analysis of a large database of concrete core tests with emphasis on within-structure variability. *Materials*, *12*(12), 1985. https://doi.org/10.3390/ma12121985

McLellan, B., Corder, G., & Ali, S. (2013). Sustainability of rare earths—An overview of the state of knowledge. *Minerals*, *3*(3), 304–317. https://doi.org/10.3390/min3030304

Mendes Protasio, F. N., Ribeiro de Avillez, R., Letichevsky, S., & de Andrade Silva, F. (2021). The use of iron ore tailings obtained from the Germano dam in the production of a sustainable concrete. *Journal of Cleaner Production*, *278*, 123929. https://doi.org/10.1016/j.jclepro.2020.123929

Méndez, D., Guzmán-Martínez, F., Acosta, M., Collahuazo, L., Ibarra, D., Lalangui, L., & Jiménez-Oyola, S. (2022). Use of tailings as a substitute for sand in concrete blocks production: Gravimetric mining wastes as a case study. *Sustainability*, *14*(23), 16285. https://doi.org/10.3390/su142316285

Mensah, S. K., Nyantakyi, E. K., Mensah, G. S., Siabi, E. K., Ackerson, N. O. B., Antwi-Agyei, P., Donkor, P., Siabi, S. E., Bandoh, T., Owusu, P. A., & Vuu, C. (2025). Assessing the environmental and socio-economic impacts of small-scale mining activities in the Atiwa East District of Ghana. *Scientific African*. https://doi.org/10.1016/j.sciaf.2025.e02542

Ministry of Mines. (2024). *Annual report 2023-24*. Government of India.

Moghaddam, F., Sirivivatnanon, V., & Vessalas, K. (2019). The effect of fly ash fineness on heat of hydration, microstructure, flow and compressive strength of blended cement pastes. *Case Studies in Construction Materials*, *10*, 1–13.

Mohapatra, D. P., & Kirpalani, D. M. (2016). Process effluents and mine tailings: Sources, effects and management and role of nanotechnology. *Nanotechnology for Environmental Engineering*, *2*(1).

Mokhtar, A., & Nasooti, M. (2020). A decision support tool for cement industry to select energy efficiency measures. *Energy Strategy Reviews*, *28*, 100458. https://doi.org/10.1016/j.esr.2020.100458

Morsy, M. I. N. (2011). *Properties of rice straw cementitious composite* [Ph.D. Thesis, Universitäts-und Landesbibliothek Darmstadt].

Mtarfi, N. H., Tounsadi, H., Maherzi, W., Taleb, M., & Rais, Z. (2023). Slag valorization from electric arc furnaces in concrete paver formulation. *Green Technologies and Sustainability*, *1*(3), 100037.

Nagaraj, H. B., Sravan, M. V., Arun, T. G., & Jagadish, K. S. (2014). Role of lime with cement in long-term strength of compressed stabilized earth blocks. *International Journal of Sustainable Built Environment*, *3*(1), 54–61. https://doi.org/10.1016/j.ijsbe.2014.03.001

Nagaraja, H. B., & Shreyasvi, C. (2017). Compressed stabilized earth blocks using iron mine spoil waste - An explorative study. *Procedia Engineering*, *180*, 1203–1212.

Nanda, R. P., Das, A. K., & Moharana, N. C. (2010). Stone crusher dust as a fine aggregate in concrete for paving blocks. *International Journal of Civil and Structural Engineering*, *1*(3), 613–620.

Nayak, G. N. (2002). Impact of mining on environment in Goa: A review. *Journal of Environmental Geochemistry*, *1*(2), 97–100.

Nex, J., & Kinnaird, J. (2018). Minerals and mining in South Africa. In *World regional geography book series* (pp. 27–35). https://doi.org/10.1007/978-3-319-94974-1_4

Ngo, S.-H., Huynh, T.-P., Le, T.-T., & Mai, N.-H. (2018). Effect of high loss on ignition-fly ash on properties of concrete fully immersed in sulfate solution. *IOP Conference Series: Materials Science and Engineering*, *371*, 012007. https://doi.org/10.1088/1757-899x/371/1/012007

Okafor, F. O., & Egbe, E. A. (2017). Models for predicting compressive strength and water absorption of laterite-quarry dust cement block using mixture experiment. *Nigerian Journal of Technology*, *36*(2), 366. https://doi.org/10.4314/njt.v36i2.7

Oner, A., & Akyuz, S. (2007). An experimental study on optimum usage of GGBS for the compressive strength of concrete. *Cement and Concrete Composites*, *29*(6), 505–514. https://doi.org/10.1016/j.cemconcomp.2007.01.001

Oti, J. E., Kinuthia, J. M., & Bai, J. (2009). Engineering properties of unfired clay masonry bricks. *Engineering Geology*, *107*(3-4), 130–139. https://doi.org/10.1016/j.enggeo.2009.05.002

Pacheco-Torgal, F., & Jalali, S. (2010). Reusing ceramic wastes in concrete. *Construction and Building Materials*, *24*(5), 832–838. https://doi.org/10.1016/j.conbuildmat.2009.10.023

Pai, I. K. (2018). Are we killing a golden goose in Goa? *Aspects in Mining & Mineral Science*, *1*(5). https://doi.org/10.31031/amms.2018.01.000521

Patankar, S. V., Ghugal, Y. M., & Jamkar, S. S. (2015). Mix design of fly ash based geopolymer concrete. *Advances in Structural Engineering*, 1619–1634. https://doi.org/10.1007/978-81-322-2187-6_123

Pati, P. K., & Sahu, S. K. (2020). Innovative utilization of fly ash in concrete tiles for sustainable construction. *Materials Today: Proceedings*, *33*(8), 5301–5305. https://doi.org/10.1016/j.matpr.2020.02.971

Patra, S., Pattanaik, A., & Rayasam, V. (2018). Characterisation of low-grade Barsua iron ore fines and identification of possible beneficiation strategies. *Canadian Metallurgical Quarterly*, *58*(1), 28–45. https://doi.org/10.1080/00084433.2018.1516598

Paul O. Awoyera , Julius M. Ndambuki , Joseph O. Akinmusuru , David O. Omole (2018). "Characterization of ceramic waste aggregate concrete".*Housing and Building National Research Center*, 14 , 282-287.

Pedro Domingos Dauce, Guilherme, Fernandes, M., & Malena, R. (2019). Characterisation and magnetic concentration of an iron ore tailings. *Journal of Materials Research and Technology*, *8*(1), 1052–1059. https://doi.org/10.1016/j.jmrt.2018.07.015

Permatasari, R., Sodri, A., & Gustina, H. A. (2023). Utilization of fly ash waste in the cement industry and its environmental impact: A review. *Jurnal Penelitian Pendidikan IPA*, *9*(9), 569–579. https://doi.org/10.29303/jppipa.v9i9.4504

Prasetia, I., & Maulana, A. (2019). Effects of crushed stone waste as fine aggregate on mortar and concrete properties. *IOP Conference Series: Materials Science and Engineering*, *620*, 012040. https://doi.org/10.1088/1757-899X/620/1/012040

Raj, A., Sathyan, D., & Mini, K. M. (2021). Performance evaluation of natural fibre reinforced high volume fly ash foam concrete cladding. *Advances in Concrete Construction*, *11*(2), 151–161.

Rajput, S. P. S. (2018). An experimental study on crushed stone dust as fine aggregate in cement concrete. *Materials Today: Proceedings*, *5*, 17540–17547.

Ramezanianpour, A. A., Ghiasvand, E., Nickseresht, I., Mahdikhani, M., & Moodi, F. (2009). Influence of various amounts of limestone powder on performance of Portland limestone cement concretes. *Cement and Concrete Composites*, *31*(10), 715–720. https://doi.org/10.1016/j.cemconcomp.2009.08.003

Rao, P. S. (2020). *Development of thermal efficient non fired bricks using iron ore tailings and perlite*. National Institute of Technology Karnataka.

Ravikumar, C. M., Kumar, A., Prashanth, M. H., & Reddy, D. V. (2012). Experimental studies on iron-ore tailing based interlocking paver blocks. *International Journal of Earth Sciences and Engineering*, *5*(3), 501–504.

Reis, E. D., Resende, H. F., Christoforo, A. L., Costa, R. M., Poggiali, F. S. J., & Bezerra, A. C. S. (2024). Assessment of physical and mechanical properties of concrete with carbon nanotubes pre-dispersed in cement. *Journal of Building Engineering*, *89*, 109255. https://doi.org/10.1016/j.jobe.2024.109255

Revilla-Cuesta, V., Skaf, M., Faleschini, F., Manso, J. M., & Ortega-López, V. (2020). Statistical approach for the design of structural self-compacting concrete with fine recycled concrete aggregate. *Mathematics*, *8*(12), 2190. https://doi.org/10.3390/math8122190

Rumbayan, R., Sudarno, & Ticoalu, A. (2019). A study into flexural, compressive and tensile strength of coir-concrete as sustainable building material. *MATEC Web of Conferences*, *258*, 01011. https://doi.org/10.1051/matecconf/201925801011

Sá, T. S. W., Oda, S., Balthar, V. K. C. B. L., & Toledo Filho, R. D. (2022). Use of iron ore tailings and sediments on pavement structure. *Construction and Building Materials*, *342*(B), 128072. https://doi.org/10.1016/j.conbuildmat.2022.128072

Saediman, H., Noraduola, & Nafiu, L. (2014). Financial feasibility of traditional small-scale brick-making enterprises in Southeast Sulawesi, Indonesia. *Ethiopian Journal of Environmental Studies and Management*, *7*(2), 870. https://doi.org/10.4314/ejesm.v7i2.7s

Safiuddin, M., Jumaat, Z., Salam, M., Islam, M., & Hashim, R. (2010). Utilization of solid wastes in construction materials. *International Journal of the Physical Sciences*, *5*(13), 1952–1963.

Sahu, A. K., Kumar, S., & Sachan, A. K. (2003). Crushed stone waste as fine aggregate for concrete. *The Indian Concrete Journal*, 845–848.

Sahu, H. B., & Dash, S. (2011). Land degradation due to mining in India and its mitigation measures. *Second International Conference on Environmental Science and Technology*, Singapore.

Saranya, P., Nagarajan, P., & Shashikala, A. P. (2018). Eco-friendly GGBS concrete: A state-of-the-art review. *IOP Conference Series: Materials Science and Engineering*, *330*, 012057. https://doi.org/10.1088/1757-899x/330/1/012057

Sedira, N., Castro-Gomes, J., Kastiukas, G., Zhou, X., & Vargas, A. (2017). A review on mineral waste for chemical-activated binders: Mineralogical and chemical characteristics. *Mining Science*, *24*, 29–58. https://doi.org/10.5277/msc172402

Segui, P., Safhi, A. e. M., Amrani, M., & Benzaazoua, M. (2023). Mining wastes as road construction material: A review. *Minerals*, *13*(1), 90. https://doi.org/10.3390/min13010090

Sekhar, D. C., & Nayak, S. (2018). Utilization of granulated blast furnace slag and cement in the manufacture of compressed stabilized earth blocks. *Construction and Building Materials*, *166*, 531–536. https://doi.org/10.1016/j.conbuildmat.2018.01.125

Senthamarai, R. M., & Devadas Manoharan, P. (2005). Concrete with ceramic waste aggregate. *Cement and Concrete Composites*, *27*(9-10), 910–913. https://doi.org/10.1016/j.cemconcomp.2005.04.003

Shah Commission. (2012). *Shah Commission report*.

Shao, Y., Parks, A., & Ostertag, C. P. (2022). Lightweight concrete façade with multiple air gaps for sustainable and energy-efficient buildings in Singapore. *Building and Environment*, *223*, 109463. https://doi.org/10.1016/j.buildenv.2022.109463

Sheikh, K. H., Kumar, V., & Kumar, R. (2018). Environmental benefits of ground granulated blast furnace slag (GGBS) as a sustainable construction material. *Environmental Science and Pollution Research*, *25*(21), 12868–12879.

Shettima, A. U., Hussin, M. W., Ahmad, Y., & Mirza, J. (2016). Evaluation of iron ore tailings as replacement for fine aggregate in concrete. *Construction and Building Materials*, *120*, 72–79.

Shreekant, R. L., Aruna, M., & Harsha Vardhan. (2016). Utilization of iron ore waste in brick making for the construction industry. *International Journal of Earth Sciences and Engineering*, *9*(2), 450–455.

Shreyas, A. (2017). Application of ground granulated blast furnace slag (GGBS) in Portland cement concrete. *International Journal of Civil Engineering and Technology*, *8*(8), 1257–1264.

Shumuye, E. D., & Zhao, J. (2018). A review on ground granulated blast slag (GGBS) in concrete. In *Proceedings of the Eighth International Conference on Advances in Civil and Structural Engineering - CSE 2018* (pp. 5–10). Institute of Research Engineers and Doctors. https://doi.org/10.15224/978-1-63248-145-0-14

Silva-Rêgo, L. L. d., Almeida, L. A. d., & Gasparotto, J. (2022). Toxicological effects of mining hazard elements. *Energy Geoscience*, *3*(3), 255–262. https://doi.org/10.1016/j.engeos.2022.03.003

Singh, R. K., Pal, D., Signh, S. K., Tripathi, N., & Singh, R. S. (2021). Utilization of iron ore tailings for brick manufacture from Donimalai mines of Karnataka, India. *Journal of Scientific & Industrial Research*, *80*(3), 210–220.

Sinha, S. (2022). *Analyzing various factors affecting low-cost housing in urban areas*. ARKA JAIN University.

Sitompul, S. D. T. (2019). The determination of the brick basic price at Toba Trading Company. *International Journal of Advanced Engineering Research and Science*, *6*(9), 76–80. https://doi.org/10.22161/ijaers.69.7

Smita Singh, Aswath M.U and Ranganath R.V. (2020). “Performance assessment of bricks and prisms: Red mud based geopolymer composite”. *Journal of Building Engineering,* 32, 1- 10.

Snellings, R., Mertens, G., & Elsen, J. (2012). Supplementary cementitious materials. *Reviews in Mineralogy and Geochemistry*, *74*(1), 211–278. https://doi.org/10.2138/rmg.2012.74.6

Song, Y., Wang, N., & Yu, A. (2019). Temporal and spatial evolution of global iron ore supply-demand and trade structure. *Resources Policy*, *64*, 101506.

Srividya, T., & Kannan Rajkumar, P. R. (2022). Mechanical and durability properties of alkali-activated binders based paver blocks derived from secondary sources. *Case Studies in Construction Materials*, *17*, e01561. https://doi.org/10.1016/j.cscm.2022.e01561

Stark, T. D., Moya, L., & Lin, J. (2022). Rates and causes of tailings dam failures. *Advances in Civil Engineering*, *2022*. https://doi.org/10.1155/2022/7895880

Stewart, A. G. (2019). Mining is bad for health: A voyage of discovery. *Environmental Geochemistry and Health*, *42*(42). https://doi.org/10.1007/s10653-019-00367-7

Sudhir, M. R., Beulah, M., Sasha Rai, P., & Gayathri, G. (2020). A microstructure exploration and compressive strength determination of red mud bricks prepared using industrial wastes. *2nd International Conference on Manufacturing Material Science and Engineering*, 1–7.

Suresh, V., & Nagaraju, G. B. (2015). Influence of GGBS replacement on strength and durability properties of high performance concrete. *International Journal of Research in Engineering and Technology*, *4*(3), 713–722.

Syed, H., Nerella, R., & Madduru, S. R. C. (2020). Role of coconut coir fibre in concrete. *Materials Today: Proceedings*, *27*, 1104–1110. https://doi.org/10.1016/j.matpr.2020.01.477

Tarigan, U., Prasetya, H. R., & Tarigan, U. P. P. (2018). Establishing value of ceramic solid waste into light weight concrete. *IOP Conference Series: Materials Science and Engineering*, *309*(1), 012121. https://doi.org/10.1088/1757-899X/309/1/012121

Tayebi-Khorami, M., Edraki, M., Corder, G., & Golev, A. (2019). Re-thinking mining waste through an integrative approach led by circular economy aspirations. *Minerals*, *9*(5), 286. https://doi.org/10.3390/min9050286

Tempa, K., Chettri, N., Thapa, G., Phurba, Gyeltshen, C., Norbu, D., Gurung, D., & Wangchuk, U. (2022). An experimental study and sustainability assessment of plastic waste as a binding material for producing economical cement-less paver blocks. *Engineering Science and Technology, an International Journal*, *26*, 101008. https://doi.org/10.1016/j.jestch.2021.05.012

The Energy and Resources Institute. (2001). *Overview of mining and mineral industry in India*. Tata Energy Research Institute, New Delhi.

Thejas, H. K., & Hossiney, N. (2021). A short review on environmental impacts and application of iron ore tailings in development of sustainable eco-friendly bricks. *Materials Today: Proceedings*. https://doi.org/10.1016/j.matpr.2021.09.522

Thejas, H. K., & Hossiney, N. (2022). Alkali-activated bricks made with mining waste iron ore tailings. *Case Studies in Construction Materials*, *16*, e00973. https://doi.org/10.1016/j.cscm.2022.e00973

Thejas, H. K., & Hossiney, N. (2022). Compressed unfired blocks made with iron ore tailings and slag. *Cogent Engineering*, *9*(1). https://doi.org/10.1080/23311916.2022.2032975

Tomiyama, S., & Igarashi, T. (2022). The potential threat of mine drainage to groundwater resources. *Current Opinion in Environmental Science & Health*, *27*, 100347. https://doi.org/10.1016/j.coesh.2022.100347

Toncheva, K., Lakov, L., Jivov, B., & Lepkova, T. (2022). Financial project for building a technological line and factory for the production of yellow pavers, tiles and other products. *International Scientific Journal "Machines. Technologies. Materials"*, *16*(9), 307–314.

Pincha Torkittikul and Arnon Chaipanich **(2010)**. "Utilization of ceramic waste as fine aggregate within Portland cement and fly ash concretes". *Cement & Concrete Composites*, 32,440-449.

Ugama, T. I., Ejeh, S. P., & Amartey, D. Y. (2014). Effect of iron ore tailing on the properties of concrete. *Civil and Environmental Research*, *6*(10), 7–13.

Valéria de Castro Almeida and Ana Catarina Evangelista **(2011)**. "Characterization of Different Types of Ceramic Waste and its Incorporation to the Cement Paste to Evaluate Pozzolanic Reactivity". *International conf. on durability of building material and components. Porto, Portugal*, 1-8.

Venugopal, K., Radhakrishna, K., & Sasalatti, V. (2016). Development of alkali activated geopolymer masonry blocks. *IOP Conference Series: Materials Science and Engineering*, *149*, 012072. https://doi.org/10.1088/1757-899X/149/1/012072

Vo, T. T. D., Tuliao, K. V., & Chen, C. (2022). Work motivation: The roles of individual needs and social conditions. *Behavioral Sciences*, *12*(2), 49. https://doi.org/10.3390/bs12020049

Wang, B., Pan, J., Fang, R., & Wang, Q. (2020). Damage model of concrete subjected to coupling chemical attacks and freeze-thaw cycles in saline soil area. *Construction and Building Materials*, *242*, 118205. https://doi.org/10.1016/j.conbuildmat.2020.118205

Wang, D., Shi, C., Farzadnia, N., Shi, Z., & Jia, H. (2018). A review on effects of limestone powder on the properties of concrete. *Construction and Building Materials*, *192*, 153–166. https://doi.org/10.1016/j.conbuildmat.2018.10.119

Weishi Li, Guoyuan Lei, Xu Ya and Huang Qifei (2018). "The properties and formation mechanisms of eco-friendly brick building materials fabricated from low-silicon iron ore tailings". Journal of Cleaner Production, 204 ,685-692.

White, N. (2005). Mining geology | Exploration. In *Elsevier eBooks* (pp. 613–623). https://doi.org/10.1016/b0-12-369396-9/00239-2

Worlanyo, A. S., & Jiangfeng, L. (2020). Evaluating the environmental and economic impact of mining for post-mined land restoration and land-use: A review. *Journal of*

Environmental Management, *279*, 111623. https://doi.org/10.1016/j.jenvman.2020.111623

Wu, K.-R., Chen, B., Yao, W., & Zhang, D. (2001). Effect of coarse aggregate type on mechanical properties of high-performance concrete. *Cement and Concrete Research*, *31*, 1421–1425. https://doi.org/10.1016/S0008-8846(01)00588-9

Yang, C., Cui, C., Qin, J., & Cui, X. (2014). Characteristics of the fired bricks with low-silicon iron tailings. *Construction and Building Materials*, *70*, 36–42.

Yao, Z., Ji, X., Sarker, P., Tang, J., Ge, L., & Xi, Y. (2015). A comprehensive review on the applications of coal fly ash. *Earth-Science Reviews*, *141*, 105–121. https://doi.org/10.1016/j.earscirev.2014.11.016

Yellishetty, M., Ranjith, P. G., & Kumar, D. L. (2009). Metal concentrations and metal mobility in unsaturated mine wastes in mining areas of Goa, India. *Resources, Conservation and Recycling*, *53*(7), 379–385. https://doi.org/10.1016/j.resconrec.2009.02.005

Yiosese, A. O., Ayoola, A. R., Ugonna, M. C., & Adewale, A. K. (2018). Partial replacement of coarse aggregate with broken ceramic tiles in concrete production. *International Journal of Scientific & Engineering Research*, *9*(8), 81–87.

Young Keun Cho, Sang Hwa Jung and Young Cheol Choi **(2019)**. "Effects of chemical composition of fly ash on compressive strength of fly ash cement mortar ". *Construction and Building Materials*, 204, 255-264.

Yousef, O., Eldein, S., Mohammed, E., Attiya, E., Hassan, H., & Muhammed, A. (2023). Utilization of recycled construction and demolition waste in the manufacture of prefabricated wall claddings to achieve sustainability. *7*(3).

Youssef, N., Rabenantoandro, A. Z., Dakhli, Z., Hage Chehade, F., & Lafhaj, Z. (2019). Environmental evaluation of geopolymer bricks. *MATEC Web of Conferences*, *281*, 03005.

Yu, H., Zahidi, I., Chow, M. F., Liang, D., & Madsen, D. Ø. (2024). Reimagining resources policy: Synergizing mining waste utilization for sustainable construction practices. *Journal of Cleaner Production*, *464*, 142795. https://doi.org/10.1016/j.jclepro.2024.142795

Zhadanovsky, B., Sinenko, S., & Slavin, A. (2018). Processing of exterior light concrete wall panels. *MATEC Web of Conferences*, *193*, 1–5.

Zhang, W., Gu, X., Qiu, J., Liu, J., Zhao, Y., & Li, X. (2020). Effects of iron ore tailings on the compressive strength and permeability of ultra-high performance concrete. *Construction and Building Materials*, *260*, 119917. https://doi.org/10.1016/j.conbuildmat.2020.119917

Zhao, Y., Gu, X., Qiu, J., Zhang, W., & Li, X. (2021). Study on the utilization of iron tailings in ultra-high-performance concrete: Fresh properties and compressive behaviors. *Materials*, *14*(17), 4807. https://doi.org/10.3390/ma14174807

Zhu, X., Zhang, Z., Luan, M., Yang, K., & Li, J. (2024). Temperature-sensitively dissolving of GGBS in neutral and alkali media. *Construction & Building Materials*, *418*, 135353. https://doi.org/10.1016/j.conbuildmat.2024.135353

List of Publications

The findings from this research have been published in one journal article and four conference papers. The corresponding publication details are outlined below.

Journal Article:

[1] Kakodkar, S. A., & Sawaiker, U. G. (2025). High-Performance, Eco-Friendly Blocks from Iron Ore Tailings : A Solution for Sustainable Construction. *Nature Environment and Pollution Technology*, *24*(1), B4220. https://doi.org/10.46488/nept.2025.v24i01.b4220

Conferences:

[1] Satyesh Kakodkar and Ulhas Sawaiker, "Design of Geopolymer Bricks Using Iron Ore Tailings ," National conference on "Recent Advances in Construction Materials and Structures" during February 2-3, 2023, held at PSG College of Technology, Coimbatore.

[2] Satyesh Kakodkar and Ulhas Sawaiker, "Unlocking the potential of Iron Ore Tailings : Towards sustainable construction materials through geopolymerization" at the Third International Scientific Conference on Environmental Research: Issues, Challenges and Strategies for Sustainable Development and Livelihood Security during 1 and 2 December 2023, held at Karwar, Karnataka.

[3] Satyesh Kakodkar and Ulhas Sawaiker *"Green Paving Solutions: Economical Concrete Mix Design with Iron Ore Tailings "* at 1st International Conference on Innovation in Sustainable and Digital Construction Practices (ISDCP 2025), Organized by Department of Civil Engineering, Dayananda Sagar College of Engineering, Bangalore, Karnataka - 560 111, India, during 23-25 January 2025.

[4] Satyesh Kakodkar and Ulhas Sawaiker, *"Reimagining the Future of Construction: A Green Approach Using Iron Ore Waste" at* International Conference on Hospitality, Tourism & Commerce 2025 held at V. M. Salgaocar Institute of International Hospitality Education, Manora-Raia, Goa, India, from 13-15 February 2025.

Patent Filing Details:

Title of the Invention: SUSTAINABLE COMPOSITE CONCRETE WITH ENHANCED COMPRESSIVE STRENGTH AND PREPARATION METHOD THEREOF
Application No.: 202521010598 A
Date of filing of Application: 07/02/2025
Publication Date: 07/03/2025